Cosmological parameter estimation with the Planck satellite data : from the construction of a likelihood to neutrino properties

Marta Spinelli

LAL 15-302
September 2015

UNIVERSITÉ PARIS-SUD XI

École Doctorale: ED-PNC-517
Laboratoire de l'Accélérateur Linéaire - UMR 8607
Centre Scientifique d'Orsay, Bâtiment 200 - BP 34, 91898 Orsay CEDEX - France

Discipline: Sciences de l'univers

THÈSE DE DOCTORAT

soutenue le 28 septembre 2015

par

Marta SPINELLI

pour obtenir le grade de

Docteur en Sciences
de l'Université Paris-Sud, Orsay

Cosmological parameter estimation with the *Planck* satellite data:
from the construction of a likelihood to neutrino properties

Composition du jury :

M.	Krzysztof M. GORSKI	Rapporteur
M.	Julien LESGOURGUES	Rapporteur
M.	Stephane PLASZCZYNSKI	Directeur de thèse
M.	Nicolas REGNAULT	Examinateur
M.	James RICH	Examinateur
M.	Achille STOCCHI	Président du jury

"El universo (que otros llaman la Biblioteca) se componte de un número indefinido, y tal vez infinito, de galerías hexagonales, con vastos pozos de ventilación en el medio, cercados por barandas bajísimas."

Jorge Luis Borges, La biblioteca de Babel

Contents

Introduction 1

Chapter 1 The Cosmic Microwave Background 3

1.1. The CMB and the Hot Big Bang model . . . 3
1.1.1. The Black Body signal . . . 3
1.1.2. Cosmological principles and General Relativity . . . 4
1.1.3. Friedmann equations . . . 6
1.1.4. The distance in an expanding universe . . . 7
1.1.5. The components of the universe . . . 8
1.1.6. The age of the universe . . . 10
1.1.7. Thermal history of the expansion . . . 10
1.2. The horizon problem and the inflation paradigm . . . 14
1.2.1. The cosmological horizon . . . 14
1.2.2. The primordial power spectrum . . . 15
1.2.3. Single field slow roll . . . 17
1.2.4. Reheating . . . 19
1.3. Temperature anisotropies . . . 20
1.3.1. Power spectrum . . . 21
1.3.2. Scalar metric perturbations . . . 23
1.3.3. The Boltzmann equation for photons . . . 23
1.3.4. Initial conditions . . . 23
1.3.5. Primary anisotropies . . . 24
1.3.6. Secondary anisotropies . . . 25
1.4. Polarization anisotropies . . . 28
1.4.1. Stokes parameters . . . 28
1.4.2. All-sky formalism: E and B modes . . . 29
1.4.3. The origin of the polarised signal . . . 30
1.4.4. Quadrupolar anisotropies at recombination . . . 31
1.4.5. Non primordial sources of polarisation . . . 33
1.5. The ΛCDM cosmology . . . 34
1.5.1. C_ℓ computation . . . 36
1.5.2. Observational status of temperature and polarisation . . . 37

Chapter 2 Neutrinos and Cosmology 41

2.1. Neutrinos in the Standard Model . . . 41

2.2. Mass generation mechanisms . . . 42
2.2.1. Dirac or Majorana? . . . 43
2.3. Neutrino mixing . . . 44
2.3.1. Oscillation measurements . . . 44
2.3.2. Neutrino hierarchy . . . 45
2.4. Mass measurements . . . 46
2.5. Neutrinos and the CMB . . . 48
2.5.1. The cosmic neutrino background . . . 48
2.5.2. Effect of Σm_ν on the CMB . . . 49
2.5.3. Effect of $N_{\rm eff}$ on the CMB . . . 50
2.5.4. $N_{\rm eff}$ from particle physics . . . 51
2.5.5. $N_{\rm eff}$ and BBN . . . 51
2.6. Neutrinos constraints from large scale structures . . . 52
2.7. Forecasts from near-future and future experiments . . . 54
2.8. CMB and sterile neutrino constraints . . . 55

CHAPTER 3 The Planck mission 59
3.1. The satellite . . . 59
3.1.1. Cryogenic system . . . 59
3.1.2. Scanning strategy . . . 60
3.2. Detectors characterisation . . . 61
3.2.1. The High Frequency Instrument . . . 62
3.2.2. The Low Frequency Instrument . . . 64
3.3. HFI data treatment . . . 65
3.3.1. TOI processing . . . 66
3.3.2. In-flight characterisation . . . 69
3.3.3. Calibration and map-making . . . 70
3.4. *Planck*-HFI maps . . . 72
3.5. *Planck* foregrounds . . . 73

CHAPTER 4 Estimation of cosmological parameters 81
4.1. The frequency and the subjectivity . . . 81
4.2. Bayesian inference via Markov Chain Monte Carlo methods . . . 82
4.2.1. Monte Carlo integration . . . 83
4.2.2. Markov Chain Monte Carlo . . . 85
4.2.3. Markov chains: basic concepts . . . 85
4.2.4. Metropolis-Hastings algorithm . . . 86
4.2.5. Choice of the Proposal Distribution . . . 89
4.2.6. The Adaptive algorithm . . . 90
4.2.7. Others sampling techniques . . . 91
4.2.8. The question of convergence . . . 93
4.2.9. Implementation of the Adaptive algorithm . . . 100
4.2.10. Cross check with CosmoMC . . . 103
4.3. Frequentist approach . . . 104
4.3.1. Maximum likelihood estimation . . . 105

4.3.2. Profile likelihoods . . . 106
4.3.3. Limit in presence of a boundary . . . 107

CHAPTER 5 The HiLLiPOP high-ℓ likelihood 109
5.1. The basic structure of the high-ℓ likelihood . . . 111
5.2. Maps . . . 112
5.3. Masks . . . 112
5.4. Calculation of spectra: *Xpol* . . . 116
5.4.1. Beam window functions . . . 118
5.4.2. Multipole range . . . 119
5.5. Covariance matrix . . . 119
5.5.1. A semi-analytical calculation . . . 119
5.5.2. Validation on simulations . . . 120
5.5.3. Effect of PS mask on the matrix . . . 120
5.6. Residual foregrounds . . . 122
5.6.1. Galactic dust . . . 125
5.6.2. Unresolved point sources . . . 126
5.6.3. Cosmic Infrared Background . . . 127
5.6.4. Unresolved thermal Sunyaev Zel'dovich (tSZ) component . . . 129
5.6.5. Kinetic Sunyaev-Zeldovich (kSZ) component . . . 130
5.6.6. tSZ-CIB correlation . . . 131
5.7. The likelihood function . . . 131
5.8. Robustness tests . . . 133
5.8.1. Consistency between datasets . . . 133
5.8.2. Masks choice . . . 134
5.8.3. Extended ℓ-range . . . 135
5.8.4. Foreground modelling . . . 137
5.8.5. Effect of calibrations . . . 138
5.9. Comparison of likelihoods . . . 142
5.10. Power spectra and residuals . . . 145

CHAPTER 6 Complementary datasets 153
6.1. The Low-ℓ likelihood . . . 153
6.1.1. Pixel based approach: LowTEB . . . 154
6.1.2. A cross-spectra approach: *lollipop* . . . 157
6.2. The CMB lensing . . . 159
6.2.1. Lensing likelihood and parameter constraints . . . 159
6.3. The very high-ℓ data . . . 161
6.3.1. Foregrounds modelling . . . 161
6.3.2. Likelihoods . . . 163
6.4. The Baryon Acoustic Oscillations . . . 164
6.4.1. A standard ruler . . . 165
6.4.2. BAO measurements . . . 166
6.5. The Supernovae Ia . . . 167
6.5.1. The JLA compilation . . . 168

6.5.2. Supernovae model and distance estimates . . . 168

CHAPTER 7 ΛCDM cosmological parameters 171
7.1. Boltzmann code(s) . . . 171
7.2. *Planck* alone . . . 173
7.2.1. Temperature results . . . 173
7.2.2. Consistency between temperature and polarisation . . . 177
7.2.3. Profile likelihood results . . . 179
7.2.4. Comparison with the `Plik` likelihood . . . 179
7.2.5. Low-ℓ data . . . 181
7.2.6. The $A_{\rm L}$ parameter . . . 182
7.2.7. Constraints on τ . . . 188
7.3. Adding the very high-ℓ data . . . 189
7.3.1. Impact on foregrounds . . . 189
7.3.2. Revised constraints on $A_{\rm L}$ and τ . . . 191
7.4. Adding BAO and Supernovae . . . 193

CHAPTER 8 Neutrino results 199
8.1. Constraints on the absolute scale of neutrino masses . . . 199
8.1.1. High-ℓ temperature alone and the $A_{\rm L}$ issue . . . 200
8.1.2. The addition of VHL data . . . 201
8.1.3. BAO and Supernova data . . . 202
8.1.4. Robustness with respect to the low-ℓ data . . . 202
8.1.5. High-ℓ polarisation . . . 203
8.1.6. Our best upper limit . . . 204
8.1.7. Is there a hint for a neutrino mass? . . . 205
8.2. Constraints on the effective number of neutrino species . . . 206
8.2.1. Temperature constraints . . . 207
8.2.2. Polarisation results . . . 210
8.2.3. Robustness of the TE result . . . 210
8.2.4. Our best constraint . . . 212

Conclusions 215

CHAPTER A Appendix *Planck* products 219
A.1. Catalogues . . . 219
A.1.1. Catalogue of Compact Sources . . . 219
A.1.2. Catalogue of clusters . . . 220
A.2. Component separation maps . . . 221

Introduction

Since its detection in the sixties, the cosmic microwave background (CMB) has offered a privileged window into the evolution of the universe; it has helped in establishing the standard cosmological model and it is still a vivid source of information that pushes the limits of our knowledge beyond what we could ever test in laboratories. Indeed, this bath of photons, relic of the hot Big-Bang, carries the traces of both the rich structure formation of the late time epochs and the energetic early phases of the universe.

The CMB accommodates precise theoretical predictions and confirms that there is, to date, a lot of unknown to be unveiled. One of the interesting open question is the absolute scale of neutrino masses. Neutrinos, known to be massive from oscillation experiments, leave, indeed, a distinct signature in the photon anisotropies, making the CMB an extremely useful tool for testing neutrino physics.

This thesis is focused on the determination of the parameters of the standard cosmological model and on the well motivated extension concerning the neutrino sector, using the *Planck* precise measurements of CMB anisotropies.

The ΛCDM paradigm is described in chapter 1, from the basic principles, to the inflationary theory, focusing on the cosmic microwave background physics and on the mechanism that creates its temperature and polarisation anisotropies. The present status of the CMB observations is also briefly reviewed.

Chapter 2 is a quick panoramic view on the neutrinos, their role in cosmology, and their effect on the CMB spectra.

In chapter 3, the ESA satellite *Planck* is described, along with its analysis pipeline that leads to the production of the CMB all-sky maps, both in temperature and in polarization, that have been used in this thesis.

Chapter 4, is dedicated to the description of the statistical methods needed to extract the cosmological parameters in the comparison between models and data. I present the Bayesian MCMC methods, their qualities and limitations, and I describe the construction of an adaptive algorithm that speeds up convergence. I also describe the frequentist profile likelihood analysis, particularly suited for the estimation of the neutrinos masses.

Chapter 5 details the way the information from the actual signal of the CMB is obtained. This involves a masking strategy for the thermal emission of the Galaxy and for some of the extragalactic contaminations. The residual foregrounds are treated directly at the power spectrum level relying on physically motivated models estimated by the *Planck* collaboration. The construction of the likelihood of the data for the intermediate and high scales is detailed and the robustness tests performed are presented. The characterisation of the likelihood is completed in chapter 6 with the description of the *Planck* large scale data and the external datasets that are used in the estimation of the cosmological parameters: the small scale data from the CMB ground based experiment ACT and SPT, the *Planck* CMB lensing information recontructed from the 4-point correlation function, the Baryon Acoustic Oscillation and the Supernovae.

In chapter 7, are presented the results obtained fitting the parameters of the "vanilla" ΛCDM model, showing the precision reached by the *Planck* satellite data especially in combination with the other datasets. Various robustness test are performed.

This naturally leads to open up the parameter space, pushing the data to a high degree of precision in order to test the neutrino sector, which is performed in chapter 8.

This thesis presents a work done for the *Planck* collaboration and it is the result of a common effort with the members of the *Planck* team at the Laboratoire de l'Accelerateur Lineaire (LAL) in Orsay: F. Couchot, S. Henrot-Versillé, O. Perdereau, S. Plaszczynski, B. Rouillé d'Orfeuil and M. Tristram.

Chapter 1

The Cosmic Microwave Background

Less than 25 years ago, all that had been detected from the microwave universe was a uniform black body signal at temperature T~2.7 K. Since then, the COBE discovery of the temperature anisotropies of the Cosmic Microwave Background (CMB) down to the 10^{-5} level (Smoot et al. 1992), opened the way for the modern cosmology. The ESA *Planck* satellite (chapter 3) has now reached the ultimate precision.

In this thesis, the *Planck* CMB measurements are compared to the accurate theory predictions developed up to now. This chapter recalls some of the basic concepts of modern cosmology (sec. 1.1) and the still open question of inflation (sec 1.2). It is then dedicated to the description of the CMB anisotropies both in temperature (sec. 1.3) and polarisation (sec. 1.4). This panoramic view will allow, in sec. 1.5, to define the ΛCDM model and its cosmological parameters, extensively tested in the rest of this thesis.

1.1 The CMB and the Hot Big Bang model

Discovered in 1965 (Penzias & Wilson 1965), the CMB constitutes a striking evidence that our universe was once dense and hot. The standard cosmological model interprets this thermal radiation as the relic signal from a *recombination* phase, namely when the temperature was weak enough for the electrons and protons to bind forming the first atoms (sec.1.1.7). Since the universe had become transparent for photons, they decoupled from the other constituents.

In this explanation we have assumed two important facts which are pillars of the Hot Big Bang theory: the universe is expanding (as first discovered by Hubble in 1929 (Hubble 1929)) and we associate at each epoch a temperature that decreases with the expansion rate. The fact that the energy of a massless particle scales as $T \propto a^{-1}$ (in other words its wavelength is stretched by expansion), naturally arises in the context of general relativity (GR).

Clearly, the dilution changes reactions between the different constituents of the universe, creating a complex evolution. In this section we briefly reconstruct the principles upon which the Hot Big Bang model is built, using GR in an expanding universe, and summarise the main phases of the evolution.

1.1.1 The Black Body signal

Before recombination, the interaction between photons and electrons allowed the thermalisation of the photon distribution. At decoupling, the CMB radiation is emitted according to Planck's law, meaning it has a spectrum that is determined by the temperature alone

$$I(\nu) = \frac{4\pi\hbar\nu^3/c^2}{e^{2\pi\hbar\nu/k_BT} - 1}. \tag{1.1}$$

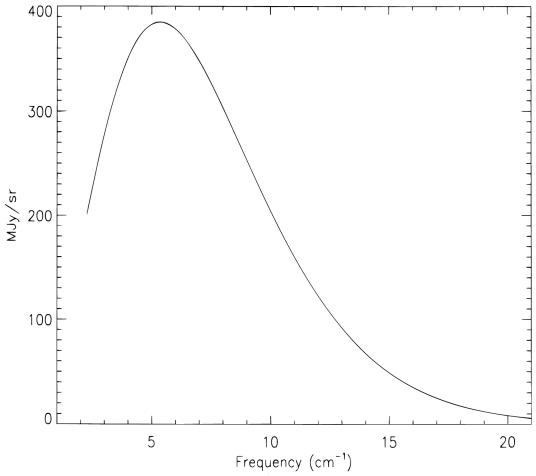

Figure 1.1: FIRAS data fitted by a Planck blackbody spectrum (Fixsen et al. 1996). Uncertainties are a small fraction of the line thickness.

This radiation is (almost) isotropic, i.e. independent of the direction.

The FIRAS instrument of the COBE satellite measured with a great precision the black body spectrum (Fig.1.1), finding $T_{CMB} = 2.725 \pm 0.002$K (Mather et al. 1999).

A blackbody of the measured temperature corresponds to $n_\gamma = (2\zeta(3)/\pi^2)T_\gamma^3 \simeq 411\text{cm}^{-3}$ and $\rho_\gamma = (\pi^2/15)T_\gamma^4 \simeq 4.64 \times 10^{-34}\text{gcm}^{-3} \simeq 0.260\text{eVcm}^{-3}$.

1.1.2 Cosmological principles and General Relativity

The afore mentioned CMB radiation *isotropy* (the universe looks statistically the same in all directions) had been assumed as a more profound characteristic of the model, namely a cosmological principle. It is important to underline that it has to be understood in a statistical sense. The model is also built on the *Copernican Principle*: as observers, we are not in a privileged place. This principle, together with isotropy, implies the *homogeneity* of the universe, namely the fact that it has the same properties at every point (e.g. Lyth & Liddle (2000)). If to assume isotropy we had forgotten the existence of anisotropies at the 10^{-5} level, the assumption of homogeneity requires an even deeper approximation since around us the universe is highly inhomogeneous. This approximation can be anyway considered valid at large scale (more that few Gpc).

The isotropy and homogeneity principles, even before the discovery of the CMB signal, were needed in order to define the metric describing our universe and are essential to solve GR equations.

In GR, the gravitation interaction has to be considered a property of the space time, that is curved in the presence of mass. The space time geometry is then related to the energy content of the universe by the legendary Einstein formula

$$R_{\mu\nu} - \frac{1}{2}Rg_{\mu\nu} + \Lambda g_{\mu\nu} = \frac{8\pi G}{c^4}T_{\mu\nu}, \tag{1.2}$$

where $g_{\mu\nu}$ is the metric tensor, $R_{\mu\nu}$ is the Riemann tensor, and $R = g^{\mu\nu}R_{\mu\nu}$ is the Ricci scalar (the local curvature of the space). We have also added the Λ term, known as the cosmological constant. In the left-hand side of the equation, it can be interpreted as a modification of the geometry of space time. It can also be moved to the right-hand side and interpreted as the intrinsic energy density of the vacuum.

A positive vacuum energy density resulting from a cosmological constant implies a negative pressure (sec. 1.1.3). This negative pressure can drive an accelerated expansion of the universe, as is observed in Supernovae (sec. 1.1.5).

$T_{\mu\nu}$ is the energy–momentum tensor. For a perfect fluid, i.e. with no heat conduction nor viscosity, of pressure p and density ρ, assuming homogeneity, it reads in comoving coordinates

$$T^{\mu}_{\nu} = \begin{pmatrix} -\rho & 0 & 0 & 0 \\ 0 & p & 0 & 0 \\ 0 & 0 & p & 0 \\ 0 & 0 & 0 & p \end{pmatrix}. \tag{1.3}$$

Friedmann-Lemaitre-Robertson-Walker metric

The significance of the metric tensor can be glimpsed in the following:

$$ds^2 = g_{\mu\nu} dx^{\mu} dx^{\nu}. \tag{1.4}$$

ds^2 represents the space-time interval between two point labelled by x^{μ} and $x^{\mu} + dx^{\mu}$. The metric tensor determines all the geometrical properties of the space time described by the system of coordinates x^{μ} (e.g. Coles & Lucchin (2002)). The hypothesis of homogeneity of the universe has as a consequence the existence of a synchronous coordinate system, where a *proper time* can be defined (e.g. Durrer (2008)). Every observer, at the time t, measures the same properties (density, temperature, ..).

The metric thus take the form

$$ds^2 = -c^2 dt^2 + \gamma_{ij} dx^i dx^j. \tag{1.5}$$

Imposing isotropy and homogeneity on the spatial metric tensor γ_{ij} one finds the Friedmann-Lemaitre-Robertson-Walker (FLRW) metric (Friedman 1922; Lemaitre 1931; Robertson 1936; Walker 1937)

$$ds^2 = -c^2 dt^2 + a(t)^2 \left[\frac{dr^2}{1 - kr^2} + r^2 d\theta^2 + r^2 sin^2\theta d\phi^2 \right]. \tag{1.6}$$

where $a(t)$ is a scale factor that has the dimension of a length (normalised such as $a(t_0) = 1$) and r, θ, ϕ are the spherical comoving coordinates, i.e. r is the proper radial coordinate rescaled by a.

The parameter k can take three values: $k = 1, 0, -1$, corresponding, respectively, to the hyper-spherical (positive curvature), Euclidean and hyperbolic (negative curvature) cases.

Observational evidences point to the classical, flat, Euclidean space as we will see in chapter 7.

An essential quantity characterizing the FLRW spacetime is the expansion rate

$$H \equiv \frac{\dot{a}(t)}{a(t)} \tag{1.7}$$

The *Hubble parameter* H has units of inverse time and is positive for an expanding universe.

It takes typically of the order of one *Hubble time* H^{-1} for the universe to expand appreciably, and while this is happening lights travels of the order of one *Hubble length* cH^{-1} (e.g. Lyth & Liddle (2000)).

The Hubble constant H_0 is the value of H today ($H(t_0)$) and is conventionally written as

$$H_0 = 100h \mathrm{kms}^{-1}\mathrm{Mpc}^{-1} \tag{1.8}$$

1.1.3 Friedmann equations

From the Einstein equation 1.2, making explicit the metric to be the FLRW one we end up with the Friedmann equations (e.g. Coles & Lucchin (2002) or Dodelson (2003))

$$\left(\frac{\dot{a}}{a}\right)^2 = \frac{8\pi G}{3}\rho + \frac{\Lambda}{3} - \frac{k}{a^2}, \tag{1.9}$$

$$\frac{\ddot{a}}{a} = -\frac{4\pi G}{3}(\rho + 3p) + \frac{\Lambda}{3}. \tag{1.10}$$

Combining Eq.1.9 and 1.10 we find the continuity equation

$$\dot{\rho} + 3\frac{\dot{a}}{a}(\rho + p) = 0. \tag{1.11}$$

This latter can also be derived by the conservation of the energy-momentum tensor ($D^\mu T_{\mu\nu} = 0$). Rewritten as $d(\rho a^3) = -pd(a^3)$, it can be interpreted as the first law of thermodynamic ($dU = -pdV$). From Eq.1.11 , assuming a relation between the density and the pressure of the type $p = \omega\rho$, one obtains

$$\rho \propto a^{-3(1+\omega)}. \tag{1.12}$$

Different cases can be distinguished:

- $\omega = 0$ describes non relativistic matter (pressureless fluid, $p_{nr} = 0$)

$$\rho_{nr} \propto a^{-3} \tag{1.13}$$

- $\omega = \frac{1}{3}$ describes radiation ($p_r = \frac{1}{3}\rho_r$)

$$\rho_r \propto a^{-4} \tag{1.14}$$

  accounting for the decrease of energy per particle as the universe expands.

- $\omega = -1$ describes the energy density of the vacuum, i.e the case with

$$\rho_v = \text{const.} \tag{1.15}$$

  In this case $\dot{\rho} = 0$ and hence $\rho_v = -p_v$.

- $\omega = -\frac{1}{3}$ describes the curvature energy density, the term $-\frac{k^2}{a^2}$ in Eq.1.9. We have

$$\rho_k \propto a^{-2}. \tag{1.16}$$

One can defines $\Omega_m = \frac{\rho_{nr}}{\rho_{crit}}$ and $\Omega_r = \frac{\rho_r}{\rho_{crit}}$, where $\rho_{crit} = \frac{3H^2}{8\pi G}$, $\Omega_\Lambda = \frac{\Lambda}{3H^2}$ and $\Omega_k = -\frac{k}{H^2a^2}$, to rewrite Eq.1.9 as

$$\Omega_r + \Omega_m + \Omega_\Lambda + \Omega_k = 1, \tag{1.17}$$

hence, the sum $\Omega_r + \Omega_m + \Omega_\Lambda$ determines the geometry of the universe.

Data show a preference for a flat universe where the total energy density is very close to the critical value defined above. In fact, from Eq.1.9, one can see that $\Omega_k = 0$ implies, if the cosmological constant term is neglected, $\rho = \rho_{crit}$.
This solution requires an unnatural fine tuning of the value of the curvature in the early time (unless the metric is Euclidean). This *flatness problem* of the universe is solved by inflation (sec.1.2).

Constraining these parameters using *Planck* data is the main goal of this thesis. In a few words, this is done comparing the CMB temperature power spectrum obtained from *Planck* data (chapter 5), with its theoretical shape that is a function of these parameters (sec.1.3.1 and 1.5.1).
Additional constraints can be obtained using late time distance measurements (chapter 6) since they are also function of these parameters, hence, in sec.1.1.4 we briefly revise some definitions of distance. In sec. 1.1.5 we anticipate the status of present understanding of the composition of the universe (see also Fig.1.13(b)). We will present in more details the measurements in chapter 7.

1.1.4 The distance in an expanding universe

The notion of distance in an expanding universe is not uniquely determined. For example, *comoving* distances remains fixed as universe expands while *physical* distances grows simply because of expansion.

Among comoving distances, the most important one is the distance the light could have travelled (in absence of interaction) since $t = 0$. With the convention $c = 1$ we have

$$\eta \equiv \int_0^t \frac{dt'}{a(t')} \tag{1.18}$$

Actually, since it is monotonically growing, η can be read as a time variable, the *conformal time*.

We can also define the comoving distance between a distant emitter and us

$$\chi(a) = \int_{t(a)}^{t_0} \frac{dt'}{a(t')} = \int_a^1 \frac{da'}{a'^2 H(a')}. \tag{1.19}$$

If we consider a flat, matter dominated (MD) universe (which for low red-shift is a fair assumption as discussed in sec.1.1.7), the integral has an analytical solution and one obtains (e.g. Dodelson (2003))

$$\chi^{\text{Flat,MD}} = \frac{2}{H_0}\left[1 - a^{1/2}\right] = \frac{2}{H_0}\left[1 - \frac{1}{\sqrt{1+z}}\right], \tag{1.20}$$

where we have used $(1 + z) = a^{-1}$.
The comoving distance goes as z/H_0 for small z and then asymptotes to $2/H_0$ for large z (Fig.1.2(a)).

From the metric of Eq.1.6, the *proper distance* can be defined,

$$D_{\text{proper}}(t) = \sqrt{|ds^2|} \tag{1.21}$$

namely the distance between two object that would be measured by a series of observers, located along the line relying two.
This can be rewritten in term of the comoving distance as

$$D_{\text{proper}}(t) = a(t)\chi. \tag{1.22}$$

Deriving with respect to time t and using Eq.1.7, one finds

$$\dot{D}_{\text{proper}}(t) = \dot{a}(t)\chi = H D_{\text{proper}}(t), \tag{1.23}$$

that is the Hubble law, i.e. the universe is expanding.

In practice the proper distance cannot be measured and other definitions of distance are needed.

The *angular diameter distance* is the ratio between the physical size of an object l and the angular size θ of the object as viewed from earth, i.e.

$$D_A = \frac{l}{\theta}. \tag{1.24}$$

It depends on the assumed cosmology of the universe as

$$D_A = \begin{cases} \frac{a}{H_0\sqrt{|\Omega_k|}} sinh(\sqrt{\Omega_k} H_0 \chi) & \text{if } \Omega_k > 0 \\ a\chi & \text{if } \Omega_k = 0 \\ \frac{a}{H_0\sqrt{|\Omega_k|}} sin(\sqrt{-\Omega_k} H_0 \chi) & \text{if } \Omega_k < 0. \end{cases} \tag{1.25}$$

Note that, if the universe is flat, D_A is a good approximation to the proper distance. For this flat case, in Fig.1.2(a), is shown the behaviour of D_A with and without a cosmological constant contribution.

Distances can also be inferred measuring the flux of an object of known luminosity L. From the definition of flux in an expanding universe one can define the *luminosity distance* as

$$D_L \equiv \frac{\chi}{a}. \tag{1.26}$$

The distance D_L is larger in an universe with a cosmological constant than in one without, as it was for the other distances (Fig.1.2(a)).

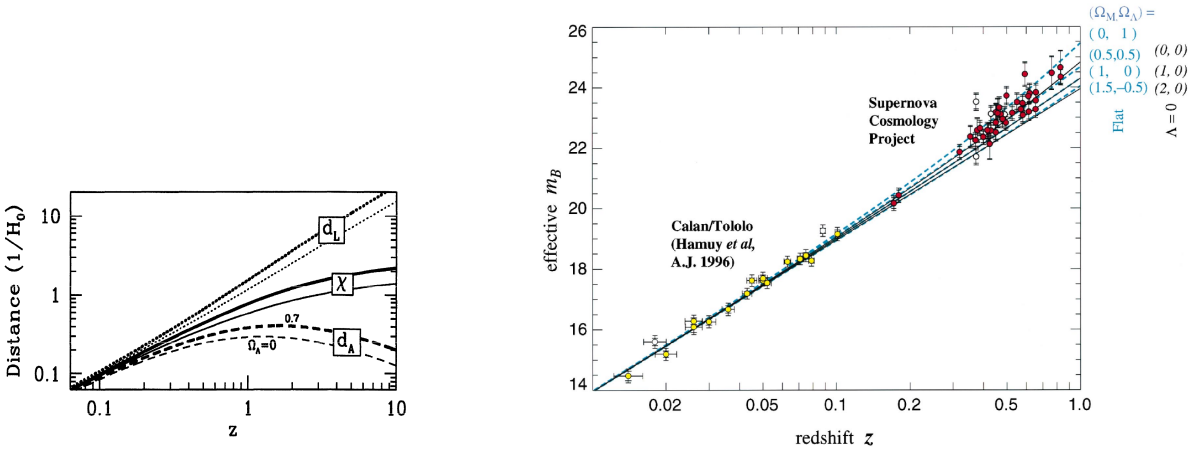

(a) (b)

Figure 1.2: (a) The comoving distance χ, the angual diameter distance d_A and the luminosity distance d_L in a universe with matter only (light curves) or with $\Omega_\Lambda = 0.7$ contribution. In the three cases these distances are larger in a Λ-dominated universe. The figure is take from Dodelson (2003). (b) Hubble diagram for 42 high-redshift type Ia supernovae from the Supernova Cosmology Project and 18 low-redshift type Ia supernovae from the Calan/Tololo Supernova Survey. The solid curves are the theoretical apparent magnitudes m (Eq. 1.30) for a range of cosmological models (Perlmutter et al. 1999).

1.1.5 The components of the universe

In sec.1.1.3 it has been shown how the different constituents of the universe evolves with the expansion. Their present value are inferred via different direct and indirect measurements. We summarise here, before entering in the detail of the CMB constraints, the present general understanding of the composition of the universe.

Radiation

The standard radiation component includes photons, neutrinos (with the approximation $m_\nu = 0$). It constitutes today only the ~0.008% of the total energy content of the universe. The *physical* energy density of photons is well measured. From the value of ρ_γ of sec.1.1.1, one can compute

$$\omega_\gamma \equiv \Omega_\gamma h^2 = 2.47 \times 10^{-5}. \tag{1.27}$$

In the massless limit, from entropy conservation one can compute the neutrino temperature and hence their energy density to be

$$\omega_\nu \equiv \Omega_\nu h^2 = 1.68 \times 10^{-5}. \tag{1.28}$$

Only recently, since the universe is cooling down they became non relativistic and hence their physical energy density can be rewritten in terms of their absolute mass scale

$$\Omega_\nu h^2 = \frac{\sum m_\nu}{93.14 \text{ eV}}. \tag{1.29}$$

Cosmological neutrinos are discussed in more details in chapter 2.

Baryons

In the literature, the nuclei and electrons in the universe are usually referred to as *baryons*. They can not be described as a gas with a certain temperature as is done for photons and massless neutrinos, so their energy density needs to be measured. As baryons are considered within the non relativistic matter, the parameter Ω_b scales as a^{-3}. There are several, different techniques to infer Ω_b. In chapter 2 we will briefly mention some direct measurements. The CMB anisotropies measure the physical energy density $\Omega_b h^2$. Roughly, all measurements agree that baryons constitutes only the 2-5% of the total energy budget, even if most of this standard matter remains entirely invisible within large atomic or molecular hydrogen clouds. This value implies however that all the rest of the energy density is of "dark" nature.

Dark matter

The ~23% of the energy density is believed to be *dark* matter (DM): something subject to gravity but weakly interacting with the other constituents of the universe. Considered as non relativistic, it scales, as baryons, with a^{-3} as the universe expands.

DM is still an open paradigm still to be included in what we know about the physical laws of the universe and is a vivid sector of research. The simplest paradigm describes DM as a "dust" component (its particles have a negligible velocity as far as structure formation is concerned), i.e. a *cold* component. The parameter $\Omega_c \sim 0.23$ can be measured with several techniques, including galaxy distributions (chapter 6). CMB anisotropies measure the physical density $\omega_c \equiv \Omega_c h^2$ as described is chapter 7.

More complex scenario with dark matter made up with a cold and a hot component are more likely to be the right modelling. In this context also massive neutrinos can have a non-negligible effect (Dodelson 2003).

Dark energy

From Fig.1.13(b) is clear that the the majority (the ~73%) of the total energy density is something of unknown nature. Supporting evidences for the existence of the Dark energy (DE) came from the supernovae observations in 1998 that lead the groups of Riess and Perlmutter (Riess et al. 1998; Perlmutter et al. 1999) to the Nobel prize.

The luminosity distance of Eq.1.26 can be used to rely the apparent magnitude m and the absolute magnitude M of a source (e.g. Dodelson (2003))

$$m - M = 5log\left(\frac{D_L}{10pc}\right) + K, \tag{1.30}$$

where K is a correction factor. The SNIa are considered standard candles, so they have nearly identical absolute magnitude after correcting the light-curve width-luminosity relation (chapter 6). In Fig.1.2(b) is shown the Hubble diagram reported in Perlmutter et al. (1999), pointing to $(\Omega_m, \Omega_\Lambda)$=(0.28, 0.72).

DE started to be important at late times. This means that the CMB is only slightly sensitive to it. It is anyway possible to put constraints, especially combining CMB with large scale structure measurements (Planck Collaboration. XIII. 2015).

1.1.6 The age of the universe

Roughly speaking, the various measurements up to now point towards a universe with $\{\Omega_m \simeq 0.3, h \simeq 0.7$ and $\Omega_\Lambda \simeq 0.7\}$. This *concordance* model (sec.1.5) allows to accommodate different direct and indirect measurements. One can trace the evolution of the Hubble "constant" using the measured present value of these parameters

$$H^2 = H_0^2\left[\Omega_m(1+z)^3 + \Omega_r(1+z)^4 + \Omega_k(1+z)^2 + \Omega_\Lambda\right], \tag{1.31}$$

and hence estimate the age of the universe at a certain redshift z

$$t(z) = \int_z^\infty \frac{dz'}{(1+z')H(z')}. \tag{1.32}$$

The age of the universe today (at $z = 0$), using these value of the concordance model, gives roughly 14 Gyr, in agreement with the *Planck* results of 13.8 Gyr (Planck Collaboration. XIII. 2015).

1.1.7 Thermal history of the expansion

If one forgets the very first instants of the universe and the investigation of what is really behind the initial singularity of the Big Bang model, then it is quite fair to say that the evolution of the universe is well know. Constituents were in thermal equilibrium in the early phases, then, as a consequence of the expansion, different species lost thermal contact with the rest and left traces in their history.

A particle is in thermal equilibrium if its interaction rate Γ is greater than the expansion of the universe, namely

$$\Gamma \gg H. \tag{1.33}$$

Here $\Gamma \sim n\sigma$, with n the particle density and σ the relevant cross section. Rewriting Eq.1.9 and considering that $\rho \propto T^4$ at sufficient early times, one also has $H \sim T^2/M_{\rm pl}$.

Around $T \sim 100$ MeV the quark hadronisation takes place and the universe is made of protons, neutrons, electrons, positrons and neutrinos. The temperature is high enough for thermal equilibrium to hold, and the non relativistic matter (for which $T \ll m$) undergoes Maxwell-Boltzmann suppression, i.e. the number density reads[1]

$$n_{\rm eq} = g\left(\frac{mT}{2\pi}\right)^{3/2} e^{-m/T}. \tag{1.34}$$

[1] In a general discussion the chemical potential can be neglected (Dodelson 2003).

Neutrinos are also kept in equilibrium by process such as $\nu e \rightarrow \nu e$ and, as fermions, obey the Fermi-Dirac distribution

$$n_{\rm eq} = g \int \frac{d^3p}{(2\pi)^3} f_{\rm eq}(p) \text{ with } f_{\rm eq}(p) = \frac{1}{e^{p/T}+1} \tag{1.35}$$

A typical cross section is $\sigma(\nu e \rightarrow \nu e) \sim G_F^2 E^2 \sim G_F^2 T^2$, where G_F is the Fermi's constant.
Since electrons are still relativistic at this epoch, their number density is $n_e \sim T^3$, hence,

$$\Gamma \sim \sigma n_e \sim G_F^2 T^5. \tag{1.36}$$

One finds that equilibrium is lost when

$$H \sim T^2/M_{\rm pl} > \Gamma \sim G_F^2 T^5, \tag{1.37}$$

thus the temperature of neutrinos decoupling is

$$T_{\rm dec} \sim \left(\frac{1}{M_{\rm pl} G_F^2}\right)^{1/3} \sim \text{ few MeV} \tag{1.38}$$

This cosmic neutrino background is discussed further in chapter 2. Constraining its properties through CMB measurements is one of the goals of this thesis.

Shortly after neutrino decoupling, electron and positrons annihilate leaving the universe only with electrons as a consequence of baryon asymmetry.
At T ~0.1 MeV, when the universe is only a few minutes old, temperature is low enough for first nucleus to form. The Big Bang Nucleosynthesis (BBN) is sensitive to neutrino physics. A more detailed discussion is postponed to chapter 2.

Eq.1.13 and 1.14 tell us that, even if at early times the radiation was dominating (RD) (i.e. the majority of the constituents were relativistic), at a certain moment in the evolution of the universe the non relativistic matter started to dominate over radiation. Matter domination (MD) is fundamental since structures can grow only in this case (e.g Dodelson (2003)).

One can compute the redshift of the *equality* simply stating $\rho_r = \rho_m$, obtaining

$$a_{eq} = \frac{4.15 \times 10^{-5}}{\Omega_m h^2} \Rightarrow z_{eq} \sim 3100. \tag{1.39}$$

At this redshift the universe was already 60000 years old.

After nucleosynthesis is complete and well inside the MD era, the temperature drops to ~1 eV. Compton scattering has coupled till now photons and electrons and Coulomb scattering has coupled electrons and protons. The binding energy of hydrogen atoms is $B_H = m_p + m_e - m_H = 13.6$ eV so one would expect them to be already formed. However, since the photon/baryon ratio is high ($\eta_{b\gamma} \sim 10^{-9}$), radiation destroys any new atoms via the reaction

$$p^+ + e^- \leftrightharpoons \gamma H \tag{1.40}$$

While this reaction is in equilibrium, from the Boltzmann equation (the formalism describing the rate of change in the abundance of a given particle as the rate of producing and eliminating this species, e.g.Dodelson (2003)) one can rewrite

$$\frac{n_e n_p}{n_H} = \frac{\chi_e^2}{1-\chi_e} = \frac{1}{n_e + n_H}\left[\left(\frac{m_e T}{2\pi}\right)^{3/2} e^{-B_H/T}\right], \tag{1.41}$$

where

$$\chi_e \equiv \frac{n_e}{n_e + n_H} = \frac{n_p}{n_p + n_H}. \tag{1.42}$$

and $n_e = n_p$ is a consequence of the neutrality of the universe.
Eq.1.41 is called the *Saha approximation* (Fig.1.3) and predicts correctly the redshift of recombination to be $z_* \sim 1000$ and T~0.25 eV. Nevertheless, it neglects the (small) number of helium atoms and fails as the electron fraction diminishes and the system goes out of equilibrium. The correct solution is shown in Fig.1.3.

The recombination era is directly related to the *decoupling* of photons. Decoupling occurs roughly when the interaction rate between electrons and photons becomes smaller than the expansion rate. The scattering rate is $n_e \sigma_T = \chi_e n_b \sigma_T$, where $\sigma_T = 0.665 \times 10^{-24} cm^2$ is the Thompson cross section. When χ_e becomes smaller than $\sim 10^{-2}$, photons decoupled (e.g. Dodelson (2003)). Given how fast χ_e drops to zero, decoupling happens during recombination (Fig.1.3).

These photons, once lost the contact with the thermal bath, redshift as the universe expands and constitute now the Cosmic Microwave Background radiation. The small anisotropies of this signal depends on the physics at recombination and are the powerful cosmological observable used in this thesis. Their shape is discussed further in sec.1.3.

The signal is anyhow almost isotropic. This experimental evidence is one of the motivation at the base of the development of the theory of inflation described in the next section.

A schematic representation of the history of the expansion can be found in Fig.1.4, where the main phases are highlighted.

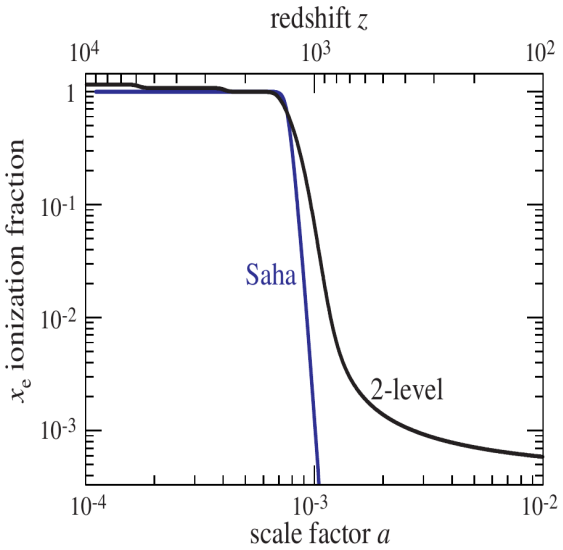

Figure 1.3: The ionization fraction χ_e as a function of the scale factor (and redshift). In blue is shown th *Saha approximation* (see text). In Black is shown a more accurate recombination model. The figure is taken from Hu (2008).

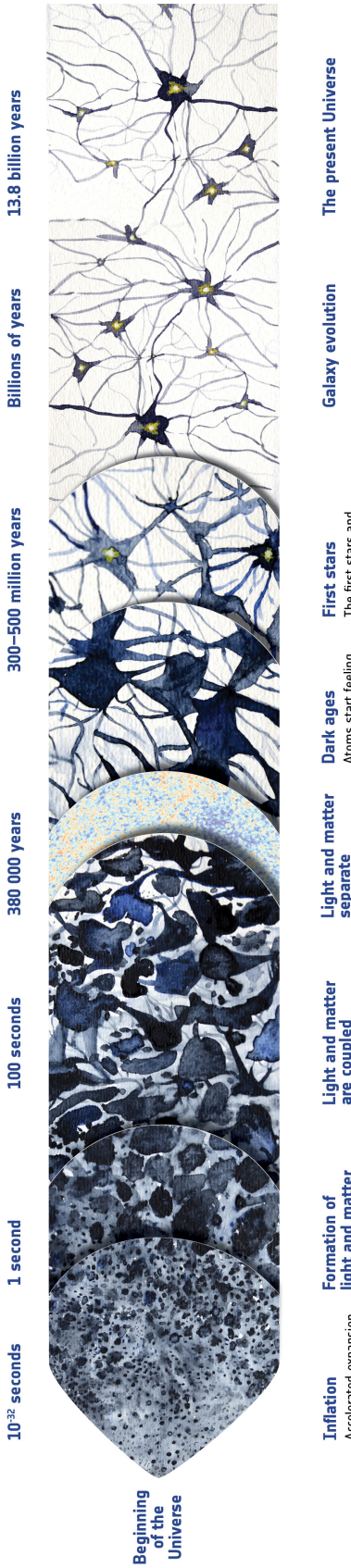

Figure 1.4: Schematic view of the different phases of the evolution of the universe. From the ESA *Planck* website http://www.cosmos.esa.int/web/planck

1.2 The horizon problem and the inflation paradigm

On all observed scales the CMB is very close to isotropic. But if the universe has an age, why is the CMB temperature so uniform? All objects separated by a comoving distance larger than the conformal time η (sec.1.1.4) have *never* been in causal contact, how could some causal physics have washed away strong deviation from isotropy? The standard solution to this *horizon problem* is that the universe underwent a phase of exponential expansion, the inflation (Guth 1981).

Inflation is not only able to increase the causal horizon at the time of decoupling explaining homogeneity (sec.1.2.1), but also to dilute curvature justifying why the total density today is so close to the critical one (sec.1.1.3).

Moreover, inflation is able to give an origin to the fluctuations we observe today (sec.1.2.2). In this section we summarise some basic concepts about inflation.

1.2.1 The cosmological horizon

We want to find the set of point able of sending light signals that could have been received by an observer in O up to some generic time t. The *paricle horizon*, namely the proper distance (sec.1.1.4) between the an observer and the horizon is

$$d_H(t) \equiv \int_0^{x_H} \sqrt{g_{\mu\nu} dx^\mu dx^\nu} = \int_0^{x_H} a(t) c d\eta = a(t) c\eta(t) = a(t) \int_0^t \frac{cdt'}{a(t')} \tag{1.43}$$

where we have used the metric of Eq.1.6. $d_H(t)$ is the product between the scale factor at the time of the observer and the *comoving distance* the light has travelled from $t = 0$ to t. It can be seen as a spherical surface centred in O and with radius $d_H(t)$. The observer cannot possibly have received light signals, at any time in its history, from sources which are situated at proper distances greater than $d_H(t)$ from him at time t (e.g. Coles & Lucchin (2002)). This definition is valid only if $d_H(t)$ converges to a finite value.

In sec.1.1.2 we have described the matter content of the universe as a perfect isotropic fluid parametrised by the energy momentum tensor T^μ_ν (Eq.1.3). From the conservation of T^μ_ν one obtains the first law of thermodynamic $d(\rho a^3) = -p da^3$, that gives, considering $p = \omega\rho$, the energy density as a function of the scale factor (Eq.1.12). Using the Friedman equations one obtains

$$a(t) \propto t^n \qquad \text{with } n = 2/3(1+\omega) \tag{1.44}$$

If $n < 1$ (thus $\omega > -\frac{1}{3}$) the integral in Eq.1.43 converges and $d_H(t)$ is dominated by the late times. We have $d_H(t) = t/(1-n)$ and so $d_H(t) > t$. This is the case during RD and MD when n is respectively 1/2 and 1/3, giving $d_H^{RD}(t) = 2t$ and $d_H^{MD}(t) = 3/2t$. $d_H(t)$ grows faster than $a(t)$. The expansion is decelerating and more and more galaxies enter in causal contact with the observer.

Assuming MD we can calculate $d_H(t_{CMB})$, where t_{CMB} is the time when the universe became transparent. From the ratio between $d_H(t_{CMB})$ and $d_H(t_0)$ we can deduce the angular size of the patches that have been in causal contact in a Big bang scenario without inflation. It turns out to be $\theta \sim$ few $^\circ$.

This is in contradiction with the isotropy of the CMB that we have discussed in sec.1.1.1, and is called the horizon problem of the hot Big Bang.

Before entering the subject of inflation we first define the *Hubble radius* as the distance from the origin O of an object moving with the cosmological expansion at the velocity of light with respect to O (e.g. Coles & Lucchin (2002)).

$$R_c = c\frac{a}{\dot{a}} = \frac{c}{H} \tag{1.45}$$

For $\omega > -\frac{1}{3}$ the Hubble radius is a multiple of the particle horizon but they are two distinct notions of distance.

The *comoving* Hubble radius is obtained just dividing by the scale factor a thus, taking the convention $c = 1$,

$$\text{comoving Hubble radius} = \frac{1}{aH} = \frac{1}{\dot{a}} \tag{1.46}$$

In order to solve the horizon problem we can imagine that during an early phase the comoving Hubble radius decreased. Particle separated by many Hubble radii today, were in causal contact before this epoch of rapid expansion . The decrease of the comoving Hubble radius implies the acceleration of the expansion,

$$\frac{d}{dt}\left(\frac{1}{\dot{a}}\right) < 0 \Rightarrow \ddot{a} > 0. \tag{1.47}$$

Clearly inflation has to last enough to explain the isotropy of the CMB. The duration of inflation can be characterise by the number of e-folds, namely the logarithm of the ratio of the scales factor when CMB were in causal contact and the end of inflation (e.g. Baumann (2009))

$$N = ln\left(\frac{a(t_{end})}{a(t_{CMB})}\right) \approx 60 \tag{1.48}$$

From the Friedmann equations 1.9 and 1.10 one also deduces that inflation requires a source of negative pressure $p \approx -\rho$ and an energy density ρ which dilutes very slowly ($\dot{\rho} \approx const$). This source of negative pressure can be found using a scalar field (the inflaton) as is discussed in sec.1.2.3. The quantum fluctuations of this field generates the primordial perturbation that have evolved into the structures we see today.

1.2.2 The primordial power spectrum

We see structures today on all scales. They are the outcome of the evolution, by gravitational collapse, of the primordial fluctuations present in the original cosmic fluid. These fluctuations are supposed to be generated by quantum fluctuation of the scalar field ϕ during the inflationary period. We are interested in the amplitude of the fluctuations as a function of scale. In term of Fourier analysis we can thus consider the *comoving wavenumber* k, related to the physical wavenumber as $k_p = ak$. The most useful way to characterise them statistically is via the *power spectrum*, namely the contribution to the variance of the fluctuations per unit logarithmic interval in k. Calling $\delta\phi(x)$, the spatial fluctuation of ϕ one defines

$$\langle \delta\phi(x)\delta\phi^*(x)\rangle = \int_0^\infty P(k)d(ln\ k) \tag{1.49}$$

Using the Fourier transform

$$\delta\phi(x) \propto \int \delta\phi_k e^{i\mathbf{k}\cdot\mathbf{x}} d^3k, \tag{1.50}$$

and considering $d^3k = 4\pi k^2 dk$ and $d(lnk) = dk/k$, one obtains

$$P(k) \propto k^3 |\delta\phi_k|^2. \tag{1.51}$$

Roughly we need to solve for an harmonic oscillator-type equation for the scalar field of which we know the quantised solutions (e.g. Hobson et al. (2006)). Since we are in an expanding universe we have a solution like

$$\delta\phi_k \propto \frac{e^{-ikt/a}}{a\sqrt{2k}} \tag{1.52}$$

The expression for the power spectrum thus reads

$$P(k) \propto \left(\frac{k}{a}\right)^2 \tag{1.53}$$

The idea of inflation is that a fluctuation of fixed comoving scale $1/k$ could have started within the horizon. All scales inside the horizon are connected by causal physics. During inflation, the comoving horizon decreases and when $k = aH$ the mode leaves the horizon and *freezes* (Fig.1.5). To know the amplitude of the primordial fluctuation we just have to evaluate Eq.1.53 at horizon crossing since the mode does not evolve any more after freeze-out.

$$P(k) \propto H^2|_{horizon\ crossing} \tag{1.54}$$

H is more or less constant during inflation (sec.1.2.3) but decreases slightly as time progress. This depends on the details of the inflation and on the choice of the potential for the *inflaton*. One gets approximately equal power per unit logarithmic interval in k as a function of k in the power spectrum coming out from inflation, but with a slightly reduced amplitude for fluctuations at large k (later times correspond to horizon exit of larger scales). The precision of the data from the *Planck* satellite allows to test this slight deviation from scale invariance. Inflation generates both scalar and tensor perturbation to the metric (sec.1.2.3). Scalar perturbations to the metric couple to the density of matter and radiation and are responsible for inhomogeneities and anisotropies in the universe. Inflation also generates tensor perturbations to the metric that are not coupled to density so do not affect the formation of large scale structures. As is explained in sec.1.4.4, they do contribute to anisotropies in the CMB. For *Planck* analysis the following model for the primordial power spectrum of scalar perturbations are used

$$P_s(k) = A_s \left(\frac{k}{k_*}\right)^{n_s-1} \tag{1.55}$$

where $k_* = 0.002$ Mpc^{-1} is a reference scale roughly in the middle of the scales probed by *Planck*. $n_s = 1$ would correspond to the perfect scale invariance. One of the major results of the 2013 release was indeed that the data show a significant deviation of n_s from scale invariance (Planck Collaboration. XVI. 2014). This is still the case for the data used in this thesis (chapter 7). At the level of the CMB power spectrum, n_s represents the tilt and A_s is the global amplitude of the CMB power spectrum (sec.1.1.5). We briefly mention here also the fact that one can test the *running* of the spectral index adding a term proportional to $\frac{dn_s}{dln\ k}$ in the exponent of Eq.1.55. No convincing evidence for the running has been found (Planck Collaboration. XVI. 2014; Planck Collaboration. XIII. 2015).

Regarding tensor perturbations we can write

$$P_t(k) = A_t \left(\frac{k}{k_*}\right)^{n_t} \tag{1.56}$$

where again $k_* = 0.002$ Mpc^{-1}. For the tensor power spectrum, scale invariance is achieved with $n_t = 0$. Actually, we fit in our analysis for the famous (after the BICEP-Planck case) parameter r defined as

$$r(k = k_* = 0.002\ \text{Mpc}^{-1}) = r_{0.002} = A_t/A_s \tag{1.57}$$

We discuss in some more details this parameter in sec.1.4.4.

Both n_s and n_t depend on the details of the inflationary theory considered. In the following section the simplest case of a single field inflation is considered and the *slow roll* condition is presented.

To complete the picture we have to add that after the end of inflation the comoving Hubble radius start to grow again as expected for standard cosmology. As already discussed, the causal contact is possible only when the mode re-enters the horizon (Fig.1.5). Clearly, the time of re-entering characterise the type of evolution the perturbation will have.

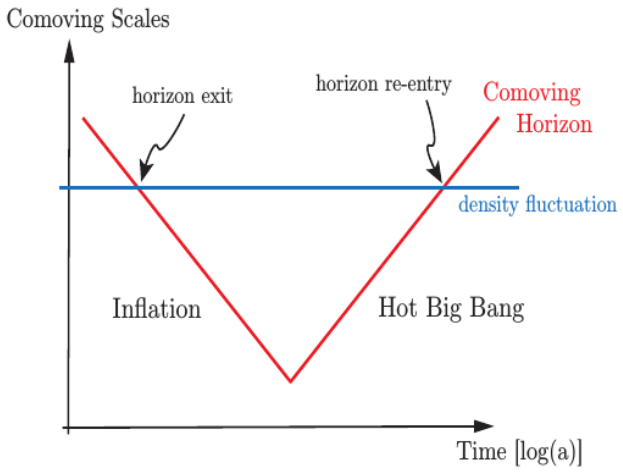

Figure 1.5: Solution of the horizon problem. All scales that are relevant to cosmological observations today were larger than the Hubble radius until $a \sim 10^{-5}$. However, at sufficiently early times, these scales were smaller than the Hubble radius and therefore causally connected. Similarly, the scales of cosmological interest came back within the Hubble radius at relatively recent times.(Baumann 2009)

1.2.3 Single field slow roll

We have seen that the scales that would otherwise be disconnected, can correlate if inflation took place, ensuring that the CMB is (almost) isotropic on all scales of interest today. Perturbations were produced when the scales were causally connected and persisted after inflation, and transformed into the actual structures.

During inflation the universe consisted primarily of a uniform scalar field ϕ and a uniform background metric. Against this background the fields fluctuate quantum mechanically with a zero average fluctuation but a non null variance (Dodelson 2003). There is in literature a large variety of families of inflationary models. Here we describe the simplest one, namely the single field inflation. The choice for the shape of the potential $V(\phi)$ depends on the details of the model.

On general ground one needs to have:

- negative pressure (sec.1.2.1)
- an almost constant H
- a duration sufficient to shrink enough the comoving Hubble horizon $(aH)^{-1}$
- creation of standard model particles (reheating) at the end of the process (sec.1.2.4)

The condition for inflation from relation 1.47 can be rewritten as

$$-\frac{\dot{H}}{H^2} < 1 \tag{1.58}$$

meaning that H varies slowly on the Hubble timescale. If $|\dot{H}| \ll H^2$, then H is almost constant over many Hubble times and we have almost an exponential expansion, $a \propto e^{Ht}$.

We have already seen that to have in order to have an almost exponential expansion we need $p \approx -\rho$. If we assume that the energy density and pressure of the cosmic fluid are dominated by scalar fields, the necessary negative pressure is achieved if the fields do not vary too rapidly (e.g. Lyth & Liddle (2000)).

The dynamic of the scalar field minimally coupled to gravity can be described by the action (e.g.(Baumann 2009))

$$S = \int d^4x \sqrt{-g}\left[\frac{M_{Pl}^2}{2}R + \frac{1}{2}g^{\mu\nu}\partial_\mu\phi\partial_\nu\phi - V(\phi)\right] \tag{1.59}$$

where $M_{Pl}^2 = (8\pi G)^{-1}$. From this we can derive the energy momentum tensor

$$T_{\mu\nu} \equiv -\frac{2}{\sqrt{-g}}\frac{\delta S_\phi}{\delta g^{\mu\nu}} = \partial_\mu\phi\partial_\nu\phi - g_{\mu\nu}\left(\frac{1}{2}\partial^\sigma\phi\partial_\sigma\phi + V(\phi)\right). \tag{1.60}$$

Assuming the metric of Eq.1.6 and supposing the universe homogeneous (hence $\phi(t, \mathbf{x}) \equiv \phi(t)$) one can compare this latter result to Eq.1.3, where the density is $\rho = -T_0^0$ and the pressure is $p = T_i^i$, obtaining

$$\rho_\phi = \frac{1}{2}\dot{\phi}^2 + V(\phi), \tag{1.61}$$

$$p_\phi = \frac{1}{2}\dot{\phi}^2 - V(\phi). \tag{1.62}$$

Also, using these into the Friedman equation (Eq.1.9) considering a flat universe and a Klein-Gordon equation for the scalar field, one obtains

$$3M_{Pl}^2H^2 = \frac{1}{2}\dot{\phi}^2 + V(\phi) \qquad \text{and} \qquad \ddot{\phi} + 3H\dot{\phi} + V' = 0 \tag{1.63}$$

where $V' \equiv \partial V/\partial\phi$.

From Eq.1.62 is clear that to have a negative pressure we need the potential energy term $V(\phi)$ to be more important than the kinetic term (Fig.1.6). We can rewrite 1.58 as

$$\varepsilon \equiv -\frac{\dot{H}}{H^2} = \frac{\frac{1}{2}\dot{\phi}^2}{M_{Pl}^2H^2} \tag{1.64}$$

The condition for inflation is thus $\varepsilon < 1$. Note that, in term of the scalar field components, it contains the same condition discussed before: we need *slow roll* condition, $\frac{1}{2}\dot{\phi}^2 \ll V(\phi)$ Actually the kinetic energy stays small and slow roll persists also if the acceleration of the field is small, $\ddot{\phi} \ll 3H\dot{\phi} \sim V'$. The condition for prolonged slow-roll inflation can be expressed as conditions on the shape of the potential, using Eq. 1.63 (Steinhardt & Turner 1984)

$$\epsilon \equiv \frac{M_{Pl}^2}{2}\left(\frac{V'}{V}\right)^2 \ll 1 \qquad \text{and} \qquad |\eta| \equiv M_{Pl}^2\frac{|V''|}{V} \ll 1 \tag{1.65}$$

A proper calculation of the primordial power spectra for scalar and tensor modes leads to (e.g. Dodelson (2003))

$$P_s(k) = \frac{1}{8\pi^2\epsilon}\left.\frac{H^2}{M_{Pl}^2}\right|_{k=aH} \tag{1.66}$$

$$P_t(k) = \frac{2}{\pi^2}\left.\frac{H^2}{M_{Pl}^2}\right|_{k=aH} \tag{1.67}$$

From Eq.1.57 we obtain $r = 16\epsilon$. Interestingly, both n_s and n_t can be written in terms of the *slow roll* parameters

$$n_s = 1 - 4\epsilon - 2\eta \tag{1.68}$$
$$n_t = -2\epsilon \tag{1.69}$$

The fact that n_t is proportional to ϵ and thus proportional to the tensor-to-scalar ratio r is one of the important prediction of inflation. This consistency relation

$$r = -8n_t \tag{1.70}$$

constitutes an important test of inflationary theories. In *Planck* analysis however, we assume the single field slow roll inflation and, as a consequence, the consistency relation to hold. Allowing r free to vary we can indeed set an upper limit on r (chapter 6.1). As a last remark we can write (e.g. Baumann et al. (2009))

$$V^{1/4} = 1.06 \times 10^{16}\text{GeV}\left(\frac{r}{0.01}\right)^{1/4} \tag{1.71}$$

that allows to relate r directly to the energy scale of inflation V. A detectable tensor amplitude would confirm that inflation occurred at energy comparable to the Grand Unification Theory scale.

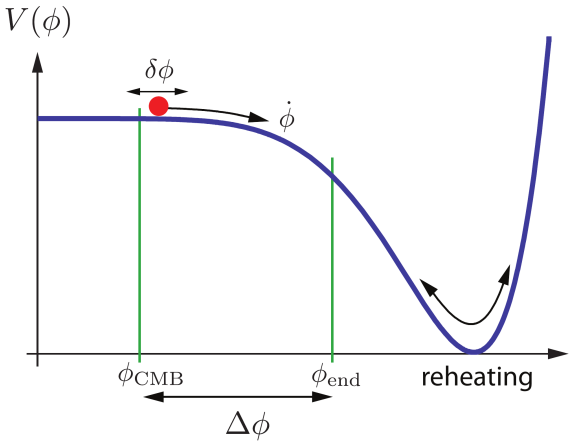

Figure 1.6: An example for the potential of the inflaton. Acceleration occurs when V is more important than the kinetic term. Inflation ends at ϕ_{end} when the slow roll conditions are violated. CMB fluctuations are created by quantum fluctuation $\delta\phi$ about 60 e-folds before the end of inflation. At reheating, the energy density of the inflaton is converted into radiation (Baumann 2009).

1.2.4 Reheating

In the original version of the reheating, at the end of inflation the field ϕ oscillates around the minimum of the potential. Its coupling to other particles leads to the decay of the inflaton energy (e.g. Lyth & Liddle (2000))

$$\frac{1}{a^3}\frac{d}{dt}(a^3|\phi|^2) = -\Gamma|\phi|^2 \tag{1.72}$$

The coupling Γ represents the complex physics that describes the decay ratio of the inflaton into generic scalars χ or spinors ψ, $\Gamma = \Gamma(\phi \to \chi\chi) + \Gamma(\phi \to \psi\psi)$. Using the expression for the energy density of the field ϕ, $\rho_\phi = \frac{1}{2}m^2|\phi|^2$. One can rewrite Eq.1.72 as (e.g. Bassett et al. (2006))

$$\dot{\rho}_\phi + 3H\rho_\phi + \Gamma\rho_\phi = 0 \tag{1.73}$$

Eventually, the inflationary energy density is converted into standard model degrees of freedom and the hot Big Bang starts. Roughly speaking, one can imagine that the decay products are ultra-relativistic, namely $m \gg m_\psi, m_\chi$ and behave as radiation while the inflaton behaves as matter. Since they are coupled, densities do not evolve completely as the free ones (the $\rho_R \propto a^{-4}$ and $\rho_M \propto a^{-3}$ of sec.1.1.3). Moreover, matter is a source for radiation, so the densities satisfy

$$\dot{\rho}_M + 3H\rho_M + \Gamma\rho_M = 0 \tag{1.74}$$

$$\dot{\rho}_R + 4H\rho_R + \Gamma\rho_R = 0 \tag{1.75}$$

While $\Gamma < H$, $\rho_M \propto a^{-3}$ is indeed a good approximation for the matter term but $\rho_R \propto a^{-3/2}$.
When $\Gamma \sim H$, radiation is the dominant component of the total energy density and reheating ends.

This reheating mechanism, however, does not describe accurately the quantum dynamics of the fields and more complicated mechanisms are required, especially for the first stages of the reheating, the preheating (Traschen & Brandenberger 1990; Kofman et al. 1994; Yoshimura 1995) . In its simplest form, preheating assumes that the inflaton ϕ has a quadratic potential at the end of inflation and it is coupled to a scalar field χ with negligible mass, through a term $-\frac{1}{2}g^2\phi^2\chi^2$. The equation for the quantum fluctuations of χ can be written as (Kofman et al. 1994)

$$\ddot{\chi}_k + 3H\dot{\chi}_k + \left(\frac{k^2}{a^2(t)} + g^2\Phi^2\sin^2(m_\phi t)\right)\chi_k = 0, \tag{1.76}$$

where $\mathbf{k}/a(t)$ is the physical momentum, $k = \sqrt{\mathbf{k}^2}$, and Φ the amplitude of the oscillations of the field ϕ. As preheating takes place in a time $\Delta t \ll H^{-1}$, in first approximation one can neglet the expantion of the universe and consider $a(t)$ as a constant. Eq. 1.76 then reduces to Mathieu equation

$$\frac{d^2\chi_k}{dz^2} + [A(k) - 2q\sin(2z)]\chi_k = 0, \tag{1.77}$$

where $q \equiv \frac{g^2\Phi^2}{4m_\phi^2}$, $A \equiv \frac{k^2}{m_\phi^2} + 2q$, and $z \equiv m_\phi t$. In certain region of the parameter space $\{A, q\}$, the solutions of Eq. 1.77 show an exponential instability within the sets of resonance bands (parametric resonance). These correspond to exponential growth of occupation numbers of quantum fluctuations that can be interpreted as particle production. The reheating mechanism is outside the scope of this thesis and can be found, for example, in Lyth & Liddle (2000).

1.3 Temperature anisotropies

In sec.1.2 we have seen how inflation generates the seeds that grow to form, not only the structures that we seed today, but also the anisotropies of the CMB. However, unlike structure formation, the smoothness of the photon distribution implies that photon perturbations are small and one can safely use linear theory for most computations. This allows fast modern Boltzmann codes (sec.1.5.1) to do precise calculations, and in the end, with the growing precision of CMB data, to precisely constrain physics.

Generally speaking, the Boltzmann equations in an expanding background, describe the evolution of a phase space distribution $f = f(\mathbf{x}, \mathbf{p})$ of a system due to all possible collision terms

$$\frac{df}{dt} = C[f]. \tag{1.78}$$

The distribution of CMB photons reads

$$f(\mathbf{x}, \mathbf{p}, t) = \left[exp\left(\frac{p}{kT(t)[1 + \Theta(\mathbf{x}, \hat{p}, t)]} \right) - 1 \right]^{-1}. \tag{1.79}$$

Here the zero-order temperature T is a function of time only. Θ is the perturbation $\Delta T/T$. Eq. 1.79 can be expanded about its zero-order Bose-Einstein value f^0

$$f \simeq f^0 - p\frac{\partial f^0}{\partial p}\Theta \tag{1.80}$$

In absence of collisions (C=0), the Boltzmann equation simply recovers that $T \propto a^{-1}$, i.e. the photon wavelength is stretched by expansion.

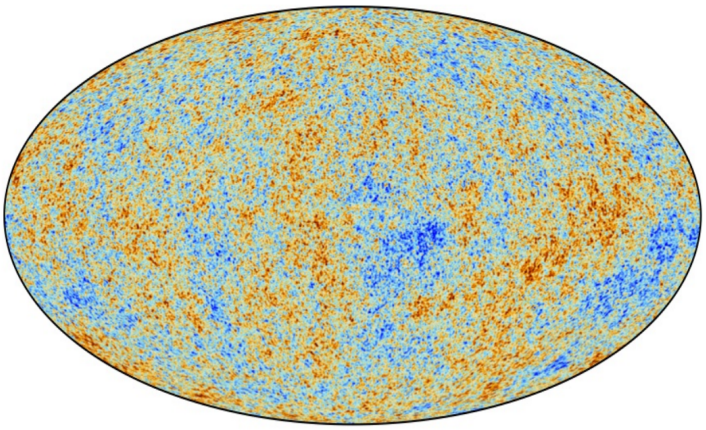

Figure 1.7: The anisotropies of the Cosmic microwave background (CMB) as observed by *Planck* (Planck Collaboration. X. 2015).

The detailed description of the Boltzmann equations for the evolution of the photon-baryon fluid and the generation of temperature anisotropies as are seen today is out of the scope of this thesis.

In this section we define the CMB privileged observable, the power spectrum (sec. 1.3.1), we then specify the gauge for the metric used (sec. 1.3.2) and sketch the equations that describe the photon fluid. Even in a simplified "instantaneous last scattering" scenario one can recognise the main physical effect that influence the CMB: the Sachs-Wolfe (SW) effect, the Doppler effect and the integrated SW (ISW) effect. The shape of the CMB power spectrum is described and linked to these effects in sec. 1.3.5.

For a more rigorous and detailed description of the physics, the interested reader has a huge literature available. Here we refer especially to Dodelson (2003) and Challinor & Peiris (2009).

1.3.1 Power spectrum

The CMB temperature anisotropies are directly related to cosmological perturbations, that are predicted to be Gaussian (sec. 1.2). If it is the case, they can be entirely captured by the the 2-point correlation function

$$C(\hat{u}, \hat{v}) = \langle \Theta(\hat{u})\Theta(\hat{v}) \rangle, \tag{1.81}$$

where $\hat{u}$ and $\hat{v}$ are two directions in the sky. The angle brackets in this equations denote the average over en ensemble of realisations of the fluctuations.

The statistical properties of the fluctuations in a perturbed cosmology are expected to respect the symmetries of the background model, hence in a FLRW metric, one imposes the isotropy and homogeneity of the universe (sec. 1.1.2). Eq. 1.81 is then simply a function of the angle θ between the two directions and the 2-point correlation function can be decomposed on the basis of Legendre polynomials

$$C(\theta) = \sum_{\ell} \frac{2\ell + 1}{4\pi} C_\ell P_\ell(\theta). \tag{1.82}$$

Eq. 1.82 naturally defines the power spectrum C_ℓ that contains all the information on temperature anisotropies. The variable ℓ is called multipole and is homogeneous to the inverse of an angular scale $\theta \sim 2\pi/\ell$. Since the signal comes from a sphere around us, it is useful to decompose it on a spherical harmonic basis to be able to construct CMB anisotropy maps (Fig. 1.7)

$$\Delta T(\hat{n}) = \sum_{\ell m} a_{\ell m} Y_{\ell m}(\hat{n}), \tag{1.83}$$

where the coefficients $a_{\ell m}$ read

$$a_{\ell m} = \int \Delta T(\hat{n}) Y_{\ell m}(\hat{n}) d\Omega, \tag{1.84}$$

and satisfy the following properties

$$\langle a_{\ell m} \rangle = 0 \tag{1.85}$$

$$\langle a_{\ell m} a^*_{\ell' m'} \rangle = C_\ell \delta_{\ell \ell'} \delta_{m m'}. \tag{1.86}$$

Eq.1.85 reflects the fact that the fluctuation have zero mean, while Eq. 1.86 is a consequence of the orthogonality of the $Y_{\ell m}$ functions on the full sky. The power spectrum estimate is

$$\hat{C}_\ell = \frac{1}{2\ell + 1} \sum_{m=-\ell}^{\ell} |a_{\ell m}|^2. \tag{1.87}$$

For every ℓ, the corresponding power is the squared mean of $2\ell+1$ coefficients. The statistical uncertainty associated to the evaluation of the C_ℓ is then given by

$$\frac{\Delta C_\ell}{C_\ell} = \sqrt{\frac{2}{2\ell + 1}}. \tag{1.88}$$

This is named *cosmic variance* and is a fundamental limit to our capacity of measuring the CMB anisotropies. Indeed, for all the small values of ℓ, corresponding to the large scales, the cosmic variance dominates over the other observational errors, since the number of pairs to compute Eq. 1.82 diminishes if the angle increases.

When built from the same map, Eq. 1.87 is called *auto spectrum*. Since every measurement comes with an associated noise, it is useful to define the notion of *cross spectrum* between two different maps A and B

$$\hat{C}_\ell^{AB} = \frac{1}{2\ell + 1} \sum_{m=-\ell}^{\ell} a^A_{\ell m} a^{B*}_{\ell m}. \tag{1.89}$$

Interestingly, if the noise components of the two maps are uncorrelated, the noise term vanishes in mean in the cross spectrum. Cross spectra are extensively used along all this thesis and are the central theme of chapter 5.

1.3.2 Scalar metric perturbations

Metric perturbations can be decomposed into a scalar, a vector and a tensor component evolving independently one from each other. This classification refers to the way in which the fields transform under three-space coordinate transformations on the constant-time hyper-surface. The vector components are generally ignored, as there are few known physical processes in which they can be generated and they decay with time. Tensor perturbations generates gravitational waves (sec. 1.4.4). Scalar perturbation are the only ones that couple with matter, and thus the ones interesting for describing the temperature anisotropies of the CMB. In *Conformal Newtonian gauge* the scalar first order metric perturbations take a simple form that depends only on two functions ψ and ϕ

$$ds^2 = a(\eta)[(1+2\psi)d\eta^2 - (1-2\phi)d\mathbf{x}^2], \tag{1.90}$$

where η is the conformal time defined in Eq. 1.18 and $\mathbf{x}$ the comoving position. The two scalar potentials, ψ and ϕ, play a role similar to the Newtonian gravitational potential. In the absence of the anisotropic stress, $\psi + \phi = 0$.

1.3.3 The Boltzmann equation for photons

Eq. 1.80 can be written explicitly for the photon fluid. The left-hand side needs to be expanded to first order. One finds

$$\left.\frac{df}{dt}\right|_{\text{1st order}} = -p\frac{\partial f^0}{\partial p}\left[\frac{\partial \Theta}{\partial t} + \frac{\hat{p}^i}{a}\frac{\partial \Theta}{\partial x^i} + \frac{\partial \phi}{\partial t} + \frac{\hat{p}^i}{a}\frac{\partial \psi}{\partial x^i}\right]. \tag{1.91}$$

The first two terms describe the *free streaming* that creates anisotropies on smaller and smaller scales while the universe expands. The second pair of terms describes the effect of gravity.

For the collision term $C[f]$ instead, one has to account for Compton scattering off free-electron (with proper number density n_e) that changes the photon distribution. Considering non relativistic electrons and a small energy transfer, the scattering term can be written as

$$C \approx -p\frac{\partial f^0}{\partial p} n_e \sigma_{\rm T}\left[\Theta_0 - \Theta(\hat{p}) + \hat{p}\cdot\vec{v}_b\right], \tag{1.92}$$

where v_b is the baryon velocity and Θ_0 is the monopole term of the spherical harmonic expansion of Θ. When the scattering Compton is efficient, only the monopole survives. Indeed, since the mean free path for photons is small, γs from different directions tend to have the same temperature.

Combining the two equations and rewriting it in Fourier domain one obtains

$$\dot{\Theta} + ik\mu\Theta + \dot{\phi} + ik\mu\psi = -\dot{\tau}\left[\Theta_0 - \Theta + \mu v_b\right], \tag{1.93}$$

with $\dot{\tau} \equiv -n_e^{\rm free}\sigma_{\rm T}a$ and $\mu \equiv \hat{k}\cdot\hat{p}$. Photons do not only have the monopole contribution but also a dipole, a quadrupole, etc.

Eq. 1.93 is partial differential equation coupling the photons to ψ, ϕ and v_b[2].

1.3.4 Initial conditions

We have reported the Boltzmann equation governing the photon perturbation around a smooth background, but the initial condition still need to be specified. At early times, the perturbation k satisfies $k\eta \ll 1$. This means that the term $\dot{\Theta} \sim \Theta/\eta$ is bigger than all terms proportional to $k\Theta$. All the relevant

[2]Note we have omitted the coupling term with polarisation.

perturbations, at early times, have k^{-1} larger than causal physics scale, implying that only the photon monopole Θ_0 is relevant. Eq. 1.93 simply reads

$$\dot{\Theta}_0 + \dot{\phi} = 0. \tag{1.94}$$

The same equation for dark matter and baryons is

$$\dot{\delta} = -3\dot{\phi}, \tag{1.95}$$

where δ describes the over-density.

From the combination of the Einstein equation and Eq. 1.94, and in the approximation $\phi = -\psi$, one finds

$$\ddot{\phi}\eta + 4\dot{\phi} = 0 \tag{1.96}$$

Setting $\phi = \eta^p$, the previous equation has two solutions. A decaying mode that has no impact in the evolution of the universe and a constant mode that, once excited, can be recognised to be responsible for the perturbation in the universe.

The combination of Eq. 1.94 and Eq. 1.95 gives

$$\delta = 3\Theta_0 + cst. \tag{1.97}$$

If the constant term is zero, the perturbations are named *adiabatic* and have $n_{\rm m}/n_\gamma$ constant (where the subscription m stands for both baryons and cold dark matter) . Otherwise, are named *isocurvature* perturbations. We consider only adiabatic initial conditions.

1.3.5 Primary anisotropies

Given the initial conditions, the formal solution of Eq. 1.93 can be obtained running a Boltzmann code like `CLASS` (sec. 1.5.1).

Approximating the last scattering as instantaneous, ignoring the effect of reionisation and the anisotropic nature of Thompson scattering, one finds

$$\Theta(\hat{n}) + \psi|_0 = (\Theta_0 + \psi)|_* + \hat{n}\cdot\vec{v}_b\big|_* + \int_{\eta_*}^{\eta_0}(\dot{\phi} + \dot{\psi})d\eta \tag{1.98}$$

The various terms correspond respectively to the SW effect, the Doppler effect and the ISW effect. These are showed in Fig. 1.8, where acoustic peaks and the damping tail are also visible.

Sachs-Wolfe effect

Eq. 1.98 says that the temperature received along $\hat{n}$ is the isotropic temperature of the CMB at last scattering event on the line of sight ($(\Theta_0|_*)$, corrected for the gravitational redshift due to the difference $\psi_* - \psi_0$. The plateau on the C_ℓ at large scales comes from the contribution of $\Theta_0 + \psi \sim \phi/3$. These mode have had no time to oscillate by recombination.

Doppler effect

From the equation for the evolution of photon energy density, is deduced that baryon peculiar velocity oscillates $\pi/2$ out of phase with the photons. This cause the Doppler term to tend to fill in the troughs of the angular power spectrum.

Integrated Sachs-Wolfe effect

A photon suffers a net redshift climbing out of a potential well that correspond to a negative temperature fluctuation (and viceversa). Hence, time variations of the metric perturbations contribute to this so called Integrated SW effect (ISW). Late-time ISW is sourced by the dark energy domination at low redshift and thus add power incoherently. It is responsible for the upturn of the C_ℓ at $\ell < 10$. There is also a contribution from early-ISW coming from the evolution of potentials around recombination. It peaks close to the first acoustic peak adding power coherently. This effect enhances the first peak since $\dot{\phi} + \dot{\psi}$ has the same sign as $\Theta_0 + \psi$.

Acoustic peaks

Before recombination, baryons are tightly coupled to photons. The perturbations in the gravitational potential, dominated by dark matter (we are already well inside matter domination), evolve driving oscillation in the photon-baryon fluid. The photon pressure and some inertia from baryon provide a restoring force to gravitation collapse. At recombination, this oscillation pattern is imprinted in the fluid and becomes projected on the sky as an harmonic series of peaks. The physical length scale associated with the peaks is the sound horizon at last scattering. This is projected onto the sky, leading to an angular scale θ_* that is our most precisely measured observable (chapter 7). The first acoustic peak (ℓ ~200), is the mode that terminates its first compression at decoupling. The second peak (ℓ ~500), correspond to a compression followed by a dilatation, while the third peak (ℓ ~800) has underwent also a second compression, etc.

Diffusion damping

The high-ℓ part of the spectrum is damped out by photon diffusion at recombination that erased the structures smaller than the mean free path of Thompson scattering l_p.

$$l_p = -\dot{\tau}^{-1} = \frac{1}{an_e\sigma_T} \tag{1.99}$$

One can thus calculate the mean-squared distance that a photon will have moved by its random walk, by the time η_*

$$\int_0^{\eta_*} \frac{d\eta'}{an_e\sigma_T} \sim \frac{1}{k_D^2}. \tag{1.100}$$

The damping scale k_D^2 damps as e^{-k^2/k_D^2} the perturbation at wavenumber k, and has on C_ℓ a similar behaviour (Fig. 1.8).

1.3.6 Secondary anisotropies

While CMB photons travelled from the last scattering surface toward us, there have been some modification in their patter due to gravitational interaction or to the interactions with the forming matter in the universe. These are called secondary anisotropies[3].

[3]The late ISW is, actually, a secondary anisotropy.

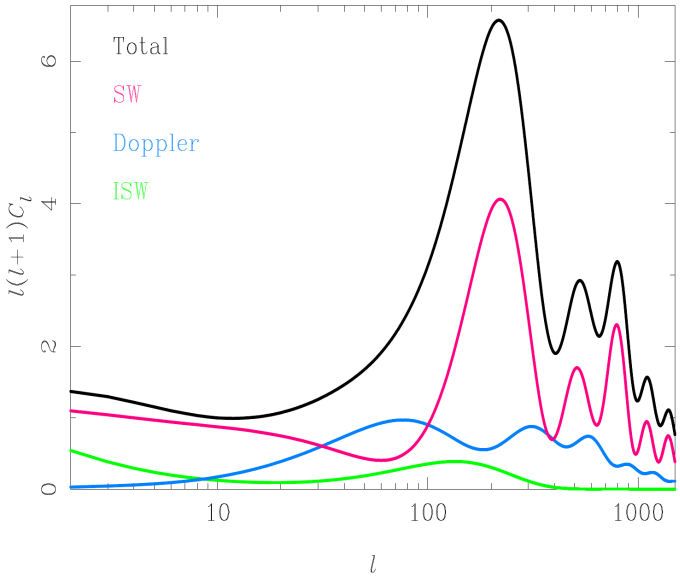

Figure 1.8: Contribution of the various terms in Eq. 1.98 to the temperature anisotropiy power spectrum from adiabatic initial condition. The figure is taken from Challinor & Peiris (2009). Note that the units of the spectrum are arbitrary.

Lensing

The CMB photons are deviated by the presence of structure gradients in their trajectory toward us. This effect is of the order of $2'$ and is a coherent effect on the degree scale. These deviations slightly smooth the acoustic peaks and generate power in the high-ℓ part of the spectrum (chapter 7). Lensing also converts some E mode into B modes as described in sec. 1.4.5. Lensing can be measured directly from the CMB 4-point correlation function (chapter 6).

Thermal Sunyaev-Zeldovich effect

Clusters of galaxies of $10^{14} - 10^{15}$ $M_\odot$ (where $M_\odot$ is the solar mass unity whose value is $(1.98855 \pm 0.00025) \times 10^{30}$ kg) trap gravitationally hot electron gas at temperature around the keV. This gas constitutes roughly a quarter of the mass of the clusters and emits via radiation bremstrasstrahlung process in the X domain. It also interacts via inverse Compton with the CMB photons. This is the so called thermal Sunyaev-Zeldovich (tSZ) effect (Sunyaev & Zeldovich 1970). The tSZ weakly distorts the CMB black body (e.g. Carlstrom et al. (2002); Planck Collaboration XXI (2014)), shifting it to higher frequencies (Fig. **??**). Its intensity is related to the integral of the pressure across the the line-of-sight via the Compton parameter

$$y = \int \frac{k_B \sigma_T}{m_e c^2} n_e T_e dl, \tag{1.101}$$

where dl is the distance along the line of sight, n_e and T_e are the electron number density and the temperature respectively. In unit of CMB temperature, the contribution for a given observation frequency ν is

$$\frac{\Delta T_{\rm CMB}}{T_{\rm CMB}} = g(\nu) y. \tag{1.102}$$

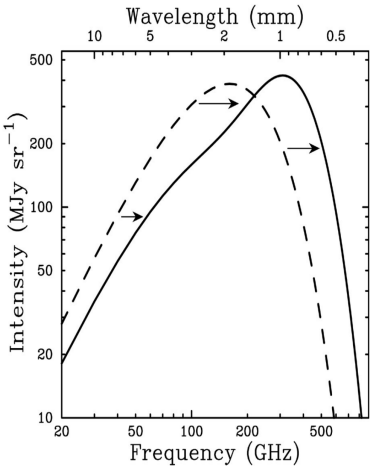

Figure 1.9: An example of the spectral distortion of the CMB photons due to thermal Sunyaev-Zeldovich effect in galaxy clusters. The figure is taken from Carlstrom et al. (2002).

In the non relativistic approximation one has

$$g(\nu) = \left[x coth\left(\frac{x}{2}\right) - 4 \right], \text{ with } x = h\nu/(k_B T_{\rm CMB}) \tag{1.103}$$

The function $g(\nu)$ has a peculiar spectral signature that vanishes at 217 GHz and is negative at lower frequencies and positive at higher frequencies. This allows the *Planck* satellite to measure the effect (chapter 3). Note that the tSZ distortion is independent from redshift, allowing to detect clusters at different z and thus to test cosmological models (Luzzi et al. 2015).

Kinetic Sunyaev-Zeldovich effect

The global movement of the thermal distribution of the hot electrons in clusters with respect to the CMB reference frame, constitutes an additional source of distortion, even if an order of magnitude smaller than the tSZ effect. This is called the kinetic Sunyaev-Zeldovich (kSZ) effect (e.g. Sunyaev & Zeldovich (1980)). The clusters peculiar velocities (of the order of $\sim$ 300km s^{-1}) creates a dipole anisotropies of the CMB photons, seen by the electrons. As a consequence, the amplitude of the effect is directly proportional to the cluster radial velocity v_r. In terms of CMB temperature one has

$$\frac{\Delta T_{\rm CMB}}{T_{\rm CMB}} = -\frac{v_r}{c}\tau_e, \tag{1.104}$$

where $\tau_e = \int n_e \sigma_T dl$ is the line of sight optical depth. The variation is positive if the cluster moves away from us and negative in the other case. Note that the kSZ effect is independent of the frequency.

Reionisation

During recombination, from a ionised state, the universe enters the so called "dark ages", becoming neutral. However, the birth of the first stars and quasars, at late epochs ($z \sim 6 - 15$), ionised again the surrounding matter (Gunn & Peterson 1965). Reionisation is not an instantaneous but a *patchy* process: every source begins ionising a growing radius bubble around it and bubbles eventually joint (Ferrara & Pandolfi 2014). Fortunately, reionisation begins sufficiently late in the evolution of the universe that

the free electron density is small enough to affect only slightly the mean free path of CMB electron. However, even in small fraction, CMB photons do diffuse on these free electrons and are deviated. For a given direction on the sky $\hat{n}$ there is a fraction of genuine "$\hat{n}$" photons that is lost and a fraction of scattered photons, originally coming from other directions, and with mean temperature $T_{\rm CMB}$, that is gained. The net effect is a suppression of temperature anisotropies parametrised by the optical depth τ

$$\frac{\Delta T}{T}(\hat{n}) \rightarrow \frac{\Delta T}{T}(\hat{n})e^{-\tau} \tag{1.105}$$

This is reflected, at the power spectrum level, as a $e^{-2\tau}$ suppression, and the amplitude of the observed spectra is proportional to $A_s e^{-2\tau}$. This degeneracy is well know and discussed in more detail in chapter 7. The effect of reionisation is peculiar also in polarisation, as described in sec. 1.4.5.

1.4 Polarization anisotropies

The standard cosmological model predicts that ∼10% of the photon radiation is polarised. This signal is unique to shed light on both the beginning of the universe through constraints on inflation (sec. 1.2), and on late time epoch through constraints on reionisation (sec. 1.3.6). Present ground based and future CMB polarization experiment will be able to measure the CMB lensing potential up to high accuracy (chapter 2). Here we revise briefly the formalism for polarization.

1.4.1 Stokes parameters

To completely determine experimentally the polarization of a beam of photons, a set of four measurements is needed (e.g. McMaster (1954)):

- the intensity of the beam
- the degree of plane polarization with respect to two arbitrary orthogonal axis
- the degree of plane polarization with respect to a set of axis oriented at 45° with respect to the previous one
- the degree of circular polarization

Consider an electromagnetic wave $\vec{E}(t) = (E_1, E_2)$ propagating in a direction $\hat{n}$. Its polarization state can generically be described by the intensity matrix

$$P_{ij} = \langle E_i(\hat{n}) E_j^*(\hat{n}) \rangle \tag{1.106}$$

where brackets denote time averaging. As P_{ij} is a hermitian 2x2 matrix, it can be decomposed into the Pauli basis

$$\sigma_0 = \begin{pmatrix} 1 & 0 \\ 0 & 1 \end{pmatrix} \quad \sigma_1 = \begin{pmatrix} 0 & 1 \\ 1 & 0 \end{pmatrix} \quad \sigma_2 = \begin{pmatrix} 0 & -i \\ i & 0 \end{pmatrix} \quad \sigma_3 = \begin{pmatrix} 1 & 0 \\ 0 & -1 \end{pmatrix} \tag{1.107}$$

It thus reads

$$P = I(\hat{n})\sigma_0 + Q(\hat{n})\sigma_3 + U(\hat{n})\sigma_1 + V(\hat{n})\sigma_2 \tag{1.108}$$

where

$$I = |E_1|^2 + |E_2|^2,\ Q = |E_1|^2 - |E_2|^2,\ U = (E_1^* E_2 + E_2^* E_1) = 2Re(E_1^* E_2),\ V = 2Im(E_1^* E_2) \tag{1.109}$$

are the Stokes parameters that encode all the electromagnetic information. I is simply the total intensity. Clearly, if $Q = U = V$ are zero, the wave is not polarised.

Q and U characterise the linear polarization. The circular polarization V can be ignored in cosmology since it cannot be generated by Thompson scattering (sec.1.4.3). Note that the temperature signal $T \equiv I/4$ is invariant under right handed rotation in the plane perpendicular to the direction $\hat{n}$, but Q and U are not. Under a rotation of an angle ψ we have

$$Q' = Qcos2\psi + Usin2\psi \tag{1.110}$$
$$U' = -Qsin2\psi + Ucos2\psi \tag{1.111}$$

In sec 1.3.1 we computed the correlation function and the corresponding power spectrum for temperature. In the analogous calculation for polarization, Q and U depend on the coordinate system. This coordinate system is well defined on a small patch on the sky (the so called flat sky limit) but not well defined on the whole sphere (Zaldarriaga & Seljak 1997).

1.4.2 All-sky formalism: E and B modes

The current power spectrum analysis for polarization uses Zaldarriaga & Seljak (1997) formalism of E and B mode. A similar formalism has been developed at the same time by Kamionkowski et al. (1997).

Eq.1.110 can be rewritten as

$$(Q \pm iU)'(\hat{n}) = e^{\mp 2i\psi}(Q \pm iU)(\hat{n}) \tag{1.112}$$

thus constructing two quantities from Stokes Q and U with a definite value of spin s=2. Temperature, that is a scalar field on the sphere, has been expanded in sec.SECCC into spherical harmonics $Y_{\ell m}(\theta, \phi)$, which form a complete and orthonormal basis. These can not be used for s≠0. Instead is used a similar basis called spin-s spherical harmonics $Y^s_{\ell m}(\theta, \phi)$, satisfying the completeness and orthogonality relations.

The decomposition on this basis reads

$$(Q \pm iU)(\hat{n}) = \sum_{\ell=2}^{\infty} \sum_{m=-\ell}^{+\ell} a^{\pm 2}_{\ell m} Y^{\pm 2}_{\ell m}(\hat{n}) = \sum_{\ell=2}^{\infty} \sum_{m=-\ell}^{+\ell} (a_{E,\ell m} \pm i a_{B,\ell m}) Y^{\pm 2}_{\ell m}(\hat{n}) \tag{1.113}$$

where the E and B mode have been defined as

$$a_{E,\ell m} = \tfrac{1}{2}(a^{+2}_{\ell m} + a^{-2}_{\ell m}) \quad a_{B,\ell m} = \tfrac{-i}{2}(a^{+2}_{\ell m} - a^{-2}_{\ell m}) \tag{1.114}$$

Under a parity transformation ($\hat{n} \to -\hat{n}$) E-modes remains invariant while B-modes change sign, similar to the gradient and the curl component of the electromagnetic field. Because of their opposite parity the cross correlation between B and E or B and T vanish. To characterize the full statistic of CMB one thus needs only four power spectra

$$C^{TT}_\ell = \frac{1}{2\ell+1} \sum_m \langle a^*_{T,\ell m} a_{T,\ell m} \rangle$$
$$C^{EE}_\ell = \frac{1}{2\ell+1} \sum_m \langle a^*_{E,\ell m} a_{E,\ell m} \rangle$$
$$C^{TE}_\ell = \frac{1}{2\ell+1} \sum_m \langle a^*_{T,\ell m} a_{E,\ell m} \rangle$$
$$C^{BB}_\ell = \frac{1}{2\ell+1} \sum_m \langle a^*_{B,\ell m} a_{B,\ell m} \rangle \tag{1.115}$$

with

$$\begin{aligned}
\langle a^*_{T,\ell'm'} a_{T,\ell m}\rangle &= C_\ell^{TT}\delta_{\ell'\ell}\delta_{m'm}\\
\langle a^*_{E,\ell'm'} a_{E,\ell m}\rangle &= C_\ell^{EE}\delta_{\ell'\ell}\delta_{m'm}\\
\langle a^*_{T,\ell'm'} a_{E,\ell m}\rangle &= C_\ell^{TE}\delta_{\ell'\ell}\delta_{m'm}\\
\langle a^*_{B,\ell'm'} a_{B,\ell m}\rangle &= C_\ell^{BB}\delta_{\ell'\ell}\delta_{m'm}\\
\langle a^*_{E,\ell'm'} a_{B,\ell m}\rangle &= \langle a^*_{T,\ell'm'} a_{B,\ell m}\rangle = 0
\end{aligned} \tag{1.116}$$

The power spectra are shown in Fig.1.10 for a standard cosmology. In order to give a more physical meaning to these quantities and understand their specific features we have first to discuss in more details the mechanisms that generates polarisation.

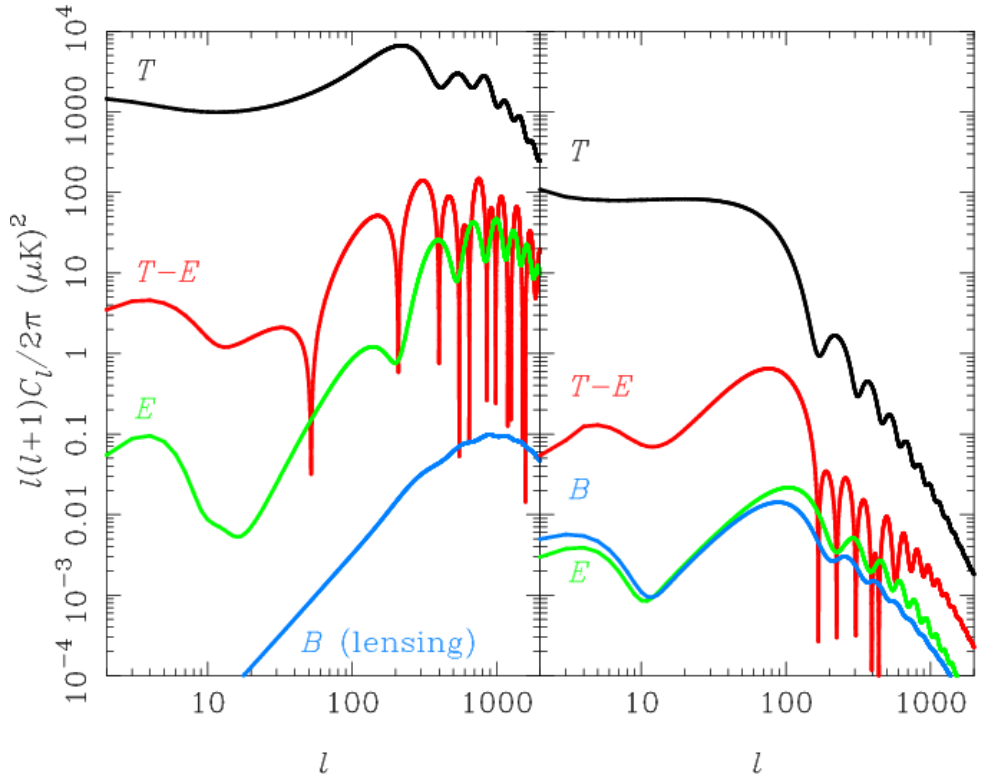

Figure 1.10: Temperature (black), E-mode (green), B-mode (blue) and TE cross-correlation (red) CMB power spectra from curvature perturbations (left) and gravitational waves (right) for a tensor-to-scalar ratio r=0.24. The B-mode spectrum induced by weak gravitational lensing is also shown in the left-hand panel (blue). The figure is taken from Challinor & Peiris (2009).

1.4.3 The origin of the polarised signal

Prior to recombination, the non polarised photons interact with free electrons via Thompson scattering, the elastic diffusion of a photon on a low energy electron. If the radiation received by the electron is isotropic and not polarised, the diffuse beam will not be polarised either. Nevertheless, a quadrupolar anisotropy in the incoming radiation can induce a linear polarisation. In fact, the Thompson differential

cross-section for an incoming wave linearly polarized in the direction $\hat{\epsilon}'$ and diffuse in the direction $\hat{\epsilon}$ is

$$\frac{d\sigma}{d\Omega} = \frac{3\sigma_T}{8\pi}|\hat{\epsilon}\cdot\hat{\epsilon}'|^2 \tag{1.117}$$

The scalar product $|\hat{\epsilon}\cdot\hat{\epsilon}'|$ favours the absorption of the components that are parallel to the incoming one. This is shown in Fig.1.11(a) where the observer see a resulting polarisation corresponding respectively to the vertical or the horizontal part of the incoming radiation. This can be shown more rigorously via direct calculation (we follow Kosowsky (1996)), combining Eq.1.117 and Eq.1.109, and considering a non polarised incoming radiation (thus $|E_1|^2 = |E_1|^2 = I/2$). We define the polarisation vector of the outgoing beam so that $\hat{\epsilon}_1$ is perpendicular to the scattering plane (we can chose $\hat{x}$) and $\hat{\epsilon}_2$ is in the scattering plane (we can chose $\hat{y}$). The Stokes Q parameters of the outgoing wave is the difference between the cross-section for photons polarised in the $\hat{\epsilon}_1$ and $\hat{\epsilon}_2$ direction

$$Q = \frac{3\sigma_T}{8\pi}\left(\sum_{j=1}^{2}|\hat{\epsilon}_1\cdot\hat{\epsilon}'_j(\hat{n}')|^2 - \sum_{j=1}^{2}|\hat{\epsilon}_2\cdot\hat{\epsilon}'_j(\hat{n}')|^2\right) \tag{1.118}$$

In our case of interest, the CMB, the outgoing wave (on $\hat{z}$) is the result of the summation of the incoming wave in all the directions. Integrating over all $\hat{n}'$ and expressing the incoming polarization in term of their cartesian coordinates, one obtains

$$Q(\hat{z}) = \int d\Omega I'(\hat{n}')sin^2\theta' cos(2\phi') \tag{1.119}$$

The Stokes U parameter can be derived in the same way just considering that it is proportional to the difference between the cross-section of the outgoing photons polarised in the $(\hat{x}+\hat{y})/\sqrt{2}$ and $(\hat{x}-\hat{y})/\sqrt{2}$ directions.

$$U(\hat{z}) = -\int d\Omega I'(\hat{n}')sin^2\theta' sin(2\phi') \tag{1.120}$$

Decomposing $I'(\hat{n}')$ on an spherical harmonic basis and using orthonormality one finds

$$(Q - iU)(\hat{z}) = \frac{3\sigma_T}{2\pi}\sqrt{\frac{2\pi}{15}}a'_{22} \tag{1.121}$$

It is now clear that polarization of the outgoing beam can be obtained if the quadrupole moment a'_{22} of the incoming radiation in not zero.

1.4.4 Quadrupolar anisotropies at recombination

Thompson diffusion can therefore generate a polarised radiation provided the existence of a quadrupolar structure in the incident radiation. Such a structure can be caused by the perturbations present in the cosmic fluid *at recombination*. As we have seen in sec. 1.3.2 these arise either from scalar or tensor perturbations (assuming vector perturbations washed out during inflation).

Polarization from scalar perturbation

For scalar perturbation, the polarised signal arises from the gradient of the peculiar velocity of the photon fluid (Zaldarriaga & Harari 1995). Near an over-density, for example, the fluid fall into the gravitational well faster the closer it is from the center (if we neglect the radiation pressure). A particular electron thus sees the rest of the fluid moving away from it in the radial direction and approaching in the transverse direction. Since our problem has a spherical symmetry, we can define the *radial* Stokes parameters U_r

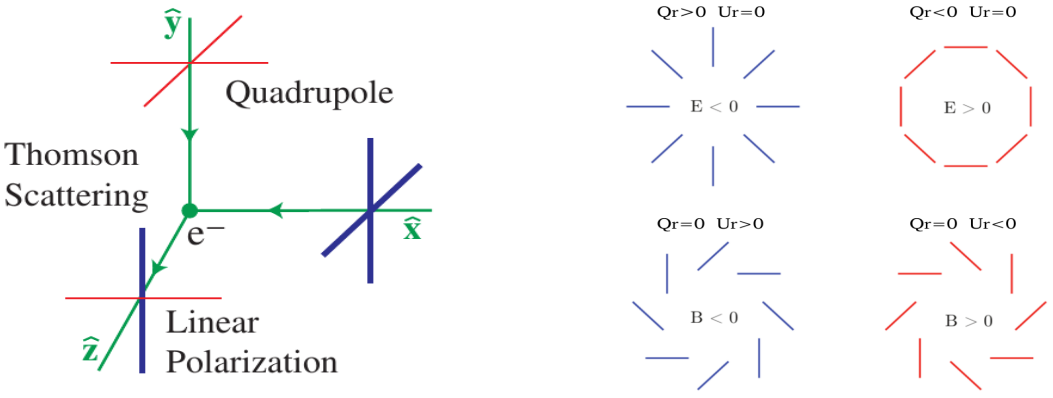

(a) (b)

Figure 1.11: (a) Thompson differential cross section (see text) favours the absorption of the components that are parallel to the incoming one. Hence, a quadrupolar anisotropy in the incoming radiation can induce a linear polarisation (Hu & Dodelson 2002). (b) Examples of E-mode and B-mode patterns of polarisation. Adapted from Baumann et al. (2009).

and Q_r. The over-density thus leads to a polarization with $U_r = 0$ and $Q_r > 0$. The case of the under-density can be easily deduced to have $U_r = 0$ and $Q_r < 0$. The gradient of the velocity is along the direction of the wavevector so we have a pure E-mode (Fig.1.11(b)). An over-density, since photons need energy to escape from the potential well, is seen as a cold spot and corresponds to $E < 0$. On the contrary, $E > 0$ is associated to a hot spot. The velocity of the fluid is 90° out of phase with respect to temperature meaning that the turning point of oscillator are zero point of the velocity. As can be seen in Fig.1.10, EE polarization peaks are at troughs of the temperature peaks.

In sec.1.4.2 we saw that B-modes do not correlate with the temperature (there is no TB contribution). Nevertheless temperature correlates with E-modes. It is actually an anti-correlation since minima and maxima of compression correspond to turning points of the velocity of the fluid. An E-mode is modulated in the direction of, or perpendicular to, its polarization axis. To be correlated with the temperature, this modulation must also correspond to the modulation of the temperature perturbation. The two options are that E is parallel or perpendicular to crests in the temperature perturbation (Hu & White 1997). Also, TE correlation, oscillates at double frequency with respect to E and T (Fig.1.10).

Polarization from tensor perturbation

The inflationary model predicts the existence of gravitational waves. They are created as vacuum fluctuations of the density perturbation and correspond to spatial metric perturbations (e.g. Dodelson (2003)).

$$ds^2 = a^2 \left[d\eta^2 - (\delta_{ij} + 2h_{ij}) dx^i dx^j \right] \tag{1.122}$$

where h_{ij} is traceless and transverse. Substituting into Einstein equation, and using Fourier modes of the form $e^{ik_i x^i}$ one finds

$$\ddot{h}_{ij} + 2aH\dot{h}_{ij} + k^2 h_{ij} = 8\pi G \Sigma^T_{ij} \tag{1.123}$$

where Σ^T_{ij} is the transverse and traceless part of the anisotropic stress. This equation has two types of solutions called in literature h_+ and $h_\times$ (Fig.1.12(a) and Fig.1.12(b)). The crossing of a gravitational waves produces a quadrupolar distortion in the temperature of the CMB and produces both E and B modes. Indeed, the $h_\times$ solution can induce a polarisation pattern with a curl component, thus a B-mode.

The E and B modes generated have similar amplitude (Zaldarriaga & Seljak 1997). The effect is only important at large scales since gravitational waves are damped inside the horizon (Fig.1.10). Note also that the tensor contribution to temperature and E-modes is weak with respect to the scalar contribution. On the contrary, tensor perturbations are the only (known) source of primordial B-modes. Gravitational waves at recombination carry a direct information about the energy scale of inflation (sec.1.2.3). Their detection at large angular scales is a fundamental goal of CMB experiments. To date, the challenge is still open (sec.1.5.2). The level of the signal is proportional to the tensor-to-scalar ratio r defined in sec.1.2.2. So the smaller r, the more challenging is the detection. At the level of precision of *Planck*, with a proper treatment of systematics, we can at least give a credible upper limit (chapter 6).

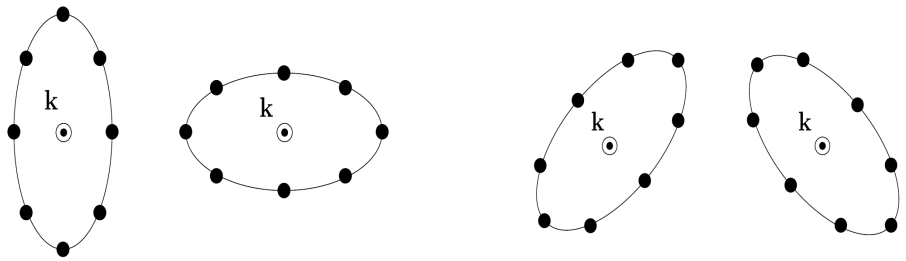

Figure 1.12: The effects of a passing gravitational wave can be visualized by imagining a perfectly flat region of spacetime with a group of motionless test particles lying in a plane (the black dots). As a gravitational wave passes through the particles along a line perpendicular to the plane of the particles, the particles will follow the distortion in space-time. In (a) the distortion follows the h_+ while in (b) the $h_\times$ solution. This latter generates a polarisation pattern with a curl component and thus a B-mode. The amplitude of the oscillation is amplified for illustration purpose.

There are features in the spectra of Fig.1.10 that we have not yet describe. Next section is thus dedicated to the effect of non primordial sources of polarisation.

1.4.5 Non primordial sources of polarisation

CMB photons are polarised by the perturbations present in the fluid at recombination. Since we observe them today, they carry also information about the late time universe and contributions from the structures from the last scattering surface to us. In sec.1.3.6 we have discussed the sources of secondary anisotropies for temperature. In polarisation we have to deal again with similar effect related to reionisation and weak lensing.

Effect of reionisation

At a late epoch, the formation of stars and quasars ionises again the universe that was neutral since the recombination. The density of free electrons is not enough to change substantially the mean free path of photons but diffusion on these free electron can be again a source of polarisation as seen in sec.1.4.3. In this case, the quadrupolar structure is carried by the CMB photons themselves.

Considering a fluctuation of scale k, the observed multipole ℓ can be calculated as $\ell \sim k(\eta_{obs} - \eta_{rec})$ where $\eta_{obs} - \eta_{rec}$ is the time elapsed from recombination up to the observation. If one considers the quadrupole $\ell = 2$ at reionisation one finds (e.g. Maurin (2013))

$$\ell_{reio}^{obs} \sim k_{reio}(\eta_0 - \eta_{reio}) \sim 2\frac{\eta_0 - \eta_{reio}}{\eta_{reio} - \eta_{rec}} \sim \sqrt{z_{reio}} \tag{1.124}$$

where the last equivalence follows from the dependence of η on the scale factor a and z during MD. Eq.1.124 is a simplified way to understand the fact that the polarised spectra in Fig.1.10 show a peak around $\ell \sim 3-4$. Polarisation is thus useful to constrain the epoch and the degree of reionisation because the amplitude is significantly increased and has this characteristic signature. Indeed $C_\ell^{TE} \propto \tau e^{-\tau}$ and $C_\ell^{EE} \propto \tau^2$. On the contrary, on the temperature spectra, reionisation tends to suppress the anisotropies at high-ℓ suffering from a degeneracy with A_s. In this thesis we have available a measurement of the low-ℓ E signal (chapter 6.1) which is crucial for breaking the $\tau - A_s$ degeneracy and improves the constraints on cosmological parameters.

Effect of weak gravitational lensing

Gravitational lensing (sec.1.3.6 and chapter 6) from the forming structures deviate locally the direction of the CMB photons. Zaldarriaga & Seljak (1998) showed that these random deflections mix E and B modes. Even for a pure scalar fluctuation, one has the generation of B-modes at small scales (Fig.1.10). This effect becomes dominant after $\ell \sim 100$ thus hiding the signal from primordial B-modes. It is anyway important as a genuine measure of the lensing field and a tracer of the underlying matter distribution. Relevant to this thesis, future ground based CMB measurements will be able to put strong constraint on the sum of neutrino masses (chapter 2).

1.5 The ΛCDM cosmology

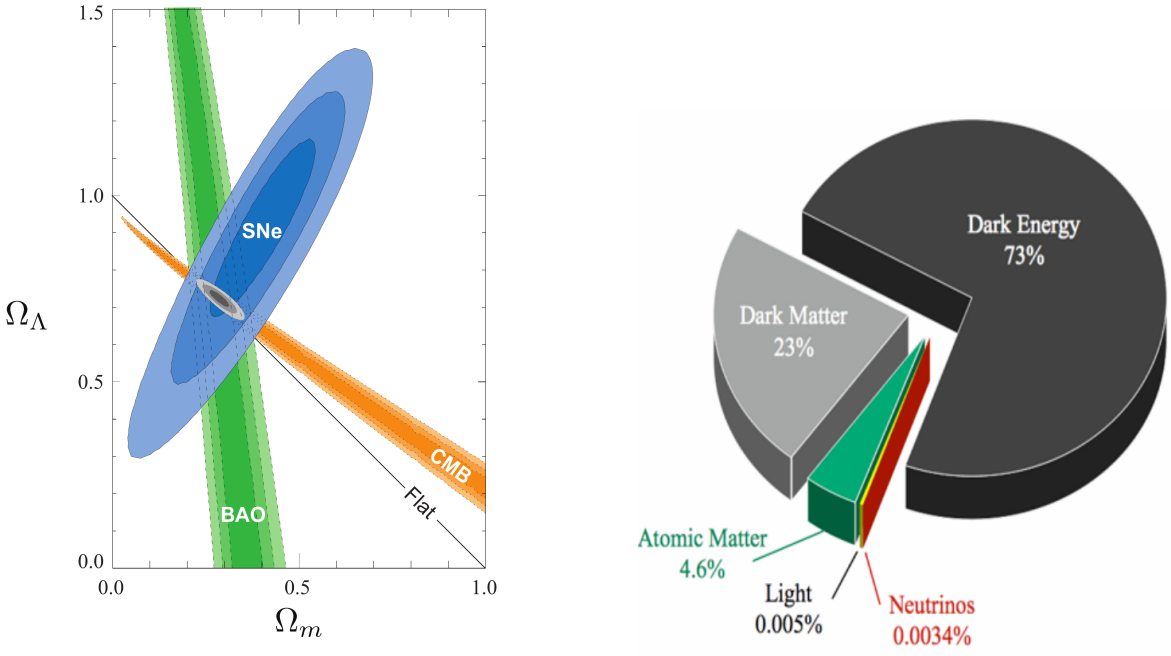

(a) (b)

Figure 1.13: (a) Different observables point toward a flat universe with the ~ 73 % made up of an unknown dark energy component that accelerate the expansion. (Kowalski et al. 2008) (b) The various component of the total energy density. Beside the dark energy component, the universe is made of ~ 23 % of dark matter. Baryonic matter, photons and neutrinos constitute only the remaining 4% of the energy density.

The present understanding of the universe and its evolution relies on a range of different types of observations that have allowed the establishment of a standard cosmological model.

This model can be described with five to ten parameters, from expansion rate and the curvature, to the matter budget of the Universe.

Here we list these parameters that have been already defined in the previous sections.

The current value of each parameter has been obtained with complementary probes providing consistency checks. Combining different observable allows to brake degeneracies and to place the strongest constraints. This is also the goal of this thesis, where we combine the *Planck* data with the latest results from other experiments (chapter 6).

The ΛCDM model consists in a perturbed Robertson–Walker space-time metric with dynamics governed by Einstein's equations.

To describe the homogeneous universe one only needs the current values of all the density parameters and the Hubble constant H_0 (or h, see Eq. 1.8). As described in sec.1.1.3, the density parameters include photons Ω_γ, neutrinos Ω_ν, baryons Ω_b, and cold dark matter Ω_c. The total present matter density is Ω_m. The *physical* densities of the matter components, $\Omega_i h^2$, is often used instead of the simple Ω_i.
The curvature density is Ω_k. Up to know, data are consistent with spatial flatness, thus Ω_k=0 (Fig.1.13(a)). This simplify the number of parameters needed to describe the energy density of the universe. For example, the dark energy density Ω_Λ is derived as $1 - \Omega_m$. It is treated as the contribution from cosmological constant, as a simple $\Omega_\Lambda \sim 0.7$ is a good match to existing different data (Fig.1.13(a),1.13(b)). This is why ΛCDM model is also called the *concordance* model.

The neutrino energy density is not taken as an independent parameter. While neutrino are relativistic and considering three active families ($N_{\rm eff}$=3.046), Ω_ν can be related to the photon density using thermal physics arguments. Also, from oscillation experiments it is known that neutrinos have a mass. Even if small, this mass has potentially observable effect on structure formation. A fixed minimal value for the mass is thus assumed in the base set of parameters, $\sum m_\nu$=0.06 eV. The neutrino sector is discussed further in chapter 2.

The statistical deviation from homogeneity is described by the power spectrum of the initial scalar perturbation, that are considered Gaussian and adiabatic. Gaussianity means that, since the phases of the Fourier modes associated with the perturbations in the value of the scalar field are independent, the central limit theorem assures that the density probability distribution at any point in space is Gaussian. Gaussianity refers to a property of the initial perturbations, before they evolve, since gravitational instability generates non-Gaussianity.
Adiabaticity means that all types of material in the universe share a common perturbation, so that if the space-time is foliated by constant-density hypersurfaces, then all fluids and fields are homogeneous on those slices, with the perturbations completely described by the variation of the spatial curvature of the slices (Olive et al. 2014).

One can approximate the spectrum by a power-law described by the spectral index n_s and the amplitude A_s (sec.1.2.2).

In sec.1.2 inflation has been presented as the simplest mechanism for generating the observed perturbations. The quantum fluctuations are amplified and stretched to astrophysical scales by the rapid expansion, and the primordial power spectrum can be expressed as a function of the slow roll parameters (sec.1.2.3).

Theory predicts also tensor perturbations but since they are believed to be weak, the base model assumes $r = 0$. If this condition is released, a simple single field inflation is in general assumed, so that r and n_t are not independent and that the consistency equation (Eq.1.70) is used.

The universe is known to be highly ionised at low redshift. This is described using the optical

depth $\tau_{\rm reio}$; in the approximation of instantaneous and complete reionisation, this could equivalently be described by the redshift of reionisation $z_{\rm reio}$.

In the base ΛCDM model used in this thesis one of the parameter is the angular scale of the sound horizon at last-scattering

$$\theta_* = r_s(z_*)/D_A(z_*), \tag{1.125}$$

where z_* is the redshift of recombination (sec.1.1.7), D_A the angular diameter distance (Eq.1.25) and

$$r_s(z) = \int_0^{\eta(z)} \frac{d\eta'}{\sqrt{3(1+\rho_b/4\rho_\gamma)}}, \tag{1.126}$$

with η being the conformal time.

The values of the cosmological parameters described above, are known at present with good accuracy. Present and future experiments will be able to put even stronger constraints and test in deeper the present understanding of the universe. This thesis describe how they can be constrained using the latest *Planck* data or in combination with other datasets from ground based CMB experiments or late time distance measurements. The general agreement between CMB and these latter is shown in Fig.1.13(a). Baryon Acoustic Oscillation (BAO) and Supernovae of type Ia (SNIa) data (chapter 6), point, with the CMB, towards a flat universe with $\Omega_m \sim 0.3$ and $\Omega_\Lambda \sim 0.7$.

The model can be extended to include non standard physics for example for the dark energy sector or for the neutrino sector. We postpone a more detailed explanation on standard model extension, when needed, to later in this thesis.

1.5.1 C_ℓ computation

For each set of the cosmological parameters, the evolution of perturbation, can be accurately followed (at least until perturbation stays small) using a linear theory numerical code such as CAMB[4] or CLASS[5], to solve the Boltzmann equations. These are suited to compute CMB anisotropies.

While official *Planck* results uses CAMB, in this thesis results are obtained using the CLASS (Blas et al. 2011; Lesgourgues & Tram 2011).

Since we perform, in chapter 7, some comparisons to *Planck* published results we check the compatibility of the results in sec. 7.1.

Codes like CLASS or CAMB are a necessary ingredient to construct a likelihood of the data (chapter 5) and to extract the constraints on the cosmological parameters (chapter 7, 8.

In Fig.1.14 are shown the different shape of the power spectra obtained with a Boltzmann solver using different values for the cosmological parameters. Changing the curvature Ω_k, for example, modifies the angular distance under which we see the CMB anisotropies, shifting the position of the peaks. The baryon density Ω_b changes the ratio between the amplitude of compression and dilatation peaks and the amplitude of the peaks, while the cold dark matter density Ω_c enhances compression peaks.
The CMB spectrum, almost entirely defined by recombination physics is almost insensitive to the late time contribution of the dark energy. Therefore, any measurements of Ω_Λ, in a non-flat cosmology, must rely on external datasets. We recall that in the standard flat cosmology $\Omega_\Lambda = 1 - \sum_i \Omega_i$ (Eq. 1.17).

Different parameters change the spectrum in similar ways and complicated degeneracies prevents a clear statement on the separate effect of each of them. While discussing our results we will however enters in more details on this.

[4] http://camb.info/
[5] http://class-code.net/

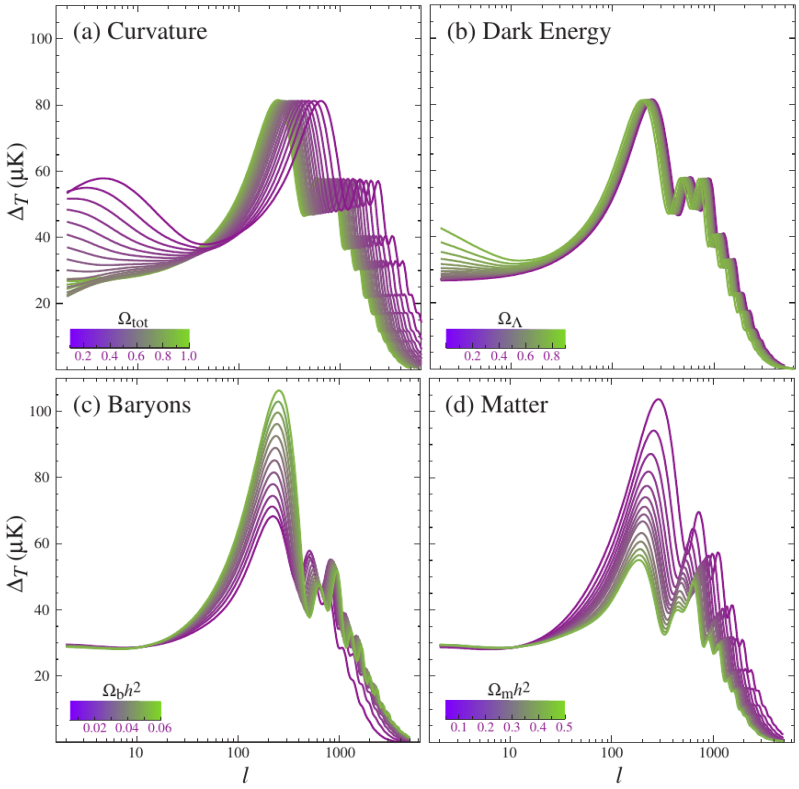

Figure 1.14: The different shapes of the temperature power spectrum with different values for the dark energy density, the baryon density, the cold dark matter density and the curvature. The figure is taken from Hu & Dodelson (2002).

1.5.2 Observational status of temperature and polarisation

The development of the present-day cosmological model was made possible by the improvement in the quality of the CMB temperature data achieved in the last decades. This thesis makes use of the latest *Planck* data, as described in details in chapter 5. Data from the previous release are shown in Fig.1.15 together with the WMAP power spectrum estimate and smaller scale results from ACT (Das et al. 2014a) and SPT (Story et al. 2013). The agreement is very good.

While the first detection of CMB temperature anisotropies dates back to 1965, polarisation, which is one or two orders of magnitude weaker, was only detected in 2002 by the DASI experiment (Kovac et al. 2002).

Nowadays, beside *Planck* data, the TE signal has been detected by many experiments from WMAP (Larson et al. 2011) to BICEP (Chiang et al. 2010), BOOMERANG (Piacentini et al. 2006), CBI (Sievers et al. 2007), DASI (Leitch et al. 2005) and QUAD (Brown et al. 2009) (Fig.1.16(a)).

The expected anti-correlation at $\ell \simeq 150$ and $\ell \simeq 300$ (see for example (Peiris et al. 2003)) are well visible. Since the polarisation anisotropies are generated at the last scattering surface, the existence of correlation at angles above about a degree (see sec.1.2.1) demonstrate that there were super-Hubble fluctuations at the recombination epoch (Olive et al. 2014). The sign of the correlation also confirm the adiabatic paradigm (sec. 1.3.4).

At large angular scales ($\ell < 10$) the excess signal compared to the one expected from temperature

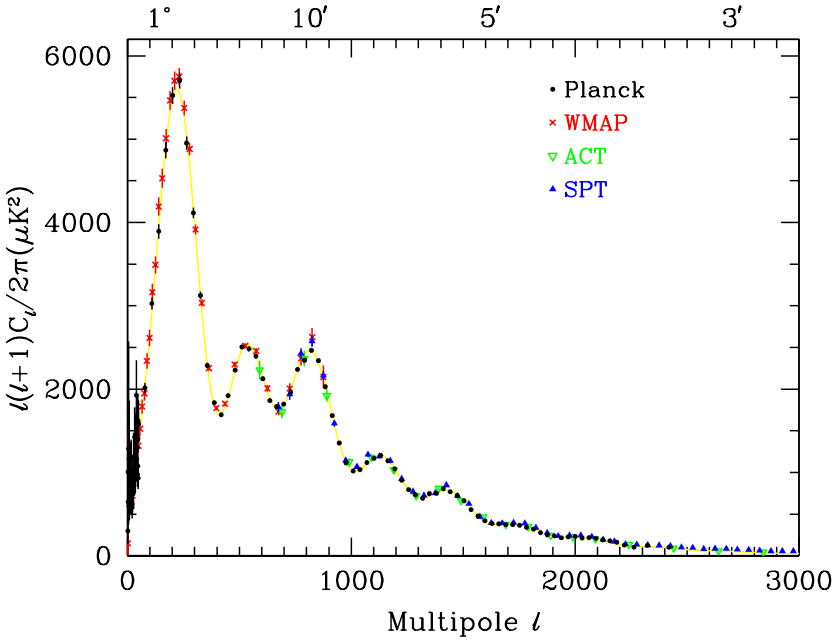

Figure 1.15: Status of the temperature power spectrum measurements. In black are shown the Planck 2013 data. The agreement with WMAP (red) and ACT (green) and SPT (blue) is very good. The figure is taken from the Particle Data Group (PDG) (Olive et al. 2014).

alone, is an indication of the reionisation bump discussed in sec.1.4.5. The effect is also confirmed in WMAP C_ℓ^{EE} results and is compatible with $z \simeq 10$ but with large uncertainties. The analysis of Planck data in this thesis (Chap.5) tells us more about reionisation.

The EE spectrum, which is even more difficult to measure, from again WMAP, BICEP, BOOMERANG (Montroy et al. 2006), CBI, DASI, QUAD, and adding CAPMAP (Bischoff et al. 2008) and QUIET (QUIET Collaboration: D. Araujo et al. 2012) experiments, is shown in Fig.1.16(b). The peak at $\ell \simeq 400$, corresponding to the first trough in temperature oscillations, is indeed clearly visible. Planck polarisation data (Chap.5) are much more precise, showing at least four peaks in the EE spectrum.

These polarisation measurements are a clear supporting evidence of the general cosmological pictures, with polarisation patterns coming from Thompson scattering at $z \simeq 1100$.

We conclude with a few word on the BB spectrum (Fig.1.17). The first indication of the existence of a BB signal has come from the detection of the lensed B modes, originated by the conversion, by the effect of gravitational lensing, of E to B-modes (sec.1.4.5). The SPT experiment derived a measurement using a cross correlation technique between polarisation and the lensing potential (Hanson et al. 2013). The POLARBEAR experiment achieved a direct measurement of the lensed B-modes in the range $500 < \ell < 2100$, rejecting the hypothesis of no B-mode polarization power from gravitational lensing at 97.5% confidence (The Polarbear Collaboration: P. A. R. Ade et al. 2014).

In Fig.1.17 are also shown the data point from the BICEP2 experiment (Ade et al. 2014) down to the recombination peak at $\ell \simeq 100$. The conclusion of the joint Planck and BICEP analysis (BICEP2/Keck and Planck Collaborations 2015) is that the signal is compatible with the polarised dust emission measured with *Planck* 353 GHz at these low scales.

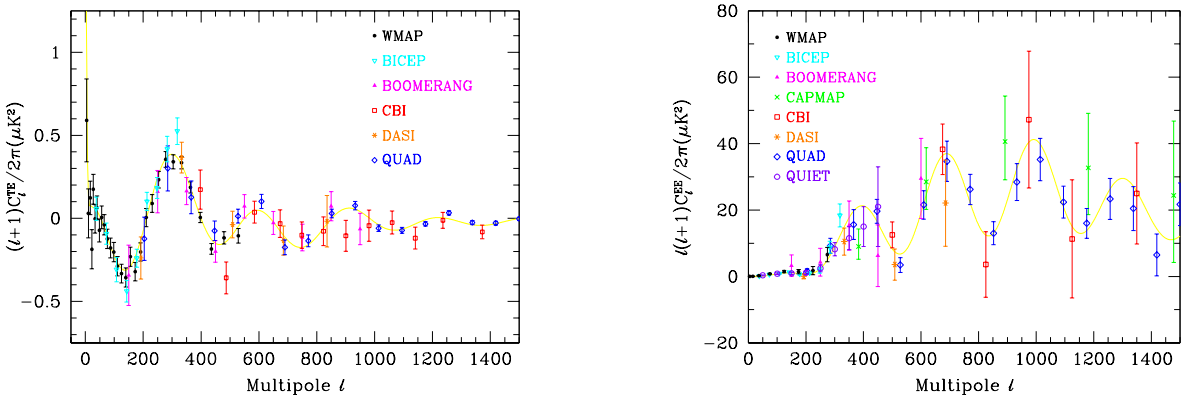

(a) (b)

Figure 1.16: Pre *Planck* status of TE (a) and EE (b) measurements. The figure is taken from the Particle Data Group (PDG) (Olive et al. 2014)

Conclusions

In this chapter we have described the standard cosmological model, the cosmic microwave background and its interplay with the evolving universe. We have summarised the assumptions of the ΛCDM model and the role of the minimal set of parameters needed to describe the present cosmological data. We have seen that the CMB is not the only relic of the hot Big Bang, there is also a background radiation composed of neutrinos that decoupled when the universe was a few seconds old. This latter, and in general the neutrino properties, are the subject of the next chapter.

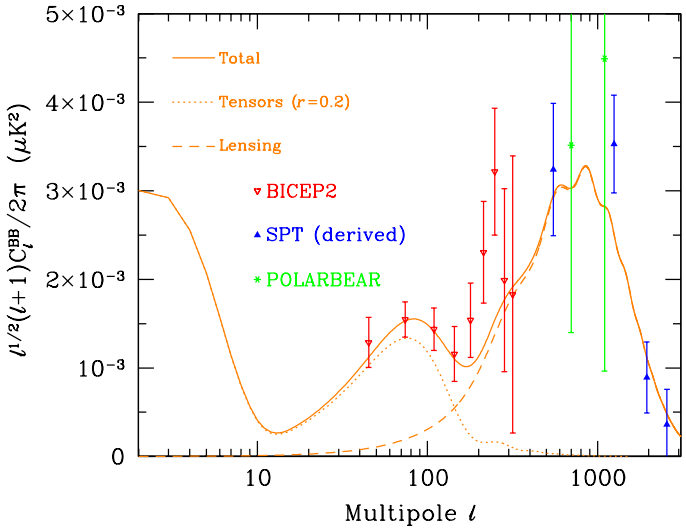

Figure 1.17: Status of BB measurements. In green the POLARBEAR direct measurements of the lensed B-modes (The Polarbear Collaboration: P. A. R. Ade et al. 2014). In blue the SPT points derived from cross correlation with lensing (Hanson et al. 2013). In red the BICEP2 measure at the level of the recombination bump (Chiang et al. 2010). The figure is taken from the Particle Data Group (PDG) (Olive et al. 2014)

Chapter 2

Neutrinos and Cosmology

In this chapter we give an overview of neutrino physics and their impact on cosmology. In sec. 2.1 we briefly describe the role they have in the standard model of particle physics and in sec. 2.2 the general idea of why new physics is required to give them mass. Indeed, we know that they are massive from neutrino oscillation measurements. In sec. 2.3 we report some of the latest results, also discussing the neutrino hierarchy question. Since in this thesis we are interested in the measurement of the absolute scale of neutrino mass using cosmological data, we report in sec. 2.4 the status and the future prospects of direct mass measurement using β- and $\beta\beta$-decays. Sec. 2.5 describes the cosmic neutrino background and its impact on the CMB through the parameters Σm_ν and $N_{\rm eff}$, the absolute scale of neutrino masses and the number of relativistic degrees of freedom, respectively. In sec. 2.6 we briefly discuss the role of massive neutrino on large scale structure (LSS) and present the forecast for future experiments on the joint constraints from CMB and LSS in sec. 2.7. We conclude the chapter reporting *Planck* constraints on sterile neutrinos (sec. 2.8).

2.1 Neutrinos in the Standard Model

Although radioactivity coming from β decays was known since the early twentieth century, it was only in 1930 that Pauli imagined the existence of a new weakly interacting light particle that could explain the observed continuous spectrum. Three years later, Fermi included the neutrino in its four-fermion contact interaction to explain the decay of the muon (Fermi 1934). This effective low energy theory has been further enriched since then and β decays are now described by the well know maximal parity violating V-A structure, where only left-handed particles and right-handed antiparticles interact (e.g. Peskin & Schroeder (1995))

$$\mathcal{L}_\beta = \frac{G_F}{\sqrt{2}}(\overline{p}\gamma_\mu(1-\gamma_5)n)(\overline{e}\gamma_\mu(1-\gamma_5)\nu), \tag{2.1}$$

It is part of the Lagrangian of weak interaction of the standard model (SM).

The standard model of particle physics is a gauge theory described by two symmetry groups: $SU(3)_C$ for strong interaction and $SU(2)_L \times U(1)_Y$ which describes the unified electro-weak interaction. The Brout-Englert-Higgs scalar field spontaneously breaks this latter symmetry down to $U(1)_Q$, which describes the electromagnetic interaction. The electro-weak model has a specific structure for the lepton sector in which the left-handed component for a charged lepton lies within a doublet with the corresponding neutrino, while the right handed component is a singlet. The SM does not contains right handed neutrinos, preventing the construction of a Yukawa term that could describe their mass, in analogy to charged leptons.

Hence, the experimental results on neutrino oscillations (sec. 2.3.1), implying a mass for the neutrino, point to the existence of new physics beyond the standard model. The physical laws that allow neutrino to be massive are still open to debate. Next section briefly describes the main idea of the mass generation mechanism.

2.2 Mass generation mechanisms

One of the open challenge of particle physics is to answer the question whether neutrinos are Dirac or Majorana particles. We start this section with some useful definition to point out the differences between the two. A rigorous treatment is out of the scope of this thesis and more on the subject can be found in Peskin & Schroeder (1995); Maggiore (2004); Giunti & Kim (2007); Lesgourgues et al. (2013) between others. The standard model Lagrangian is constructed to be invariant under gauge and relativistic transformations. The SM is thus a Lorentz-invariant field theory. Since parity is know to be violated by the weak interaction, the *Weyl* (chiral) spinors ψ_L and ψ_R are commonly used to describe the matter content. One can define the operation of charge conjugation C on Weyl spinors to be

$$\psi_L^c = i\sigma^2\psi_L^*, \tag{2.2}$$

where σ^2 is the Pauli matrix and $\sigma^2\psi_L^*$ transform as a right handed spinor. Charge conjugation thus transforms a left spinor ψ_L in a right one.

Beside Weyl spinors, it is also possible to construct a *Dirac* field such as

$$\Psi = \begin{pmatrix} \psi_L \\ \psi_R \end{pmatrix} \tag{2.3}$$

This has four complex components, and it provides a basis for a representation of both Lorentz and parity transformations. With a Dirac field is possible to construct the bilinear term $\overline{\Psi}\Psi = \Psi^\dagger\gamma^0\Psi$ that is scalar under a Lorentz transformation. Associated with a dimensionful constant it plays the role of a *Dirac mass term*

$$m\overline{\Psi}\Psi = m(\psi_R^\dagger\psi_L + \psi_L^\dagger\psi_L), \tag{2.4}$$

that is invariant under the redefinition $\Psi \to e^{i\alpha}\Psi$ and thus under the global charge symmetry associated with it.

Dirac spinors are not the only four-component spinors having the correct transformation rules under a Lorentz transformation, one can also construct a spinor in which ψ_L and ψ_R are not independent, but rather $\psi_R = i\sigma^2\psi_L^*$

$$\Psi_M = \begin{pmatrix} \psi_L \\ i\sigma^2\psi_L^* \end{pmatrix}. \tag{2.5}$$

This is called a *Majorana* spinor and is invariant under charge conjugation C

$$(\Psi_M)^c = \eta\Psi_M, \tag{2.6}$$

where η is a global phase factor. For a Majorana spinor the particle and the antiparticle are identical. Also, it is possible to write a *Majorana mass term* (Majorana 1937)

$$m\overline{\Psi}_M^c\Psi_M = m(\psi_{L,R}^\dagger\sigma^2\psi_{L,R}^* + \psi_{L,R}^T\sigma^2\psi_{L,R}) \tag{2.7}$$

Contrary to Eq.2.4, this term violates the conservation of any global charge associated to Ψ_M. This means that a spin 1/2 particle which carries a U(1) conserved charge cannot have a Majorana mass. However, a possible candidate for a particle which could have a Majorana mass is the neutrino.

Both Dirac and Majorana mass terms are not invariant under the gauge group $SU(2)_L \times U(1)_Y$. However, Dirac terms for the charged lepton are generated in the standard model by the spontaneous symmetry breaking (SSB) mechanism. In the absence of right handed neutrino ν_R, the same can not be done to generate a Dirac neutrino mass. On the other hand, the generation of a Yukawa term with $\overline{\nu_L^c}\nu_L$ term via SSB requires an Higgs scalar field with isospin I=1 that is not the standard one. A neutrino mass term thus requires extensions to the standard model. Considering the SM as a low energy effective theory valid only up to a certain energy scale, one can introduce an effective non-renormalisable dimension 5 operator, built with the Higgs field H (Weinberg 1979)

$$\mathcal{L} = \mathcal{L}_{\mathrm{SM}} + \frac{(\tilde{H}^\dagger \nu_L)^2}{2\Lambda_L} + ... \tag{2.8}$$

where Λ_L is an energy scale related to new physics. Inserting the Higgs VEV, one end up with a Majorana mass term with $m_\nu \sim \frac{v^2}{\Lambda_L} \sim 0.1$ eV and thus $\Lambda_L \sim 10^{14}$ GeV, just below the GUT scale ($\Lambda_{\mathrm{GUT}} \sim 10^{16}$ GeV).

2.2.1 Dirac or Majorana?

The straightforward extension to the standard model is the addition of a right handed neutrino ν_R. Since it is not seen in weak interaction it needs to be "sterile" or interacting much more weakly than the left-handed neutrinos. The neutrino ν_R allows to construct a Dirac mass term. The Yukawa term $m_\nu \overline{\nu_R}\nu_L + \overline{\nu_L}\nu_R$, is proportional to the Higgs vacuum expectation value (VEV) v, since $m_\nu = \lambda \frac{v}{\sqrt{2}}$. The order of magnitude of $m_\nu \sim 0.1$ eV thus requires low coupling constant $\lambda \sim 10^{-12}$. Also, gauge invariance allows to construct a Majorana mass term for the neutrino right, so a pure Dirac-type neutrino would require this mass to be zero.

In the general case where the SM is enlarged with the addition of right handed chiral fields that are gauge singlet, one can define

$$\nu = \frac{\psi_L + (\psi_L)^c}{\sqrt{2}}, \quad X = \frac{\psi_R + (\psi_R)^c}{\sqrt{2}}. \tag{2.9}$$

The most general mass term reads

$$\mathcal{L}_m = -M_L \bar{\nu}\nu - M_R \overline{X}X - M_D(\bar{\nu}X + \overline{X}\nu), \tag{2.10}$$

where M_L and M_R are Majorana mass term and M_D a Dirac mass term that couples the two fields. One can assume $M_L = 0$ since, as previously pointed out, a Majorana mass term for the left-handed neutrino can not be generated by the SM Higgs field. Eq. 2.10 can be rewritten in matrix form for N flavours

$$\mathcal{L}_m = -(\bar{\nu} \quad \overline{X})\mathcal{M}\begin{pmatrix} \nu \\ X \end{pmatrix}, \quad \mathcal{M} = \begin{pmatrix} \mathbf{0} & \mathcal{M}_D^T \\ \mathcal{M}_D & \mathcal{M}_R \end{pmatrix} \tag{2.11}$$

where now $\mathcal{M}_R$ et $\mathcal{M}_D$ have dimension $N \times N$. Note that if $\mathcal{M}_R$ also vanishes one is left with N Dirac neutrinos. This matrix can be diagonalised. In the simpler problem of only one flavour one can see that, if $M_D \ll M_R$, the eigenstate are Majorana neutrinos: a light one with mass $m \sim M_D^2/M_R$ and a heavier one with mass M_R. This is the basic principle of the *see-saw* mechanism (e.g. Mohapatra & Senjanović (1980)). It allows to justify the smallness of the active neutrino mass and leave open to new physics the generation of the mass for the sterile neutrino. Also, integrating out ν_R, the NR interaction of Eq. 2.2 is recovered.

Neither oscillation experiments or cosmology are able to clarify the nature of neutrino mass and the only dedicated experiment is the search for neutrino-less double-β ($0\nu2\beta$) decays briefly discussed in sec. 2.4.

2.3 Neutrino mixing

The results of oscillation experiments (sec. 2.3.1) state that neutrinos are massive, in analogy with the quark sector and the CKM matrix (Kobayashi & Maskawa 1973), the flavours eigenstates (ν_e, ν_μ, ν_τ) are not the mass ones (ν_1, ν_2, ν_3) and the two are related by a unitary matrix

$$|\nu_\alpha\rangle = \sum_{k=1}^{3} U^*_{\alpha k}|\nu_k\rangle \qquad (\alpha = e, \mu, \tau). \tag{2.12}$$

Using the notation $c_{ij} = \cos\theta_{ij}$ and $s_{ij} = \sin\theta_{ij}$, the Pontecorvo-Maki-Nakagawa-Sakata (Maki et al. 1962) mixing matrix can be decomposed as

$$U = \begin{pmatrix} 1 & 0 & 0 \\ 0 & c_{23} & s_{23} \\ 0 & -s_{23} & c_{23} \end{pmatrix} \begin{pmatrix} c_{13} & 0 & s_{13}e^{-i\delta} \\ 0 & 1 & 0 \\ -s_{13}e^{-i\delta} & 0 & c_{13} \end{pmatrix} \begin{pmatrix} c_{12} & s_{12} & 0 \\ -s_{12} & c_{12} & 0 \\ 0 & 0 & 1 \end{pmatrix} \begin{pmatrix} 1 & 0 & 0 \\ 0 & e^{-i\lambda_2} & 0 \\ 0 & 0 & e^{-i\lambda_3} \end{pmatrix} \tag{2.13}$$

The parameter of the first matrix describe the mixing in the atmospheric sector, the second is related to reactor neutrinos (the phase δ describes CP-violation), the third one to the solar sector, and the last one contains the Majorana phases. One can show that the oscillation probabilities depend on the square mass differences. The measurements of oscillation thus confirm that neutrino are massive. However, they cannot establish the absolute scale of neutrino masses. There are direct mass measurements dedicated to this (sec 2.4), but a privileged laboratory is indeed cosmology, both from neutrino mass effect on LSS (sec. 2.6) or on the CMB (sec. 2.5). This latter is the central theme of chapter 8.

2.3.1 Oscillation measurements

In this section we briefly describe some of the experimental techniques for the determination of the oscillation parameters.

Solar sector

The solar sector is historically the first one to have been investigated, even if the imprecise knowledge of the Sun model prevented to have a clear idea on the results. The Solar model is now well established and electron neutrinos ν_e are known to be produced mainly by *pp* and *pep* chains. The density in the center of the Sun is such that electron neutrinos are produced as pure mass eigenstates ν_2. The electron density decreases going towards the outside of the Sun and this affects the propagation of neutrinos since the effective potential can strongly modify the transition probability with respect to the vacuum state. Indeed, via the Mikheyeyev-Smirnov-Wolfestein (MSW) effect (e.g. Wolfenstein (1978)), if the electron density reaches a critical value, a resonance is produced and the eigenstate ν_2 is no more a ν_e but a linear combination of ν_μ and ν_τ. Once the surface of the sun is reached, the neutrinos undergo the standard vacuum oscillation till the Earth. Hence, solar neutrino experiments are sensitive to disappearance of electronic neutrinos and allow the measurement of θ_{12} and Δm^2_{21}. This latter parameter is known to be positive, since the MSW resonance is not otherwise possible. This information is important for neutrino hierarchy (sec. 2.3.2).

Solar neutrinos can be detected via inverse β-decay or neutrino elastic diffusion on electrons using water as the target. It is however the Sudburby Neutrino Observatory[1] (SNO), that, using heavy water

[1] http://www.sno.phy.queensu.ca

and thus both charged and neutral current interaction, has definitively proven the oscillations in the solar sector. The current results on solar neutrino parameters are (Olive et al. 2014)

$$\Delta m^2_{21} = 7,58^{+0,22}_{-0,26} \times 10^{-5}\text{eV}^2 \qquad \sin^2\theta_{12} = 0,306^{+0,018}_{-0,015}. \tag{2.14}$$

Atmospheric sector

Atmospheric neutrinos are produced as secondary products of the interaction between the atmosphere and the cosmic rays. Being very energetic, also muon neutrinos ν_μ can be observed with Cherenkov detectors. These experiments are sensitive to ν_μ disappearance caused by the oscillation $\nu_\mu \rightarrow \nu_\tau$, allowing the measurement of the parameter θ_{23} and $|\Delta m^2_{23}|$. Since oscillations are in vacuum, this latter is known without the sign. This missing information is at the origin of the hierarchy problem (sec. 2.3.2). The best constraints come from long-baseline neutrino experiments. Recent results are from MINOS[2] and T2K[3] with similar precision. This latter reported (Abe et al. 2014)

$$|\Delta m^2_{23}| = 2,51 \pm 0.10 \times 10^{-3}\text{eV}^2 \qquad \sin^2\theta_{23} = 0,514^{+0,055}_{-0,056} \tag{2.15}$$

Reactors/Accelerators

With reactor and accelerator experiments is possible to measure the angle θ_{13}. Roughly speaking, reactor experiments search for $\bar{\nu}_e$ disappearance, while accelerator experiment search for appearance of other flavour from muon neutrinos. θ_{13} is an important measurement since this angle is coupled to the CP violation phase δ (Eq. 2.13). The best constraint has been obtained combining the results from the reactor experiments Daya Bay[4], RENO[5], and Double Chooz[6] (Olive et al. 2014)

$$\sin^2\theta_{13} = 0.0251 \pm 0.0034. \tag{2.16}$$

The CP phase is still unknown but there are some preferences for $sin\delta \sim -1$ that could be strengthened by the T2K antineutrino appearance results.

2.3.2 Neutrino hierarchy

Oscillation measurements leave open the question of neutrino hierarchy, since it is still not known whether the solar neutrino doublet (ν_1, ν_2) has a mean mass smaller than or greater than the remaining atmospheric neutrino (ν_3). Indeed, as just seen in sec. 2.3.1, while the solar sector measures the mass square difference with the sign (a peculiarity of neutrino oscillation in matter), the atmospheric neutrino results is known only with an absolute value. As shown in Fig. 2.1, if the solar doublet has smaller mass than ν_3, the hierarchy is said to be *normal*, otherwise it is called *inverted* (e.g. Mena & Parke (2004)). Up to now there is still no statistically significant information on hierarchy from the available data. Although it might be possible to measure hierarchy using long base lines (at least at 3σ) (LBNE Collaboration et al. 2013), crucial results will come from the new dedicated extension of neutrino telescopes, e.g ORCA (Franco et al. 2013).

As discussed in sec. 2.7, also future cosmological data will be able to distinguish between the two hierarchies. Indeed, the two cases have different lower limits for Σm_ν (the sum of the mass eigenvalues), deduced from oscillation results.

[2] https://www-numi.fnal.gov/
[3] http://t2k-experiment.org/
[4] http://dayabay.ihep.ac.cn/twiki/bin/view/Public/
[5] http://hcpl.knu.ac.kr/neutrino/neutrino.html
[6] http://doublechooz.in2p3.fr

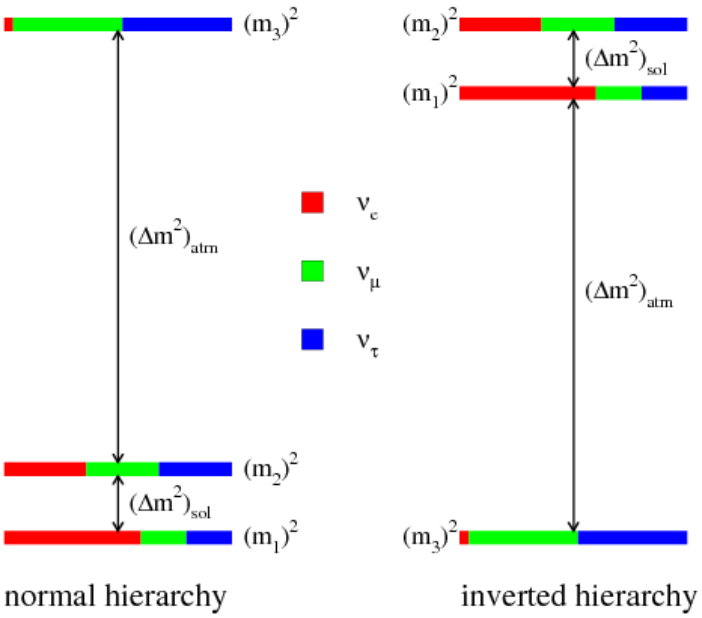

Figure 2.1: The two possible hierarchies are shown. The three mass eigenstate are color coded with an example of the flavour content of the three neutrino mass eigenstates consistent with all existing data. Figure taken from Hew (2012).

- *Normal Hierarchy*: $m_1 \ll m_2 < m_3$ with

$$m_2 \simeq (\Delta m^2_\odot)^{1/2} \simeq 0.0087 \text{ eV} \qquad \text{and} \qquad m_3 \simeq |\Delta m^2_A|^{1/2} \simeq 0.050 \text{ eV} \tag{2.17}$$

- *Inverted Hierarchy*: $m_3 \ll m_1 < m_2$ with

$$m_{1,2} \simeq |\Delta m^2_A|^{1/2} \simeq 0.050 \text{ eV} \tag{2.18}$$

In NH and considering the lightest neutrino to be massless, one obtains $\Sigma m_\nu \geqslant 0.06$ eV, as assumed in the base ΛCDM model used in this analysis (sec. 1.5). For the IH, one gets $\Sigma m_\nu \geqslant 0.10$ eV. This means that, if one measures with sufficient precision $\Sigma m_\nu < 10$ eV, the IH can be excluded.

2.4 Mass measurements

The oscillation results described in sec. 2.3.1 are not able to constraint the total value of the neutrino masses. In the next section we will see how cosmological data can constraint the absolute scale via the neutrino impact on the growth of structures. It is however possible to constrain directly the electronic neutrino mass via β or $0\nu2\beta$ decays.

- The end of the β decay spectrum is sensitive to the mass of the electronic neutrino defined as $m^2_\beta = \sum_i |U_{ei}|^2 m^2_i$. The best limit up to date comes from the Troitsk experiment (Aseev et al. 2011)

$$m_{\bar{\nu}_e} < 2.05\text{eV } 95\% \text{ CL.} \tag{2.19}$$

  KATRIN (KATRIN collaboration 2001), a new generation tritium beta decay experiment, is currently under commissioning and will have sub-eV sensitivity ($\sim$ 0.2eV). This measurement is kinematic and independent of whether the neutrino is of Dirac or Majorana type.

- The typical time of the neutrinoless double β decay can be related to the effective Majorana mass

$$m_{\beta\beta} = c_{12}^2 c_{13}^2 m_1 + e^{2i\lambda_2} s_{12}^2 c_{13}^2 m_2 + e^{2i(\lambda_3 - \delta)} s_{13}^2 m_3 \tag{2.20}$$

with c_{ij} and s_{ij} the cosine and sine of the angle of the mixing PMNS matrix of Eq. 2.13. δ is the CP violation phase and λ_2 and λ_3 the Majorana phases. In Fig. 2.2 $m_{\beta\beta}$ is shown as a function of the lightest neutrino mass with 2σ uncertainties. Note that there are combination of the PMNS matrix for which the effective mass can vanish.

The detector NEMO[7], for example, non observing a signal studying 7 kg of ^{100}Mo, fixed the limit

$$T_{1/2}^{0\nu}(^{100}\text{Mo}) > 1.0 \times 10^{24} \text{ans } 90\% \text{ CL}, \tag{2.21}$$

which corresponds to a limit on the $m_{\beta\beta}$ mass of

$$|m_{\beta\beta}| \leq (0.31 - 0.96) \text{ eV } 90\% \text{ CL}. \tag{2.22}$$

The next generation SuperNEMO, is expected to have a sensitivity of

$$|m_{\beta\beta}| \leq (0.048 - 0.118) \text{ eV } 90\% \text{ CL}. \tag{2.23}$$

A detailed analysis can be found in Blondel (2013). Similar sensitivities will be attained by other experiments like CUORE (Giachero et al. 2015) and GERDA[8].

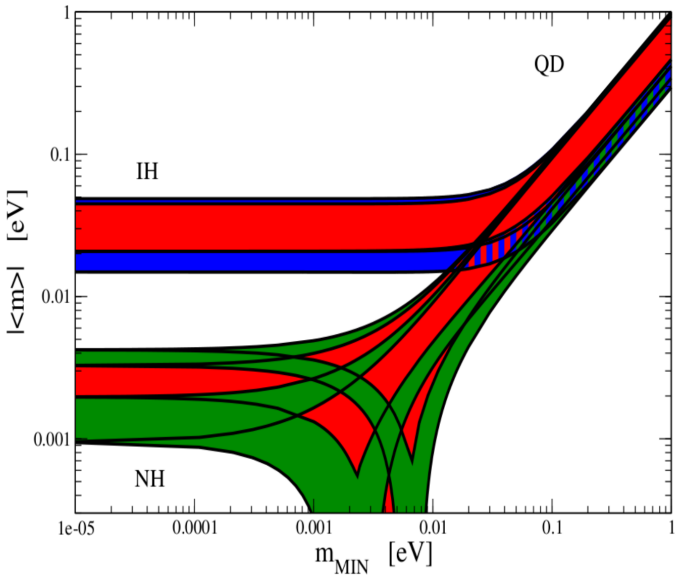

Figure 2.2: Effective Majorana mass $m_{\beta\beta}$ (with 2σ uncertainties) as a function of the lightest neutrino. Prediction are indicated for normal hierarchy (NH), inverted hierarchy (IH) and the quasi degenerate case (QD). Red zones are in correspondence of CP violation. (Olive et al. 2014)

[7] http://nemo.in2p3.fr
[8] http://www.mpi-hd.mpg.de/gerda/

2.5 Neutrinos and the CMB

In sec. 1.1.7, while going through the thermal history of the universe, we have said that, at $T_{\rm dec} \approx 1$ MeV, neutrinos decoupled from the plasma creating what is nowadays called the cosmic neutrino background (CνB). Since neutrinos are fermions, their distribution is a Fermi-Dirac (with negligible chemical potential) and their average momentum is a given function of the temperature $\langle p \rangle = 3.15 T_\nu$. A direct detection of this signal is still far but there are some proposal using capture on tritium (e.g. PTOLEMY (Betts et al. 2013)). Indirect detection of the cosmic neutrino background can be achieved using its effects on the CMB power spectrum and it is thus possible to study it with experiments such as *Planck*.

2.5.1 The cosmic neutrino background

The standard cosmological model predicts that the CνB temperature today is $T_\nu^0 = 1.9$ K. This temperature is computed in relation to the well known CMB temperature, using conservation of the quantity $S(a)a^3$, where S is the entropy density (e.g. Dodelson (2003)). Neutrino where already decoupled at $T \approx m_e$ when electron positron annihilation heated the photons. This argument leads to the prediction

$$T_\nu = (4/11)^{1/3} T_\gamma. \tag{2.24}$$

As for the CMB, T_ν simply falls as a^{-1}. Neutrinos have no impact on recombination history. At the level of background cosmology, they only affect the expansion rate, during radiation domination when they are relativistic, and during matter and the late dark energy domination era when they become non-relativistic (Lesgourgues et al. 2013). This section gives an overview of how the impact of the CνB is in general treated in CMB studies, i.e. the parameters Σm_ν and $N_{\rm eff}$.

- Σm_ν is the sum of the masses of the three active neutrinos ($m_1 + m_2 + m_3$). As discussed in sec 2.3.2 its minimal value is 0.06 eV (0.10 eV) in normal (inverted) hierarchy. In principle, cosmology, although insensitive to the nature of neutrino mass (Dirac or Majorana) would be sensitive to the three mass splitting. However, at the level of accuracy of *Planck* (and of the next generation of CMB experiments) one can safely consider the degenerate scenario. Note that large scales structures (sec. 2.6) are potentially much more sensitive to the separate effect of masses than the CMB (Jimenez et al. 2010). The effects of Σm_ν on the temperature power spectrum are discussed in sec. 2.5.2.

- The parameter $N_{\rm eff}$ is in general associated with neutrinos, but it accounts for any (~massless) degree of freedom beyond photons, relativistic during radiation domination. These include axions, any light relics, or even background of gravitational waves (Henrot-Versillé et al. 2015). It is defined as (e.g. (Lesgourgues et al. 2013; Abazajian et al. 2013)

$$\rho_\nu = \frac{7}{8}\left(\frac{4}{11}\right)^{\frac{4}{3}} N_{\rm eff}\rho_\gamma \simeq 0.2271 N_{\rm eff}\rho_\gamma, \tag{2.25}$$

  where the 7/8 comes from the F-D statistic. In sec. 2.5.3, the effects of $N_{\rm eff}$ on the temperature spectra are examined.

In chapter 8, we will discuss in details the constraints on these quantities from our analysis.

The energy density of massive neutrino species as a function of the comoving momentum $q \equiv pa$ and T_ν^0 reads

$$\rho_\nu(a) = \frac{1}{a^4}\int \frac{q^2 dq}{\pi^2}\frac{1}{e^{q/T_\nu^0}+1}\sum_i \sqrt{q^2 + m_{\nu,i}^2 a^2}. \tag{2.26}$$

Using the definition of $N_{\rm eff}$ of Eq. 2.25, and assuming neutrino species have equal mass, one can write Eq. 2.26 as Komatsu et al. (2011)

$$\rho_\nu(a) = 0.2271 N_{\rm eff} \rho_\gamma f(m_\nu a/T_\nu^0), \tag{2.27}$$

with

$$f(y) \equiv \frac{120}{7\pi^4} \int_0^\infty dx \frac{x^2 \sqrt{x^2+y^2}}{e^x+1}. \tag{2.28}$$

Eq. 1.31 can now be rewritten exactly for the more general case of massive neutrinos

$$H(a) = H_0 \{ \frac{(\Omega_c + \Omega_b)}{a^3} + \frac{\Omega_\gamma}{a^4}[1 + 0.2271 N_{\rm eff} f(m_\nu a/T_\nu^0)] + \frac{\Omega_k}{a^2} + \Omega_\Lambda \}^{1/2} \tag{2.29}$$

2.5.2 Effect of Σm_ν on the CMB

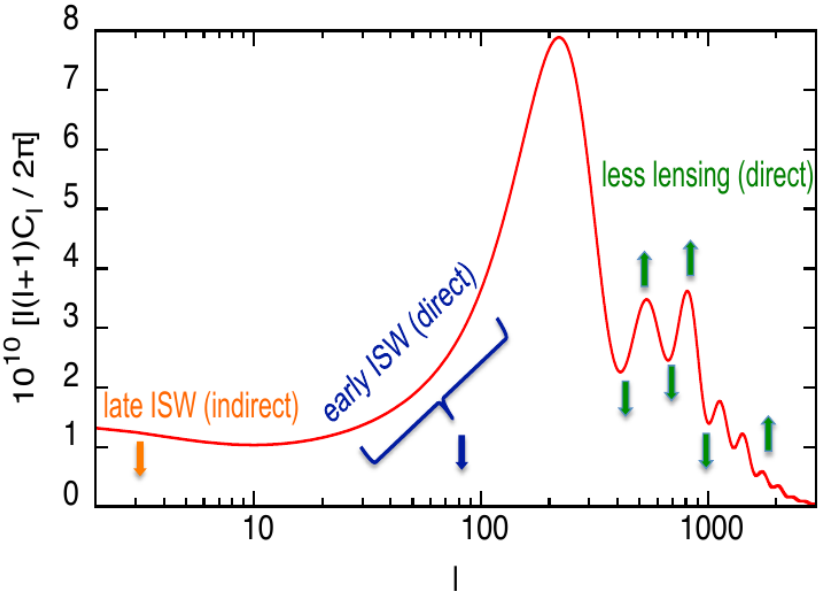

Figure 2.3: The location of three main effects of massive neutrinos on the temperature power spectrum. The figure is taken from a talk of Julien Lesgourgues.

Today, standard neutrinos for which Eq. 2.24 can be considered valid, have

$$\langle p \rangle_0 = 3.15(4/11)^{1/3} T_0 = 5.28 \times 10^{-4} \text{ eV} \tag{2.30}$$

and have had, at equality,

$$\langle p \rangle_{\rm eq} = (1 + z_{\rm eq})\, 5.28 \times 10^{-4} \text{ eV} \simeq 1.5 \text{ eV} \tag{2.31}$$

So neutrinos with mass between this range, become non relativistic during matter or dark energy domination (e.g.Lesgourgues et al. (2013)). More massive neutrinos $\Sigma m_\nu > 1.5$ eV would had been already non relativistic at recombination with much deeper impact on the CMB.

It is in general difficult to properly describe the effect of a specific parameter on the CMB spectra since there are degeneracies and some parameters combinations can mimic other different parameters.

It is important, for example, to keep unchanged the redshift of equality or the positions of the peaks since they are well constrained by present CMB data. Three main effects for massive neutrino can be recognised Lesgourgues et al. (2013), as depicted in Fig. 2.3.

- The variation of Σm_ν keeping z_{eq}, $\eta_{b\gamma}$, and θ_* fixed, induces a variation in $\Omega_m h^2$ that can be compensated by changes in h and Ω_Λ. Neutrinos thus play an indirect role in the duration of the Λ dominated era, the induces a late-time ISW effect at very low multipole (sec. 1.3.5). This effect is however hidden by cosmic variance (Eq. 1.88).

- The largest effect is in the range $20 < \ell < 500$ and is caused by the early-ISW effect (sec. 1.3.5) since the neutrino masses impact the evolution of $\phi + \psi$. Its amplitude is approximately given by

$$\frac{\Delta C_\ell}{C_\ell} \simeq -\left(\frac{m_\nu}{10\ \mathrm{eV}}\right). \tag{2.32}$$

  Note that the effect decreases with neutrino mass. The *WMAP* limit on Σm_ν comes from this effect.

- The last effect is due to CMB lensing (sec. 1.3.6). The lensing deflection can probe the growth of structure at small redshift and is thus sensitive to neutrino masses. Neutrinos damp the scales smaller than their free-streaming length, hence wave-numbers bigger than

$$\bar{k} \simeq 0.018\Omega_m^{1/2}\left(\frac{m}{1\ \mathrm{eV}}\right)^{1/2}\ h\ \mathrm{Mpc}^{-1}, \tag{2.33}$$

  where $\bar{k}$ is calculated at their non relativistic transition

$$(1 + z_{\mathrm{NR}}) \simeq 2000(m/1\ \mathrm{eV}) \qquad \text{imposing} \qquad m_\nu = 3.15 T_\nu^0 (1 + z_{\mathrm{NR}}). \tag{2.34}$$

  It is a high multipole effect and *Planck* offers a unique opportunity to precisely constrain Σm_ν since it measures small scales down to $\ell = 2500$.

2.5.3 Effect of N_{eff} on the CMB

To catch the true effect of N_{eff} on the CMB spectra, one should keep fixed the z_{eq} (Eq. 1.39) and the angular size of the sound horizon θ_* (eq. 1.125), resulting in a high-ℓ effect almost entirely due to increased Silk damping, caused by the increased expansion rate (Hou et al. 2013). Indeed, N_{eff} affects the ratio r_d/r_s between the diffusion distance at recombination r_d and the sound horizon r_s. Since $r_d \propto 1/\sqrt{H}$ but $r_s \propto 1/H$, globally

$$\frac{r_d}{r_s} \propto \sqrt{H} \tag{2.35}$$

Thus, the CMB can measure the expansion rate in the early universe and, as a consequence, N_{eff}. The effect on the damping tail can be seen in Fig. 2.4. Also, during radiation domination, neutrinos reduce metric fluctuation resulting in a reduction of the oscillation amplitude (Hu & Sugiyama 1995; Lesgourgues et al. 2013)

$$\frac{\Delta C_\ell}{C_\ell} = \left(1 + \frac{4}{15}\left[\frac{0.2271 N_{\mathrm{eff}}}{1 + 0.2271 N_{\mathrm{eff}}}\right]\right)^{-2}. \tag{2.36}$$

A further effect of the presence of a neutrino background is a unique phase shift of the CMB mode oscillations, caused by the "neutrino drag", the gravitational effect of neutrino perturbations on CMB (Bashinsky & Seljak 2004). This results in a smaller value of ℓ for the acoustic peaks, with a shift of $\Delta\ell_{\mathrm{peak}} \simeq 10$ (Lesgourgues et al. 2013). This effect can be used to constrain the properties of the neutrino background perturbations, described via the parameters c_{eff} and c_{vis}, respectively the neutrino sound

speed in its reference frame and a viscosity parameter (due to the anisotropic stress) (Hu 1998). Results are, up to now, compatible with the expected values for a standard, non-interacting, neutrino background $(c^2_{\rm eff}, c^2_{\rm vis}) = (1/3, 1/3)$ (Smith et al. 2012). *Planck* results, with the addition of polarisation, exclude a vanishing value for $c_{\rm vis}$ at 9σ (Planck Collaboration. XIII. 2015).

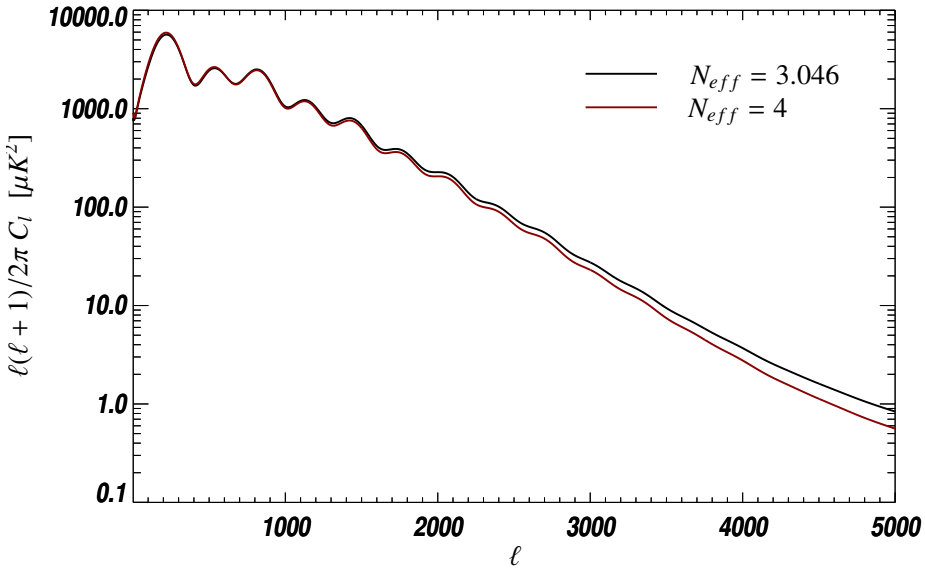

Figure 2.4: The effect of $N_{\rm eff} = 4$ on the CMB temeprature spectra (in red) with respect to the standard 3.046 value (in black). There is globally en effect on the damping tail (see text). The C_ℓ have been computed with `CLASS`.

2.5.4 $N_{\rm eff}$ from particle physics

The standard model of particle physics still miss an explanation on why the number of active neutrino families N_ν should be three[9]. However, it has been precisely measured from studies of Z production in e^+e^- collisions (Groom et al. 2000). The difference between the total Z width and the width corresponding only to Z decays into quarks and charged leptons, is called the invisible partial width $\Gamma_{\rm inv}$. It is assumed to be due to N_ν light neutrino species each one contributing to the neutrino partial width Γ_ν as given by the standard model. To reduce the model dependency, instead of using directly $(\Gamma_\nu)_{\rm SM}$, the ratio of neutrino to charged leptonic partial widths $(\Gamma_\nu/\Gamma_\ell)_{\rm SM}$ is used. The combined result from the four LEP experiments is

$$N_\nu = \frac{\Gamma_{\rm inv}}{\Gamma_\ell}\left(\frac{\Gamma_\ell}{\Gamma_\nu}\right)_{\rm SM} = 2.984 \pm 0.008 \tag{2.37}$$

2.5.5 $N_{\rm eff}$ and BBN

In sec. 1.1.7, we have mentioned that, when the universe was about three minutes old, the first light elements synthesised. The so called Big-Bang nucleosynthesis (BBN) is sensitive to physical conditions

[9] We call this number N_ν and not $N_{\rm eff}$ just because it has a different definition. In the case of only three active families and no light relic in the early universe, the two coincide.

in the early radiation dominated universe and primordial abundances inferred from observational data are in agreement with the standard cosmological model (Olive et al. 2014). These abundances have been determined by different processes which happened around $T \sim 1$ MeV. Indeed, this is roughly the typical binding energy for light nuclei ($Q = m_n - m_p \sim 1.3$ MeV), the neutrino decoupling temperature (Eq. 1.38), and the electron non-relativistic transition temperature. This latter has only an indirect effect (e.g. Strumia & Vissani (2006)): at $T \sim m_e$ the $e\bar{e} \rightarrow \gamma$ annihilation heated photons and not neutrinos[10]. The neutron fraction at "freeze-out" $n/p = e^{-Q/T_{\rm fr}} \simeq 1/6$ (using Eq. 1.35), is indeed sensitive to both strong and electromagnetic interactions. After neutrino decoupling, the neutrons β-decay until the universe is sufficient cold to bound them in nuclei. The n/p fraction is reduced to 1/7. Note that this happens at $T \sim 0.07$ MeV (Fig. 2.5). Almost all neutrons form ^4He because it is the light nucleus with the largest binding energy. The prediction for the ^4He mass fraction[11] is $Y_p \approx 2n_n/(n_n + n_p) \approx 0.25$, and it weakly depends on the baryon/photon ratio $\eta_{b\gamma}$ and on $N_{\rm eff}$ (e.g. Strumia & Vissani (2006)). The other nuclei (D, ^3He, T, ^7Li, ...) have smaller abundances (Fig. 2.5) that also depend on $\eta_{b\gamma}$ and $N_{\rm eff}$.

Although produced ~ 180 seconds after the Big-Bang, BBN abundances are observed at much later epochs and are polluted by stellar processes, inducing systematics errors in the measurements. It is, however, possible to estimate from them constraints on $\eta_{b\gamma}$ (and thus $\Omega_b h^2$) and $N_{\rm eff}$. In Planck Collaboration. XIII. (2015), using the `PArthENoPE` code (Pisanti et al. 2008), which gives a prediction for $Y_p(\Omega_b h^2, N_{\rm eff})$, BBN measurements are compared to CMB predictions on these parameters. In particular, the ^4He bounds from Aver et al. (2013) and the deuterium bounds from Cooke et al. (2014) are used. In Fig 2.6, 68% and 95% constraints in the $\Omega_b h^2 - N_{\rm eff}$ plane from *Planck* temperature and polarisation data are plotted together with the direct BBN bounds. The agreement between CMB and BBN is clear, and CMB constraints lie at the intersection between ^4He and deuterium estimates.

2.6 Neutrinos constraints from large scale structures

We have seen in sec. 2.5, that the CMB is sensitive to neutrino masses since their free streaming suppresses the growth of structures. However, the derivation of the initial conditions in sec. 1.3.4 considers that structure formation does not distinguish between photons and neutrinos. A qualitative discussion on the effect of neutrino on LSS (e.g. Strumia & Vissani (2006)) is interesting at this point. For a more detailed and rigorous treatment see for example Lyth & Liddle (2000); Lesgourgues et al. (2013).

Small fluctuations in the dark matter density $\delta_{\rm DM} = \delta\rho_{\rm DM}/\rho_{\rm DM} \ll 1$ evolve according to

$$\ddot{\delta}_{\rm DM} + 2H\dot{\delta}_{\rm DM} = 4\pi G\delta\rho, \tag{2.38}$$

where $\delta\rho$ is the fluctuation around the average total density, accounting for both dark matter and neutrinos. Until neutrino are relativistic, they can not cluster and $\delta\rho_\nu = 0$. Eq. 2.38 can be rewritten as

$$\ddot{\delta}_{\rm DM} + 2H\dot{\delta}_{\rm DM} = 4\pi G\rho(1 - f_\nu)\delta_{\rm DM}, \tag{2.39}$$

where $f_\nu \equiv \rho_\nu/\rho_{\rm DM}$. If $f_\nu = 0$, structures evolve during matter domination, only in the presence of dark matter as $\delta_{\rm DM} \propto t^{2/3} \propto T^{-1}$, increasing primordial fluctuations by a factor roughly $\mathrm{eV}/T_{now} \sim 5000$ producing the observed LSS.

[10] Note that, as said in sec. 2.5.3, that this is not entirely true since the small correction to $N_{\rm eff} = 3$ comes from non-completed neutrino decoupling by the time of electron-positron annihilation.

[11] The most important experimental parameter for this prediction is the neutron lifetime τ_n. In *Planck* analysis is used the fiducial value 880.3 s.

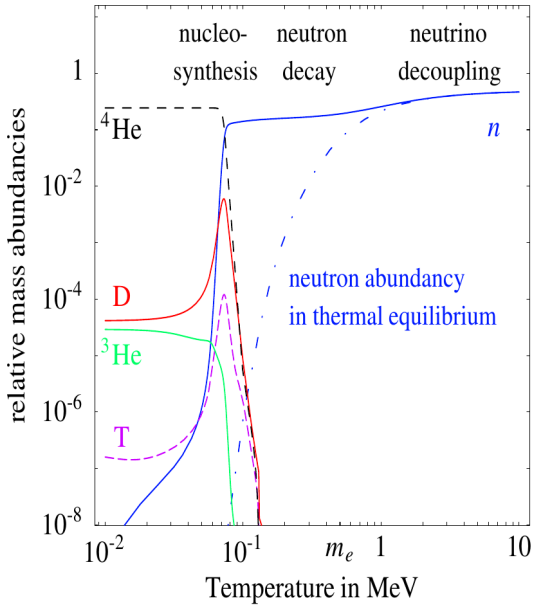

Figure 2.5: Evolution of the main nuclear components of the BBN. The figure is taken from Strumia & Vissani (2006)

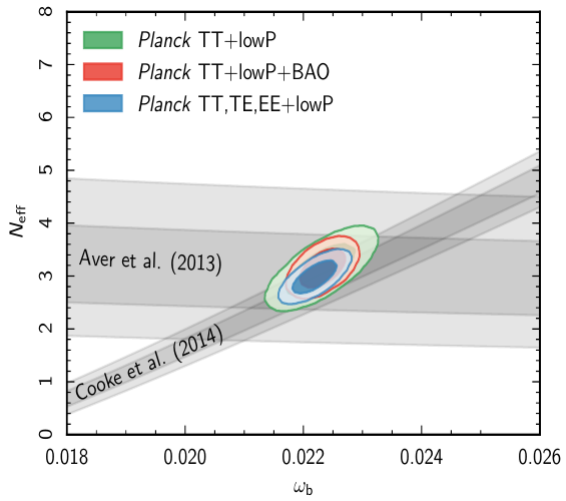

Figure 2.6: *Planck* constraints in the $\Omega_b h^2 - N_{\rm eff}$ plane compared to confidence regions derived from ^4He and deuterium measurements. Y_p is fixed as a function of $\Omega_b h^2$ and $N_{\rm eff}$. Figure is taken from Planck Collaboration. XIII. (2015).

On the contrary, if $f_\nu > 0$, there is a suppression of the growth of structures and the solution, for constant f_ν, becomes

$$\delta_{\rm DM}(t) \propto a(t)^p \qquad \text{with} \qquad p = \frac{\sqrt{1 + 24(1 - f_\nu)} - 1}{4}. \tag{2.40}$$

Note that fluctuations do not grow if $f_\nu = 1$ (i.e. a universe dominated by relativistic particles) and one recovers the decay mode of sec. 1.3.4. If neutrino started to be non relativistic at $a_{\rm NR}$, for $a > a_{\rm NR}$, the term f_ν slows the growth of fluctuation suppressing the matter power spectrum $P(k)$. This suppression can be approximated as

$$\frac{P_{\Sigma m_\nu}}{P_{\Sigma m_\nu=0}} = a_{\rm NR}^{2(1-p)} \approx e^{-8 f_\nu} \tag{2.41}$$

This is a maximal effect realised only at small scales. The results of a more accurate calculation are reported in Fig. 2.7 for different values of Σm_ν. The wave-number $\bar{k}$ of Eq. 2.33 determines the begin of suppression. In principle, the different masses for the three neutrinos have slightly different effects, allowing to be sensitive to the hierarchy. In Fig. 2.7 are also reported the sensitivity ranges of various cosmological probes. Indeed, galaxy surveys, 21 cm surveys, and the Lyman-α forests trace the underlying baryonic matter clustering in LSS, and it can be shown that this follows, up to a bias, the dark matter distribution, allowing to measure the matter power spectrum.

Via Lyman-α forests in quasar spectra, one can reconstruct the hydrogen density fluctuations along several lines of sight in a given redshift range. If only linear scales are probed, the hydrogen fluctuations can be assumed equal to the total baryon fluctuations. However, Lyman-α observations typically constraint the matter power spectrum in the wavenumber range $0.3 < k < 3h/\mathrm{Mpc}$ (Fig. 2.7) and in the redshift range $2 < z < 5$, where also mildly nonlinear scales are concerned (Croft et al. 2002), requiring hydrodynamical treatment of baryons. Viel et al. (2010) presented a conservative analysis based on Ly-α-SDSS data that includes massive neutrinos as hot dark matter in N-body simulations, finding the constraint $\Sigma m_\nu < 0.9$ eV (95% CL). More recent constraints using 1D Ly-α flux power spectrum measurements from SDSSIII-DR9 data release in combination with CMB data leads to an upper limit of $\Sigma m_\nu < 0.15$ eV (95% CL) (Palanque-Delabrouille et al. 2013).

Redshift-space distortions could, in principle, be an even more powerful probe since these measurements can break the degeneracy between the bias and the amplitude of the dark matter fluctuations (Abazajian et al. 2013). Also, via high angular resolution observations one can reveal the gravitational weak lensing of background galaxies in the presence of other LSS (cosmic shear). This can be used to infer neutrino mass since it provides a way to measure the matter fluctuation spectrum at low redshift (the CFHTLens survey data (Heymans et al. 2012), for example, are used in (Planck Collaboration. XIII. 2015)).

2.7 Forecasts from near-future and future experiments

The *Planck* measurements of the full sky temperature and polarization anisotropies used in this thesis provide good constraints for the parameters Σm_ν and $N_{\rm eff}$. However, in the search for B-modes, an accurate estimation of CMB polarization still needs a deep understanding of foregrounds and systematics as well as new data from suborbital experiments and future space missions. The Simons array, the funded expansion of PolarBear, and similar experiments, will be able to measure the sum of the neutrino masses via the measurement of lensed B modes (sec. 1.4.5). These accurate lensing measurements will have an uncertainty of only 58 meV, which will reduce to 16 meV when combined to BAO data[12]. Large-scale structure data provide a precious late-time measurement of distances, allowing to break the intrinsic degeneracies of the CMB. The significant improvement on the constraint of Σm_ν might allow to reach the limit to discern between normal or inverted hierarchy (sec. 2.3.2). In the longer term the combination of CMB data with Euclid [13], to be launched in 2020, will constrain the sum of the neutrino masses with

[12] http://bolo.berkeley.edu/polarbear/
[13] http://sci.esa.int/euclid/

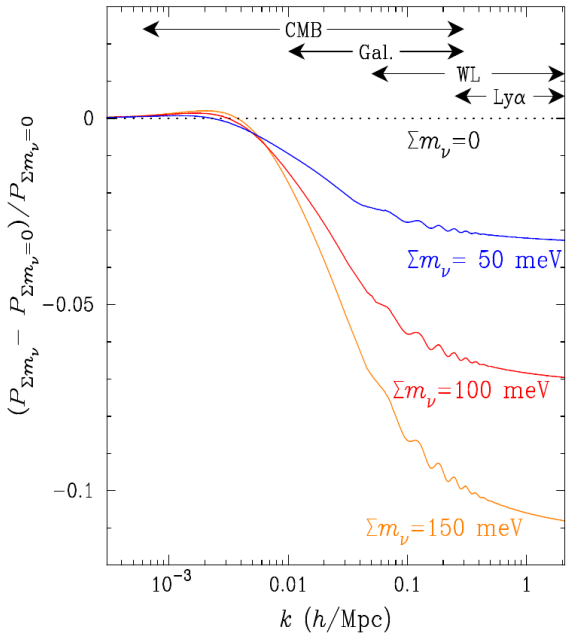

Figure 2.7: Fractional change in the matter density power spectrum as a function of the comoving wavenumber k for different values of Σm_ν. On the top of the figure the range of sensitivity for representative probes are also shown. Figure taken from Abazajian et al. (2013)

a statistical error of only 3 meV, sufficient to distinguish unambiguously between the two hierarchies. In Fig. 2.8, taken from Abazajian et al. (2013), are shown the current constraints and the forecast sensitivity of cosmology to the neutrino mass in relation to the hierarchy. The current cosmology bound on Σm_ν is the subject of this thesis and it is discussed in chapter 8. The KATRIN limit on the lightest neutrino mass has been mentioned in sec. 2.4. The sensitivity from future long base line experiments, already mentioned in sec. 2.3.2, is also shown.

2.8 CMB and sterile neutrino constraints

Neutrino oscillation experiments reported some hints for eV-scale sterile neutrinos from $\overset{(-)}{\nu}_e$ and $\overset{(-)}{\nu}_\mu$ disappearance and $\overset{(-)}{\nu}_\mu \to \overset{(-)}{\nu}_e$ appearance (Lasserre 2014). The global fits of the data involve one or two sterile neutrinos mixing with the three active ones (the so called 3+1 and 3+2 schemes). An explanation of all hints in terms of oscillations seems to suffer from tensions between appearance and disappearance neutrino data (Kopp et al. 2013). It is however interesting to search for sterile neutrino in cosmological data. This kind of analysis is model-dependent so results should be compared with care. In sec. 2.5 we have described the two parameters Σm_ν and $N_{\rm eff}$. Let's clarify again that Σm_ν account for the mass of the three *active* neutrinos and $N_{\rm eff} > 3$ would be a sign of the presence of extra *massless* degrees of freedom. To search for *massive sterile* neutrino one need to specify another framework. We report in this section the result from Planck Collaboration. XIII. (2015) on this subject. There, it is assumed a model where there are one massive active neutrino, carrying the whole mass Σm_ν, two massless active neutrinos[14] and one

[14] As already notice, considering three degenerate neutrinos with mass $m_\nu = \Sigma m_\nu/3$ or one massive neutrino $m_\nu = \Sigma m_\nu$ and two massless, makes no important differences in the results. However, this latter configuration is computationally faster in

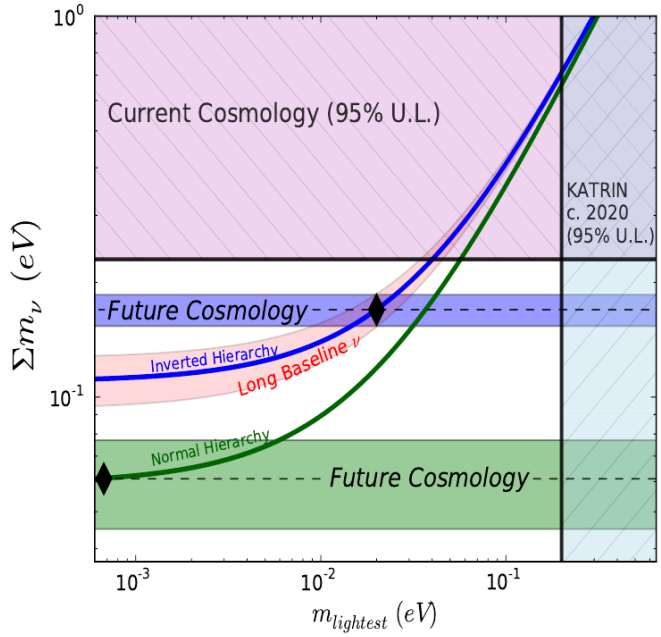

Figure 2.8: Current constraints and the forecast sensitivity of cosmology to the neutrino mass in relation to the hierarchy. The two black diamonds present two typical cases, the lowest Σm_ν value would be measured at 4σ level. Note that forecast are performed using Fisher matrix approach where the likelihood is supposed to be Gaussian. Figure is taken from Abazajian et al. (2013).

massive sterile neutrino. This latter is assumed to be thermally distributed with an arbitrary temperature T_s. Since $\rho \propto T^4$, one has

$$N_{\rm eff} - 3.046 = \Delta N_{\rm eff} = (T_s/T_\nu)^4. \tag{2.42}$$

If T_s coincides with the thermalisation temperature of the active neutrino T_ν (Eq. 2.24), this model has one extra degree of freedom and thus $N_{\rm eff} \approx 4$. For cosmological data this parametrisation is undistinguishable from the Dodelson-Widrow scenario Dodelson & Widrow (1994) with active-sterile neutrino mixing (Lesgourgues et al. 2013). The massive sterile neutrino is parametrised by $m^{\rm eff}_{\nu,\rm sterile}$, that is related to the true mass via

$$m^{\rm eff}_{\nu,\rm sterile} = (\Delta N_{\rm eff})^{3/4} m^{\rm thermal}_{\rm sterile}. \tag{2.43}$$

In Fig. 2.9 are reported samples of the *Planck* temperature chains in the $N_{\rm eff}$-$m^{\rm eff}_{\nu,\rm sterile}$ plane. The dashed lines constrain the physical thermal mass and report values in eV. For low values of $N_{\rm eff}$ this physical mass is very large. It thus describes sterile neutrinos that are already non relativistic well before recombination. In this case they behave like dark matter and cannot be uncorrelated from the $\Omega_c h^2$ parameter[15] (see also the results in Planck Collaboration. XVI. (2014)). It is thus considered a prior $m^{\rm thermal}_{\rm sterile} < 10$ eV or even 2 eV for the following final tighter constraint

$$95\%,\ \textit{Planck}\ \text{+lensing+BAO} \begin{cases} N_{\rm eff} < 3.7 \\ m^{\rm eff}_{\nu,\rm sterile} < 0.38\ \text{eV} \end{cases} \tag{2.44}$$

CLASS.

[15] Note that *warm* dark matter (~keV) as well is completely unconstrained by CMB data.

Note that the the combination $N_{\rm eff} \approx 4$ and $m^{\rm thermal}_{\rm sterile} \approx 1$, the one preferred to solve oscillation anomalies, is disfavoured by *Planck* data. In Fig. 2.9, the sample are also color coded to show the vale of σ_8. As we will discuss in chapter 8, a non standard neutrino sector has been proposed to solve, for example, the tension between *Planck* power spectrum analysis and *Planck* cluster counts or CFHTLens galaxy weak lensing constraints on this parameter (Planck Collaboration. XIII. 2015). One can obtain a low value of σ_8 with low values of $\Delta N_{\rm eff}$ and allowing for a massive sterile neutrino, helping in reducing the tension with ΛCDM estimate. However, *Planck* is perfectly consistent with no massive sterile neutrinos.

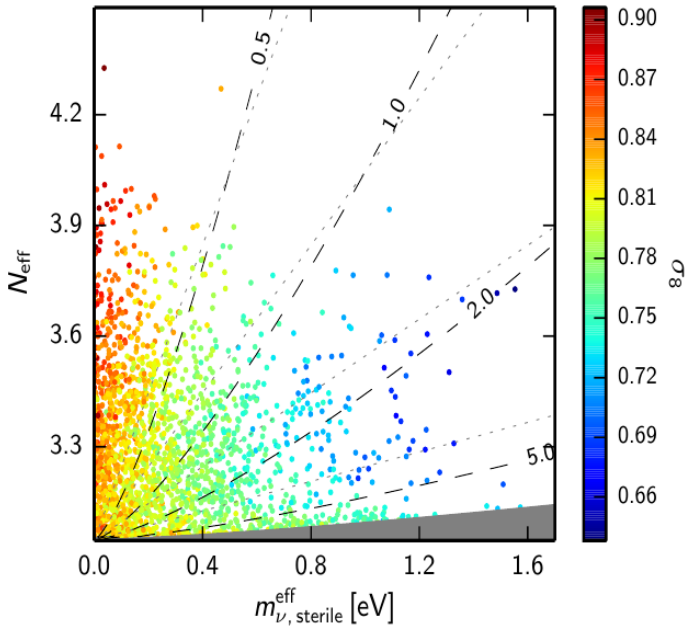

Figure 2.9: Samples from *Planck* data in the $N_{\rm eff}$-$m^{\rm eff}_{\nu,\rm sterile}$ plane, color coded by σ_8. The physical mass of the sterile neutrino $m^{\rm thermal}_{\rm sterile}$ is constrained along the grey dashed, with indicated the mass in eV. The grey region is excluded in the analysis. (Planck Collaboration. XIII. 2015).

Conclusions

In this chapter we have discussed the need for physics beyond the standard model to justify a mass term for the neutrino. The striking evidence that neutrinos are massive comes from the measurements of neutrino oscillations of which we have presented the current status and the open hierarchy question. While oscillation experiments are insensitive the the absolute scale of neutrino masses, this can be measured using cosmological data. The relic neutrino background and its subtle impact on the CMB, encoded in the two parameters Σm_ν and $N_{\rm eff}$, has been described. For constraining these parameters, one needs high quality CMB data. In this thesis we use the results from the *Planck* satellite, that is presented in the next chapter.

Chapter 3

The Planck mission

Third generation spatial mission after COBE (Smoot et al. 1992) and WMAP (Bennett et al. 2003), Planck is an ESA satellite dedicated to the measurement of the CMB anisotropies. A picture is shown in Fig.3.1(a). Launched in May 2009, it has collected data until October 2013 from the Lagrange L2 point of the Earth-Sun system. The *nominal mission* data, released in 2013, consisted in 15 months of observations. The *full mission* data, used in this thesis, consider all the 29 months of the High Frequency Instrument (HFI) data and include polarisation.

In this chapter we describe the satellite, the data processing and the main products of the mission, focusing in particular on what is relevant for this thesis.

3.1 The satellite

As described in Tauber et al. (2010), *Planck* is an imager based on an off-axis Gregorian telescope. The optical system is made of two mirrors: the primary of about 1.5m and the secondary of about 1m (Fig.3.1(b)). They have to stay cooled to stem thermal noise. Their operative temperature is around 45K obtained by isolating with a baffle that shields also from parasite light. With the focal plane, the optical system and the baffle compose the *payload* of the satellite. The remaining part assures the correct behaviour of the instrument and is the *service module*. It contains the solar panels, all the necessary electronics, and the attitude control, the antenna, the cryogenic system and the helium and hydrazine reservoirs for manoeuvres. The two parts are isolated via a V-grooves passive cooling. A schematic picture of the satellite can be found in Fig.3.1(b).

3.1.1 Cryogenic system

Conceived to achieve a full-sky cartography of unprecedented precision and angular resolution, *Planck* focal plane contains two separate instruments: the Low frequency Instrument (LFI) (Bersanelli et al. 2010) and the High Frequency Instrument (HFI) (Lamarre et al. 2010).

To achieve the required precision the noise level has to be controlled and kept very low. To this purpose, LFI and HFI have to be kept cooled down to 20K and 0.1K respectively. This is achieved with a complex structure combining the passive cooling of the V-grooves with an active cooling system. Mechanical cooling is delicate since one has to minimise the impact of vibration and transfer of momentum to the focal plane.
There are three successive stages to reach the desired temperature (Planck early results. II. 2011):

- The *sorption cooler* is a closed-cycle sorption cooler using hydrogen as the working fluid with a Joule- Thomson (JT) expansion, which produces temperatures below 20 K. It cools the LFI focal

plane to its working temperature of 20K and provides a pre-cooling to HFI.

- The $^4He - JT\ cooler$ is a closed-cycle cooler using a Stirling cycle compressor and ^4He as the working fluid with a JT expansion, which produces temperatures of 4 K. It is the temperature of the LFI reference loads and another pre-cooling stage for HFI.
- The *dilution cooler* phase is twofold. The first phase is a cooling to 1.6K again throw a JT expansion, this time of ^4He and ^3He. The second phase is based on a micro-gravity dilution cooler principle (Benoit et al. 1997). Dilution of ^3He bubbles in ^4He capillaries allows to reach 100mK on the HFI focal plane. After dilution the gas is expelled into space.

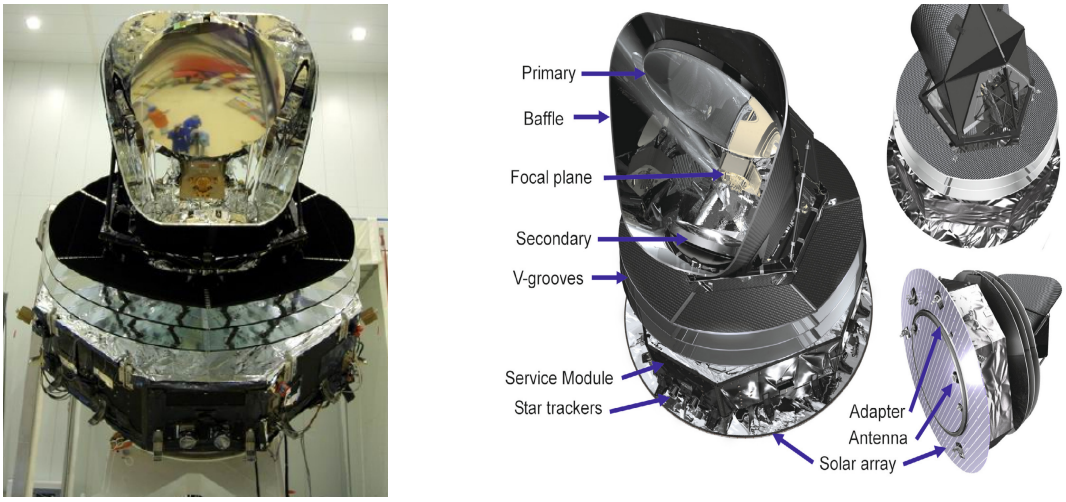

(a) (b)

Figure 3.1: (a) A picture of *Planck*. (b) Schematic representation of the satellite. The various components are highlighted. (Tauber et al. 2010).

3.1.2 Scanning strategy

Planck observes the sky from the Lagrangian L2 point of the Earth-Sun system. Its scanning strategy (Delabrouille et al. 1998; Dupac & Tauber 2005) has been conceived to optimise data redundancy, sky coverage and also to attain a measure for polarisation. Its spin axis is almost aligned with the Sun-L2 axis and the solar panels are kept oriented towards the Sun. The direction of observation, is oriented at 85° with respect to the spin axis. *Planck* scans the sky with wide circle every minute (Fig.3.2(a)). It is kept stable for periods ~40-50 minutes long called *rings* for which data are redundant. This redundancy is vital for optimising SNR and for treating systematics, in particular 1/f noise.

After a ring, the satellite is then shifted by 2 arcmin resulting in a mean shift of 1° per day. If the angle between the spin axis and the direction of observation were exactly 90° we would have had a perfect full sky coverage in 6 months and ring intersection exactly at the ecliptic poles. In order to have a more homogeneous sky coverage, the spin axis of the satellite precedes around the Sun-L2 axis, describing a cycloid with an amplitude of 7.5° and a 6 months period. This has been chosen to respect the constraints imposed by the thermal stability (thus avoiding Sun exposure) and also to assure the dispersion of the orientations of detectors needed for the reconstruction of polarisation (sec.3.2).

An almost complete scan of the sky, called *survey* is realised in 6 months. Full mission data, that are used in this thesis, consists of ~5 surveys (29 months). Surveys 1,3 and 5 and 2, 4 respectively, are

similar in sky coverage and scanning path, while 1,2 and 3, 4 scanned almost the same sky with opposite directions.

In Fig.3.2(b) is reported, in galactic coordinates, the number of observations per pixel (clipped at 5000 for illustration purpose). Hits counts show that the sky coverage is not homogeneous and that there is redundancy around the ecliptic poles.

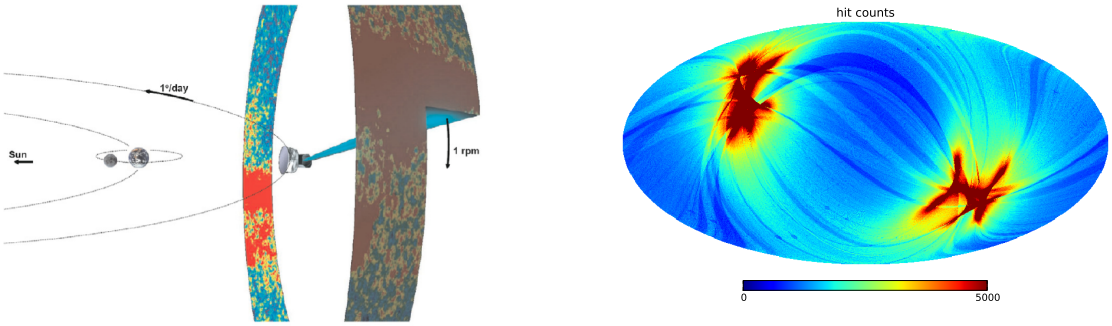

(a) (b)

Figure 3.2: (a) The *Planck* satellite is located in the lagrange point L2 and its spin axis is in precession around the Sun-L2 axis. It pivots around the spin axis at the speed of 1 tour per minute, keeping a fixed pointing for ~40 minutes (a *ring*). It progress of 1° per day. (b) Hit number maps in galactic coordinates (Mollweide projection), cut at 5000 for representation purpose.

3.2 Detectors characterisation

The *Planck* focal plane contains the two instruments LFI and HFI, observing the sky at different frequencies from sub-millimeter to micro-waves. LFI measures the sky in three bands centred respectively on 30, 44 and 70 GHz, and based on radiometer technology (sec.3.2.2). HFI uses bolometers and focuses on higher frequencies from 100GHz to ~1THz sampled in 6 bands (sec.3.2.1). The actual detectors for the two instruments are preceded by corrugated horns serving as wave-guides. The wide frequency coverage is designed to target the peak of the CMB emission but also the foreground emissions like synchrotron, free-free, and Galactic dust thermal emission.

Detector photometry

At each time t, the response of a polarisation sensitive detector to a polarised signal can be approximated as (Jones et al. 2007):

$$d_t = g(I + \rho[Qcos(\psi_t + \alpha) + U sin(\psi + \alpha)]) + n_t \tag{3.1}$$

in which n is the noise, g is the total gain, ρ is the polarisation efficiency, ψ is the angle between the focal plane and the reference system in which Q and U are defined and α stands for the relative detector orientation with respect to the focal plane.

Polarisation reconstruction

The reconstruction of the full-sky polarised signal requires the combination multiple polarisation sensitive devices. To determine (I,Q,U) we need to combine the signal of at least three detector that have measured d with different values of the total angle $\psi + \alpha$ (modulation). The *Planck* scanning strategy (sec.3.1.2) does not allow to have this variety of angles for a single detector (with the exception of the

spot around the ecliptic poles). It is thus necessary to combine detectors with different orientations. As can be seen in Fig.3.5(b), different pairs of detectors, for a given frequency, are tilted by 45°. This configuration allows for the optimal reconstruction of the polarisation, where the measurement errors in the Stokes parameters I, Q and U are independent of the direction of the focal plane and decorrelated (Couchot et al. 1999).

Nevertheless, combining more than one detector has inevitably some problems. Any difference between intensity measurements will induce leakage of intensity to polarisation. In particular, an error on the relative calibration causes a leakage between the reconstructed Stokes parameters; this induces temperature to polarisation leakages, and E to B leakage at the level of the spectra(Rosset et al. 2010), with dramatic consequences on the precision we can reach. This is why a calibration (sec.3.3.3) is very important.

Next section describes in more details the HFI instrument that it is the of this thesis. Some notions on LFI are given in sec.3.2.2.

3.2.1 The High Frequency Instrument

HFI measures the sky in 6 frequencies centred respectively at: 100, 143, 217, 353, 545, 857 GHz. These numbers have been chosen for attaining specific scientific goals, from the characterisation of the CMB anisotropies to the study of Galactic and extragalactic foregrounds. They are discussed in more detail in sec. 3.5.

The HFI detectors are bolometers. The radiation energy is left via Joule effect on an absorber of low heat capacity, which is a grid of gold wires on a silicium nitrate support. The incoming radiation is absorbed causing a rise in temperature measured through a thermistor, namely, a Neutron Transmutation Doped (NTD) germanium thermistor. The thermistor is polarised in current so that the rise in temperature causes a measured change in the bolometer output voltage.

HFI is equipped of two types of bolometers: those sensitive only to the intensity of the incoming radiation and those sensitive to polarisation. The placement of the wires determines this specific property.

Spider Web Bolometers (SWB) (Bock et al. 1995), in Fig.3.3(*left*), collect the CMB total power with a spider-web-like grid. This configuration enhances sensitivity and robustness to vibration, and reduces time response and cross section with astro-particles (Tristram & Ganga 2007). The grid characteristic scale is related to the wavelength of the radiation of interest, reducing the background coming from lower wavelength. The NTD thermistor is at the center of the web.

For Polarisation-Sensitive Bolometers (PSB) (Jones et al. 2003), in Fig.3.3(*right*), the grid is rectangular. In this configuration, only the two perpendicular directions are important. In each PSB, absorbers do cover only one of these directions, giving sensitivity to the linear polarisation in to this orientation.

Ideally, the polarisation efficiency ρ of Eq.3.1 is one for a PSB. Inversely, $\rho = 0$ for a perfect SWB and thus only a measurements of the total intensity is obtained.

In practice, SWBs are slightly sensitive to polarisation ($\rho \sim$ few%) and PSBs have $\rho \sim 90\%$ since there are some leakages in the direction orthogonal to the polarisation we want to measure (Rosset et al. 2010).

A system of horns leads the radiation through bolometers (Fig3.5(a)). In Fig.3.4 are shown the various stages of this optic line with the cryogenic temperature associated. The collection of incoming photons is achieved via two back-to-back horns. This stage at 4K is a waveguide in between the two horns that pre-filter the accepted frequencies. The next stage, at 1.6K, completes the filtering. There is then a last horn at the working temperature of 100mK. It is isolated from the rest of the optic line and optic coupling is ensured by a lens.

Fig.3.5(b) is a schematic representation of the focal plane. HFI consists in 52 bolometers plus 2 blind bolometers for the estimation of instrumental effect like temperature fluctuation of the focal plane. 20

bolometers are SWBs and 32 are PSBs. PSBs are assembled in pairs of orthogonal polarisation sensitivity (called PSB-a and PSB-b). Only the four lower frequencies are sensitive to polarisation.

The angular acceptance, called *beam*, depends on the whole optic chain, from the shape of the mirrors to the shape of the horns. It is estimated from the observation of planets, mainly Saturn and Mars[1]. For a given direction of observation, the signal received is the convolution of the real signal with the beam. When the beam are not rotationally invariant, the total signal depends on the orientation of the satellite. Beams are thus important in the map-making process and in the building process for spectra. We will come back to this in chapter 5.

In general the angular resolution of the instrument is defined as the full width at half maximum (FWHM) of the Gaussian adjusted on the mean beam for each frequency. The ellipticity has to be accounted for. HFI angular resolution varies between 10 and 5 arcmin. A summary of the properties of HFI can be found it Table3.1.

Table 3.1: Characteristics of the HFI detector (Planck Collaboration. I. 2015)

Central freq. (GHz)	100	143	217	353	545	857
Bandwidth (GHz)	32.9	45.8	64.5	101.4	171.3	245
Num of detectors	8	8	8	8	4	4
(of which polarised)	(8)	(4)	(4)	(4)	-	-
Effective beam FWHM$_1$ [arcmin][a]	9.68	7.30	5.02	4.94	4.83	4.64
Effective beam FWHM$_2$ [arcmin][b]	9.66	7.22	4.90	4.92	4.67	4.22
Effective beam ellipticity ϵ[c]	1.186	1.040	1.169	1.166	1.137	1.336
Temperature noise [μK_{CMB}deg]	1.29	0.55	0.78	2.56		
Temperature noise [$kJysr^{-1}$deg][d]	...	...	...	...	0.78	0.72
Polarisation noise [μK_{CMB}deg]	1.96	1.17	1.75	7.31	...	... [e]

[a] FWHM of the Gaussian whose solid angle is equivalent to that of the effective beams.
[b] FWHM of the elliptical Gaussian fit.
[c] Ratio of the major to minor axis of the best-fit Gaussian averaged over the full sky.
[d] Estimate of the noise in intensity scaled to 1° assuming that the noise is white.
[e] Estimate of the noise in polarisation scaled to 1° assuming that the noise is white.

HFI noise sources

There are several physical processes that give a white noise contribution to the measurements.

- *photon noise* is an unavoidable contribution. It is due to the Poisson fluctuations of the number of photons that hit the detector and comes from the CMB signal itself.
- *phonon noise*, residual thermal noise
- *Johnson noise* from electronics, reduced by the low temperature.

The last two are reduced thanks to the cryogenic cooling at the very low temperature of 100mK, to the control of the thermal noise, and to the readout electronics that is fast and low noise.
A supplementary parasite effect for some of the channel is the random telegraphic signal of unclear origin

[1] There is also a tiny contribution from the far-side lobes originated by multiple reflections, diffraction and diffusion of the light, that are estimated with full simulation of the optical architecture .

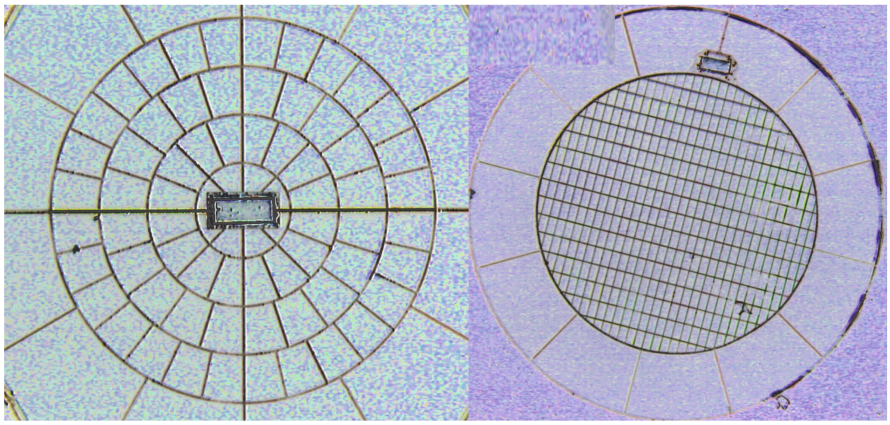

Figure 3.3: Picture of a 143 GHz spider web bolometer (*left*) and of a 217 GHz polarisation-sensitive bolometer (*right*). The temperature sensor is at the center of the SWB and at the upper edge of the PSB (Lamarre et al. 2010).

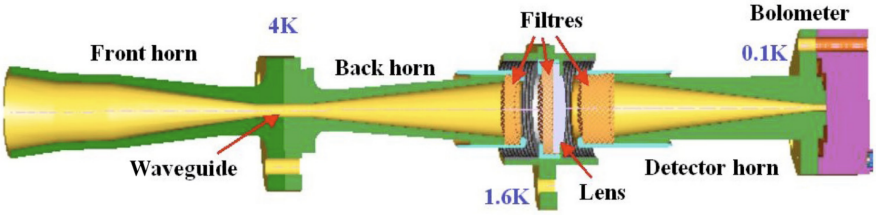

Figure 3.4: System of horns and bolometers. The three horns back-to-back guide the wave through the frequency filters and to the bolometer. Different cooling levels are also shown (Lamarre et al. 2010)

that causes a rapid random shift of the mean level of data (the “pop-corn" noise). The bolometer 143-8, 545-3, and 857-4 has been excluded from the analysis for an excess of this noise.

3.2.2 The Low Frequency Instrument

As the COBE Differential Microwave Radiometer (DMR) and WMAP, LFI is composed of differential radiometers. A radiometer is a device whose output voltage is proportional to the power received by a horn antenna. This output is then amplified by a High Electron Mobility Transistor (HEMT). HEMTs are well suited for CMB experiments since they have a low noise and a wide bandwidth but their sensitivity is limited by long scale gain variations. The 1/f noise can be reduced using differential radiometers where the input is not a single antenna but an antenna and a reference load. The two signal paths are in antiphase so that common 1/f vanishes.

LFI differential radiometers, based on the same technologies than previous space missions, represent however a step forward in terms of performances. They are cryogenically cooled down at 20K to reduce amplifier noise and make them more sensitive. The reference load temperature is the 4K stage of HFI. Having the reference load temperature close to the temperature of the signal limits the effects systematics (Tristram & Ganga 2007).

In the focal plane (Fig.3.5(a)) LFI horns are around HFI ones since they are less sensitive to optical aberrations. There are 22 radiometers all sensitive to polarisation. OrthoMode Trasducters (OMT) are

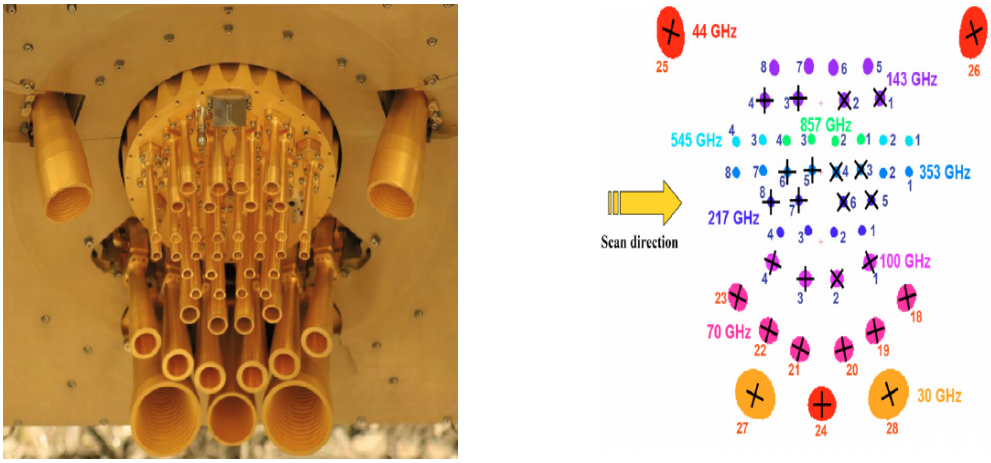

(a) (b)

Figure 3.5: (a) HFI and the LFI horns picture taken during ground tests. (b) Focal plane scheme: frequencies are identified by colors and the horn identification numbers are also indicated (LFI horns in red, HFI horns in blue). The black crosses indicate the direction of sensitivity to linear polarisation for pairs of bolometers or radiometers within each horn (horns with no cross correspond to bolometers sensitive to total power only) (Tauber et al. 2010).

used to separate the orthogonal polarisations with minimal losses. Relative sensitivity per pixel ($\Delta T/T$ par pixel) is of a few 10^{-6} and the angular resolution is of 33, 28 and 13 arcmin for the 30, 44, and 70 GHz respectively. There are 4 detector at 30 GHz, 6 at 44GHz and 12 at 70GHz. This latter has a larger number of detectors, since it is in the window where foregrounds are minimal and thus has a special interest for cosmological results.

The LFI instrument can be used to constrain the large scale part of the CMB power spectrum and its polarisation data can be used to put constraint on reionisation. In chapter 6.1 we briefly describe how the low-ℓ part of the likelihood can be built using the 70GHz maps cleaned with the 30GHz for the synchrotron and HFI 353GHz for Galactic dust.

3.3 HFI data treatment

The exploitation of *Planck* measurements to achieve precise cosmological and astrophysical results, relies on a complex chain of data treatment and analysis. We focus here only on the HFI detector. In Fig3.6 this three level process is reported in a schematic view.

At **Level 1** raw data transmitted by the satellite are uncompressed and re-organised to create the time ordered data (Time Ordered Information, TOI). At this stage a number of checks on the parameters of the instruments are also performed to understand if the instrument and its devices are working correctly (looking at the *housekeeping* telemetry) and to assess the quality of scientific data (looking at the Science Telemetry).

Level 2 includes a series of modules for the processing of the TOI (Fig3.7). The final products of this stage are the sky maps for each frequency. TOI processing is briefly described in sec.3.3.1. The main stages of the calibration process are summaries in sec.3.3.3

At **Level 3** the maps and the relevant informations on the instruments are used for the realisation of several products of high scientific interest that are released to the community. These are the component maps, where the different spectral properties of the CMB and the foregrounds are used to disentangle

them (Appendix A.2), compact source catalogs (Appendix A.1), and the likelihood. This latter is the central theme of this thesis and is discussed in details in chapter 5.

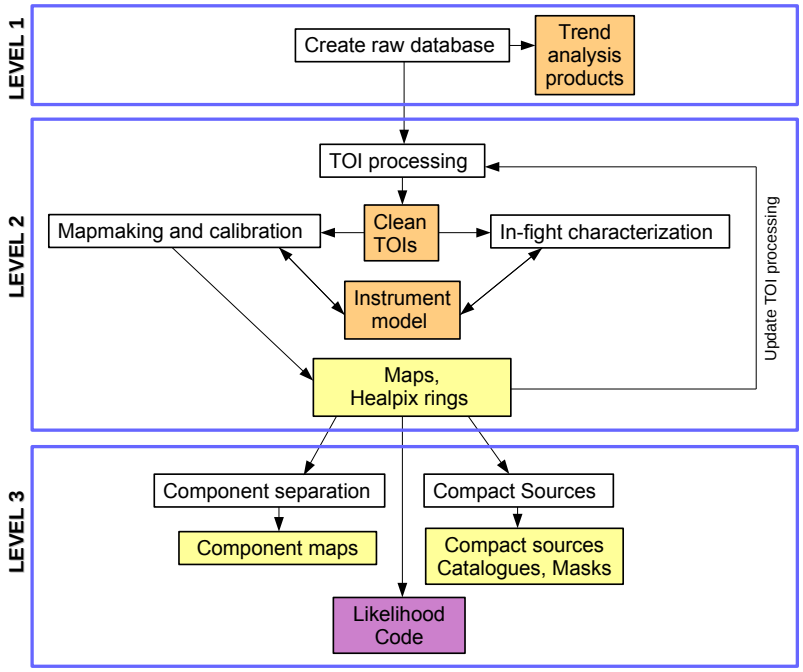

Figure 3.6: Schematic picture of the data analysis pipeline. Adapted from Planck Collaboration. VI (2014).

3.3.1 TOI processing

At the L2 level, the raw timelines are corrected for the effect of systematics induced by the detection chain or by the environmental effects. To identify and subtract properly all these effects, an on-the-fly characterisation of the instrument has been performed along the entire mission, updating constantly the instrument model that is then used to TOI processing (Fig.3.6). The various steps of TOI processing include demodulation, degliching, correction for bolometers non linearities and for temperature fluctuations of the environment, correction of 4K lines and, finally, flagging of the unusable samples. In this section we briefly review these steps. For a detailed description see Planck Collaboration. VI (2014); Planck Collaboration. VII (2015).

Demodulation

To avoid as much as possible $1/f$ noise due to electronics, the polarisation current at the bolometer bounds is alternate (AC bias) (Lamarre et al. 2010). To optimise this process, the modulation frequency is chosen to be $f_{mod} = f_{acq}/2 = 90Hz$, where $f_{acq} = 180Hz$ is the frequency at wich data are sampled. The first step in TOI processing is thus the demodulation and decompression of the signal.

ADC correction

An analog-to-digital converter (ADC) device is used to convert the continuous voltage measurement to a digital number that represents the voltage's amplitude. ADCs suffer from non-linearity errors caused by

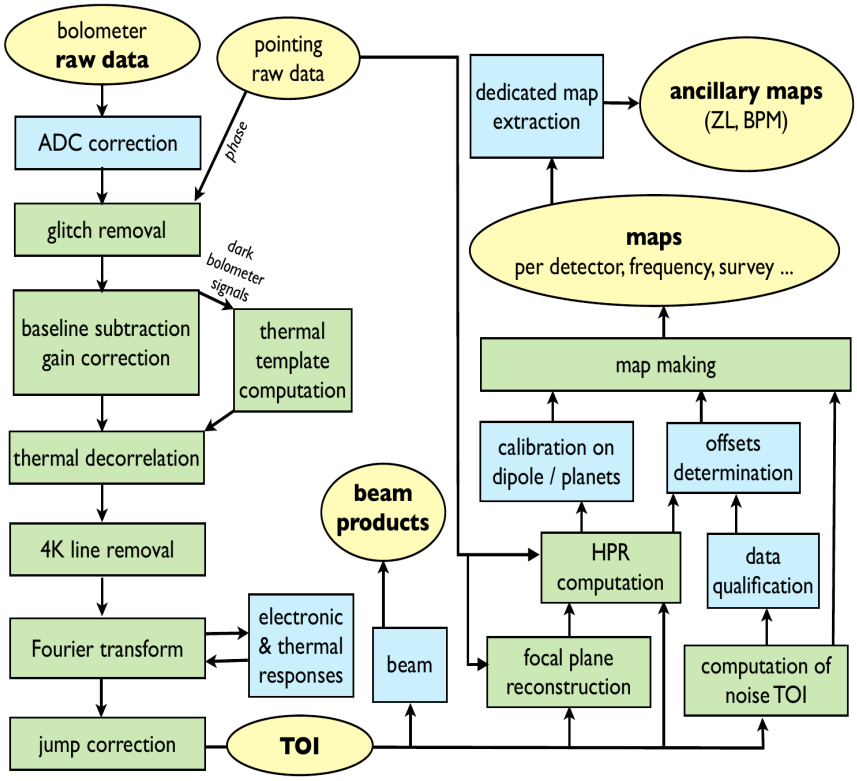

Figure 3.7: Level2 schematic HFI pipeline (Planck Collaboration. VII 2015). The left part of the schematic involves TOI processing and beams production, while the upper-right part represents the map-making steps. *Blue*: what has been update between the 2013 and 2015 analysis. *Yellow*: released data products.

their physical imperfections, resulting in a deviation from linearity in their response.

In the 2013 analysis, this errors where found responsible for an apparent gain variation in the data, that had been treated at the map-making stage (Planck Collaboration VI 2014). For the 2015 data release, the correction for this systematic errors has been implemented as a direct ADC correction at the TOI level.

In general, the defects of an ADC chip are fully characterised by the input levels corresponding to the transitions between two consecutive output values. An ADC defect mapping is usually run on a dedicated ground test bench. This had not be performed for HFI ADC devices. Nevertheless, dedicated flight data (”warm data"), were recorded during the 1.5 years of the LFI extended mission, between February 2012 and August 2013. During this period the bolometer temperature was stable at about 4 K and HFI bolometers where measuring no signal anymore but only Gaussian noise. The defect mapping was obtained by inverting the histograms of the accumulated fine-grain sampled raw data and has been use to correct the non-linearity.

Degliching

One of the main systematic effects that need to be subtracted is the energy deposition from high energy cosmic rays for which the shielding of the baffles is not sufficient. There is on average one event per

seconds. The rate is anti-correlated with solar activities[2] and includes mainly cosmic rays of Galactic origin. The typical signal is a *glich*, namely a rapid rise of the signal followed by a slower decrease. These gliches are iteratively detected and subtracted at the TOI level.

Gain non-linearities correction

The timelines must be corrected to account for slightly varying power absorbed by the bolometers. These variations comes from the sky load and 100mK bolometer plate temperature fluctuations. To cure these non linear effects, the Voltage-to-power conversion step is parametrised by a second order polynomial and fitted over the sky.

Thermal drift decorrelation

A common mode due to temperature fluctuation of the 100mK cooler stage has to be removed during this step of TOI processing. This correction relies on the measurements of the coupling coefficients between the bolometers and the bolometer plate temperature. The variations of this latter are measured using the two dark bolometers as proxies[3]. The effect is anyway not big and negligible for the 1.6K and 4K stages.

4K cooler line removal

Frequency vibrations of the 4K cryogenic stage are harmonics of the signal sample frequency (10, 20, 30, 40, 50, 60, 70, 80 and 17 Hz). This electromagnetic interference produces peculiar lines in the signal power spectrum that are removed using a Notch filter reducing contamination to be less then 3% of other sources of noise[4].

In 2013 data, there was, however, a residual effect affecting multipoles at $\ell \simeq 60(f/1Hz)$ i.e., 600, 1020,1200,1800,..with a particularly visible features at $\ell \sim 1800$.

In the 2015 analysis, additional selection processes has been introduced to mitigate the effect and the $\ell \sim 1800$ feature has disappeared (Planck Collaboration. VII 2015).

Transfer function deconvolution

The temporal response of a bolometer and its electronic have to be properly taken into account. There is typically a delay in the reaction to a rapid signal that acts like a low-pass filter. The time constants are generally from a few milliseconds to few tenths of seconds. They are characterised using the response to intense point source as planets.

The identification of very long time constants (VLTC) of the order of a few seconds and their inclusion in the analysis, is one of the calibration process greatest improvement of the 2015 analysis with respect to the 2013 results (Planck Collaboration. VIII 2015). VLTCs, if not corrected, introduce a significant shift in the apparent position of the Solar dipole, resulting in a leakage of the Solar dipole in the orbital dipole. This is important since the dipole is used for the calibration of the data. Some details of the calibration process are described in sec.3.3.3.

Jump correction and Sample flagging

In some pointing periods, signal removed TOI show sudden jumps. The jumps (in average a few per day) are corrected subtracting a constant template from the timelines and are *flagged* around the recovered

[2]More solar activities means stronger magnetic fields that deviates away the cosmic rays that are charged particles.
[3]HFI 100mK thermometers have too many cosmic hits to be used.
[4]It affects anyhow the ability to characterise and remove ADC nonlinearities

position (these flags correspond to only a fraction 10^{-5} of data). Flags are also associated to unstable pointing periods (7% of data), gliches (8-20%), and transit of solar system objects (planets and asteroids). The flagging of data is important to distinguish which data need to be projected at the map making level.

In Fig.3.8 is shown a portion of TOI data after processing. At the end of TOI processing, there are still some systematics in the data seen as a correlated noise component at low frequency. This is treated at mapmaking level.

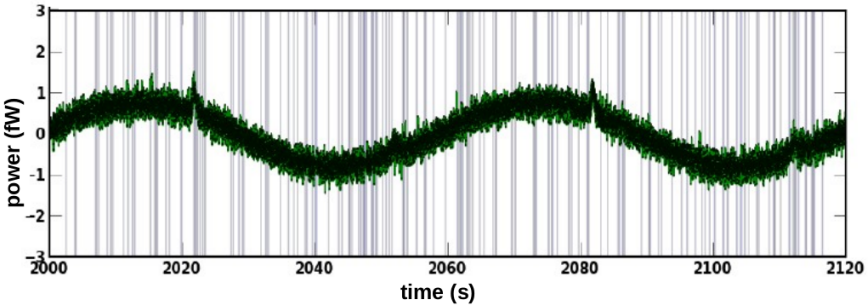

Figure 3.8: Two minutes portion of a *ring* from bolometer 143-a after TOI processing. The global modulation is the dipole. At 2020 seconds we recognise the Galaxy; 30 seconds after there is again the signal from the Galaxy but weaker (we are farther from the center). Grey lines are the flags (17% of the whole ring). Figure taken from (Racine 2014).

3.3.2 In-flight characterisation

As shown in Fig.3.6, at Level 2, data are used to build a model for the HFI instrument, the IMO. The IMO is used to update the TOI processing and optimise mapmaking and calibration.

We have already underlined, for example, that the knowledge of the temporal response of the bolometers is vital for a correct analysis of the TOIs. The characterisation of the transfer function comes together with other in-flight detector descriptions that are necessary for any further analysis.

Detector pointing

The mapmaking process requires the knowledge of the pointing of individual detectors. The satellite pointing comes from the star tracker camera subsystem but in practice we need pointing of each detector. The detailed geometry can be measured by comparison with the position of Mars, that is a bright and nearly pointlike object. The actual construction of *rings* (sec.3.3.3) is done using this reconstructed focal plane geometry.

Detector beams

As said in sec.3.2.1, the estimation of beams relies on the observations of planets. We have quoted in Table 3.1 the mean value, for each HFI frequency, of the beam using a Gaussian approximation. A more complete characterisation for the beams can be done using a decomposition on two different orthogonal basis: the Gauss-Hermite polynomials and the B-spines[5] (Planck Collaboration. VI 2014). This latter

[5]A spline is a numeric function that is piecewise-defined by polynomial functions, and which possesses a sufficiently high degree of smoothness at the places where the polynomial pieces connect (which are known as knots). Any spline function of

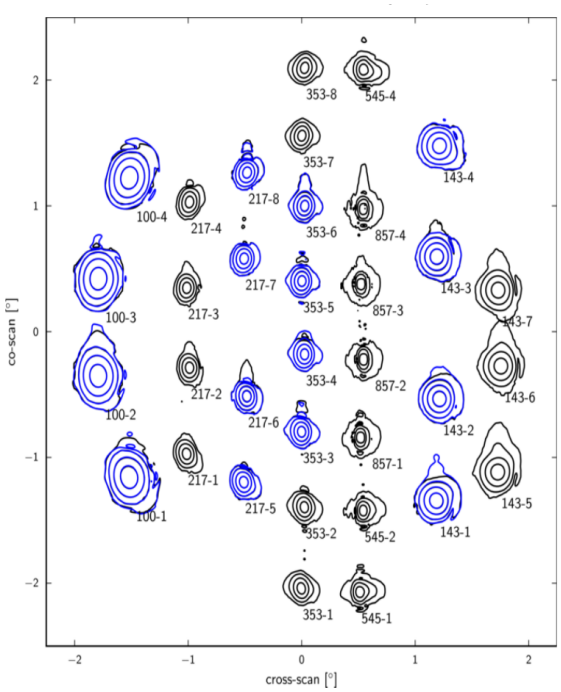

Figure 3.9: B-spline hybrid scanning beams reconstructed from Mars, Saturn, and Jupiter. The beams are plotted in logarithmic contours. PSB pairs are indicated with the *a* bolometer in black and the *b* bolometer in blue (Planck Collaboration. VII 2015).

is the one used by the *Planck* Collaboration. In Fig.3.9 are shown B-spline hybrid[6] *scanning beams* reconstructed from Mars, Saturn, and Jupiter. Their shape depends on the optic of the instrument but also on the time-response of bolometers and the scanning strategy since the focal plane sees the sky with a fixed scanning direction. This direction is indeed recognisable from the beams “tails" in the figure.

The map-making process (sec.3.3.3) implies that each pixel in a map is the sum of different samples in the timelines, and each of this sample has a different location within the pixel and a different scan direction. This is why, *effective beams* are also calculated taking into account the specific scanning strategy in order to include any smearing and orientation effects on the beams themselves.

3.3.3 Calibration and map-making

The representation of the data in full-sky maps requires a choice for the *pixelisation* for the celestial sphere and of a coordinate system. The Hierarchical Equal Area isoLatitude Pixelisation (HEALPix) framework (Górski et al. 2005) has been chosen. Each pixel has the same area (quadrangles of different forms) and its center lies on sets of rings at constant latitude. This is the most common pixelisation scheme in CMB since it is well suited for the fast Fourier transform analysis used for the decomposition of the map into spherical harmonics. The resolution of the map is defined by the parameter $N_{\rm side}$, the number of divisions of the side on 12 base pixels. The total number of pixels is then $n_{\rm pix} = 12 \times N_{\rm side}^2$ and the resolution is $\sim \sqrt{4\pi/n_{\rm pix}} = \sqrt{\pi}/(\sqrt{3}N_{\rm side})$.

Maps are then represented in the Mollweide projection and the privileged coordinate system is the

given degree can be expressed as a linear combination of the B-splines (basis-spline) of that degree.

[6]Hybrid scanning beams include sidelobes.

Galactic one where the Milky way lies in the center.

In this section, after the presentation of the map-making problem (Tristram et al. (2011) and references therein), we briefly describe the procedure used by the *Planck* Collaboration for the production of the various maps.

The TOIs (with the flags) issued from the cleaning process are measurements in Watt units and need to be calibrated into astrophysical units. Maps and their calibration are obtained iteratively.

The map-making problem

Given the pointing (a given direction in the sky) and the instrumental beam, HFI bolometers measure the brightness of the sky. The time ordered data at time t of Eq.3.1, d_t can thus be modelled as:

$$d_t = A_{tp} \cdot T_p + n_t \tag{3.2}$$

where:

- A_{tp} are the elements of the pointing matrix that relates each time sample t to the corresponding pixel p.
- T_p is the signal from the sky
- n_t is the noise

In general, we can include the effect of the beam in the signal, solving for beam-convolved maps. The pointing matrix $\mathbf{A}$ contains only three (we have to reconstruct I,Q and U) non null value in each row, as each sample is sensitive to only one pixel. Its size is thus $N_s \times 3N_p$. Here we consider noise as Gaussian and stationary. All its statistical information is thus included in its covariance matrix $\mathbf{N} = \langle \mathbf{n}\mathbf{n}^T \rangle$.

The most general solution of the mapmaking problem is obtained by minimising the likelihood of the data given a noise model which is the generalised least squares (GLS) equation (Tristram et al. 2011). The estimate for the signal $\hat{\mathbf{T}}$ and its covariance $\hat{N}$ reads

$$\hat{\mathbf{T}} = \left(\mathbf{A}^T\mathbf{N}^{-1}\mathbf{A}\right)^{-1} \cdot \mathbf{A}^T\mathbf{N}^{-1}\mathbf{d}, \tag{3.3}$$

$$\hat{N} = \mathbf{A}^T\mathbf{N}^{-1}\mathbf{A} \tag{3.4}$$

Planck angular resolution allows the reconstruction of maps with $N_{\rm side}$=2048 including more than 50 millions of pixels making the calculation of the covariance matrix computationally prohibitive. Nevertheless, if one approximates the noise as white, the matrix for $\mathbf{N}$ is diagonal. This means that the estimation of the signal $\hat{\mathbf{T}}$ reduces to the mean of the measurements for every pixel, weighted by the noise. This is called *co-addition*.

The first step of the *Planck* analysis is the construction of HEALPix rings (HPR). As explained in sec.3.1.2, a *ring* is the time-ordered collection of circular scans obtained with a stable position for the spin axis. An HPR is the collection of pixels visited during the ring. It is a partial map of the sky, already at the good resolution, where the signal is obtained at each pixel by co-addition. It also allows to improve the pointing (Planck Collaboration. VIII 2015).

The determination of HFI noise properties points out that beside the white noise contribution, a low frequency 1/f component is still present in the data. This means that, after TOI processing, there are still systematics left (Fig.3.10(a)), resulting in a wrong reconstruction of the mean level of the signal in a pixel when combining measurements spread in time leading to "stripes". This is treated directly at map-making stage via a procedure called *destriping* (Tristram et al. 2011), where these mean level

derivatives are estimated at ring level and subtracted before projection. In this approach, the noise in a ring r is represented by an offset o_r (Fig.3.10(b)) and a white noise part n[7].

Orbital-dipole calibration

The bolometer signal is proportional to the small variations in the incoming power from the sky. To obtain the measurement in sky temperature units, we need to determine a *gain* for each detector (see sec.3.2) using a known source in the sky. At high frequencies (545 and 857 GHz), calibration is performed on planets. For the lower HFI frequencies, the central CMB channels which are the mostly used in this thesis, the primary calibrator is the orbital dipole (Planck Collaboration. VIII 2015).

The relative motion of the satellite with respect to the last scattering surface causes a Doppler effect

$$T_{\text{Doppler}} = \frac{T_{CMB}}{\gamma_t(1 - \boldsymbol{\beta}_t \cdot \hat{\boldsymbol{u}})}, \tag{3.5}$$

where $\hat{\boldsymbol{u}}$ is the unit vector along the line of sight, $\boldsymbol{\beta}_t = \boldsymbol{v}_t/c$, with $\boldsymbol{v}_t$ the satellite velocity, and $\gamma_t = 1/\sqrt{1-\beta_t^2}$. The dominant component of $\boldsymbol{v}_t$ is the solar system motion with respect to the last scattering surface, the solar dipole. It can be considered stationary during *Planck* observations and it contributes as an $\ell = 1$ component. A residual contribution comes from the yearly motion of the satellite with respect to the solar system barycentre, the orbital dipole. Its brightness is an order of magnitude lower than the solar one but its time variability is determined by the satellite velocity. Calibration using orbital dipole, peculiar of the 2015 release, has allowed for an independent measurement of the solar dipole (3364.5 ± 0.8 μK), and a recalibration of the HFI spectra lading to a better agreement with WMAP and a precision of ±0.1% (Planck Collaboration. XIII. 2015).

3.4 *Planck*-HFI maps

The whole process of map-making for HFI (HEALPix ring making, destriping and calibration, and projection) is carried out at LAL and is summarise in the right part of Fig.3.2(a). Revising eq.3.2, we obtain for a given bolometer (Planck Collaboration. VIII 2015):

$$d_t = g\left(A_{tp} \cdot T_p + t_{solar} + t_{orb}\right) + \Gamma_{tr} \cdot o_r + n_t \tag{3.6}$$

where Γ_{tr} is the ring-pointing matrix (a data sample t is associated with the ring r) and t_{solar} and t_{orb} are the contributions from the solar and orbital dipole respectively. The non stationary contribution from the thermal emission of the Solar system, namely the *Zodiacal light*, is also subtracted prior to the final projection on a map.

The main product of the mapmaking pipeline are six intensity maps that cover the six frequencies (100-857 GHz) for the full mission (Fig.3.11). Maps resolution is N_{side}=2048 and the pixel size is 1'7.

In Figure 3.12 are presented the polarization maps at the four first frequencies (100, 143, 217, and 353 GHz), degraded to lower resolution (N_{side}=256) in order to enhance the signal-to-noise ratio. In both intensity and polarization, the emission from the Galactic dust (sec.3.5) increase with frequency. In intensity, CMB anisotropies are visible at high latitude in the low-frequency channels (between 100 and 217 GHz).

For each frequency, temperature and polarisation maps are also produced using detector sets (DS), or pairing Survey 1-2 and 3-4 to obtain Year 1 and Year 2 maps. Half Mission (HM) maps are also produced

[7] Also, for breaking the degeneracy between the signal and the offsets the mean level for these latter is arbitrary fixed to zero.

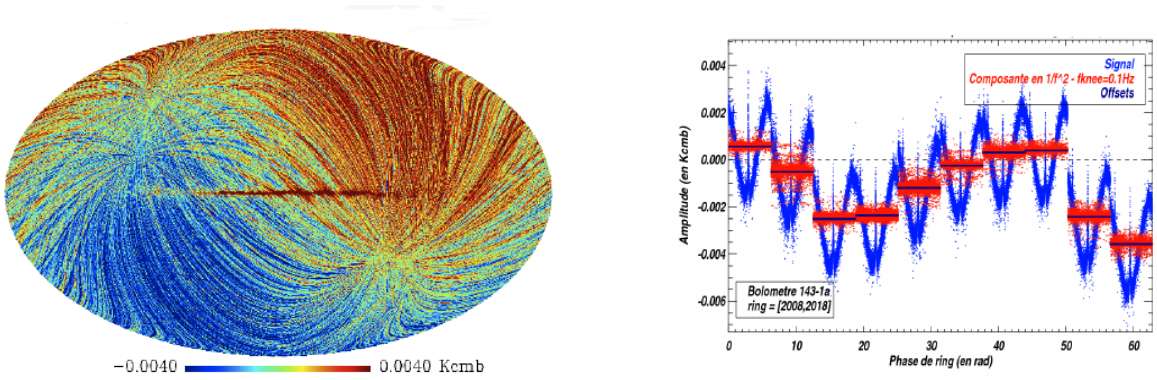

(a) (b)

Figure 3.10: (a) The effect of low frequency noise on a map are peculiar strips parallel to the scan direction. We can also recognise the Galactic plane and the solar dipole. (b) Illustration of 1/f noise. The offset are considered constant for each ring. and are fitted and subtracted at mapmaking level (Filliard 2012).

adding Survey 5 and splitting in two halves. These latter are the maps from which the official values of the cosmological parameters are obtained (Planck Collaboration. XIII. 2015).

For checking the noise and the consistency of the data many more maps are produced. For example maps from different halves of each ring period since half ring half differences give a good estimation of the noise level in a map. These kind of null test, called *jacknives*, can be constructed also for HM and DS maps.

Noise spectra (Fig.3.13) show significant deviation from white noise, resulting in a correlation between pixel.

- The half-ring difference is sensitive to high-frequency noise since most low-frequency modes are common to both data sets and thus vanish. At high resolution, pixels are correlated by time response deconvolution and filtering (sec.3.3.1). At large scales is the low frequency noise residual due to the destriping that dominates.

- The half-mission differences, allows to check for long-time-scale variations and for apparent gain variation with time due to ADC nonlinearities.

- Detector-set map differences shows systematic effects that are bolometer-dependent. Also, there is a tilt in the spectrum of the detector-set difference maps relative to the half-ring or half-mission split. This is due to a different time response function for the two halves in the case of detector set. At 353 GHz, signal residuals are larger due to relative calibration uncertainties between detectors. Despite these comments, DS maps are used in this thesis since their systematic effects are not dramatic and they provide a strong consistency check for the robustness of cosmological parameter estimation.

3.5 *Planck* foregrounds

Revealing the cosmological information concealed in the CMB signal comes together with the study of the foregrounds emission from the cosmic structures at all scales located between the CMB and us.

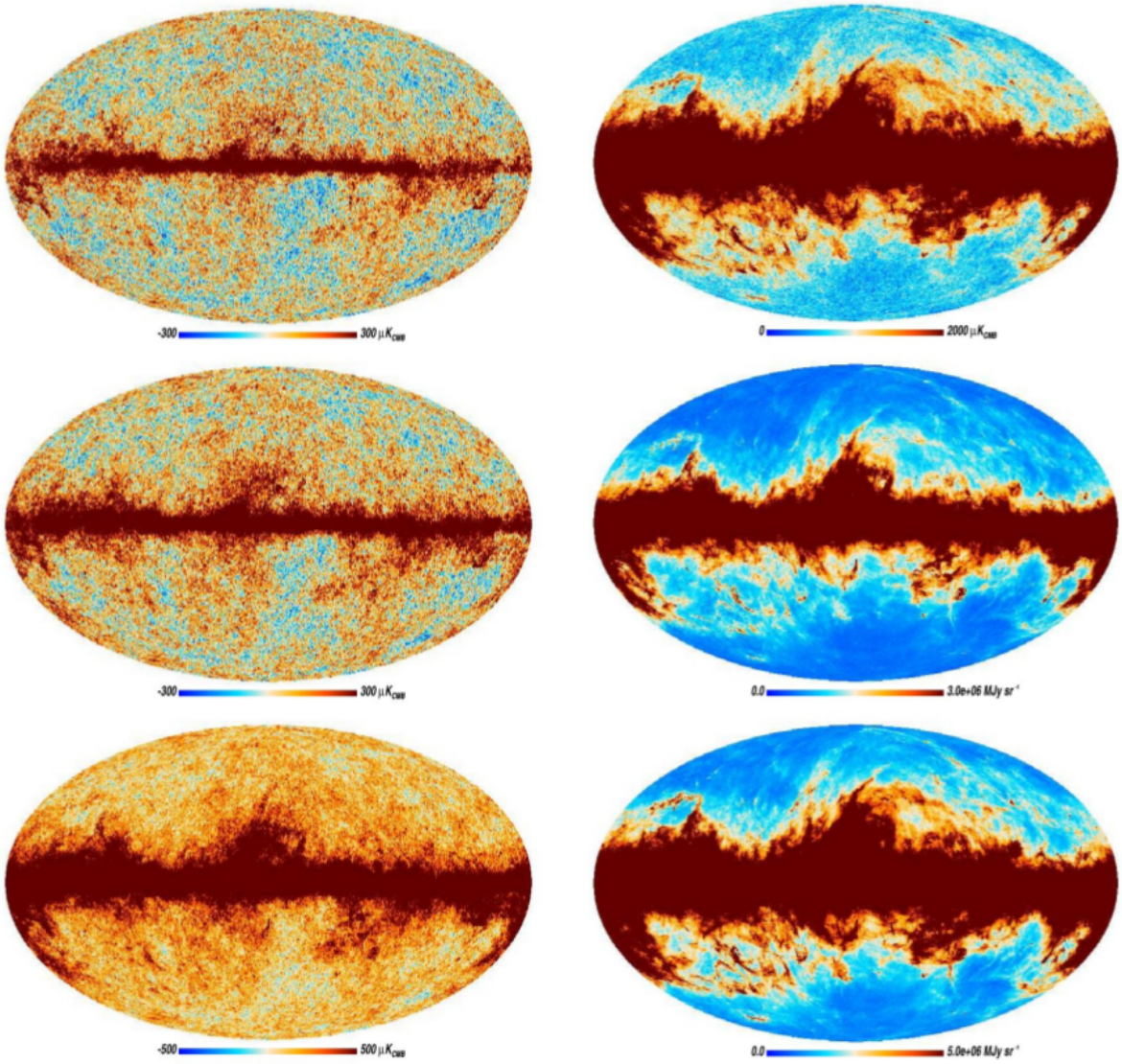

Figure 3.11: *Planck* HFI full mission intensity maps at 100, 143, 217, 353, 545 and 857 GHz (Planck Collaboration. VIII 2015).

In appendix A.1 we briefly describe some of the astrophysical products of the *Planck* Collaboration, as the catalogue of Compact Source that is relevant for us since we need to construct a mask to avoid this contamination for cosmological parameter estimation.

Also, the wide frequency coverage of the *Planck* mission is fundamental to characterise and separate *diffuse* foregrounds. Eight types have been identified: dust thermal emission; dust anomalous emission (from rotating small grains); three CO rotational lines; free-free emission; synchrotron emission; the Cosmic Microwave Background (CIB); Sunyaev-Zeldovich secondary CMB distortions; and the background of unresolved radio sources.

The characterisation of these foregrounds is fundamental for a proper estimation of the cosmological parameters. In this section, to revise the various component, we show some results extracted from *Planck* maps, using different techniques, and in some cases with the help of external ancillary maps tracing

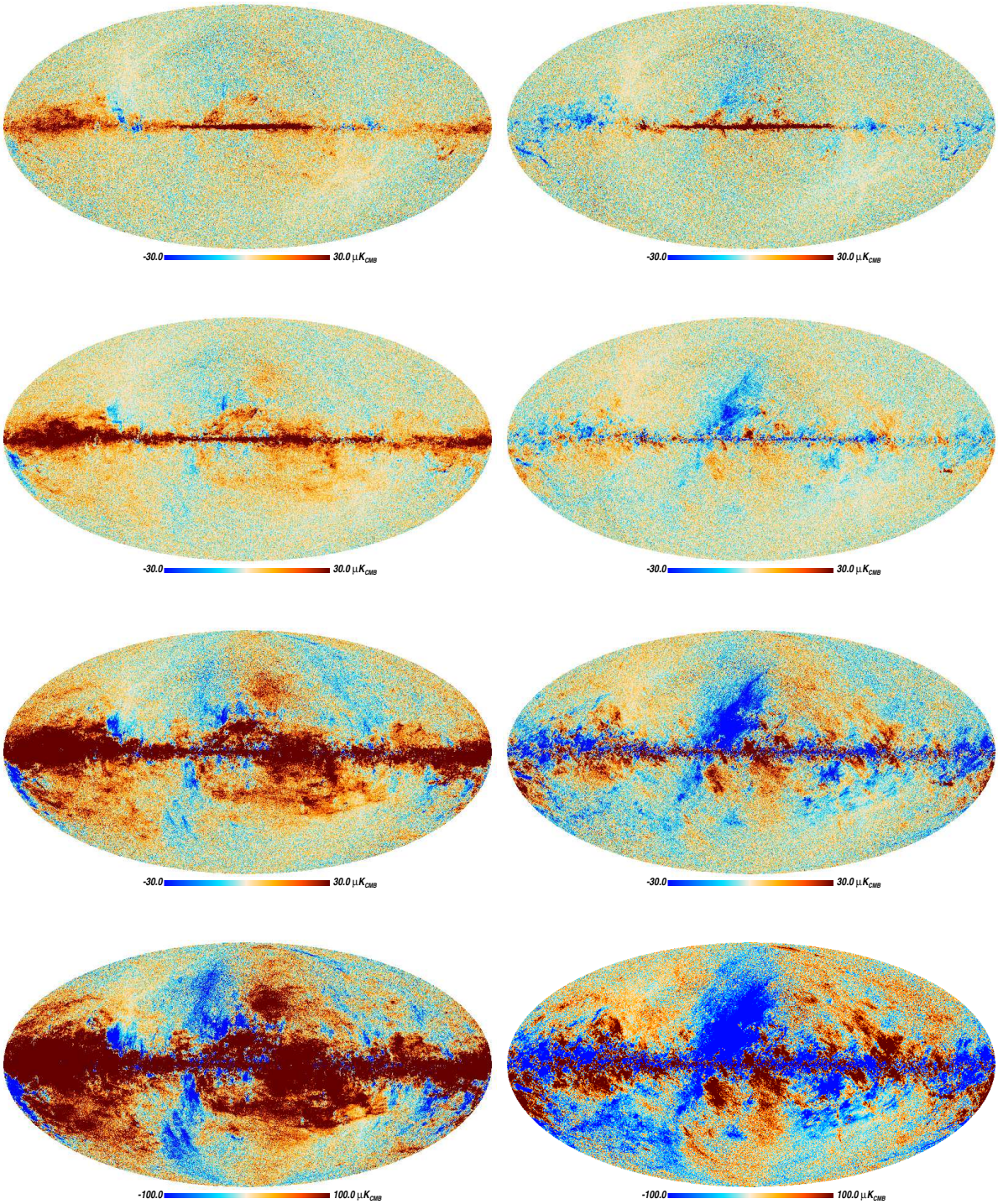

Figure 3.12: *Planck*-HFI full mission Q (*left*) and U (*right*) polarization maps. *from top to bottom*: 100 GHz, 143 GHz, 217 GHz, and 353 GHz

specific astrophysical components or prior knowledge of the spectral energy distribution of the power spectrum.

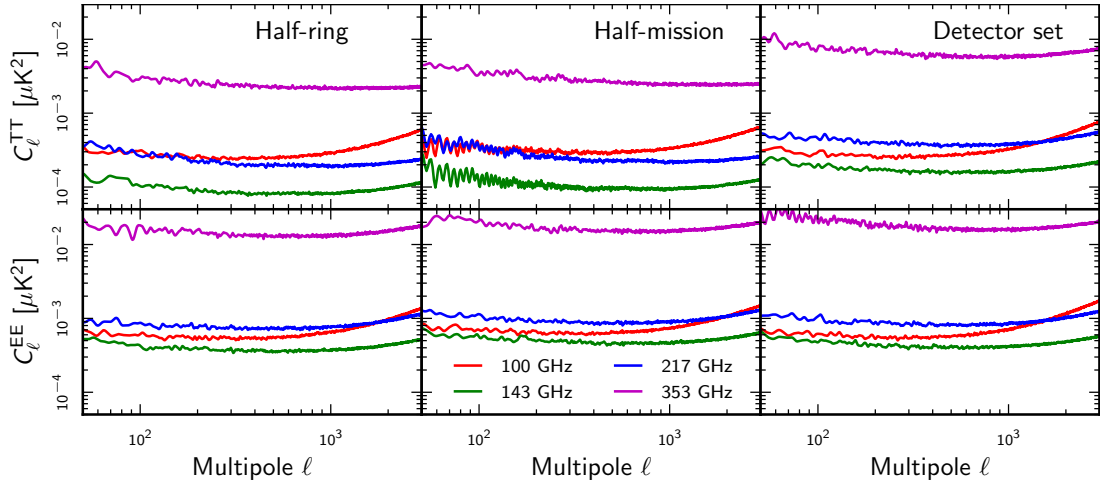

Figure 3.13: TT and EE power spectra reconstructed from the half-difference between data subset maps (Planck Collaboration. VIII 2015).

Foregrounds maps can be obtained using CMB component separation techniques. In this thesis, component separated maps are not directly used since a more detailed ℓ-by-ℓ removal of foregrounds and a proper account of different frequencies contribution is needed to obtain the best cosmological parameters. A brief description of component separation methods is postponed to appendix A.2.

However, it is interesting to have an overview of all the foregrounds seen by *Planck* satellite, both to justify the choices of the frequencies bands and to have a first description of the foreground models relevant for the `HiLLiPOP` likelihood, discussed in more details in chapter 5.

Fig.3.14, 3.15(a) and 3.15(b) are obtained using the `Commander` algorithm (sec. 6.1.1).This component separation algorithm employs detector and detector set maps and adds 9-year WMAP temperature sky maps (Bennett et al. 2013) and 408 MHz survey map (Haslam et al. 1981, 1982).

Main temperature foregrounds

In the foreground emission a Galactic and an extragalactic component can be identified.

In temperature, one can distinguish the following *Galactic* contaminations:

- Above 100 GHz the dominant radiation mechanism is thermal emission from the interstellar dust grains mostly made of graphites, silicates, and PAHs (Polycyclic Aromatic Hydrocarbons) in the Galaxy (e.g.Ichiki (2014)). *Thermal dust emission* is thus the most important foreground that we have to treat in our likelihood analysis.

  Its spectrum is well described by a modified black-body of the form $I(\nu) \approx \nu^{\beta_d} B_\nu$ where $B_\nu(T)$ is the Planck spectrum. Along the Galactic plane, a temperature gradient can be seen from the outer Galactic regions to the Galactic center from $T \approx 14 - 15$ K to $T \approx 19$ K probably due to more active star formation in the inner regions of the Galaxy (Planck Collaboration 2011). Clearly, considering only a gray-body with a single component of grains is a rude approximation and a more complete description has to deal with different sizes and compositions for the grains. To proper model Galactic dust also the subtraction of extragalactic sources, appearing as Cosmic Infrared Background (CIB) is needed[8] (sec.5.6.1).

[8]The model used by the `Commander` does not separate the Galactic thermal dust emission from CIB fluctuations. These

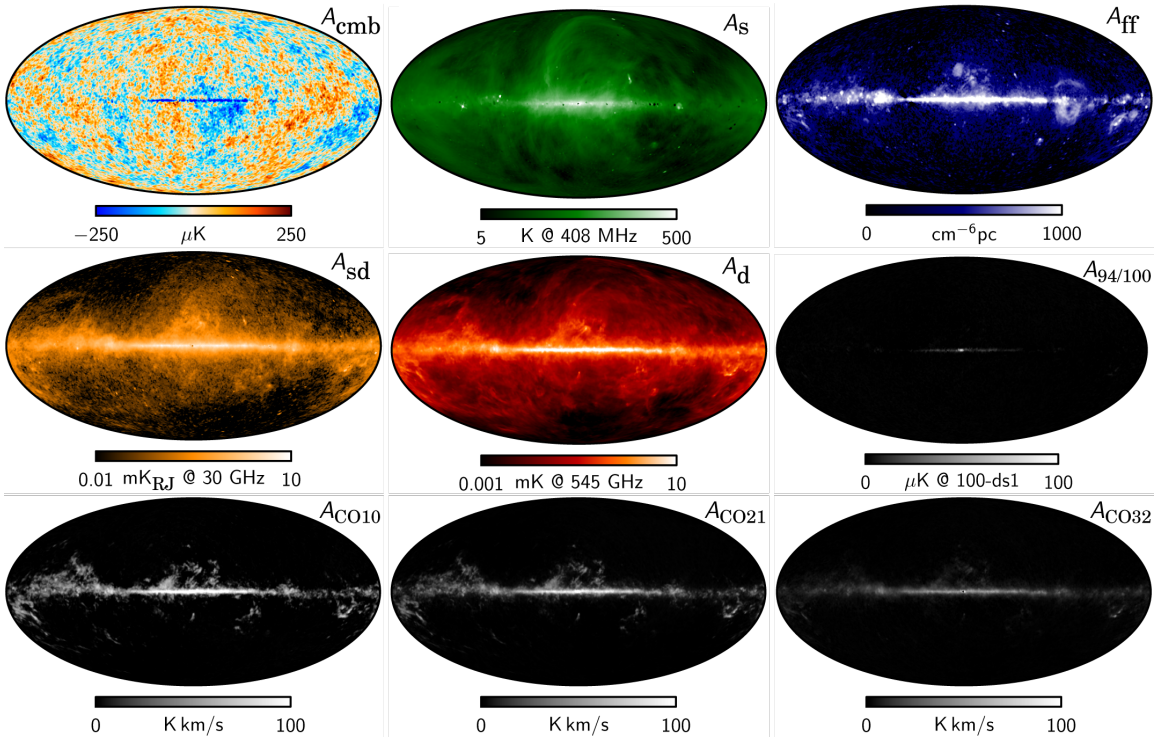

Figure 3.14: Maximum posterior intensity maps obtained using the `Commander` algorithm. From left to right, up to down: CMB, syncrotron, free-free, spinning dust, 94/100 GHz (a general line emission map which capture a combination of emission line detected with HFI 100 GHz and WMAP W bands (94 GHz)), and CO lines $J = 1 \rightarrow 0$, $J = 2 \rightarrow 0$ and $J = 3 \rightarrow 2$ respectively (Planck Collaboration. X. 2015).

- At lower frequencies there is the *diffuse synchrotron emission*, generated by relativistic cosmic-ray electrons spiraling in the galactic magnetic field. Its intensity follows a power law $I \sim \nu^{\alpha}$ with $\alpha \sim -3$. Although the lowest *Planck* frequency is dominated by synchrotron emission, the map in Fig.3.14 is also completely determined by the 408 MHz survey.

- The *free-free* is the bremsstrahlung radiation from electron-ion collision. The spectral emission is again a power law but the spectral index is weaker ($\alpha \sim -2$). For `Commander` the free parameter in the model is the emission measure (EM) namely the integrated squared electron density along the line of sight, measured in cm^{-6}pc.

- There is also an anomalous foreground emission at 20–60 GHz for which the currently most plausible candidate is tiny PAH particles spinning with dipole moments, i.e., *spinning dust* (e.g.Lazarian & Finkbeiner (2003); Ichiki (2014)).
  Using `Commander`, neither WMAP nor *Planck* data have the statistical power to disentangle spinning dust from synchrotron but the joint global analysis give the results in Fig.3.14. There is however a disagreement with WMAP results on the relative amplitude of synchrotron and spinning dust, sign of the complexity of the astrophysical foregrounds at low frequencies (Planck Collaboration. X. 2015).

therefore constitute a significant contaminant in this thermal dust model on small angular scales.

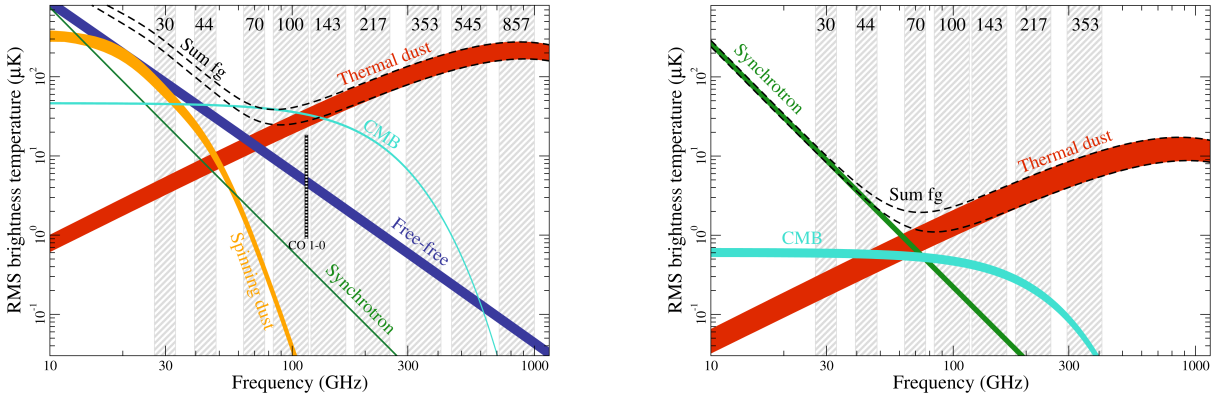

Figure 3.15: (a) Brightness temperature rms as a function of frequency and astrophysical component for temperature. Each component is smoothed to an angular resolution of 1° FWHM, and the lower and upper edges of each line are defined by masks covering 81 and 93% of the sky, respectively. (b) The same is shown here for polarization, the corresponding smoothing scale is 40′, and the sky fractions are 73 and 93%. (Planck Collaboration. X. 2015)

- Between the foreground emissions of the Galaxy at microwave frequencies, also the rotational transitions of carbon monoxide (CO) have to be considered. In fact, the frequencies of the lowest three rotational transitions of CO, namely $J = 1 \rightarrow 0$ at 115 GHz, $J = 2 \rightarrow 0$ at 230 GHz, and $J = 3 \rightarrow 2$ at 345 GHz are respectively in the 100 GHz, 217 GHz, and 353 GHz transmission bands of HFI. In Fig.3.14 a general line emission map which capture a combination of emission line detected with HFI 100 GHz and WMAP W bands (94 GHz) is also shown together with CO lines maps for the three transitions respectively.

Residual extragalactic foregrounds are composed of emissions from SZ clusters, radio sources, and dusty galaxies. They contain Poisson terms and, for SZ and the CIB, correlated terms as well.

- The Sunyaev Zel'dovitch effect (SZ) is the distortion of the CMB spectrum dues to inverse Compton interaction with electrons in clusters (sec.1.3.6). The *Planck* Collaboration has released a catalogue of clusters detected via the SZ effect (appendix A.1). Via adapted component separation techniques, is possible to extract the angular power spectrum of the unresolved thermal SZ (tSZ). This techniques has some advantages over cluster counts since no explicit measurement of cluster masses is required. However, the tSZ angular power spectrum include potential contamination from point sources and other foregrounds (Planck Collaboration. XXI. 2014).

- The relic emission from galaxies formed throughout cosmic history appears as a diffuse, cosmological background. The CIB is the far-infrared part of this emission and it contains about half of its total energy. Produced by the stellar-heated dust within galaxies, the CIB carries a precious information about the process of star formation (Lagache et al. 2005). First seen with the COBE satellite (Puget et al. 1996), it is now well measured by the *Planck* satellite (Planck Collaboration. XXX. 2013).

- The unresolved part of point sources contains both synchrotron emission from radio galaxies and a component from dust emission in galaxies. The spatial correlation of this sources can be considered negligible and, therefore, their power spectrum is simply Poissonian.

Main polarisation foregrounds

For polarisation, at the level of sensitivity of current experiments, only two diffuse components, beside CMB, have been clearly detected:

- Synchrotron photons are emitted by cosmic ray electrons accelerated by the magnetic fields, and therefore are polarized perpendicular to the field lines. and the mean polarization degree is $\sim 14\%$ at high Galactic latitudes. It is however negligible in polarization at high frequencies, so it will be not included in our analysis. Interesting, while synchrotron is polarised, the thermal free-free emission is intrinsically unpolarised because the scattering directions of electrons are isotropic and random (Dulk 1985).
- The only polarised foreground relevant for our analysis is the thermal emission rising from aligned interstellar dust. It is really important to have a deep understanding of this foreground since it limits our capabilities of measuring large scale E and B modes and all the interesting physics that goes with it (sec.1.4). Even if one suppose to know the composition of grains, their polarization depends on the grain shape and grain alignment. The latter is quite complex to characterise since one may expect variations of alignment depending on grain environment, which can introduce substantial variations of the polarization with frequency.

Fig.3.15(b) summarises these polarised contributions in term of brightness temperature rms. This is the first version of such a plot that is based on observations alone.

Conclusions

In this chapter we have described the *Planck* satellite, an ESA project with two main instruments in the focal plane, LFI and HFI. Based on the bolometric technology, the data from this latter are the central theme of this thesis. Its three lowest frequency channels are indeed dominated by the CMB signal we want to study. We have briefly presented the HFI data treatment pipeline unto the map-making process to produce temperature and polarisation full-sky maps that are used in chapter 5. The last part of the chapter has been dedicated to the description of the unavoidable foreground emission present in the *Planck* wide frequency coverage. This will also be useful in chapter 5 when dealing with the masks and the residual foreground contamination.

Chapter 4

Estimation of cosmological parameters

In chapter 5 we will describe how to build a model for the *Planck* experiment in the form of a likelihood

$$\mathcal{L}_{Planck}(\boldsymbol{\theta} = (\boldsymbol{\Omega}, \boldsymbol{\psi})) = \mathcal{L}_{Planck}(data|C_\ell(\boldsymbol{\Omega}), \boldsymbol{\psi})) \tag{4.1}$$

where the model depends on the cosmological parameters $\boldsymbol{\Omega}$ through the C_ℓ and we have included in $\boldsymbol{\psi}$ all the nuisance parameters.

In this chapter we anticipate the description of the statistical methods used to extract from $\mathcal{L}(\boldsymbol{\theta})$ the "best" estimations of the parameters $\hat{\boldsymbol{\theta}}$ and their credible or confidence intervals.

We present two different methods:

- The Bayesian Monte Carlo Markov Chain (MCMC), main-stream method in cosmology, is presented in sec.4.2. MCMC is not intrinsically a Bayesian method but allows to avoid lengthy (or impossible) calculation of high dimensional integrals; its application to cosmological parameter estimation for the CMB, proposed in Christensen et al. (2001), has known a growing success in the last decades.

- The second method (sec.4.3) adopts the frequentist Profile Likelihood approach, widely used in particle physics, and recently exploited for the 2013 Planck release (Planck Collaboration A54 2014).

The comparison of the two methods is particularly interesting for the determination of the sum of neutrino mass, where the presence of a physical boundary (the sum of the masses being greater then zero) can be a subtle issue to deal with. It is also interesting in the case of highly correlated variables as (τ, A_s) in the high-ℓ region, treated differently in the two cases. While in this chapter we detail these methods, we postpone a discussion on the results obtained with *Planck* data to chapter 8.

4.1 The frequency and the subjectivity

The founding concepts of frequentist and Bayesian statistics are deeply different. More naturally applied in the context of particle physics analysis, the frequentist approach is not popular in cosmology. The contrary is also true, even if Bayesian analysis exist in particle physics (e.g. Casadei & Kröninger (2015)). Alongside the adepts of one or the other, there is a part of the scientific community that uses both methods, choosing the most suited one to answer some questions of interest. In this thesis, joining this *agnostic* community, we use the two methods for the extraction of cosmological parameters. However,

the profound conceptual interpretation remains incompatible between the two methods. This section outlines these differences[1].

In frequency theory, the *probability* of an event A is defined as the limit of the number of times we observe the event

$$P(A) = \lim_{N\to\infty} \frac{n}{N} \tag{4.2}$$

The frequency of occurrence of a random event, despite the irregular behaviour of a single event, converges to a constant value when the number of experiments (performed in stable conditions) tends to infinity. In a finite sample, the frequency is subject to fluctuations but these are assumed to decrease when the sample size increases and eventually tend to the *true value*.

A typical example is the measurement of the lifetime of unstable atoms, the true unknown value being τ. We measure a sequence of results $\{t_1, t_2 \cdots t_N\}$. Although unknown, τ is fixed and we can not make probability statement on it. The t_i are, on the contrary, random variable distributed with a likelihood

$$t \sim f(t|\tau) \tag{4.3}$$

The values of τ that produce an unlikely value of the data have to be rejected.

In Bayesian statistics, the fact that τ is unknown means that it is subject to probabilistic statements. On the contrary, data, once measured, are no longer random variables, but are fixed. The likelihood $f(t|\tau)$ is a subjective distribution that express the experimenter's believe on τ, prior to the data. Thus, while in frequency theory probabilities are absolute as they expresses a status of nature, in Bayesian theory they are just assigned and reflect our belief in the proposition. It is a measure of plausibility expressed as a real number between 0 and 1. Before doing the experiment, we have a *prior* knowledge on τ, $P(\tau)$. Then we measure t_1 and we can use Bayes theorem[2] to invert the expression

$$P(\tau|t_1) = \frac{f(t_1|\tau)P(\tau)}{\int f(t_1|\tau)P(\tau)d\tau} \tag{4.4}$$

Our knowledge has increased and we can use the *posterior* probability $P(\tau|t_1)$ as the prior for the next measurements, showing how our subjective degree of belief evolves with time and knowledge.

The prior $P(\tau)$ represent what we know about the parameter which may result from other experiments or just our opinion on its value. It is a very natural way of encoding our previous knowledge but what if two different scientists have different opinions? The defence to this point is that there are indeed priors that are shared by the community (for example we built experiments to search for value of r strictly smaller then one (sec.1.2.2)). Logical consistency difficulties may arise also if we would like to keep the priors un-informative (imagine we know nothing and we have no a-prior opinion). Different choices for the parametrisation of the same data can lead to different results because the constant probability has been associated to different parameters. There are however several methods that try to define them consistently (Jefferys 1983).

4.2 Bayesian inference via Markov Chain Monte Carlo methods

We can rewrite the Bayesian posterior for our likelihood in Eq.4.1, using Eq.4.4

$$P(\boldsymbol{\theta}|Planck) = \frac{\mathcal{L}_{Planck}(C_l, \boldsymbol{\psi})P(\boldsymbol{\theta})}{\int \mathcal{L}_{Planck}(C_l, \boldsymbol{\psi})P(\boldsymbol{\theta})d\boldsymbol{\theta}} \tag{4.5}$$

[1] The discussion about the Bayesian *vs.* frequentist approaches is addressed in many books and articles. This section is inspired by the public available notes on statistic of T. del Prete: https://delprete.web.cern.ch/delprete/statistics.html

[2] $P(A|B)P(B) = P(B|A)P(A)$

Given the data, the degree of belief in the assumed model is given by this posterior probability. $P(\boldsymbol{\theta})$ represents the priors.

As has been described in chapter 5, the likelihood of Eq.4.1 (and thus $P(\boldsymbol{\theta})$ and $P(\boldsymbol{\theta}|Planck)$) depends on a sizeable number of parameters. These includes the six ΛCDM parameters (plus the parameters for some extended models, in our case $\sum m_\nu$ or $N_{\rm eff}$ but also $A_{\rm lens}$ or the DE sector or Ω_k, r, etc.), plus all the astrophysical parameters and the calibrations. The dimension of the problem is thus already greater than 20. We may also want to add all the parameters needed to describe the very-high-ℓ data of SPT and ACT (describe in chapter 6), growing faster to about 40 parameters.

For computing the mean or a credible interval for each parameter we have to integrate the posterior distribution which is a computationally challenging high-dimensionality integration. Also the calculation of the normalising constant at the denominator of Eq.4.5 poses the same problem, even though it can be forgotten in the inference problem being only important for model selection.

The complexity of the problem at hands makes impossible an analytic solution and we have to rely on numerical techniques. A classical non-probabilistic method is to use a regular grid to perform numerical integration. Unfortunately, the problem grows extremely fast with the dimension in this case.

Monte Carlo methods propose to use stochastic samples instead of the grid. The development of these techniques is thus intrinsically linked to random number generators. Beside Fermi's studies on neutron diffusion in the 1930s, the modern Monte Carlo technique have been invented by Ulam during the wartime period at Los Alamos, and successfully applied by von Neumann and others (Ulam et al. 1947). The fundamental role of this technique in physics, decisively boosted by the beginning of the era of digital computers, is now an evidence. In the next section we briefly revise the Monte Carlo principles and describe some famous techniques. These standard algorithms are limited when dealing with high dimensionality (say greater than ∼10). The principle of using ergodic Markov Chains for Monte Carlo integration is described in sec.4.2.3. In MCMC methods the time needed to sample a distribution grows approximately *linearly* with dimension, allowing to find in reasonable time a solution to our problem.

Note that Monte Carlo and MCMC are not intrinsically Bayesian. They provide only approximate integrals and sample from distributions. We present them in this section because they are fundamental to the Bayesian formulation. Interestingly, the story went the other way: the capabilities of these techniques to compute high-dimensional integrals boosted the popularity of Bayesian statistics.

4.2.1 Monte Carlo integration

Imagine we have a probability density function $\pi(x)$ (e.g. the posterior distribution of Eq.4.5) and we would like to calculate the expectation value

$$E[f(x)] = \int f(x)\pi(x)dx \tag{4.6}$$

We can approximate it numerically using a grid of equally spaced points and reconstruct the entire integral. This is inefficient and computationally costly. The Monte Carlo principle suggests to evaluate $E[f(x)]$ by drawing identical and independent distributed (i.i.d) samples $x_t, t = 1, ..., N$ from $\pi(x)$, and use

$$E[f(x)] \simeq \frac{1}{N}\sum_{t=1}^{N} f(x_t) \tag{4.7}$$

Using the i.i.d samples from $\pi(x)$ is more efficient since there will be more points in the high probability regions of $\pi(x)$, that weights more in the calculation of the integral. Moreover, the *Law of large numbers*

tells us that, by increasing N, the approximation can be as accurate as desired. The standard deviation of the approximated integral is proportional to $1/\sqrt{N}$. This dependence is characteristic of the sampling nature of the method and is the same independently of the dimensionality of the problem. But we must be able to draw i.i.d samples from $\pi(x)$.

In some simple cases the problem of sampling from $\pi(x)$ can be bypassed by a transformation of variable that guides us to an easier-to-sample distribution. In other cases, if the cumulative distribution is known, is sufficient to draw sample from an uniform distribution U in $[0, 1]$ since $F^{-1}(U) \sim \pi$.

More interesting are the techniques to deal with more complex $\pi(x)$

Rejection Sampling

If we are able to find a simple distribution q and a constant $M > 0$, such that

$$\pi \leq Mq \tag{4.8}$$

where in general q is a Gaussian or a Gamma distribution, then we can sample according to q. The point is then accepted or rejected using the following criterion developed by von Neumann

- sample $x^* \sim q$ and $u \sim U_{[0,1]}$
- if $u < \frac{\pi(x^*)}{Mq(x^*)}$ accept x^*
- else reject x^*

This guarantees that the final accepted sample are distributed according to $\pi(x)$.

A good knowledge of q and M is required; the closer Mq to π, less samples are rejected. It is however not obvious to be able to find good q and M. In this case, important sampling can be used.

Importance Sampling

This method is based on the following identity

$$\int f(x)\pi(x) = \int f(x)\left(\frac{\pi(x)}{q(x)}\right)q(x)dx = E_{q(x)}\left[f(x)\left(\frac{\pi(x)}{q(x)}\right)\right] \tag{4.9}$$

If we are able to sample $q(x)$, then using Eq.4.7, we can write

$$\int f(x)\pi(x) \simeq \frac{1}{N}\sum_{t=1}^{N} f(x_t)\left(\frac{\pi(x_t)}{q(x_t)}\right) \tag{4.10}$$

where $x_t \sim q(x)$.

The idea behind this formula is to get samples from the interesting and important region of $\pi(x)$. This is done by sampling from a distribution that overweights the important region, hence the name importance sampling. In Eq.4.10, by making a multiplicative adjustment to f, we compensate for sampling from q instead of π. The adjustment factor $\frac{\pi(x)}{q(x)}$ is called the *likelihood ratio*, the distribution q is the *importance* distribution and π is the *nominal* distribution. This method allows to avoid wasting of samples but the choice of a good importance sampling distribution requires some "educated guessing" and sometimes numerical search[3].

[3]For a more detailed discussion see for example the notes of Professor Art B. Owen from Stanford University http://statweb.stanford.edu/ owen/courses

Going to high dimensionality, these methods have limitations. Let σ be the variance of π. For rejection sampling, the fraction of accepted samples goes as σ^{-d} thus a lot of samples are wasted and the algorithm is very inefficient.

For importance sampling, the variance of the likelihood ratio can go as σ^d (Bardenet 2013).

The methods that can replace standard Monte Carlo integration efficiently when dealing with high dimensional integrals are described in the rest of this section. We use no more i.i.d. samples but ergodic Markov chains.

4.2.2 Markov Chain Monte Carlo

Monte Carlo Markov Chain methods supply a way to sample from a high dimensional probability distribution $\pi(.)$ (where (.) means any vector) using an ergodic Markov chain X with desired stationary distribution. The main idea is thus to substitute the Monte Carlo principle of Eq.4.7 with

$$E_\pi[f] \simeq \bar{f}_N = \frac{1}{N}\sum_{t=1}^{N} f(X_t) \tag{4.11}$$

where now X_t is the t-th element of the Markov chain and the sum is an *ergodic* average.

Next section is dedicated to the clarification of some basic concepts regarding Markov chains. In sec. 4.2.4 the classical Metropolis-Hasting algorithm is presented with an analysis on how to tune it for proper and efficient convergence. This motivates the choice for an easier-to-tune version of the algorithm, the adaptive MCMC, detailed in sec. 4.2.6. This latter is used for CMB parameter estimation in the rest of this thesis.

4.2.3 Markov chains: basic concepts

We follow here the discussion of Gilks et al. (1996) and Walsh (2004).
A Markov chain is a random process $\{X_0, X_1, ...\}$ with the following property: the system at X_t depend only on X_{t-1}. In other words, the only information about the past needed to predict the future (X_t), is the current state (X_{t-1}). This can be written as

$$P(X_t \in X|X_0, X_1, ..., X_{t-1}) = P(X_t \in X|X_{t-1}), \tag{4.12}$$

where X is the set of values that compose the chain. In a compact notation one can define $P_{ij}(t) = P(X_t = j|X_0 = i)$ as the *transition probability* or *kernel* to go from a point i in parameter space to a point j.

Under several conditions the distribution of X converge to a *stationary distribution*. For this to happen, the chain needs to be irreducible, aperiodic and positive recurrent.

- X is called *irreducible* if $\forall\ i, j\ \exists\ t > 0\ s.t.\ P_{ij}(t) > 0$.
  In some number of iterations, one can always go from a state to another.

- An irreducible chain X is called *aperiodic* if the number of steps required to move between two states is not a multiple of some integer. The chain is thus not oscillating between different sets of states in a periodic way.

- An irreducible chain X is called *recurrent* if $P[\tau_{ii} < \infty] = 1$, where $\tau_{ii} = min\{t > 0 : X_t = i|X_0 = i\}$, i.e. the minimum number of steps to come back on a point in parameter space.

- An irreducible recurrent chain X is called *positive recurrent* if $E[\tau_{ii}] < \infty$, or equivalently

$$\forall j, t \geq 0 \; \exists \, \pi(.) \; s.t. \; \sum_i \pi(i) P_{ij}(t) = \pi(j), \tag{4.13}$$

  where $\pi(.)$ is the stationary distribution. This means that if the initial value X_0 is sampled from $\pi(.)$, also the subsequent iterates will be distributed according to it.

A sufficient condition for a unique stationary distribution is that

$$\pi(i) P_{ij} = \pi(j) P_{ji} \tag{4.14}$$

in this case the chain is said to be *reversible*. This condition implies Eq.4.13. One can consider that this condition holds for the chains produced via MCMC algorithms.

If X is positive recurrent and aperiodic then its *stationary distribution* is the unique one satisfying 4.13. Then one says that X is *ergodic* and:

- $P_{ij}(t) \to \pi(j)$ as $t \to \infty \;\; \forall i, j$
- $If \; E_\pi[|f(X)|] < \infty, \; then \; P[\bar{f}_N \to E_\pi[f(X)] = 1$

This latter condition is the crucial point validating MCMC methods in the sense of Eq.4.11. Nevertheless, we have no clue on how long to run a Markov chain before its iterations are distributed according to $\pi(.)$ and we have no estimate of the error on $\bar{f}_N$. One can thus require a particular kind of ergodicity.

A chain X is *geometrically* ergodic, if there exist $0 \leq \lambda \leq 1$ and a function $V(.) > 1$ such that

$$\sum_j |P_{ij}(t) - \pi(j)| \leq V(i) \lambda^t \tag{4.15}$$

for all i. The smallest λ (λ^*) for which there exist a function $V(.)$ satisfying this condition is called rate of convergence. The geometric convergence allows the existence of the central limit theorem for ergodic averages

$$N^{1/2}(\bar{f}_N - E_\pi[f]) \to N(0, \sigma^2) \tag{4.16}$$

for some positive constant σ, as $N \to \infty$. It can also be demonstrated that $\sigma^2 \leq \frac{1+\lambda^*}{1+\lambda^*}$. Clearly to asses the validity of the MCMC method one need to be able to estimate σ^2. The precise mathematical framework to describe convergence criteria is out of the scope of this thesis. We will however treat how, in practice, a diagnostic of convergence can be performed (sec.4.2.8).

4.2.4 Metropolis-Hastings algorithm

The use of Markov chains for Monte Carlo methods date back to the Monte Carlo origins at the Los Alamos Scientific Laboratory (Metropolis & Ulam 1949; Metropolis et al. 1953). The algorithm proposed by Metropolis and others was generalised by Hastings in 1970 (Hastings 1970). Both require the use of an auxiliary function $q(X|Y)$, such that $q(.|Y)$ is the probability density for each Y. As for standard MC methods, one wants to explore a support spending more time in place where $\pi(.)$ is high. The transition probability density from the point X to Y thus read

$$P_{XY} = q(X|Y)\alpha(X, Y) \text{ where } \alpha = \min\left[1, \frac{\pi(Y)q(X|Y)}{\pi(X)q(Y|X)}\right] \tag{4.17}$$

Since we want to deal with d-dimensional problems, each point X in the chain is a vector of d components.
The Metropolis-Hastings (MH) algorithm is the following

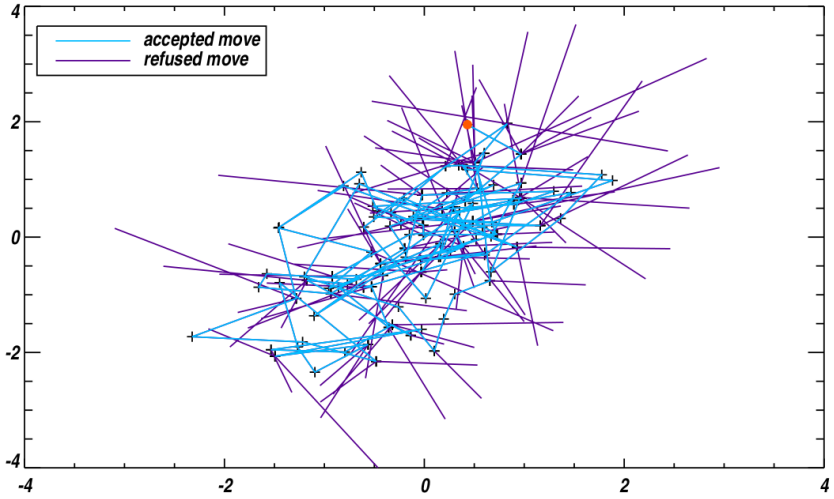

Figure 4.1: A visual representation of Metropolis-Hastings algorithm. The target distribution $\pi(.)$ is a 2D Gaussian. The stating point is in red. The chain explores the space spending more time where $\pi(.)$ is high. Rejected moves are showed in violet, accepted moves in light blue. Already from this first few point we can guess the shape of the target distribution.

1. Choose a starting point X_0;
2. generate a value Y from a proposal density $q(Y|X_t)$;
3. evaluate the test ratio α (Eq.4.17);
4. generate a value u uniformly distributed in $[0, 1]$;
5. if $u \leq \alpha(X_t, Y)$ set $X_{t+1} = Y$ else set $X_{t+1} = X_t$;
6. increment t.

There is indeed also the possibility to reject a proposed move. This is done with probability 1-α. A visual example of the behaviour of the algorithm is presented in Fig.4.1.
The difference between the Metropolis and the Hastings version of the algorithm reside in the properties of the proposal density q.
We have considered an arbitrary transition probability function $q(Y|X) = P(X \to Y)$ that is not necessarily symmetric in X e Y. The Metropolis algorithm is a special case of the MH, where $q(Y|X) = q(X|Y)$. Looking at Eq.4.17 we see that in this case the expression for α simplifies to

$$\alpha = \min\left[1, \frac{\pi(Y)}{\pi(X)}\right]. \tag{4.18}$$

For a problem similar to the one we have to deal with, the most convenient choice is a symmetric proposal. We will come back on this soon. Note that the posterior appears always in a ratio. This means that one is not force to calculate the normalisation factor of $\pi(.)$, i.e. the integral at denominator in Eq.4.5.

Single-component Metropolis-Hastings

At every step in the iteration, MH algorithm updates simultaneously the the n-dimensional element of the chain X. There are however methods where, for every step of the chain, the components of the vector $X_{.} \{X_{.1}, ..., X_{.n}\}$ are considered separately. Here $_{.}$ means whatever iteration.

Following again the notation of Gilks et al. (1996) one can define

$$X_{t.-i} \equiv \{X_{t.1}, ..., X_{t.i-1}, X_{t.i+1}, ..., X_{t.n}\}. \tag{4.19}$$

At step t, $X_{t.-i}$ is a $n-1$-dimensional vector that comprises all of X_t except $X_{.i}$.

At iteration $t+1$, to update X_t, one uses the MH algorithm for every component of the vector. Imagine at step i of iteration $t+1$, one has already updated the components $1, 2, ..., i-1$. To update $X_{t.i}$, a candidate from distribution $q_i(Y_{.i}|X_{t.i}, X_{t.-i})$ is proposed. This is indeed a candidate only for the i-th component of X_t. It may depend on the current values of any of the other component. This candidate is accepted with probability

$$\alpha(X_{.-i}, X_{.i}, Y_{.i}) = \min\left(\frac{\pi(Y_{.i}|X_{.-i})q_i(X_{.i}|Y_{.i}, X_{.-i})}{\pi(X_{.i}|X_{.-i})q_i(Y_{.i}|X_{.i}, X_{.-i})}\right), \tag{4.20}$$

where $\pi(X_{.i}|X_{.-i})$ is the full conditional distribution for $X_{.i}$ under $\pi(.)$. If the candidate is accepted $X_{t+1.i} = Y_{.i}$, otherwise $X_{t+1.i} = X_{t.i}$.

A special case of this single-component version of MH is the Gibbs sampling (Geman & Geman 1984). In this case the proposal distribution for the update of the i-th component reads

$$q_i(Y_{.i}|X_{.i}, X_{.-i}) = \pi(Y_{.i}|X_{.-i}). \tag{4.21}$$

From Eq.4.20 it is easy to see that α is always one, in other word the point is always accepted.

This is probably one of the most used MCMC sampler, since it is powerful and easy to implement. In Planck data analysis it pops up frequently. It is used for component separation inside the Commander algorithm (see sec.A.2) but also to provide a nuisance-free version of the likelihood to the community (Planck Collaboration A13 2015).

Note that this version of the algorithm updates components always in the same order. This is not necessary and one can imagine more complicated techniques where the i-th component is selected with fixed probability, or where we spend more time updating the more correlated ones. All these techniques can speed up the convergence but inevitably complicate the mathematical justification of the method.

A bunch of other MCMC techniques are discussed later in this chapter but the discussion is by no means exhaustive. For a detailed discussion see again Gilks et al. (1996) or Berg (2004) and Hobson et al. (2010).

Marginalisation

The posterior distribution of Eq.4.5 is a joint distribution of the cosmological parameters and the nuisance parameters, but one may want to reconstruct the posterior distribution of a single parameter of interest.

Imagine we have a 2D distribution depending on two parameters, α and β. The marginalised distribution of β reads

$$p(\beta|D) = \int p(\alpha, \beta|D)d\alpha. \tag{4.22}$$

This can be easily generalised to a multidimensional problem, requiring the integration of the posterior distribution over all the parameters that one would like to exclude.

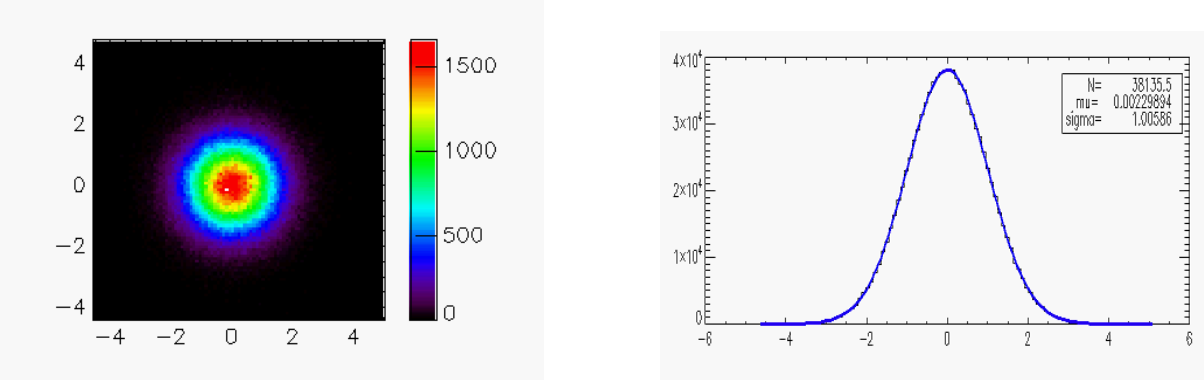

(a) (b)

Figure 4.2: (a) Posterior distribution of bivariate Normal distribution sampled via MCMC algorithm. (b) The marginalised posterior distribution of one of the two is automatically obtained as the histogram of the element of the chain corresponding to it.

Indeed, one of the great advantage of using MCMC techniques is the simplification of this marginalisation problem. Going back to our 2D example, using whatever MCMC algorithm one generates a chain (α_t, β_t) from the joint distribution $p(\alpha, \beta|D)$. This automatically provides (β_t) from the marginalized PDF. There is no need to compute the integral. The distribution of the parameter β of the chain follows the distribution of Eq.4.22. Clearly this is true also for α: the values α_t are distributed according to $p(\alpha|D) = \int p(\alpha, \beta|D)d\beta$. A simple visual example is given in Fig.4.2(a) and 4.2(b).

4.2.5 Choice of the Proposal Distribution

A proper choice of the proposal distribution $q(Y|X_t)$ is fundamental for an efficient exploration of the posterior. If we have small trial steps, the acceptance rate (the number of accepted moves on the total tried) is too high since the difference between $\pi(Y)$ and $\pi(X_t)$ is in general small for close points in a smooth distribution. In this case the chain behaves locally like a random walk and it is not spending more time where $\pi(.)$ is high with respect to the tails. On the contrary, for too large trial steps, the chain remains stuck at one point before accepting a step, resulting in a very low acceptance rate. The initial and final point are almost uncorrelated but the jump occur infrequently. The exploration is slow and possibly inaccurate.

So how do we choose the proposal? This is not a trivial issue and depends of the problem at hands. Mostly for practical reasons, the standard choice is a multivariate Gaussian distribution centred on the last point of the chain $q(.|X_t) = N(X_t, \Sigma)$. A Gaussian distribution is a symmetric proposal in the sense of $q(Y|X) = q(X|Y)$. Eq.4.18 is thus valid and we are in the case of simple Metropolis algorithm.

Let's imagine we have a simple problem for which we do not need the off-diagonal terms of the matrix Σ. We are left with a collection of one-dimensional Gaussian proposals with variance σ^2. We can thus reformulate the problem: how can one choose the tuning parameter σ? A simple example of how the value of σ intervenes in the exploration of the posterior is shown in Fig.4.3(a) and Fig.4.3(b), where the target distribution is a χ^2-distribution with 3 d.o.f.. With $\sigma = 1$ for the proposal (Fig.4.3(a)) the number of consecutive rejections stays small and the acceptance rate is too high. With $\sigma = 10$ (Fig.4.3(b)), consecutive rejections are much more common and acceptance rate is low. In practice, building an histogram with these samples would give very poor results. A good rule of thumbs, for the

acceptance rate when both the proposal and the target are Gaussian is (Gelman et al. 1996):

$$\frac{\sigma_{\text{prop}}}{\sigma_{\text{target}}} = \frac{2.4}{\sqrt{d}}, \tag{4.23}$$

where d is the dimension of the problem. Then:

- for $d = 1, 2$, acceptance rate should be ~ 0.5
- for $d \geq 3$, acceptance rate should be ~ 0.25

In our example of sampling a χ^2-distribution with 3 d.o.f., the target distribution is unidimensional but not Gaussian. However, this standard value of 0.5 for the acceptance rate is still an indication to follow, as we will see in sec. 4.2.8. In Fig.4.6(b) is shown the posterior distribution obtained using a tuned value of the proposal.

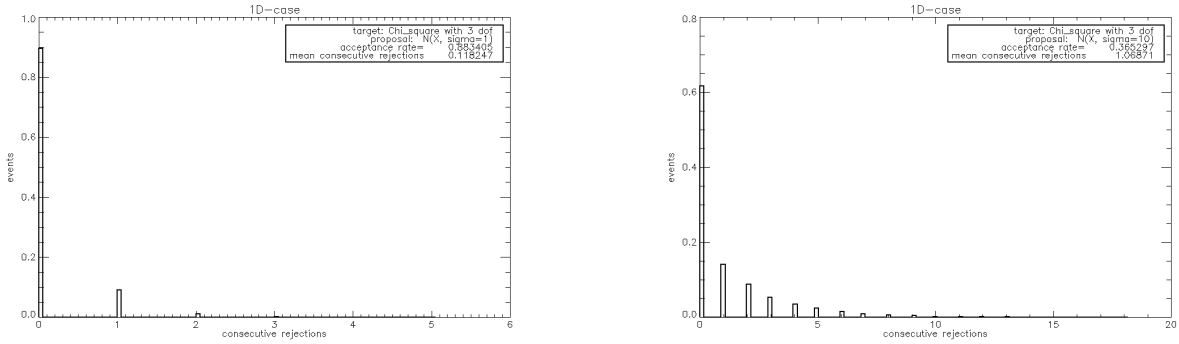

(a) (b)

Figure 4.3: Histograms of the number of consecutive rejections obtained sampling a χ^2-distribution with 3 d.o.f. using, for the proposal, a Gaussian distribution with $\sigma = 1$ in (a) and $\sigma = 10$ in (b). In these two cases the acceptance rate is respectively too high (0.88) and too low (0.36).

Interestingly for our problem of estimating cosmological parameter, Eq.4.23 tells us that, up to a rescaling factor, the best choice for the tuning parameter σ_{prop} is the σ_{target}. This means that if we know it already, or if we have an idea of it, we are able to use the Metropolis algorithm in a fast and efficient way. On the contrary, choosing a good proposal requires a long fine tuning especially when there are unknown correlation among the parameters. The Adaptive algorithm (sec.4.2.6) that we have implemented to estimate cosmological parameters in this thesis obviates this problem.

4.2.6 The Adaptive algorithm

The Metropolis algorithm works very well on all the toy Gaussian cases that we have studied. We can easily sample any multivariate normal distribution using another multivariate normal distribution with a simple diagonal covariance matrix. Using the rule of thumb of Eq.4.23, if we have an idea of the order of magnitude of $\Sigma_{ii} = \sigma_i$ (i.e. the error on each parameter in our problem), we reach convergence in a reasonable time. This remains true when we run the algorithm on toy cosmological models, namely a multivariate normal distribution that mimics the dimensionality (the ∼20 parameters discussed in chapter 5), the correlations and the order of magnitudes of the errors of the posterior distribution of a full-sky CMB experiment like Planck or WMAP.

When we are facing the real posterior distribution of Eq.4.5 this is no more the case. The Metropolis algorithm becomes slow if the covariance matrix of the proposal is not well estimated. We are forced to

run long chains, then try to guess the covariance matrix from them, and use again this estimation as a new input tp the proposal. With this reiterated procedure we time since every call of the likelihood function implies a call to the Boltzmann code (sec.1.5.1) that can need up to a few seconds to complete. Moreover, if the shape of the foreground posteriors is highly non Gaussian the algorithm may not properly converge at all.

Clearly, a simple Metropolis algorithm is not what is used in general for estimating CMB cosmological parameters (e.g. (Lewis & Bridle 2002; Lewis 2013; Das & Souradeep 2014)). There are plenty of fancy solutions to speed up the estimation. For the work in this thesis we have implemented an adaptive (AM) version of the base algorithm (Haario et al. 2001) as proposed to us by the *AppStat* group at LAL. In this case the tuning of the design parameter of the algorithm (i.e. the entries of the Σ_{prop} of the proposal) is automatic and on the fly. It makes use of *all* the previous steps of the chain. The implementation is easy since we may apply a recursion formula and, more importantly, the rapid start of the adaptation diminishes the number of function evaluations needed.

Keeping memory of all its history, the process is no more Markovian. So, does the adaptive algorithm have the correct ergodicity properties? It is indeed mathematically difficult to deal with non basic MCMC methods, and a lot of the algorithm used by the scientific community are not assured to have the right properties for convergence. Nevertheless, for the AM algorithm, the asymptotic dependence between the elements of the chain is weak enough to apply the theorems of large numbers (Andrieu & Moulines 2006).

The Adaptive Metropolis algorithm is the following:

1. Choose a starting point X_0, a starting covariance matrix Σ_0 and a tuning parameter c;
2. generate a value Y from a proposal density $N(X_{t-1}, c\Sigma)$;
3. evaluate the test ratio $\alpha = min[1, \frac{\pi(Y)}{\pi(X)}]$;
4. generate a value u uniformly distributed in $[0, 1]$;
5. if $u \leq \alpha(X_t, Y)$ set $X_{t+1} = Y$ else set $X_{t+1} = X_t$;
6. update running mean and covariance:

$$\mu_t = \mu_{t-1} + \frac{1}{t}(X_t - \mu_{t-1}), \quad \Sigma_t = \Sigma_{t-1} + \frac{1}{t}((X_t - \mu_t)(X_t - \mu_t)^T - \Sigma_{t-1}) \tag{4.24}$$

7. Increment t.

In practice, we have implemented some changes to the algorithm to use it properly in our case. These are discussed in sec.4.2.9.

4.2.7 Others sampling techniques

The diffusion of Bayesian techniques in many fields of research has motivated the widespread of different MCMC techniques. Each algorithm is in general tailored to particular problems and comparisons between algorithms exist in literature (e.g. (Allison & Dunkley 2014)) and point in general to more efficient techniques than the Metropolis or the Gibbs algorithms. To obtain the official *Planck* results, and often for cosmological parameter estimation in general, the CosmoMC code, based on the MH algorithm, is used (Lewis & Bridle 2002; Lewis 2013). CosmoMC is briefly described in sec.4.2.10 and compared

to the Adaptive Metropolis we have developed in this thesis.
Clearly, other interesting algorithms exist. The *Nested sampling* (Skilling 2004, 2006), for example, after a first rapid exploration of the entire volume, oversamples the more likely regions. The samples are then reweighed appropriately. Starting with Bassett & Kunz (2004), this technique has known a growing success and is particularly suited for the Bayesian evidence estimation. When dealing with multi-modal and curving distributions, more refined techniques need to be developed. Luckily, the current knowledge of CMB data is strong enough to know that we deal in general with uni-modal and smooth distributions. We have however implemented the *Affine-invariant ensemble sampler* (Goodman & Weare 2010). This *multi-particles* method is also quite popular (e.g. (Akeret et al. 2012; Foreman-Mackey et al. 2013)) and its main property is the invariance under linear transformation of the parameters space. As presented later on, a curved distribution as the one in Fig.4.4(b), is as easily treated as a isotropic Gaussian. Even if we do not use it for cosmological parameter estimation, this method is interesting in the presence of computer clusters allowing for massive parallelisation (Allison & Dunkley 2014).

Ensemble samplers with affine invariance

The affine-invariant sampler presented in this section (in literature sometime called *stretch move*) is realised simultaneously evolving an ensemble of k walkers $S = \{X_k\}$ (Goodman & Weare 2010). Considering parallel chains is the basic idea of the multi-particle methods.

Let $\pi(.)$ be the target distribution. Any walker is a d-dimensional chain, with d the dimension of the posterior to sample.

The proposal for one walker is based on the current position of the others. Indeed, the proposed move Y of the walker i drawing randomly a walker j from the set $S_{-i} = \{X_1, .., X_{i-1}, X_{i+1}, .., X_k\}$

$$X_i(t) \rightarrow Y = X_j + Z[X_i(t) - X_j], \tag{4.25}$$

where Z is a random variable drawn from a distribution $g(z)$.

If $g(z^{-1}) = zg(z)$ the proposal of Eq.4.25 is symmetric and the ergodic theorem is valid. The distribution used is:

$$g(z) \propto \begin{cases} \frac{1}{\sqrt{z}} & \text{if } z \in [\frac{1}{a}, a] \text{ with } a = 2 \\ 0 & \text{otherwise} \end{cases} \tag{4.26}$$

The algorithm is the following:

for $i = 1, ..., k$ **do**

1. Draw a walker X_j at random from S_{-i};
2. generate a value z from the distribution $g(z)$;
3. draw Y using Eq.4.25;
4. calculate $q = z^{d-1}\pi(Y)/\pi(X_i(t))$;
5. Generate a value u uniformly distributed in $[0, 1]$;
6. if $u \leq q$ set $X_i(t+1) = Y$ else set $X_i(t+1) = X_i(t)$;

end for.

We follow some implementation advices from (Foreman-Mackey et al. 2013). We keep acceptance rate in agreement with the rule of thumb of Eq.4.23. This can be done tuning the parameter a of Eq.4.26

that is inversely proportional to the acceptance rate. It is also preferable to run the algorithm with a large number of walkers ($\sim$ 100). In Fig.4.4(a) we show the posterior distribution for one of the dimension of a 6D parameter space, the target distribution being a multivariate Gaussian. Using 10 walkers and running the chains for 1000 steps is indeed less efficient in the reconstruction of the target distribution than running 100 walkers for 100 steps (this is linked to the discussion on multi chains convergence of sec.4.2.8)

To reveal the advantages of the method we challenge it on a difficult 2D-case.
Let $\pi(.)$ be the Rosenbrock density:

$$\pi(x_1, x_2) \propto exp(-\frac{100(x_2 - x_1^2)^2 + (1 - x_1)^2}{20}). \tag{4.27}$$

The anisotropic cases pose, in general, severe problems to all MCMC samplers (for example our metropolis algorithm fails to converge).

However, under affine transformation Eq.4.27 turn into a much easier problem. With almost no need to tune the algorithm we obtain the posterior of Fig.4.4(b).

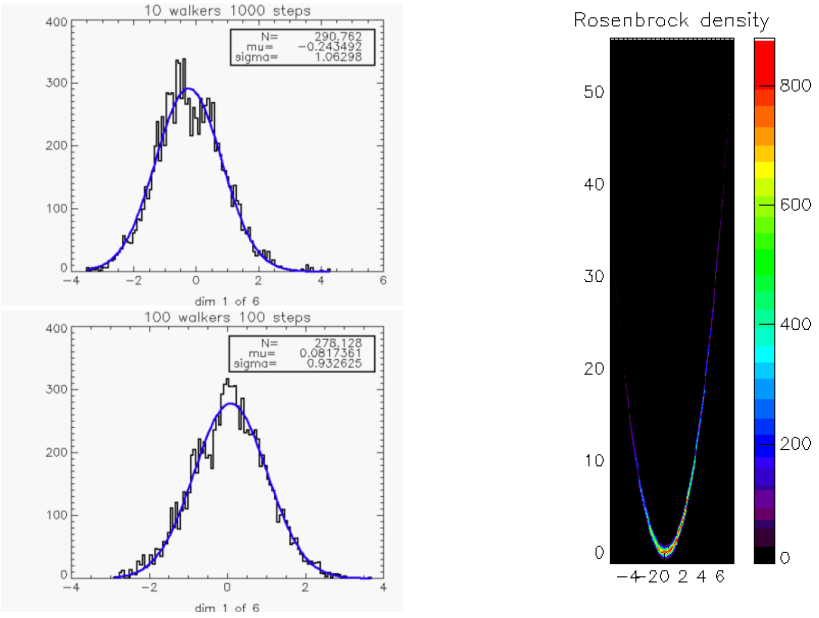

(a) (b)

Figure 4.4: (a) Posterior distributions for one of the six dimensions of a 6D multivariate Normal distribution using the *stretch move* algorithm in different configurations: 10 walkers with 1000 steps (top) and 100 walkers with 100 steps (bottom). In fitting the distribution, we note a trend (that is general) of better performance of the algorithm when the number of walkers is larger. (b) Histogram of the posterior distribution of the Rosenbrock density (Eq.4.27) easily sampled via the *stretch move* algorithm.

4.2.8 The question of convergence

The way MCMC works, does not rely on the Monte Carlo principle of having identical and independent samples $X_1, X_2, ...$, neither on the fact that the chain has marginal distribution $\pi(.)$. However, we have seen that the marginal distribution of X_t is close to $\pi(.)$ if the number of samples is large Geyer (1991).

This consideration introduces the fundamental idea that, for being useful, our chain needs to be long enough for Eq.4.11 to hold. Thus, to properly use a MCMC algorithm, convergence needs to be checked. The issue is not trivial. What is typically done is to run a chain until the starting point is "forgotten". This period is called the *burn-in*. In Fig.4.5 is shown how, in a few steps, from four different starting points, as many chains find the peak of the distribution. In general burn-in periods are chosen quite long for safety, although Geyer (1991) argues that there is no need to wait too long and discarding 5% is enough. After the burn-in each draw follows the stationary distribution.

The length of the burn-in phase is not easy to calculate. If the starting point is far from the peak of the distribution, the "no dependence" regime is luckily to be reached in a longer time. Another example in this sense is in Fig.4.6(a).

In practice, since our computational resources are limited, a too long burn in period is intractable. As a consequence we have to make sure that the chain is really efficiently exploring the parameter space. In literature this is often referred to as *mixing*. A by eye check on the behaviour of the chain is again a useful test. In Fig.4.7(a) is shown an example of bad mixing while the chain in Fig.4.7(b) has a good mixing.

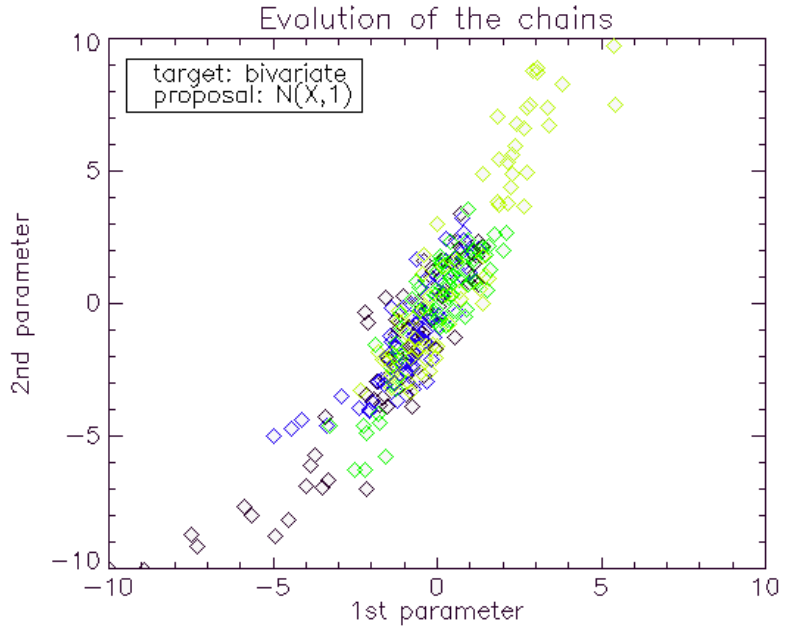

Figure 4.5: Example of burn-in phase. Using Metropolis algorithm with a Gaussian proposal distribution (see sec.4.2.5), the space is explored with four chains, having different starting points. The target distribution is a simple bivariate (2D correlated Gaussian centred in (0,0)) so in a few steps every chain finds the peak.

Beside this simple diagnostic of bad mixing there are a lot of more sophisticated methods that have been developed by the community. We present here some of them.

Gelman-Rubin test

In Fig.4.5 and 4.6(a) we have shown the behaviour of multiple chains on the same problem. In sec.4.2.7 we have also presented results using a multi particle method. As discussed in Geyer (1991), the use of many short run, say m independent realisations of the same algorithm, should not be preferred to a

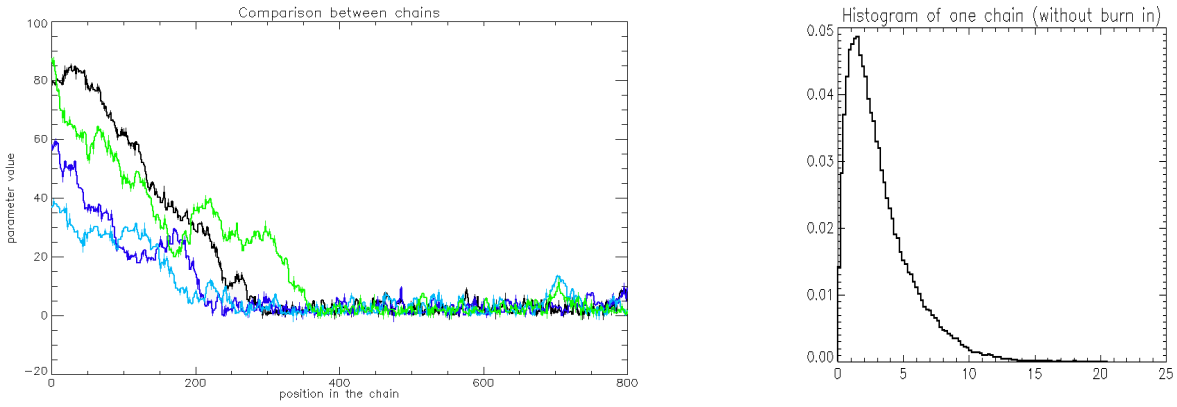

(a) (b)

Figure 4.6: (a) The target distribution is a χ^2-distribution with 3 d.o.f. The proposal distribution is a Gaussian with fixed σ (see sec.4.2.5). Four chains are run using different starting points. After step=400 the chains are clearly sampling the same distribution. (b) Posterior from one of the chains after burn-in phase is cut out which agrees properly with a χ^2_3.

single long chain[4]. First because the burn-in period has to be thrown away from each chain and secondly because the sum

$$\frac{1}{m}\sum_{j=1}^{m} f(X_n^j), \tag{4.28}$$

has not the right ergodic convergence property. If $m \to \infty$ some kind of law of large number enters the game while a proper convergence would require not only $m \to \infty$ but also $n \to \infty$, i.e. long chains. Multiple chains have, however, a diagnostic power and we always run more than one chain (in general four) in the case of estimation of cosmological parameters and then merge the chains together, after throwing the burn-in period. One of the test based on multiple chains that one can use to check convergence is the Gelman-Rubin (GR) test (Gelman & Rubin 1992).

The basic idea of this test is to compare several sequences drawn from different starting points and check if they are indistinguishable. Moreover, GR test gives an idea of how much the distribution estimate may improve as iteration continues.

Suppose one runs m chains of $2n$ elements and considers only the last half n: X_i^j with $i = 1, .., n$ and $j = 1, ..., m$. The following quantities can be defined:

- $\bar{X}^j = \frac{1}{n}\sum_{i=1}^{n} X_i^j$ *mean of the chain*;
- $\bar{X} = \frac{1}{nm}\sum_{i=1}^{n}\sum_{j=1}^{m} X_i^j$ *mean of the distribution*;
- $B = \frac{n}{m-1}\sum_{j=1}^{m}(\bar{X}^j - \bar{X})^2$ *variance between chains*;
- $W = \frac{1}{m(n-1)}\sum_{i=1}^{n}\sum_{j=1}^{m}(X_i^j - \bar{X}^j)^2$ *variance within a chain*;

From this quantities one calculates the potential scale reduction factor (PSRF)

$$R \equiv \frac{\frac{n-1}{n}W + \frac{B}{n}(\frac{m+1}{m})}{W}. \tag{4.29}$$

[4]This is of course not a definitive statement but may depends on the type of problems and algorithm at hands.

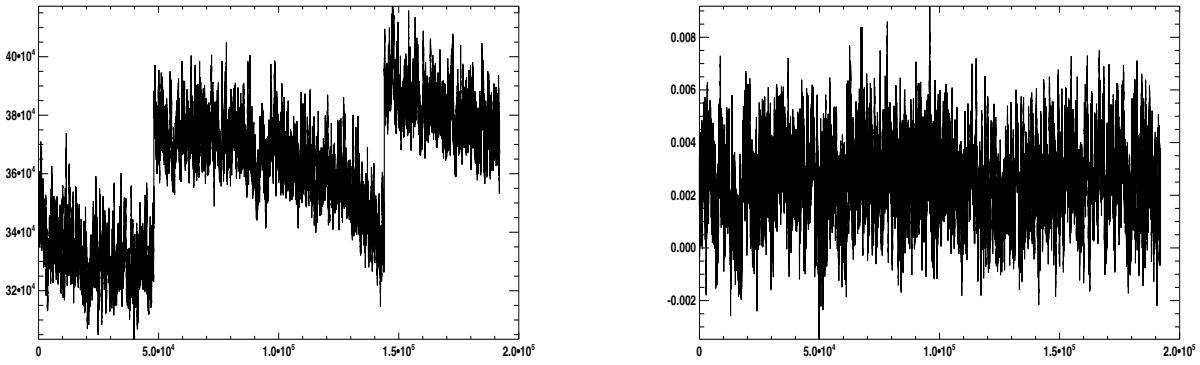

(a) (b)

Figure 4.7: (a) Example of bad mixing for a given variable (b) Example of good mixing for another given variable. These example are nuisance parameters taken from different test run of our CMB likelihood.

The numerator is an estimate of the variance that is unbiased if one is sampling from the stationary distribution, otherwise is an overestimation.
The denominator is, on the contrary, an underestimation of the variance of the target distribution if the single chain is not yet converged. If R is high, either the chain has not reached yet the stationary distribution, either W can still decrease meaning that the single chain has not yet explored the entire target distribution. One expects R to be ~ 1 when the chains are converged.

The prescription (e.g. Verde (2007)), which is used for the results of this thesis, is then to run the test until:

$$R - 1 \text{ always } < 0.03 \tag{4.30}$$

A value of R as a function of the length of the chain should be calculated for each dimension of the parameter space. The results of the test on the `HiLLiPOP` likelihood (chapter 5) is shown in Fig.4.8. Four chains are run using the Adaptive algorithm (sec.4.2.6).

Estimation of autocorrelation

Another method to analyse the convergence of a chain is the estimation of its *autocorrelation*. At a fixed distance between elements, called the *lag*, we can calculate

$$\hat{\gamma}(lag) = \frac{1}{N}\sum_{i=1}^{N-lag}[f(X_i) - \bar{f}_N][f(X_{i+lag}) - \bar{f}_N], \tag{4.31}$$

where $\bar{f}_N$ is defined in Eq.4.11. We would expect this autocorrelation to be smaller as the *lag* increases, since in presence of good mixing the chain should forget its past.

If, on the contrary, autocorrelation is still relatively high for high values of the *lag*, this indicates that there is still a high degree of correlation between our draws; a sign that mixing is slow and the chain is stuck somewhere instead of exploring the whole parameter space.

It is also useful to calculate the *integrated autocorrelation time* $\hat{\tau}_{int}$, namely the sum, over all possible values of the *lag*, of the autocorrelation $\hat{\gamma}(lag)$. In order to get a god estimate it is necessary to down-weight the terms for a large *lag* which are essentially noise due to the lower combinatorics (Geyer 1991).

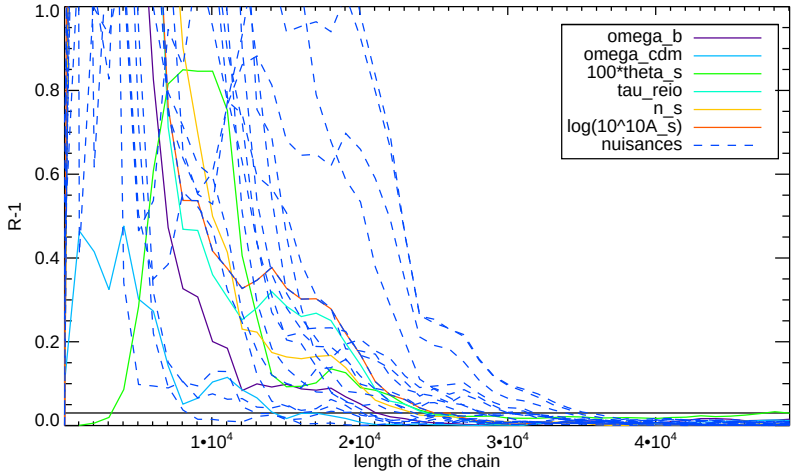

Figure 4.8: The Gelman-Rubin test R (Eq.4.29) as a function of the length of the chains. Four chains are used for sampling the `HiLLiPOP` likelihood, then R is calculated for each parameter. We show with different colors the cosmological parameters and in dahed blue all the nuisances parameters included in the likelihood (chapter 5). The test is passed when $R - 1 < 0.03$.

σ proposal	0.5	1	3	6	10	20
acceptance rate	0.93	0.88	0.70	0.50	0.36	0.45
$\hat{\tau}_{int}$	64.12	16.07	4.44	3.50	3.60	4.45

Table 4.1: Using χ^2-distribution with 3 d.o.f. as the target distribution, we explore different choices for the σ of the Gaussian proposal distribution. For every value we compute the value of the acceptance rate and of the autocorrelation time (using Eq. 4.32). The minimum for $\hat{\tau}_{int}$ corresponds to $\sigma = 6$ and acceptance rate ~ 0.5, in agreement with the expectations.

One can write

$$\hat{\tau}_{int} = \sum_{lag=-\infty}^{\infty} \omega(lag)\hat{\gamma}(lag) \tag{4.32}$$

where $\omega(lag)$ is 1 for a small lag and 0 for a large lag, with any smooth curve connecting the two extrema as a scaled cosine.
This estimate $\hat{\tau}_{int}$ is a useful diagnostic of convergence, the higher it is, the more samples are needed. This can be used also the other way round: chains with lower value of the autocorrelation time have better mixing. A simple example is given in Fig.4.9(a) and 4.9(b). We chose again a χ^2_3-distribution as the target and we plot the evolution of the autocorrelation as a function of the lag. We then fit the exponential decay. The value of τ obtained in the fit is roughly equivalent to the one of Eq.4.32. We conclude for this case that a value of $\sigma = 1$ for the proposal is less efficient than $\sigma = 6$. The values in Table.4.1, obtained directly using Eq. 4.32, confirm that the choice $\sigma = 6$ coincides with the lowest value for the autocorrelation time. Note that this also correspond to an acceptance rate of 0.5 as suggest by the rule of thumb of Eq.4.23.

We have mentioned in sec.4.2.3 that the ergodic theorem allows the existence of the Central Limit Theorem for ergodic averages for $N \to \infty$ (Eq.4.16) with some finite σ. This latter can be estimated

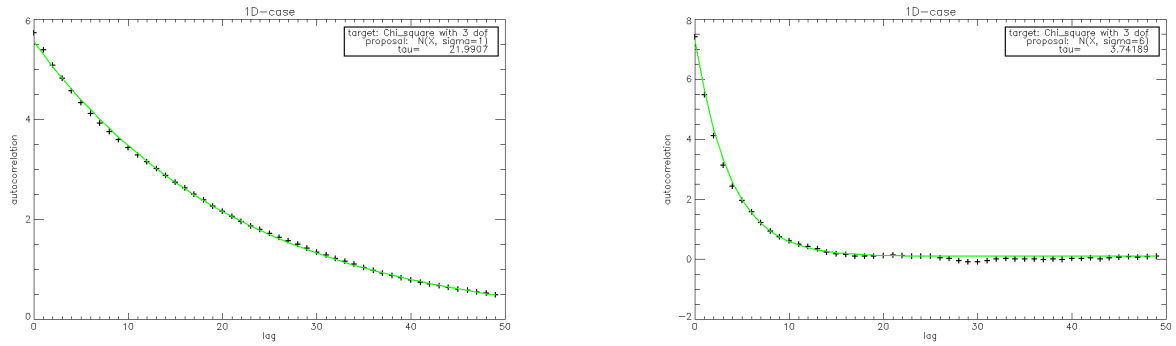

(a) (b)

Figure 4.9: Value of the autocorrelation $\hat{\gamma}$ as a function of *lag* (computed using Eq.4.31) for two chains with different σ for the Gaussian proposal distribution ($\sigma = 1$ for (a) and $\sigma = 6$ for (b)). The target distribution is a χ^2_3. Fitting for an exponential decay we can recover approximately the value of the the integrated autocorrelation time $\hat{\tau}_{int}$ of Table 4.1.

directly from the Markov Chain (Geyer 1991). One has

$$\hat{\sigma}^2_{\pi} = var(\bar{f}_N) \propto \hat{\tau}_{int}. \tag{4.33}$$

This justifies the diagnostic we used just before. A high value of $\hat{\tau}_{int}$ goes with a bigger error on the proper estimation of the target distribution.
We show in Fig.4.10(a), in the case of multivariate distribution of different dimensions, the value of $\hat{\tau}_{int}$ as a function of the scaling factor between the covariance matrix of the proposal and the target (the ratio $\sigma_{\text{prop}}/\sigma_{\text{target}}$). The minimum of it is around what is expected from the rule of thumb of Eq.4.23. In Fig.4.10(b), we can also see that these values correspond to the prescription of an acceptance rate of approximately 0.25.

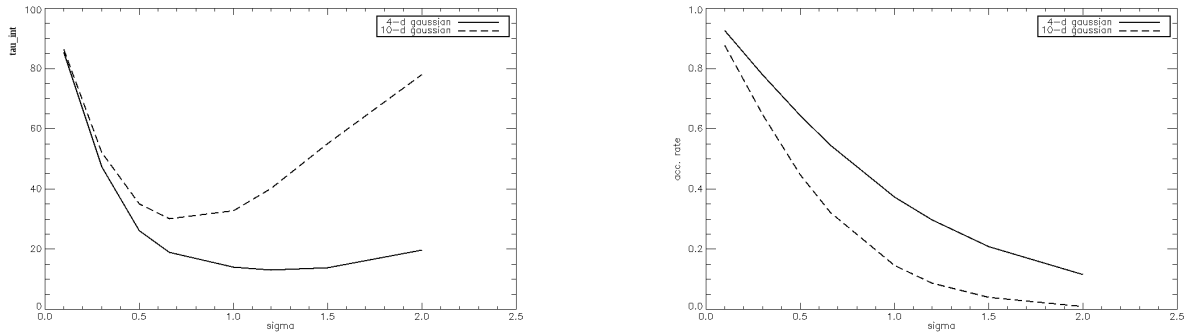

(a) (b)

Figure 4.10: (a) Integrated autocorrelation time $\hat{\tau}_{int}$ as a function of $\sigma_{\text{prop}}/\sigma_{\text{target}}$ for two multivariate Gaussian distributions of dimension $d = 4$ (solid line) and $d = 10$ (dashed line). The minimum is around the value expected from Eq.4.23, and corresponds indeed to an acceptance rate around 0.25 (b).

Interestingly, when checking mixing using the autocorrelation, one can see the gain we have using the Adaptive Metropolis as our baseline algorithm. We chose, as target distributions, multivariate Gaussian distributions of different dimensions and covariance matrices with non negligible off-diagonal terms

shoot at random. Then, we use both the Metropolis and Adaptive algorithm starting with a diagonal proposal distribution. In Fig.4.11(a), we show that, for the Adaptive algorithm, the autocorrelation of the chains decrease more rapidly and convergence is faster. Clearly, when the covariance matrix of the target distribution is diagonal, both algorithm are equivalent (Fig.4.11(b)).

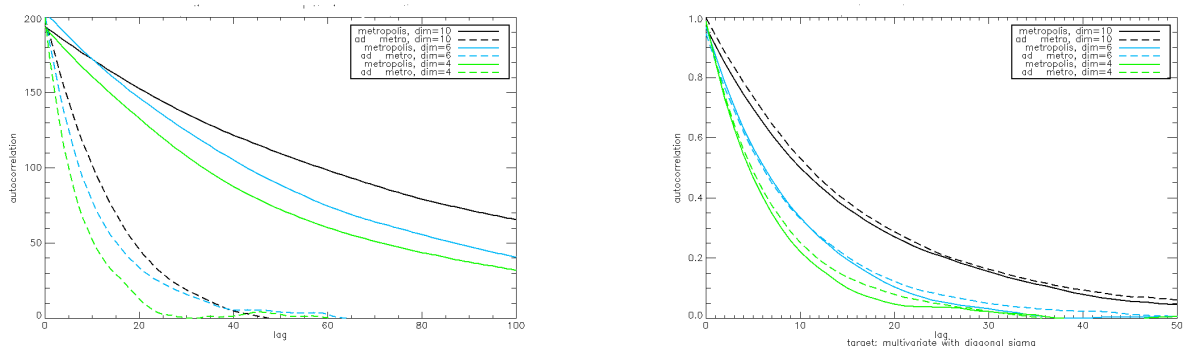

(a) (b)

Figure 4.11: Autocorrelation as a function of *lag* to compare Matropolis (in solid) and the Adaptive (in dashed) algorithm for the case of a multivariate Gaussian posterior with different dimensions (d=10 in black, d=6 in blue, and d=4 in green). The proposal distribution is a Gaussian with diagonal covariance matrix. Note that the Adaptive algorithm performs better than the standard Metropolis (a). In the case the covariance matrix of the target distribution is diagonal, the Adaptive algorithm gives equivalent results to the Metropolis one.

Fourier analysis

Another interesting instrument of diagnostic is the spectral analysis of the MCMC chains since estimating the autocorrelation of a chain is equivalent to estimating its power spectrum $P(k)$. For a good sampler, the correlation of the successive element of the chain is almost zero thus we expect a flat (white noise) power spectrum. The nature of an actual MCMC sampler, however, always induces some small scale correlation and thus a suppression of power at high k. The small scale behaviour is well approximated by a power law of the form $P(k) \propto k^{-\alpha}$, with $\alpha \sim 2$, since we are not far from a random walk ($\alpha = 2$). Also, the position of the "knee" that distinguishes the regime of white noise from the approximate random walk, reflects the inverse correlation length.
A template form to fit this behaviour is (Dunkley et al. 2005)

$$P(k) = P_0 \frac{\frac{k^*}{k^\alpha}}{\frac{k^*}{k^\alpha} + 1} \tag{4.34}$$

where P_0 is the amplitude in the $k \to 0$ limit and k^* the position of the knee.

The criteria for being sure that the chain has converged are then:

- $j^* = k^*(\frac{N}{2\pi}) > 20$, this ensure k_{min} to be in the white noise regime;
- convergence ratio $r = \frac{\sigma_x^2}{\sigma_0^2} \simeq \frac{P_0}{N} < 0.01$.

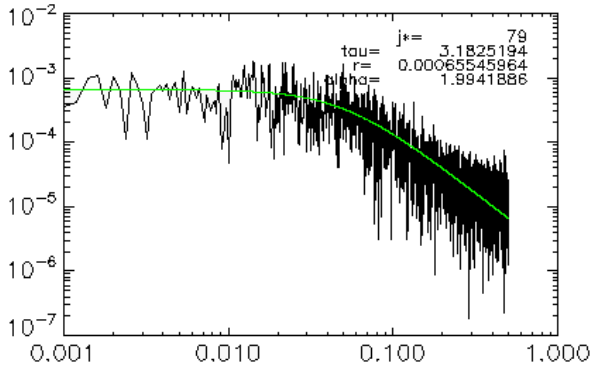

Figure 4.12: The posterior here is a 6-D correlated Gaussian distribution. We select one of the dimension to show the spectral analysis proposed by e.g Dunkley et al. (2005). In green is shown the fit of the power spectrum $P(K)$, obtained with an FFT, using the template formula of Eq.4.2.8. We find $j^* = 79$ and $r = 0.001$. As expected, $\alpha \sim 2$.

In Fig.4.12 we show the power spectrum of a selected dimension of a six dimensional multivariate problem. We then fit with the template form of Eq.4.2.8 and check the relevant parameter for convergence.

As a further example we check again the case of the χ^2_3-distribution of Fig.4.9(a). Using the Fourier analysis we arrive at the same conclusion than before on the optimal choice of the σ for the proposal (Fig.4.13(a) and 4.13(b)).

When convergence is under control, MCMC techniques are a powerful tool to simulate direct draws from a complex distribution of interest. The root method is the Metropolis algorithm widely use for parameter estimation, however, for what concerns the cosmological results discussed in this thesis, we remind that we use the Adaptive algorithm that is an easy and powerful modification of the standard algorithm.

We have also discussed other methods (multi-particle methods, nested sampling) but we conclude that Adaptive is the most suited for our purposes since it allows an automatic search for an efficient covariance matrix for the proposal, able to explore a correlated posterior distribution. Indeed, as we will see in chapter 7 and 8, the cosmological and nuisance parameters of the CMB likelihood have complex correlations.

In the following section we discuss some technicalities on the implementation of the Adaptive algorithm when dealing with the CMB likelihoods.

4.2.9 Implementation of the Adaptive algorithm

In sec.4.2.6 we have described the Adaptive algorithm as was formulated in Haario et al. (2001). For a toy case of multivariate Gaussian distributions it works very well as it is.
However, to obtain satisfactory results in the case of more complex target distributions as the one built in chapter 5 *ad hoc* changes are needed.

We would like to start with a diagonal Σ_0 as the first guess matrix. This is not always possible since, when the number of nuisance parameters is high, and correlations are strong (for example when we add data from ACT and SPT to *Planck*), the adaptation process can be inefficient. In these cases we are forced to use an empirical covariance of the chains as a new input to the algorithm. Also, we can use a

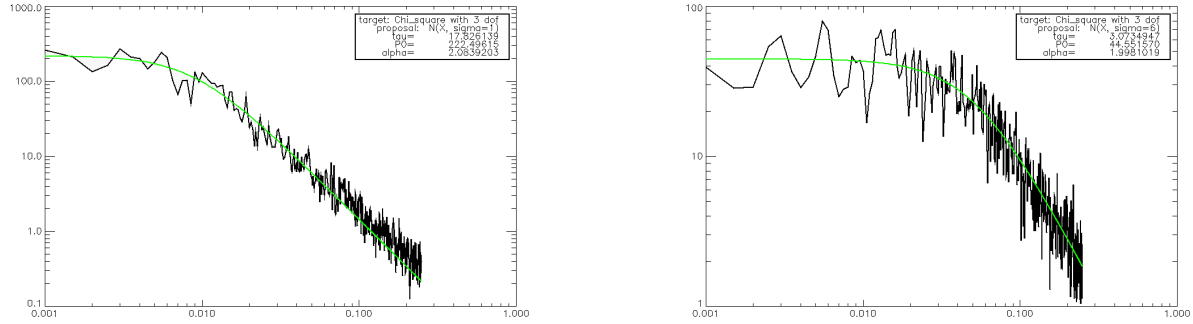

(a) (b)

Figure 4.13: Fourier diagnostic (template fit of the power spectrum using Eq.4.2.8) for the case of a χ^2-distribution with 3 d.o.f. In (a) we have chosen $\sigma = 1$ for the proposal. The convergence criteria (see text) are not respected, in agreement with what we has estimate before using the autocorrelation method. In (b) are presented the fitted values for a proposal with $\sigma = 6$. The convergence is achieved, again as expected.

minimiser like MINUIT (sec.4.3) and use the Hessian matrix associated to the minimisation as the input matrix.

We implemented also other upgrades, based on the indications of the AppStat team at LAL. First we recall the recursive formula for the adaptation of the covariance matrix. At step t we have

$$\mu_t = \mu_{t-1} + \frac{1}{t}(X_t - \mu_{t-1}), \quad \Sigma_t = \Sigma_{t-1} + \frac{1}{t}((X_t - \mu_t)(X_t - \mu_t)^T - \Sigma_{t-1}). \tag{4.35}$$

The proposed move is then $Y \sim N(X_{t-1}, c\Sigma_t)$, where c is some scale factor.
In practice, if we try to start the adaptation from the first steps, the correction we make to the initial guess matrix Σ_0 is too big and numerically unstable. We thus introduce the parameter t_0, that can be tuned, and that represents the number of steps we have to wait before starting the adaptation. In general this phase does not need to be long and $t_0 \sim 10d$ (where d is the dimension of the parameter space) is a safe assumption. Clearly, the algorithm is only weakly dependent on this choice, for example, going from the ~ 20 parameter of the `HiLLiPOP` likelihood to the ~ 50 of `HiLLiPOP` +ACT/SPT we can use the same value for t_0.
For all steps before t_0, the algorithm is thus a simple Metropolis. In this phase the chain starts exploring the parameter space, and it is not essential to have a very reliable first estimate for the covariance matrix; it is preferable to have a high acceptance rate and underestimate the optimal step than to risk remaining stuck at the starting point. The scale c in the proposal is thus chosen to be quite small, say 0.001 (Fig.4.14(a)).

At step t_0 we calculate the sample variance of the chain. The estimate of the covariance between the parameter j and the parameter k is simply

$$\Sigma_{jk} = \frac{1}{t_0 - 1}\sum_{i=1}^{t_0}(X_{ij} - \bar{X}_j)(X_{ik} - \bar{X}_k). \tag{4.36}$$

If t_0 is properly tuned, the constructed matrix is a fair first guess of the covariance of the posterior. Hence, the scale c (Fig.4.14(a)) can be set to the standard value of $2.4^2/d$ (Eq.4.23).

In sec.4.2.5 we have seen that the optimal acceptance rate (a.r.) is around 0.25 and that it can be controlled via the size of the steps for exploring the parameter space. It is hence possible to tune the

scale factor c accordingly.

$$c_{t+1} = c_t \cdot (1 - \frac{1}{t}) + \frac{1}{t}(\text{a.r.} - 0.25) \tag{4.37}$$

To switch on this kind of adaptation, we introduce in the algorithm the parameter t_s. For $t > t_s$, the scale factor is modified according to Eq.4.37. The a.r. is computed "locally" using, each time, only the previous 100 steps of the chain. Clearly, t_s needs to be greater than t_0. If we set $t_s = t_0$ the adaptation of the scale factor starts immediately after the Metropolis phase. This can be useful if the estimation of the covariance matrix is still really poor at the end of this phase.

Different configurations have been tried until an optimal one was found for our `HiLLiPOP` likelihood. The algorithm has also been tested on several versions of other *Planck* likelihoods (Plik and CamSpec). The different foreground modellings for the likelihoods play a role in how to optimally tune the algorithm since they change the full correlation matrix. However, the ergodic properties of the algorithm reassures on the fact that the choice for t_0 and t_s is not unique. In practice, a lot of the results presented in this thesis have been obtained with $t_0 = 200$ and $t_s = 10000$.

If the process of adaptation is going too fast, the algorithm can be slowed down by re-weighting, in Eq.4.35, each step with $1/t^\alpha$ instead of a simple $1/t$, with $\alpha \in (\frac{1}{2}, 1]$. While the AppStat team advocated a value $\alpha = 0.7$ we found that for the case of CMB this lowering of α leads to an underestimation of the posterior variance that depends on the dimension of the problem. The best results was obtained with the standard $\alpha = 1$ value.

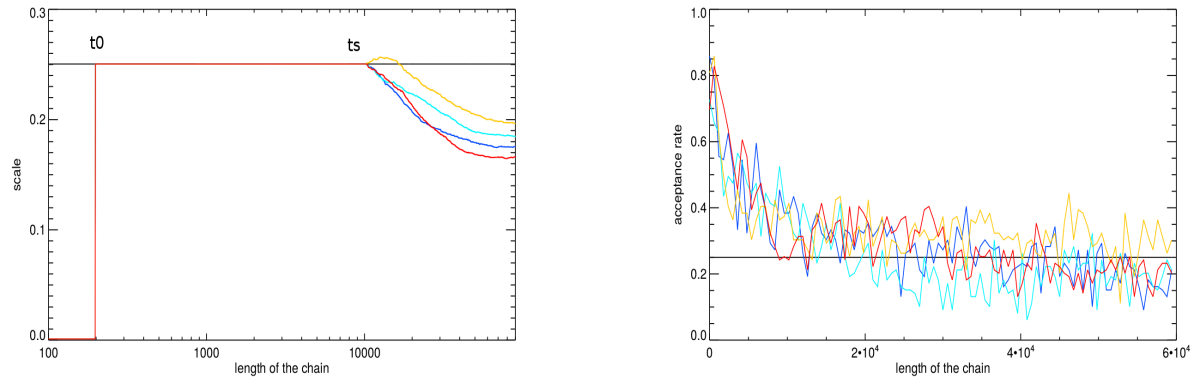

(a) (b)

Figure 4.14: An example of a configuration for t_0 and t_s for the Adaptive algorithm for the `HiLLiPOP` likelihood. The four different chains are shown with different colors. In (a) is plotted the evolution of the scale factor c as a function of the length of the chain. Until $t_0 = 200$, c is kept very low, then is set to the optimal value of Eq.4.23 until $t_s = 10000$. From t_s on we start adapting c as in Eq.4.37. These choices for the value of c allow the acceptance rate to reach the standard value of ~ 0.25. In (b), we report the consequent evolution of the a.r as a function of the length of the chain.

Generating random numbers

The performance of all the Monte Carlo methods depends on the reliability of the random number generators. For our analysis we use the `AbsRand` package[5], that consists in a set of efficient C++ classes

[5] http://planck.lal.in2p3.fr/wiki/pmwiki.php/Softs/AbsRand

organised in an object oriented framework. It contains high quality uniform and Gaussian generators. We also mention that it contains a very fast $1/f^2$ noise generator based on random-walk, and a $1/f$ fast generator based on the previous one (Plaszczynki 2007). This software is used in the Planck experiment.

- The random number generator is `planck_rng`, an implementation, in the context of the Planck satellite experiment, of a new generation algorithm: the `xorshift` generator described in Marsaglia (2003). This class of pseudo random number generator gives the next number in its sequence by repeatedly taking the *exclusive or* of a number with a *bit shifted* version of itself. It has been performed and tested by M. Reinecke (Max Planck Institute fur Astrophysik, Garching)
- for generating $x \sim N(0,1)$ the radial Box-Muller transform (Box & Muller 1958) is used.

As described in sec.4.2.5, for our MCMC methods we need to generate d-dimensional samples distributed as a multivariate Gaussian distribution with a given μ and Σ.
This is done using the *Cholesky decomposition* $\Sigma = LL^T$ (e.g. Nash (1990)).

Once the covariance matrix is decomposed, giving the lower-triangular L, one has just to multiply it with a vector of uncorrelated samples, $x \sim N(0,1)$.
The vector Lx has the covariance properties of the system modelled with Σ.

4.2.10 Cross check with CosmoMC

The public CosmoMC code[6], combined with the Boltzmann code Camb (sec.1.5.1) are the official setting for the analysis of *Planck*data.

This algorithm is based on the Metropolis-Hastings one with some important CMB-oriented upgrades (Lewis & Bridle 2002; Lewis 2013).

The scaling with dimension is improved separating the *slow* from the *fast* parameters. An example of slow parameter is the matter density (changing it requires a full recalculation of the evolution of the background model and the perturbation) while all the nuisance parameters are in general fast (only the dependent likelihood function needs to be recomputed, not the C_ℓ).

The base parameters are orthogonalised so that proposals are made to nearly independent combinations of the original base. Even if fast and slow parameters are correlated, it is possible to make a linear parameter redefinition to keep the fast parameters independent of the slow ones. Parameters are then grouped in sets of similar "speed" and the proposed moves are made along random directions in these equal speed sub-spaces. This allows to oversample the fast sets.

Another peculiarity of the algorithm is the actual shape of the proposal distribution which is a radial function not necessarily with the same dimensionality than the posterior. It is also corrected to increase the probability for small or large steps for a better exploration in the case of a non-Gaussian posterior.

In Fig.4.15 we show the comparison, using the Plik likelihood, between the posterior distribution obtained with CosmoMC+`CAMB` and the Adaptive algorithm implemented in this thesis in combination with the CLASS Boltzmann code (sec.1.5.1). The agreement is very good with minor differences that may come from the slight difference at high-ℓ between the spectra computed by two Boltzmann codes. The disagreement on θ is expected since it is defined differently in the two codes (sec. 7.1).

In Fig.4.16 we juxtapose the correlation matrix obtained with CosmoMC and the one obtained with the Adaptive algorithm to show the agreement between the methods.

[6] http://cosmologist.info/cosmomc/

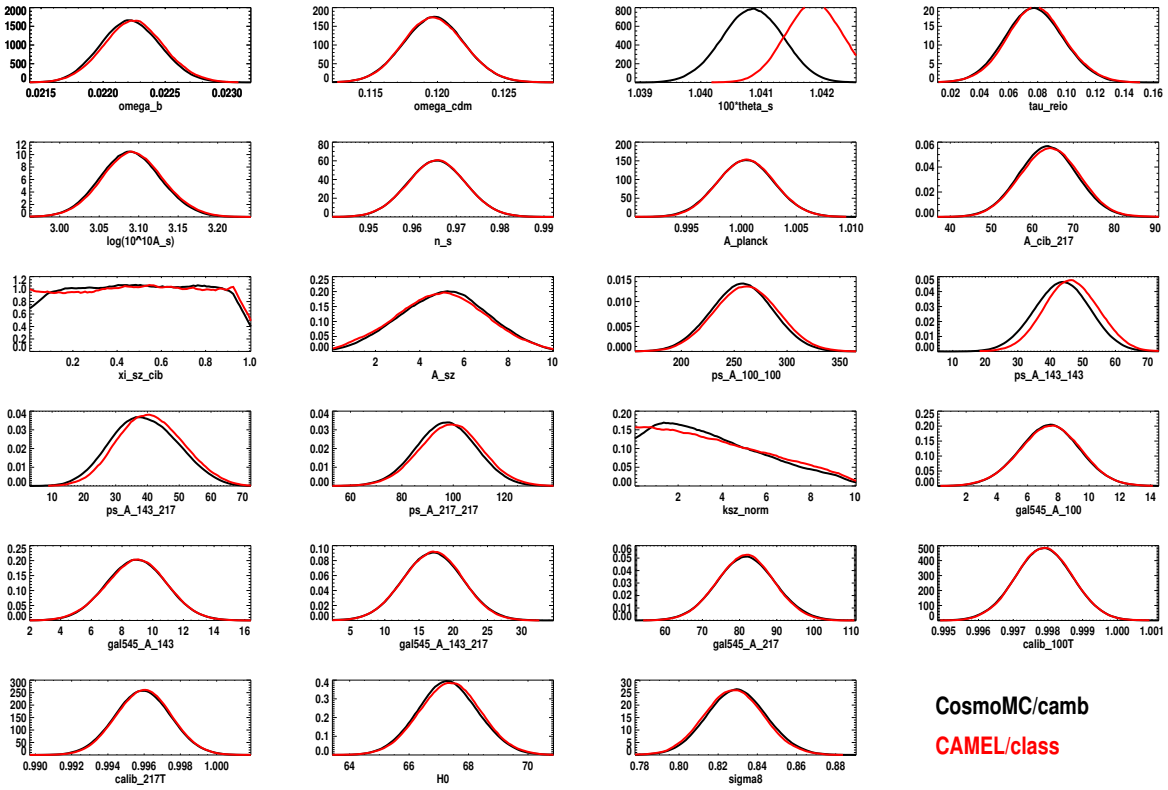

Figure 4.15: Posterior distributions obtained using the Adaptive algorithm for the Plik likelihood and the CLASS code (red) against the results from the official chains obtained using CosmoMC and Camb (black). The difference in θ comes from a different definition of this parameter in the two codes. The minor disagreement on some foreground parameters can originate from the differences at high-ℓ between CLASS and Camb (sec. 7.1).

4.3 Frequentist approach

The extreme precision of the data used in this thesis offer the possibility of a fine check on the robustness of the results with respect to the statistical methodology.

Unlike the Bayesian method, the frequentist approach do not have priors (and therefore the conceptual difficulties that may arise in defining them properly, see sec.4.1). By definition, the quantity one wants to measure has a true fixed value and hence can not have a distribution. This can be an important difference since it have been shown that priors may affect parameter determination (Hamann et al. 2007; Gonzalez-Morales et al. 2011; Hamann 2012). Moreover, the process of marginalisation (sec.4.2.4), favours regions of parameter space that contain a large volume of the probability density in the marginalised directions, and this may lead to the so called *volume effects* (e.g. (Hamann et al. 2007)).

In this section, some of the methods of the frequentist framework are presented. First the search for a "best fit" is performed using a high precision minimiser (sec.4.3.1) and then the procedure for extracting error bars is described (the profile likelihood, sec.4.3.2).
The subtle case of a limit in the presence of a physical boundary is illustrated in sec.4.3.3. In Bayesian statistic, with the possibility of adding a "step-like" prior, it is straightforward to define a credible interval with respect to the no boundary case. For the frequentist framework, where a confidence interval has to preserve the right *coverage* properties, one needs to refine the procedure (Feldman & Cousins 1998).

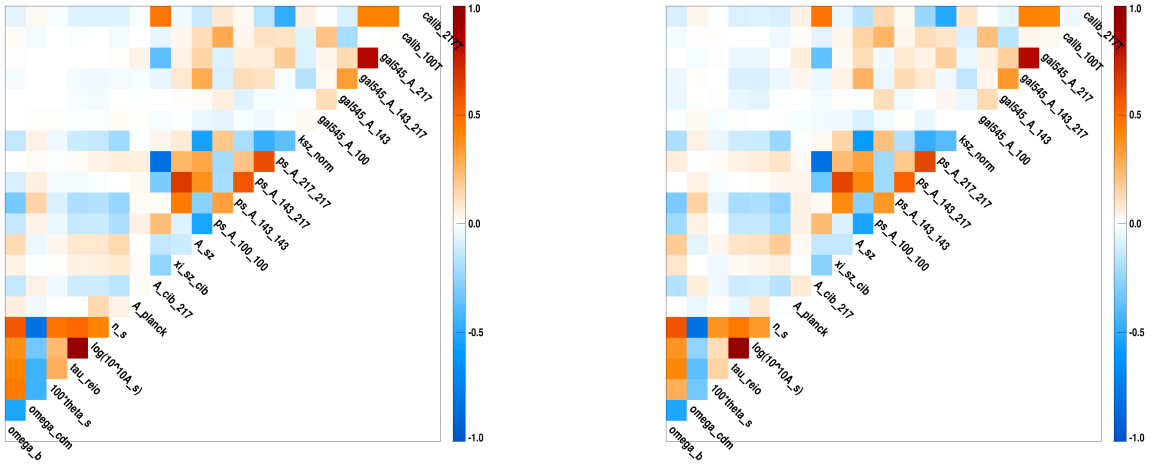

Figure 4.16: Correlation matrix obtained sampling the Plik temperature likelihood with CosmoMC+Camb (a) or with the Adaptive algorithm described in this thesis + CLASS (b).

4.3.1 Maximum likelihood estimation

What is commonly called "best-fit" is the maximum of the likelihood function (MLE) or equivalently the minimum of the $\chi^2 = -2 \ln \mathcal{L}$ function. To be properly determined, complicated numerical derivatives, have to be computed, relying on a high precision minimizer. For the work in this thesis, and also for the one presented in Planck Collaboration A54 (2014), the powerful `MINUIT` software [7] has been used. This package is fundamental in High Energy Physics, its role in the Higgs mass determination (ATLAS Collaboration 2013) being only one example. Initially developed at CERN in the 70's (James & Roos 1975), it has been continuously improved and recently rewritten into `C++` (we use this `C++` version, `MINUIT2`). It contains several tools for minimizing a function and for special error analysis.

For our purpose of cosmological parameters estimation, we minimize the χ^2 function using the `MIGRAD` algorithm, which is based on Fletcher's "switching" algorithm (Fletcher 1970). This is done in a two step process. At first, all parameters are bounded by large (or physical) limits during the exploration. Then, once a minimum is found, all cosmological parameters limits are released, and again the `MIGRAD` minimization is performed. The limits on nuisance parameters are kept in order to avoid exploring unphysical regions.
`MIGRAD` belongs to the category of *variable metric methods* (e.g. Davidon & Laboratory (1959)) which allows to calculate a factor of merit for the convergence, the "Expected Distance to Minimum" (EDM), hence helping in rejecting poor fits. At the end of these operations, we use the `HESSIAN` procedure to refine the local covariance matrix.

However, since the problem is highly non-linear, the Hessian is only a crude approximation to the parameters "errors" and a complete treatment goes through the construction of the profile-likelihood. As explained in sec. 4.2.9, it can serve, however, as a starting covariance matrix for the Adaptive MCMC.

[7] http://seal.web.cern.ch/seal/work-packages/mathlibs/minuit/index.html

4.3.2 Profile likelihoods

Using the minimisation procedure described in the previous section we are able to estimate the global maximum likelihood (or the $\chi^2_{\rm min}$) given the entire set of parameters.
A profile-likelihood allows instead to estimate the MLE of a chosen parameter θ of this d-dimensional parameter space and its confidence level interval. Formally, one builds

$$\mathcal{L}_p(\theta) = \mathcal{L}(\theta, \hat{\hat{\psi}}(\theta)), \tag{4.38}$$

with $\hat{\hat{\psi}}(\theta)$ the ψ that maximizes $\mathcal{L}$ at fixed θ.
One often speaks about the minimum $\chi^2 = -2\ln\mathcal{L}$ instead of the maximum of $\mathcal{L}$.
An example of the result is shown in Fig.4.17: to obtain the profile, one *scans*, within some range, different value of θ and, at each point, runs the χ^2 minimization with respect to all other parameters. The minimum χ^2 value is reported for this θ value.

Given the procedure, the solution at the minimum of $\chi^2(\theta)$, for every parameter, coincides with the standard χ^2_{min} solution, which ensures we are avoiding the potential "volume effects" that appear in projecting MCMC samples.

To extract a confidence region, which has the correct frequentist coverage properties, one needs to build the likelihood ratio statistic, or, equivalently, the $\Delta\chi^2(\theta) = \chi^2(\theta) - \chi^2_{\rm min}$ distribution (that is actually what is shown in Fig.4.17).
For a parabolic $\chi^2(\theta)$ shape (*i.e.* gaussian estimator distribution), a 1-α-level confidence interval, is obtained by the set of values $\Delta\chi^2(\theta) \leq \chi^2_1(\alpha)$, where $\chi^2_1(\alpha)$ denotes the 1-α quantile of the χ^2-distribution with 1 degree of freedom, and is 1, 2.7, 3.84 for $1-\alpha = 68, 90, 95\%$ respectively. In other words, if we are looking for a 68% CL, we have just to cut the profile at 1 (see again Fig.4.17).

This procedure is still valid if the profile-likelihood is non-parabolic. The MLE in fact, does not depend on the choice of the set of parameters: if $\hat{\theta}$ is the MLE of the parameter θ, the MLE of any function of θ, $\tau(\theta)$, is simply $\hat{\tau} = \tau(\hat{\theta})$. For example, one can build the $\Delta\chi^2(A_s)$ distribution from the $\Delta\chi^2(\log(10^{10}A_s))$ profile by simply switching the $\log(10^{10}A_s) \to A_s$ axis.
This *invariance* property allows to build an approximate confidence interval since one can imagine a transformation that would make it quadratic in the new variable. The (asymmetric) confidence interval is obtained by cutting the non-parabolic $\Delta\chi^2$ curve at the corresponding $\chi^2(\alpha)$ values of the parabolic case (Wilks 1938). In `MINUIT`, the routine implementing this method is called `minos` and it is exact up to order $O(\frac{1}{N})$, N being the number of samples (James 2007).

In chapter 7 results on cosmological parameters obtained using the profile-likelihood based confidence intervals, will be discussed and confronted to Bayesian credible intervals, finding agreement between the two methods. This is somehow expected since, for ΛCDM, the shapes of the posteriors are all almost Gaussian (parabolic $\Delta\chi^2$).

Nevertheless, the profile-likelihood can be useful in exploring strong degeneracy as the (A_s, τ) one as discussed in sec. 7.2.7.
Also, the procedure described above is not well defined if the parameter of interest has a physical boundary. As an example, the neutrino absolute scale parameter Σm_ν, that is central to this thesis, is necessarily greater than zero ($\Sigma m_\nu > 0$).
Clearly, also the marginalized posterior distribution is not Gaussian any more but largely peaked towards zero, making the estimation of the upper limit sensitive to its detailed shape. Hence we may expect some relevant differences between the frequentist and Bayesian methods, or at least a finer diagnostic power for the robustness of the upper limit on Σm_ν in this comparison. Postponing the detailed discussion of the results to chapter 8, we present in the next section the revised frequentist procedure for such an estimate.

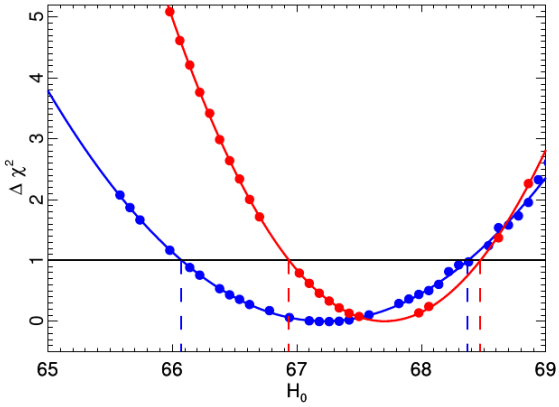

Figure 4.17: Profile-likelihood based 68% confidence interval (see text) on H_0 for CMB only (in blue) and CMB + BAO (in red). This figure is taken from Planck Collaboration A54 (2014).

4.3.3 Limit in presence of a boundary

We describe here the procedure to statistically set an upper-limit near the physical boundary $\Sigma m_\nu > 0$ (Fig.4.18). First, as before, we scan different *physical* value for the Σm_ν parameter (i.e. positive) and we report the $\Delta\chi^2(\Sigma m_\nu)$ after the minimisation on all the other parameters. Then we perform a parametric parabolic fit

$$\chi(\Sigma m_\nu) = \chi^2_{min} + [(\Sigma m_\nu - m_0)/\sigma_\nu]^2 , \tag{4.39}$$

for estimating the minimum m_0 and the curvature σ_ν.
Far from its minimum, the function is not necessarily quadratic, hence the farthest points are discarded in the fit.

If there were no boundary the 95%CL interval would have been obtained "thresholding" at 3.84 (sec.4.3.2). In a correct approach, we cannot do this any more; instead we use the classical "unified approach", i.e. the Feldman-Cousins prescription (Feldman & Cousins 1998).

This procedure first constructs the ordering principle based on the likelihood ratio R:

$$R = \frac{\mathcal{L}(x|\mu)}{\mathcal{L}(x|\mu_{best})} \tag{4.40}$$

where x is the measured value of the sum of neutrino masses, μ is the true value and μ_{best} is the best fit value of $\sum m_\nu$ given the data and the physically allowed region for μ. Hence, we have $\mu_{best} = x$ if $x \geq 0$ and $\mu_{best} = 0$ if $x < 0$, and the ratio R is given by:

$$R = \begin{cases} \exp(-(x-\mu)^2/2) & \text{for x} > 0 \\ \exp(x\mu - \mu^2/2) & \text{for x} \leq 0 \end{cases} \tag{4.41}$$

We then search for the interval $[x_1, x_2]$ such that

$$R(x_1) = R(x_2) \text{ and } \int_{x_1}^{x_2} \mathcal{L}(x|\mu)dx = \alpha \tag{4.42}$$

with $\alpha = 95\%CL$. These intervals are tabulated in (Feldman & Cousins 1998).

We then read off the confidence interval $[\mu_1, \mu_2]$ for $x = m_0/\sigma_\nu$ extracted from the parabola fit on the χ^2 profile. The upper limits are calculated as $\mu_2 \times \sigma_\nu$.

As a check, we vary the range of points used in the parabolic fit to ensure that the limit we obtain is always lower than the one we report as the result, in other words, ensuring that we are conservative.

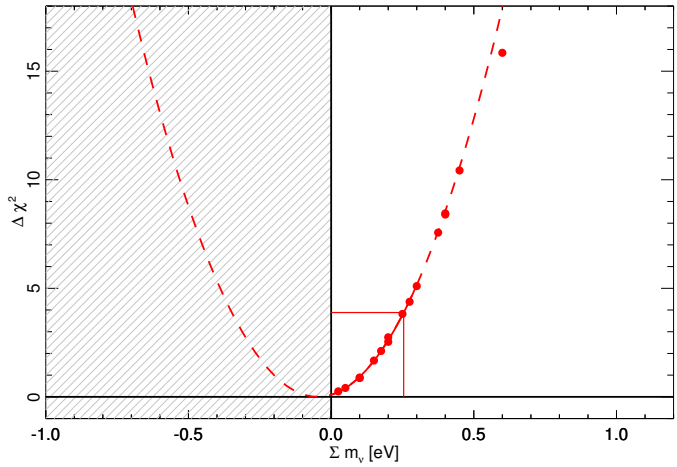

Figure 4.18: Example of profile likelihood for $\sum m_\nu$. In presence of a physical limit at zero the Feldman-Cousins prescription has to be applied to correctly extract the upper limit at the 95% CL.

Conclusions

In this chapter we have described the estimation of cosmological parameters using the Bayesian Markov Chain Monte Carlo method and the frequentist profile likelihood analysis. The former efficiently extend the idea of Monte Carlo integration to problems in high dimensions, using the Markov chain properties. We have discuss convergence tests and the implementation of an Adaptive algorithm that has been used to obtain all the posterior distributions presented in this thesis. The frequentist profile analysis has been also presented. This method is particularly suited for the estimation confidence intervals in the case of highly correlated variables, as τ and A_s (chapter 7), or a physical boundary, as for Σm_ν (chapter 8).

Both methods apply to any likelihood function. The next chapter is dedicated to the construction of a high multipole likelihood from the *Planck* CMB data described in chapter 3. In chapter 6 we will complete the description of the cosmological data used in this thesis, briefly presenting the large scale, the lensing, and the very high-ℓ CMB likelihoods together with the BAO and Supernovae ones.

Chapter 5

The HiLLiPOP high-ℓ likelihood

With the aim of extracting the cosmology encoded in the CMB, the full-sky high resolution of the *Planck* temperature and polarisation maps presented in chapter 3, are impossible to be handled directly. Fortunately, since primordial fluctuation are believed and observed to be Gaussian (sec.1.5), all the information contained in maps can be translated into angular power spectra (sec.1.3.1).

The angular power spectrum of the CMB, before the large WMAP and *Planck* sets of data, was mainly obtained through maximum likelihood estimators requiring the inversion and multiplication of $N_d \times N_d$ matrices, where N_d is the size of the data vector (e.g. Tegmark (1997)). These methods, although allowing to obtain a precise estimation of spectra and the error bars of the covariance matrix, become computationally prohibitive to be used for all the *Planck* detectors and at the full resolution ($\ell_{\rm max} \simeq 2500$).
Efstathiou (2004) has proposed an hybrid strategy that uses maximum likelihood methods only for the low-ℓ part of the spectrum on low resolution maps. The high-ℓ ($\ell \gtrsim 30$) part, is estimated using the *cross spectra methods* that are more tractable and almost optimal. These methods require approximations for the covariance matrix that are less accurate at low-ℓ but precise at high-ℓ. The use of cross spectra (sec.5.10 and 5.5.2) allows the reconstruction of the correlation between two different sky maps. The advantage of cross spectra is that they are not biased by the noise since it cancels out in mean between the two maps.

The composite strategy just described, is the one adopted in *Planck* data analysis. The cross spectra approach is used at high-ℓ, where a Gaussian likelihood approximation is appropriate (Hamimeche & Lewis 2008). For $\ell \leq 30$, low resolution `Commander` temperature maps derived from *Planck*, WMAP, and 408MHz are combined with template cleaned LFI 70 GHz polarization maps in a *pixel based approach*. We refer to this likelihood as `LowTEB`. A more detailed discussion is postponed to sec.6.1, where is also discussed a different approach called Lollipop based on the modification of the Hamimeche-Lewis likelihood (Mangilli et al. 2015).

For the high-ℓ part, in *Planck* there are four likelihood codes (Planck Collaboration A13 2015):

- `Plik`: the Paris LIKelihood developed at IAP and official likelihood for the 2015 release
- `CamSpec`: from the Cambridge team, official likelihood for the 2013 release
- `Mspec`: from the USA team, which include a simplified component separation step
- `HiLLiPOP`: developed at the Laboratoire de l'Accelerateur Lineaire and topic of this chapter

Having different likelihoods allows to test the robustness of the results to different approximations and allows a more profound understanding of the effects of foreground or instrumental modelling arising from different parametrization choices.

Indeed, the main difficulty in the analysis is how to treat the astrophysical foregrounds. Using the HFI 100, 143 and 217 GHz channels, dominated by the CMB signal, we can safely extract the C_ℓ from the maps with appropriate masks and deal with foregrounds at the power spectra level. Doing this, one is assuming that the two-point correlation function completely describes the shape of the foregrounds. This is the choice adopted by the four likelihood codes mentioned above. Another strategy can be to use directly the spectra computed from the component separation maps and estimate the cosmological parameters from these CMB only spectra. This is done by the `XFaster` likelihood (Planck Collaboration. IX. 2015).

This chapter describes in details the `HiLLiPOP` likelihood (**Hi**gh **L** **L**ikelihood **P**lanck **O**rsay **P**roject). The final result is shown in Fig.5.1 and 5.2.

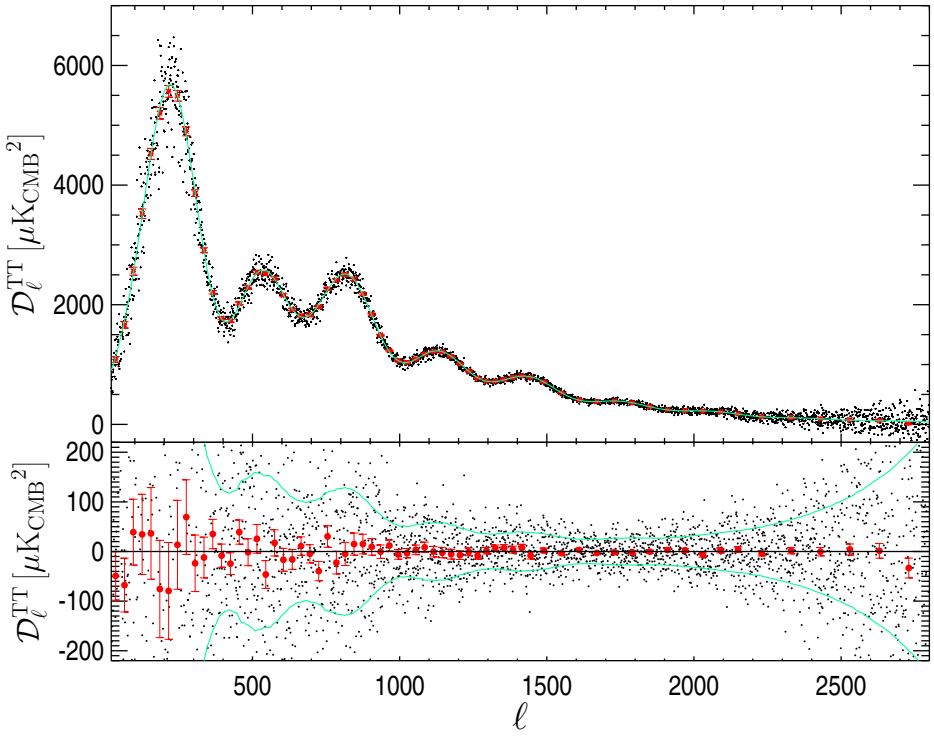

Figure 5.1: The `HiLLiPOP` cross-half-mission coadded temperature power spectra at $\ell \geq 50$. The red data point are binned in $\Delta_\ell = 31$, while the grey data points are unbinned. In green in the upper panel is plotted the best-fit base ΛCDM theoretical fitted to the combined `HiLLiPOP` + `LowTEB` likelihood. Residuals with respect to this model are shown in the lower panel. The green lines show the 68% unbinned error bars.

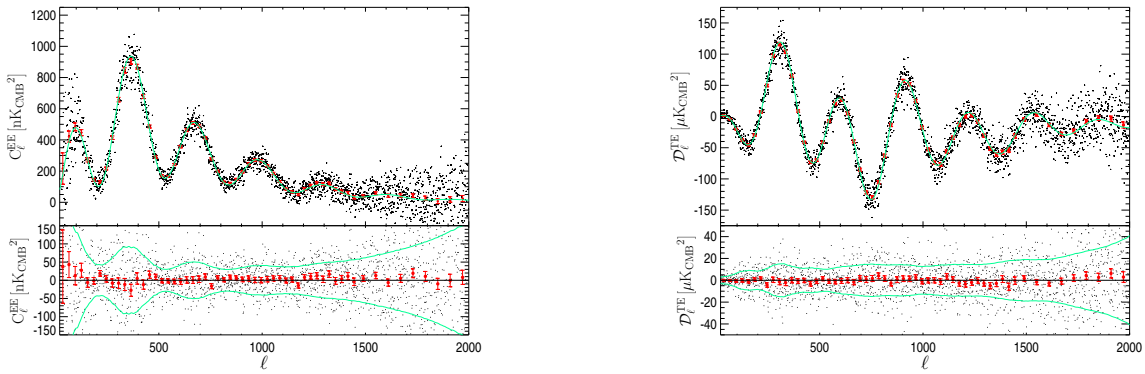

(a) (b)

Figure 5.2: Same as Fig. 5.1 for EE (a) and TE (b).

5.1 The basic structure of the high-ℓ likelihood

At high-ℓ, the likelihood can be written as the one for a Gaussian distributed variable and thus simply reads:

$$-2ln\mathcal{L}(C_\ell^{\rm model}) = \sum_{\rm modes}\sum_{\rm cross}(C_\ell^{\rm data}-C_\ell^{\rm model})\Sigma^{-1}(C_\ell^{\rm data}-C_\ell^{\rm model}). \tag{5.1}$$

Where the sum is on all the cross spectra used and on all the modes that we want to include (TT, EE, TE) and Σ is a constant covariance matrix. Note that, in principle, the matrix Σ depends on the CMB signal $C_\ell^{\rm CMB}$. We use here a model fixed around the minimum which ensure a good approximation for the error bars and no bias in the posteriors.

The CMB cross power spectrum (sec.1.3.1) is the central element of the likelihood. Hence, an estimation of the C_ℓ need to be extracted from maps. Although we have available *Planck* all-sky maps (sec.3.4), the thermal emission from the galaxies largely dominates over the CMB signal at low galactic latitude. We are thus forced to mask this contamination, searching, at each frequencies, for a compromise between a cleaner signal and statistics. We postpone a detailed discussion on the masks used to sec.5.3. Partial sky coverage correlates the power spectrum estimators at different ℓ and complicate its extraction (sec.5.4).

The construction of the covariance matrix Σ is addressed in Sec.5.5. In the limit of an ideal full-sky surveys this calculation would have been simple. Masks and beams effects (sec.5.4.1) induce ℓ-by-ℓ correlations that need to be properly handled.

Residual foregrounds, still present after masking, are then parametrised in terms of power spectrum models. As detailed in sec.5.6, we use physically motivated template result of *Planck* internal works. These residual foregrounds vary with multipole and frequency ranges and are modelled as a contribution, beside the signal part from the CMB

$$C_\ell^{\rm model,XY} \propto C_\ell^{\rm CMB,XY} + \sum_{\rm fg} A_{\rm fg}({\rm X},{\rm Y})C_\ell^{{\rm fg},XY}, \tag{5.2}$$

where we have written explicitly the cross spectra notation XY. For each foreground and each cross spectrum, the angular shape of the residual foreground is fixed. A scaling parameter is let free in each case.

The last part of the chapter is dedicated to some consistency checks and a discussion of the differences between our likelihood and the other likelihoods approaches.

5.2 Maps

As described in sec.3.4 different sets of maps have been produced. The likelihood has been developed in parallel to successive internal releases of data, but the results presented in chapter 7 and 8 refer only to the public latest release. We remind that only the 100, 143 and the 217 GHz maps are used in the analysis. We use two maps per frequency that we will refer to as: 100A, 100B, 143A, 143B, 217A, 217B. More details are given in Table 5.1. The maps used are:

- *Detector Set* (DS) maps. These have been used to put constraints on cosmological parameters also in the 2013 analysis, although our DS maps are constructed slightly differently (see Table 1 in Planck Collaboration XV (2014) for the definition of DetSet);
- *Half Mission* (HM) maps, from which have been obtained the 2015 results;
- in this thesis also *Year* maps (Yr) have been considered. Yr maps are similar to the HM maps but do not include the 5th *Planck* survey.

map name	*Detector* maps		*Year* maps	*Half Mission* maps
	Temperature	Polarization		
	combination of PSB and SWB			
100A	100-DetSet1	100-DetSet1	100-Yr1	100-HM1
100B	100-DetSet2	100-DetSet2	100-Yr2	100-HM2
143A	143-DetSet1 + 143-5 + 143-7	143-DetSet1	143-Yr1	143-HM1
143B	143-DetSet2 + 143-6	143-DetSet2	143-Yr2	143-HM2
217A	217-DetSet1 + 217-1 + 217-3	217-DetSet1	217-Yr1	217-HM1
217B	217-DetSet2 + 217-2 + 217-4	217-DetSet2	217-Yr2	217-HM2

Table 5.1: Maps used in the analysis. We refer to Fig.5.3 for the identification of the various PSB and SWB. Details on the construction of DetSet can be found in Table 1 of Planck Collaboration XV (2014)

5.3 Masks

The contamination of the foregrounds discussed in sec.3.5 has to be handled if we want a proper estimation of the CMB signal. The first, immediate strategy is to get rid of the strongest foregrounds masking their emission. Hence, frequency dependent Galactic, CO and Point Source masks are applied on the maps described in sec.5.2.

Galactic masks

Diffuse Galactic dust emission is the main foreground for CMB measurements in both temperature and polarization and is dominant at high frequency ($\nu > 300$ GHz) (sec.3.5). The masks for the Galactic thermal dust emission are derived from the 353 GHz map in intensity. For polarisation analyses we

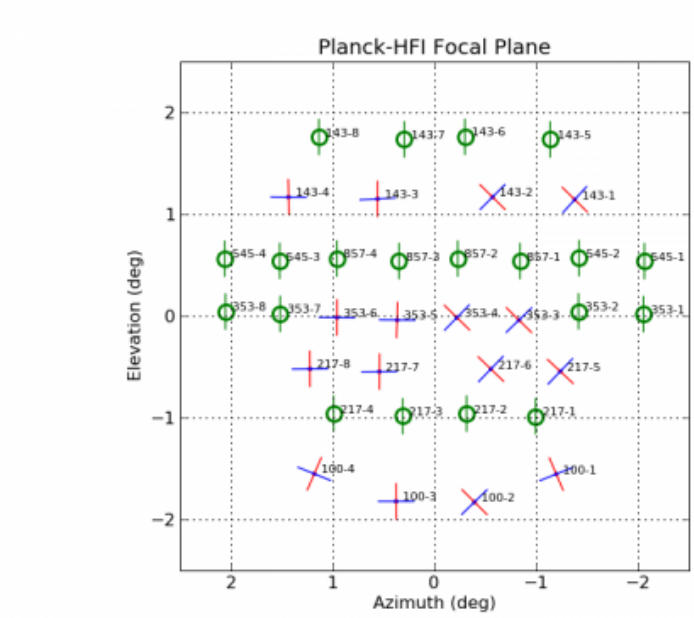

Figure 5.3: HFI Focal plane layout as seen from outside the celestial sphere. PSB orientations are indicated, with a red rod for the "a" elements and a blue rod for the "b" elements. Green circles are for the SWBs. Near each detector is reported its name.

employ the masks derived for temperature, as they are relevant to cut off polarised dust emission on small scales.

Dust polarisation at large scale does not look like dust in intensity, since, at these scales, one sees only the effect of the magnetic field, which is quite different from the distribution of matter, responsible for the emission of dust. Down to smaller scales however, one starts seeing the effect of turbulence, that is due to the distribution of matter. This means that, for small scales (typically smaller than 2°), the dust polarisation is traced very well by the intensity of its emission. Hence, a good mask for intensity, is also a good mask for polarisation.

Conversely, if one builds the mask using the polarisation of the dust, the large scale structures of polarisation will be well masked, but not the small scales. Since we are interested in small scales, this justifies our choice of using the same masks in intensity and in polarisation.

The mask are based on a threshold in intensity of the 353 GHz map. In practice, the procedure for constructing the masks is the following. First the 353 GHz map is smoothed with large Gaussian beams, then, the histograms of the map are derived and used to obtain the cumulative distribution of the pixel value. These distributions are used to obtain the list of the N brightest pixels that will be set to 0 in order to mask a $N/N_{\rm pix}$ fraction of the sky, $N_{\rm pix}$ being the total number of pixels in the map. Hence, mask are in general identified via the sky fraction $f_{\rm sky}$ that is kept in the analysis.

In Fig.5.4 we show an example of a binary mask covering the 30% of the sky, hence with $f_{\rm sky}$=70%. As it is, the mask causes problems at the Fourier analysis level since the transition between the pixel at 0 and at 1 is step-like. To avoid spurious effects in the $a_{\ell m}$ extracted from the map (Fig. 5.5(a)), a procedure of *apodisation* is necessary: as can be seen in Fig. 5.5(b), the C_ℓ of the unapodised map show structures at high-ℓ that are non physical.

Apodisation can be done applying an apodising profile, that can be any smooth function that goes from zero to one, to the distance map of a mask. The distance map represents the distance of each pixel

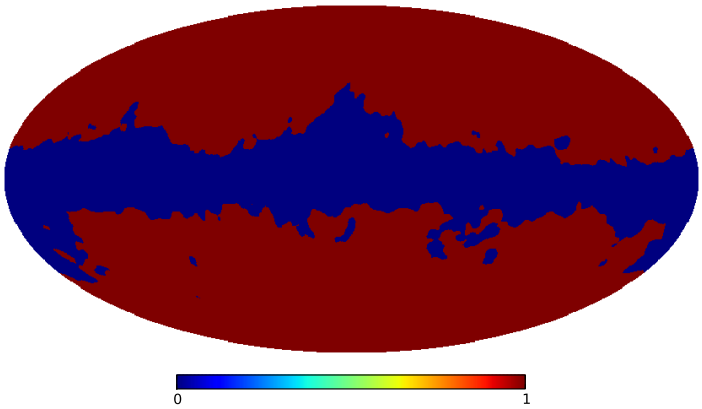

Figure 5.4: An example of a binary mask covering the 30% of the sky ($f_{\rm sky}$=70%). The mask needs to be apodised to be properly used in the analysis.

to the nearest zero pixel of the mask. This technique is used for Point Sources for example. However, apodisation using the distance map, present some "spiky" features along particular directions where the distance is almost constant. This is why, for the Galactic mask, we chose to smooth the masks with a Gaussian in the $a_{\ell m}$ space rather than using the distance map function. The procedure has the drawback of injecting some signal in the initially blocked regions. This can be handled using initially a slightly bigger mask and, after the smoothing procedure, a smaller mask to make sure the signal is erased in the blocked regions, or using a threshold to remove part of the leakage in the mask. Note that, with our procedure, the $f_{\rm sky}$ stays the same before and after apodisation.

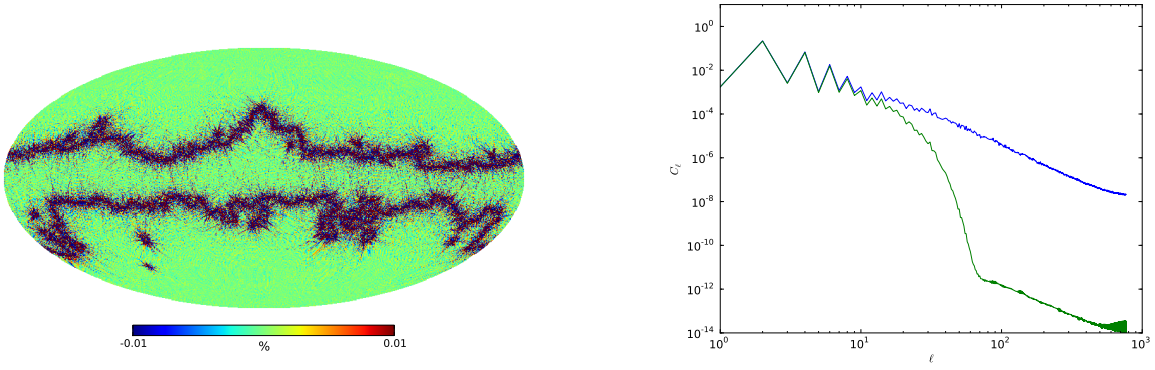

(a) (b)

Figure 5.5: (a) % residuals of the subtraction between the $f_{\rm sky}$=70% unapodised mask and the same mask Fourier (i.e. Harmonic) transformed back and forth. (b) In blue is shown the power spectrum of the unapodised mask of Fig. 5.4. There are structures at high-ℓ that arise from the ringing artefacts near the sharp transitions of the mask. The apodised mask has a different C_ℓ spectrum (in green) where the high frequency power is reduced.

The mask are thus apodised through a Gaussian smoothing with a large FWHM of 8°. Once the smoothing is applied, we set the threshold such that all pixels of the map with values less than 10^{-4} are

forced to 0 and pixels with values greater than $1 - 10^{-4}$ are forced to 1. In Fig. 5.5(b) we can see how the apodisation process suppresses spurious structures at high-ℓ in the power spectrum of mask.

For galactic masks, $f_{\rm sky}$ decreases with frequency since the emission of the Galaxy becomes more and more important from 100 GHz to 217 GHz.

CO masks

For our analysis, CO emission has to be masked at 100 GHz and at 217 GHz since there are emission lines from molecular clouds at 115 GHz and 230 GHz that enter the bandwidth (sec.3.5). The CO masks are constructed by first smoothing the CO map to 30 or 120 arcminutes. Those two smoothed maps are then cut using a threshold in $K_{\rm cmb}$ units. The resulting masks are apodised at 15′. In Fig. 5.6(a) and 5.6(b) the two masks with different smoothing are shown. We have used both during the analysis but the final results have been obtained with the 30 arcmin smoothing mask that is more conservative and masks more structures at high latitude. In practice, the CO masks are almost completely covered by the Galactic one, causing a diminution of $f_{\rm sky}$ of only few %.

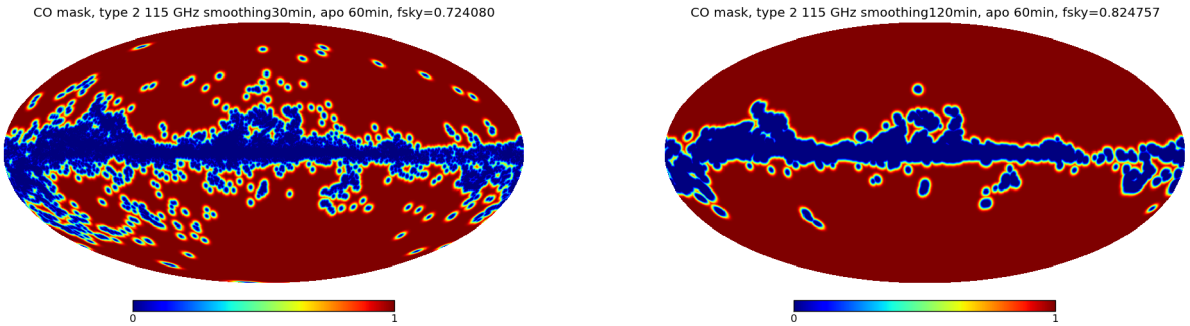

(a) (b)

Figure 5.6: CO masks at 100 GHz obtained smoothing the CO maps to 30 (a) and 120 (b) arcmin. Apodisation is at 60′. The masks have been producted by the *Planck* Consistency Group.

Point Source masks

The mask used in the 2013 analysis is the union of the point sources detected in the PCCS (appendix A.1) from frequencies 100 to 353 GHz (Planck Collaboration. XVI. 2014). This mask, as the ones used in the `Plik` likelihood for the analysis of the latest *Planck* data, are based on simple high flux cuts that are shown to remove too many knots that are not real point sources but rather Galactic structures or bright cirrus. Hence, in this thesis, we prefer to use the masks produced by the *Planck* consistency group (PSCG) where cirrus are first identify before constructing the mask.

Final combined masks

The characteristics of the masks that are used for the results presented in this thesis are summarized in Table 5.2. We show in Figure 5.7 the M72, M62 and M48 ($f_{\rm sky} = 72\%, 62\%, 48\%$) masks associated with the 100 GHz, 143 GHz and 217 GHz channels, respectively. These are not the only ones used; along the analysis other masks have been tested. A lot of test has been carried out using more conservative Galactic masks named M65, M55 and M40 for 100, 143 and 217 GHz respectively (and with $f_{\rm sky} = 65\%, 55\%, 40\%$). Their sky coverage is, however, bigger than the one used in the 2013 *Planck* analysis

where only the 58%, and 37.3% of the sky was retained at 100 GHz and 143 and 217 GHz , respectively. This choice was made to ensure the Galactic dust emission to be small. We postpone a discussion on the robustness of results to the mask choices to sec. 5.8.2.

mask name	Galactic mask	compact objects mask
M72	$f_{\rm sky} = 72\%$	100 GHz point source mask 100 GHz Conservative CO nearby galaxies masks
M62	$f_{\rm sky} = 62\%$	143 GHz point source nearby galaxies masks
M48	$f_{\rm sky} = 48\%$	217 GHz point source 217 GHz Conservative CO nearby galaxies masks

Table 5.2: Details of the masks used in the analysis. Galactic masks are apodised at 8°, while compact object masks are apodised at 15'.

5.4 Calculation of spectra: *Xpol*

We have seen in chapter 1 that the cross-spectrum of Eq. 1.89, is an unbiased estimator of the CMB power spectrum. If one decomposes directly the observed maps in harmonic space, the cross power spectrum is a biased estimator, where the bias is introduced by instrumental effects as the beams and the incomplete sky coverage. This estimator defined from decomposition of data in spherical harmonics

$$\tilde{C}_\ell^{\rm AB} \equiv \frac{1}{2\ell+1} \sum_{m=-\ell}^{\ell} d_{\ell m}^{\rm A} d_{\ell m}^{\rm B*} \tag{5.3}$$

is called cross *pseudo-*C_ℓ. The $d_{\ell m}$ are the decomposition into spherical harmonics of the observed maps. For example, for temperature

$$d_{\ell m} = \int d\hat{n} T^{\rm map}(\hat{n}) W(\hat{n}) Y_{\ell m}(\hat{n}), \tag{5.4}$$

where the window function $W(\hat{n})$, takes into account the mask and can be, in turn, decomposed into spin-0 spherical harmonics

$$W(\hat{n}) = \sum_{\ell m} w_{\ell m} Y_{\ell m}(\hat{n}). \tag{5.5}$$

To unbias the estimator of cross-power spectra from the maps, we use *Xpol*, an extension of the *Xspect* algorithm (Tristram et al. 2005) to polarisation. *Xpol* is a *pseudo-*C_ℓ based method which is able to compute analytically the error bars and the covariance matrix directly from data.

The cross-pseudo-C_ℓ of Eq. 5.3, for an experiment such as *Planck*, can be written in term of the true value C_ℓ as

$$\tilde{C}_\ell^{\rm AB} = \sum_{\ell'} M_{\ell\ell'}^{\rm AB} B_{\ell'}^{\rm A} B_{\ell'}^{\rm B} \langle C_{\ell'}^{\rm AB} \rangle, \tag{5.6}$$

where we remind that, considering independent detector, there is no contribution from noise. The B_ℓ are the effective beams window function (sec.5.4.1) and $M_{\ell\ell'}^{\rm AB}$ is the mode coupling matrix that depends only on the masks. For temperature, the $M_{\ell\ell'}$ calculation is described in Hivon et al. (2002) and involves

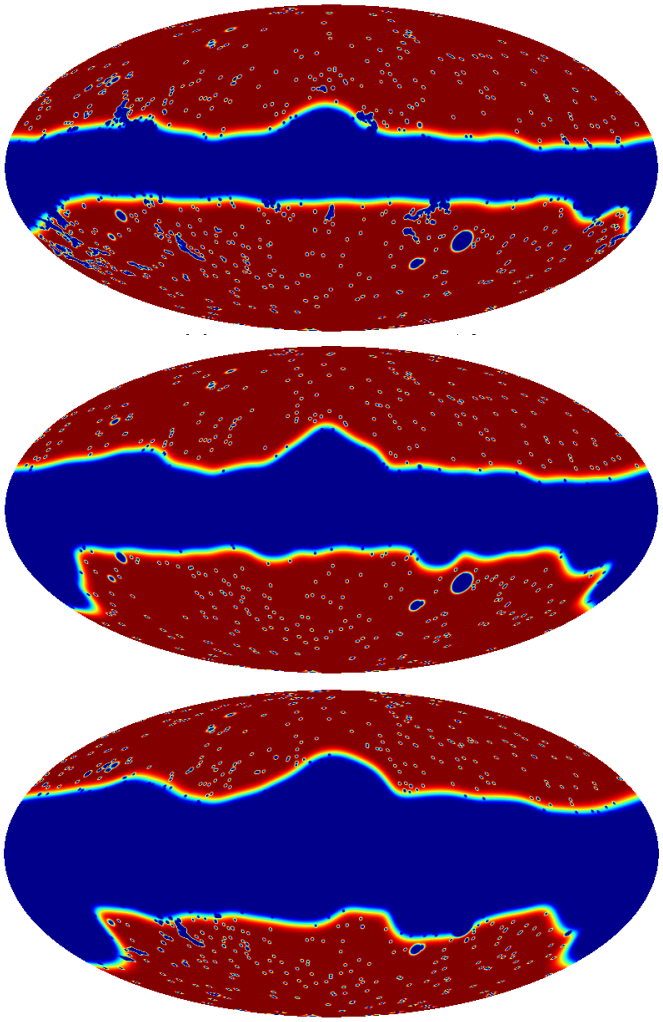

Figure 5.7: The M72, M62 and M48 masks. A combination of apodized Galactic mask and apodized compact objects mask is used at each frequency as described in Table 5.2.

product of integrals of three spherical harmonics that can be rewritten in term of 3j-wigner symbols. The generalisation to cross-spectra reads

$$M^{\rm AB}_{\ell_1\ell_2} = \frac{2\ell_2+1}{4\pi}\sum_{\ell_3}(2\ell_3+1)\tilde{W}^{\rm AB}_{\ell_3}\begin{pmatrix} \ell_1 & \ell_2 & \ell_3 \\ 0 & 0 & 0 \end{pmatrix}^2 \tag{5.7}$$

with $\tilde{W}^{\rm AB}_\ell = \sum_m w^{\rm A}_{\ell m} w^{\rm B*}_{\ell m}/(2\ell+1)$, the scalar cross-power spectrum of the masks.

The cross spectra $C^{\rm AB}_{\ell'}$ can be obtained solving Eq. 5.6, namely inverting the mode coupling matrix $M^{\rm AB}_{\ell\ell'}$.

In our analysis, using *Xpol* we also include polarisation. The extension to polarisation can be found in (Kogut et al. 2003).
For $\mathbf{C}^{\rm AB}_\ell = \left(C^{T_{\rm A}T_{\rm B}}_\ell, C^{E_{\rm A}E_{\rm B}}_\ell, C^{B_{\rm A}B_{\rm B}}_\ell, C^{T_{\rm A}E_{\rm B}}_\ell\right)$, the relation between pseudo-C_ℓ ($\tilde{C}_\ell$) and C_ℓ is a generalisation of Eq.5.6

$$\tilde{\mathbf{C}}^{\rm AB}_\ell = \mathcal{M}^{\rm AB}_{\ell\ell'}\mathbf{C}^{\rm AB}_{\ell'}, \tag{5.8}$$

where we have defined $\mathcal{M}_{\ell\ell'} = \mathbf{M}^{\rm AB}_{\ell\ell'} B^{\rm A}_{\ell'} B^{\rm B}_{\ell'}$ to include beam window functions. The coupling matrix that translate pseudo spectra to power spectra reads

$$\mathbf{M}^{\rm AB}_{\ell\ell'} = \begin{pmatrix} \Xi_{TT,TT} & 0 & 0 & 0 \\ 0 & \Xi_{EE,EE} & \Xi_{EE,BB} & 0 \\ 0 & \Xi_{BB,EE} & \Xi_{BB,BB} & 0 \\ 0 & 0 & 0 & \Xi_{TE,TE} \end{pmatrix} (\ell, \ell'; w_{\rm A}, w_{\rm B}) \tag{5.9}$$

where $\Xi_{TT,TT}$ is the matrix defined in Eq.5.7, and

$$\begin{cases} \Xi_{EE,EE}(\ell_1, \ell_2; {\rm A}, {\rm B}) &= \dfrac{2\ell_2+1}{16\pi} \displaystyle\sum_{\ell_3} (2\ell_3+1) \tilde{W}^{\rm AB}_{\ell_3} (1+(-1)^L)^2 \begin{pmatrix} \ell_1 & \ell_2 & \ell_3 \\ -2 & 2 & 0 \end{pmatrix}^2 \\ \Xi_{EE,BB}(\ell_1, \ell_2; {\rm A}, {\rm B}) &= \dfrac{2\ell_2+1}{16\pi} \displaystyle\sum_{\ell_3} (2\ell_3+1) \tilde{W}^{\rm AB}_{\ell_3} (1-(-1)^L)^2 \begin{pmatrix} \ell_1 & \ell_2 & \ell_3 \\ -2 & 2 & 0 \end{pmatrix}^2 \\ \Xi_{TE,TE}(\ell_1, \ell_2; {\rm A}, {\rm B}) &= \dfrac{2\ell_2+1}{8\pi} \displaystyle\sum_{\ell_3} (2\ell_3+1) \tilde{W}^{\rm AB}_{\ell_3} (1+(-1)^L) \begin{pmatrix} \ell_1 & \ell_2 & \ell_3 \\ 0 & 0 & 0 \end{pmatrix} \begin{pmatrix} \ell_1 & \ell_2 & \ell_3 \\ -2 & 2 & 0 \end{pmatrix} \end{cases} \tag{5.10}$$

with $L = \ell_1 + \ell_2 + \ell_3$.

From the six maps of sec. 5.2, we thus derive 15 cross-power spectra *i.e.* one 100x100, 143x143, 217x217 and four 100x143, 100x217, 143x217 *for each CMB mode* (TT, EE and TE).

Even if the final results are on HM maps, DS maps have been used all along the development of the final likelihood. We remind that we have two maps at each frequency. For DS, we could have used more maps. For example, the 5 and 6 individual DetSet maps of Table 1 of Planck Collaboration XV (2014) can also be used at 143 GHz and 217 GHz, respectively. Therefore, more cross-power spectra can be estimated at 100x143, 100x217, 143x143, 143x217 and 217x217. On the other hand, each map that we consider is significantly less noisy than any of the individual DS map at 143 GHz and 217 GHz. So we prefer to keep using only two maps with lower noise.

5.4.1 Beam window functions

In sec.3.3.2 we mentioned how the instrument beams can be reconstructed observing point-like bright sources as the planets. Beam convolution smooths small structures on the maps, resulting in a reduction of high-ℓ power in multipoles. A correct estimation of the power spectra of the measured maps, needs the inclusion of the effect of these beams, hence, in the power spectrum estimation, we correct for this using their respective beam window functions. The effective beam window functions B_ℓ account for the scanning strategy and the weighted sum of individual detectors performed to obtained the combined maps (Planck Collaboration. VII 2015). It is constructed from MC simulations of CMB convoluted with the measured beam on each TOI sample. Note that temperature and polarization beams are different. This is due to the fact that we consider a combination of PSB and SWB in temperature while only PSB are used in polarization. The uncertainties in the determination of the HFI effective beams come directly from the MC and can be described in terms of beam *eigenmodes*. It is possible to solve for the beam eigenmode amplitudes for each spectra used in the likelihood. In the 2013 analysis it was found that, in practice, only the first beam eigenmode for the 100×100 spectrum was relevant (Planck Collaboration. XVI. 2014). For the 2015 analysis, the higher quality estimation of the beams allows to avoid considering the beam eigenvalues in the likelihood. The results of this thesis have been obtained using the latest beam produced by the *Planck* collaboration.

5.4.2 Multipole range

The multipole ranges have been chosen to limit the contamination of the Galactic dust emission at low-ℓ and the noise at high-ℓ. Table 5.3 gives the multipole ranges, $[\ell_{\rm min}, \ell_{\rm max}]$, considered for each of the six cross-frequencies in TT, EE, TE and ET. Note that $\ell_{\rm max}$ increases with frequencies since the 217 GHz channel has smaller beams than the 100 GHz. Also $\ell_{\rm min}$ increase with frequency since the contamination from Galactic dust emission at low-ℓ follows the same trend (Fig. 3.11 and 3.12).

To allow consistency checks, we use the same ℓ-range for every datasets (HM, Yr, DS). The lower $\ell_{\rm min}$ in our analysis is 50 (higher than the $\ell_{\rm min} = 30$ of `Plik` and `CamSpec`). This choice keeps us safer in the Gaussian approximation for the likelihood function and avoids worsening residual dust contamination without any significant change in the results.

	100x100	100x143	100x217	143x143	143x217	217x217	n_ℓ
TT	[50,1200]	[50,1500]	[500,1500]	[50,2000]	[500,2500]	[500,2500]	9 556
EE	[100,1000]	[100,1250]	[400,1250]	[100,1500]	[400,1750]	[400,2000]	7 256
TE	[100,1200]	[100,1500]	[200,1500]	[100,1750]	[200,1750]	[200,2000]	8 806

Table 5.3: Multipole ranges used in the analysis. The numer of degree of freedom is $n_\ell = \ell_{\rm max} - \ell_{\rm min} + 1$. The full likelihood (TT+EE+TE) has $n_\ell = 25\,618$.

5.5 Covariance matrix

The 15 spectra that we have at disposal for each CMB mode of interest (TT,EE,TE), are not independent. We thus need an estimation of their correlation. Furthermore, as a result of the masking, we also expect each cross power spectrum to be correlated for adjacent multipoles. The complex resulting matrix $\Sigma^{\rm AB,CD}_{\ell\ell'}$ thus includes the correlations between the pseudo cross- power spectra (AB) and (CD) and multipoles ℓ and ℓ'.

5.5.1 A semi-analytical calculation

The matrix can be defined as

$$\Sigma^{\rm AB,CD}_{\ell\ell'} \equiv \langle \Delta\hat{C}^{\rm AB}_{\ell} \Delta\hat{C}^{\rm CD*}_{\ell'} \rangle = \left(M^{\rm AB}_{\ell\ell_1}\right)^{-1} \langle \Delta\tilde{C}^{\rm AB}_{\ell_1} \Delta\tilde{C}^{\rm CD*}_{\ell_2} \rangle \left(M^{\rm CD*}_{\ell'\ell_2}\right)^{-1} \tag{5.11}$$

with

$$\langle \Delta\tilde{C}^{\rm AB}_{\ell} \Delta\tilde{C}^{\rm CD*}_{\ell'} \rangle = \langle \tilde{C}^{\rm AB}_{\ell} \tilde{C}^{\rm CD*}_{\ell'} \rangle - \tilde{C}^{\rm AB}_{\ell} \tilde{C}^{\rm CD*}_{\ell'}. \tag{5.12}$$

This second order correlation term can be rewritten as

$$\langle \Delta\tilde{C}^{X_a X_b}_{\ell} \Delta\tilde{C}^{X_c X_d *}_{\ell'} \rangle = \frac{1}{(2\ell+1)(2\ell'+1)} \sum_{mm'} \left\{ \langle X^a_{\ell m} X^{c*}_{\ell' m'} \rangle \langle X^{b*}_{\ell m} X^{d}_{\ell' m'} \rangle + \langle X^a_{\ell m} X^{d*}_{\ell' m'} \rangle \langle X^{b*}_{\ell m} X^{c}_{\ell' m'} \rangle \right\}, \tag{5.13}$$

where we have used the notation $X = T, E$.
The actual calculation, implemented in *Xpol*, thus need the determination of all the first order correlation term. Some approximations are made along the calculation, similar to that of Efstathiou (2006).

In *Xpol*, the computations relies on data estimates. More specifically, we use a smooth version of each power spectrum such that the contributions from noise (correlated and uncorrelated), sky emission (from astrophysical and cosmological origin) and the associated *cosmic variance* are implicitly taken

into account in this computation. The coupling matrix is then used to translate the correlation between pseudo cross-power spectra into cross-power spectra (Eq. 5.11).

Note that TE and ET do not carry exactly the same information since computing T from the map A and E from the map B is not the same as computing E from the map A and T from B. Hence, both TE and ET blocks are computed individually and are eventually averaged.

The full covariance matrix has $25\,618 \times 25\,618$ elements (see Table 5.3). It is symmetric, definite positive and needs to be inverted to be used in the likelihood function. The inverse of the full covariance matrix is shown in Figure 5.8. It has been derived for the cross-power spectra estimated on HM maps. The condition number is $\sim 10^8$.

The expression for $\Sigma_{\ell\ell'}^{\mathrm{AB,CD}}$ can be simplified if the variation in multipole space of the CMB spectrum is smaller then the spectral width of the window function (i.e. small mask). In this case the matrix is dominated by the diagonal part and the effect of inhomogeneity in the sky coverage becomes a simple function of the i-th moment of the mask W (Hivon et al. 2002).

For illustration purpose we show the validity of this approximation in computing the error bars on a given cross spectra

$$\Sigma_{\ell\ell}^{\mathrm{AB,AB}} \equiv (\Delta C_\ell^{\mathrm{AB}})^2 \simeq \frac{1}{f_{\mathrm{sky}}^{\mathrm{AB}}} \left[(C_\ell^{\mathrm{AB}})^2 + C_\ell^{\mathrm{AA}} C_\ell^{\mathrm{BB}} \right] \tag{5.14}$$

where $f_{\mathrm{sky}}^{\mathrm{AB}}$ is estimated from the first moments of the mask used for A and B. The cross spectra C_ℓ^{AB} contain only signal but the auto-spectra C_ℓ^{AA} and C_ℓ^{BB} contain a contribution from noise N_ℓ^{A} and N_ℓ^{B}, respectively. Eq. 5.14 can thus be rewritten as

$$(\Delta C_\ell^{\mathrm{AB}})^2 \simeq \frac{1}{f_{\mathrm{sky}}^{\mathrm{AB}}} \left[2(S_\ell)^2 + S_\ell (N_\ell^{\mathrm{A}} + N_\ell^{\mathrm{B}}) + N_\ell^{\mathrm{A}} N_\ell^{\mathrm{B}} \right] \tag{5.15}$$

In Fig. 5.9 the various terms of the approximation of Eq. 5.15 are shown. Their sum (in red) is plotted together with the analytical computation from *Xpol* (in black). As expected, the approximation works better, both in temperature and in polarisation, at 100 GHz than at 217 GHz since the sky coverage is larger. We also show the results from the simulations to give an idea of the level of accuracy of both the analytical and the approximate solutions. Validation on simulations is discussed further in sec. 5.5.2.

5.5.2 Validation on simulations

The precision of the semi-analytical estimation has been tested using Monte-Carlo simulations. The procedure, uses the *Planck* 2013 ΛCDM best fit to generate the signal. A CMB map is then generated on top of which we add realistic noise. For each simulation, this procedure is repeated six times using the beams and the variance map associated to each of the six maps. The same mask used for the analysis are then applied and cross-power spectra are computed. A total of $\sim 15\,000$ sets of cross-power spectra have been produced. When comparing the diagonal of the covariance matrix from the analytical estimation with the corresponding simulated variance, a precision better than a few percents is found. This is illustrated in Fig 5.10 for the 143-143 GHz block. For a Gaussian likelihood, this percents precision on the covariance matrix do not bias the results and has negligible consequences on the final error bars.

5.5.3 Effect of PS mask on the matrix

As can be noted in Fig 5.10, the ratio between the estimation of the diagonal of the covariance matrix from simulation and its analytical calculation shows an oscillation pattern. This is due to the the point source (PS) mask contribution. We remind that we use the PSCG mask, from the consistency working

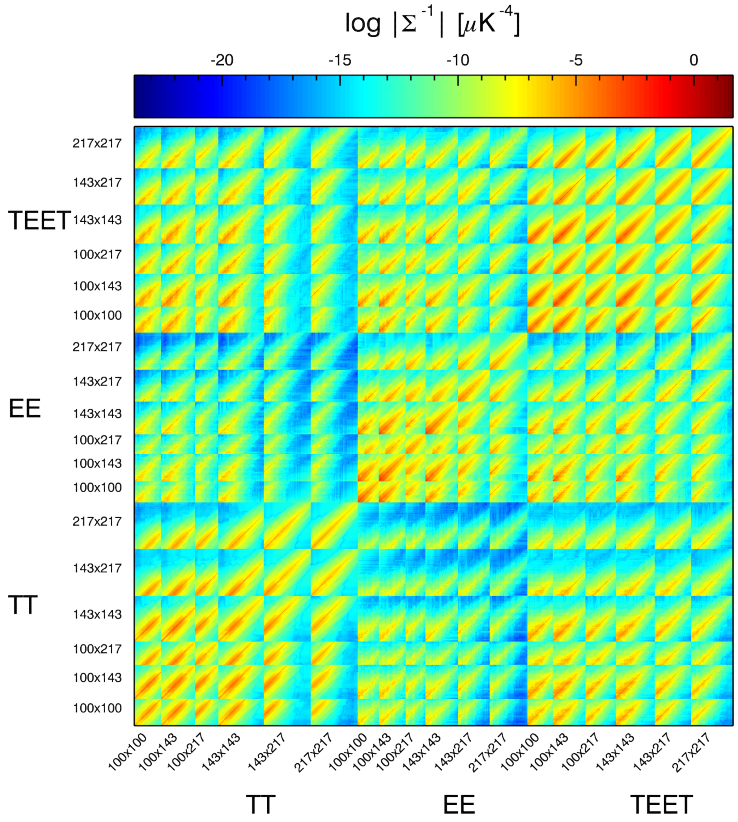

Figure 5.8: The inverted full covariance matrix that is used in the likelihood analysis. Each block describes a different combination of cross-spectra and has different dimensions depending on the different $[\ell_{\rm min}, \ell_{\rm max}]$ ranges of Table 5.3. We also recognise the different blocks for CMB modes, TT, EE and TEET (the combination of TE and ET).

group. The choice for the PS has consequences also on the modelling of the residual thermal dust emission (sec.5.6.1). In Fig. 5.11 we compare simulations and analytical calculation with or without the PS masks. For the cross involving the 217 GHz channel, there is an additional effect of the PS masks: the approximations made in the analytical result overestimate the error bars up to a maximum of 5 % effect.

The significance of the effect of the PS masks changes with the PS masks being considered. We remind that

- the PCCS mask, used in the 2013 analysis, is the union of the point sources detected from frequencies 100 to 353 and based on simple high flux cut;
- the PSCG is the mask that we use. It has been produced by the *Planck* consistency group to avoid masking cirrus at high latitude.

In Fig. 5.12 we compare the effect found using our masks with the results of the `Plik` likelihood if the PCCS based mask are used. The oscillation pattern follow the signal in both cases but the amplitude is reduced when the PSCG is used.

This shows that the analytical estimation of the covariance matrix has difficulties in handling the specific shape of the PS mask. These tests lead to the conclusion that the PSCG mask, with its proper treatment of the cirrus and a smaller numbers of holes in the mask, gives an analytical estimate of higher precision.

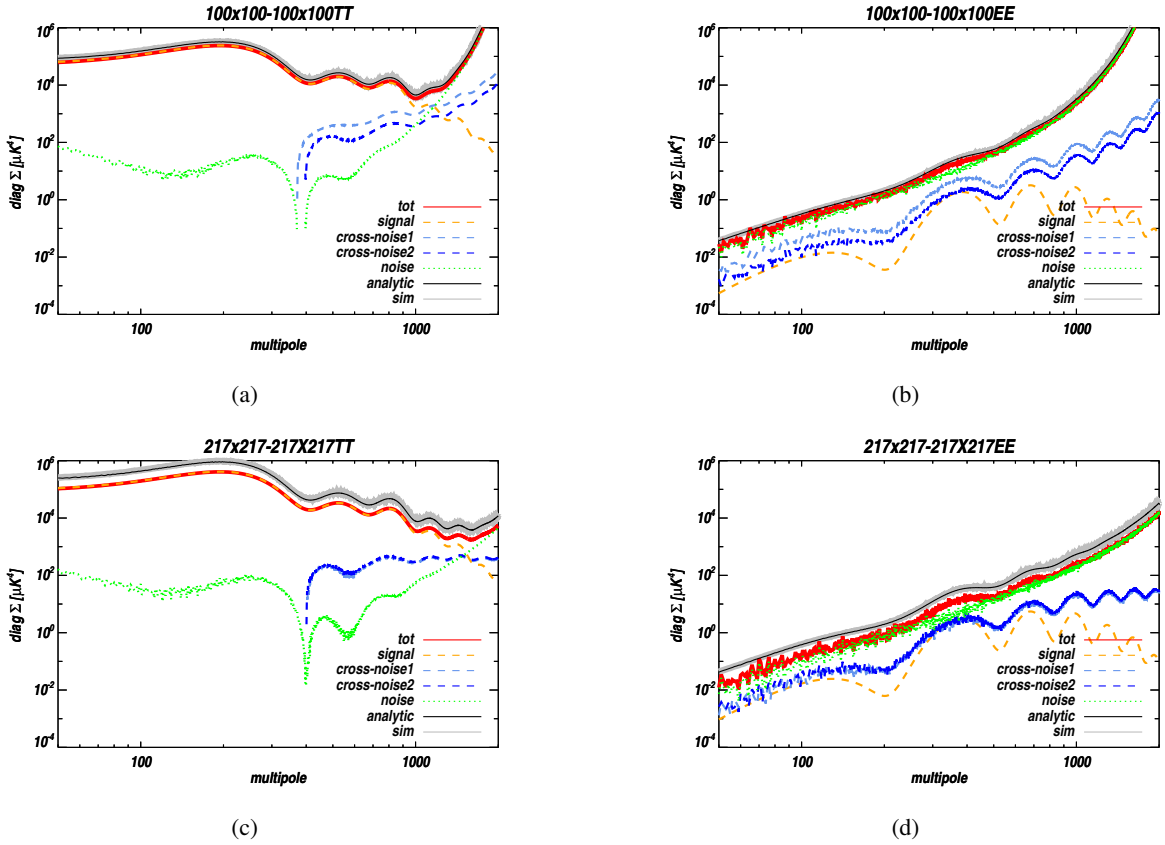

Figure 5.9: The analytic computation of the diagonal of the covariance matrix Σ (in black) is compared to the approximation of Eq.5.14 (in red). The various terms of the equation are also shown. In (a) is reported the error bars for the cross 100×100 in temperature and in (b) in polarisation EE. $f_{\rm sky}^{\rm AB}$ in this case is simply the $f_{\rm sky}$ used for the 100 GHz (72%). The same is shown in (c) and (d), for TT and EE respectively, for the cross 217×217, with $f_{\rm sky}$=48%. In all the figures is also shown (light grey) the results from simulation discussed in sec. 5.5.2.

5.6 Residual foregrounds

The foreground emissions present in the range of frequencies covered by the *Planck* satellite have been introduced in sec.3.5.
The masking strategy discussed in sec.5.3, and an appropriate choice of ℓ-range, help in reducing their impact. There are, however, still some residual contaminations left. For a proper estimation of the CMB signal, and thus of the cosmological parameters, they need to be properly taken into account *at the power spectrum level*.

Generally speaking one expects residual diffuse Galactic foregrounds to dominate at low-ℓ, with a minimum in the 70 to 100 GHz range, while extragalactic residuals dominates at multiple larger than ~200 (Planck Collaboration. I. 2014).

In temperature, for the three frequencies of interest in this thesis (100 GHz, 143 GHz, and 217 GHz), free-free and synchrotron can be safely neglected. On the contrary, thermal dust emission is the most important foreground to deal with, together with unresolved PS, CIB, tSZ, kSZ and the cross correlation between tSZ and CIB.

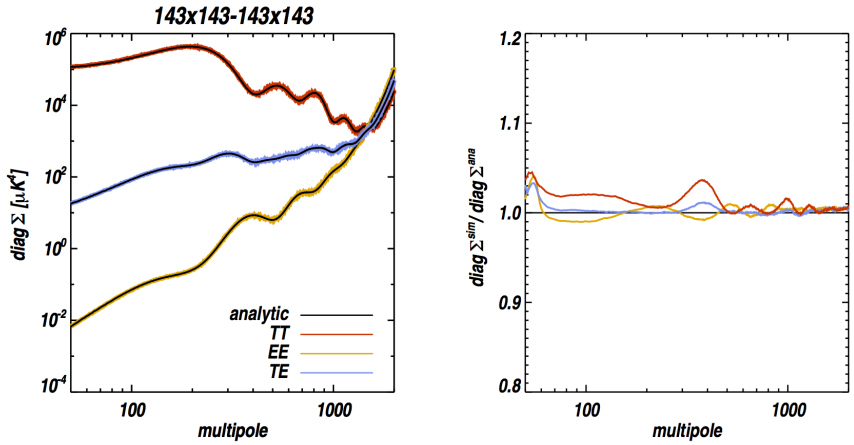

(a)

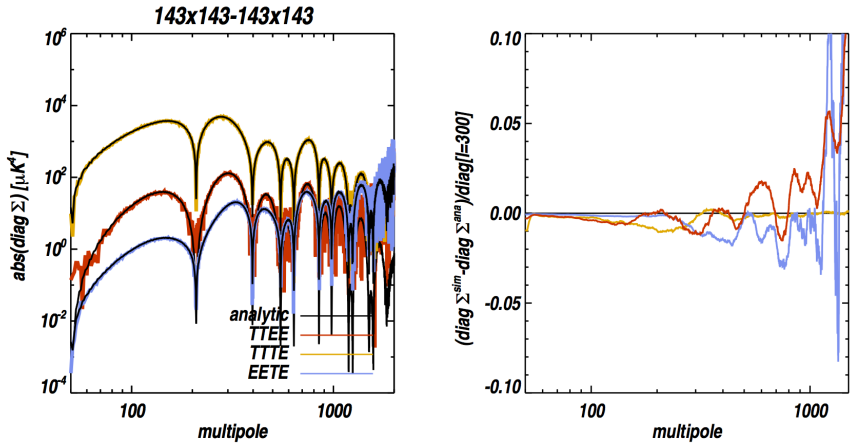

(b)

Figure 5.10: The analytical estimation of the covariance matrix $\Sigma^{\mathrm{AB,CD}}_{\ell\ell'}$ is validated on simulations. The covariance matrix is estimated from 15.000 simulations (see text). As an example, the results are shown for the diagonal in multipole space for the 143×143-143×143 block. (a) *Left*. The diagonal TT-TT (red), TE-TE (blue) and EE-EE (yellow) extracted from simulations are plotted against the analytic result (black). *Right*. Here is reported the ratio between the results from simulations and the analytic results, color coded as before. The agreement is at % level. The oscillation pattern is due to the effect of the PS mask (sec.5.5.3). (b) *Left*. Here are shown the off-diagonal block for the CMB modes, i.e. the TT-EE (red), TT-TE (yellow) and EE-TE (blue), again with the analytical result in black. *Right*. We report the difference between the simulation and the analytic results rescaled with respect to the value at $\ell = 300$.

The model used to describe the *Planck* TT power spectra thus reads:

$$\begin{aligned} C_\ell^{\mathrm{model},T_iT_j} \quad \propto \quad & C_\ell^{CMB,TT} + A_{dust}^{TT} C_\ell^{\mathrm{dust},T_iT_j} + A_{\mathrm{PS}}^{T_iT_j} \\ & + A_{CIB} C_\ell^{\mathrm{CIB},T_iT_j} + A_{\mathrm{tSZ}} C_\ell^{\mathrm{tSZ},T_iT_j} \\ & + A_{\mathrm{tSZxCIB}} C_\ell^{\mathrm{tSZxCIB},T_iT_j} + A_{\mathrm{kSZ}} C_\ell^{\mathrm{kSZ}} \end{aligned} \tag{5.16}$$

In polarization, the only relevant foreground is the polarised dust. Synchrotron emission is known to

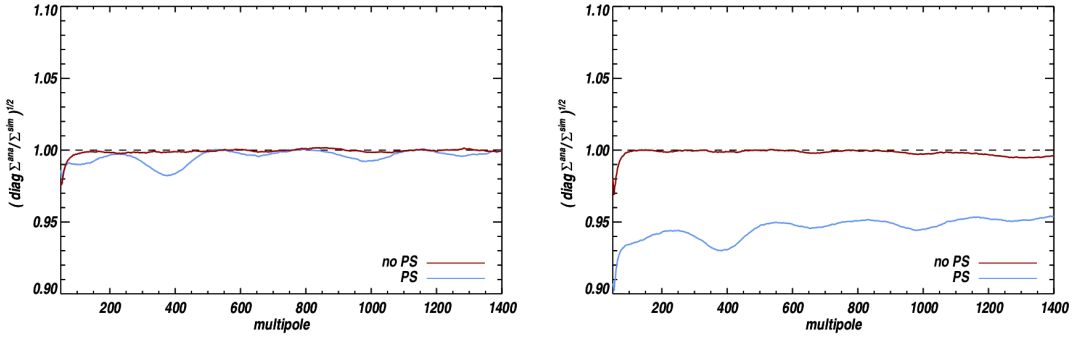

(a) (b)

Figure 5.11: Ratio between the diagonal of the covariance matrix extracted from simulations and the analytical calculation. In red is shown the result using a different set of simulations that does not include the PS masks; in blue the result from simulations including the PS masks. In (a) we consider the 100×100-100×100 block in temperature. In (b) the 217×217-217×217 block, again in temperature. In this case the PS mask induce also an additional effect besides the signal-like oscillation: the error bars are underestimated by a 5%.

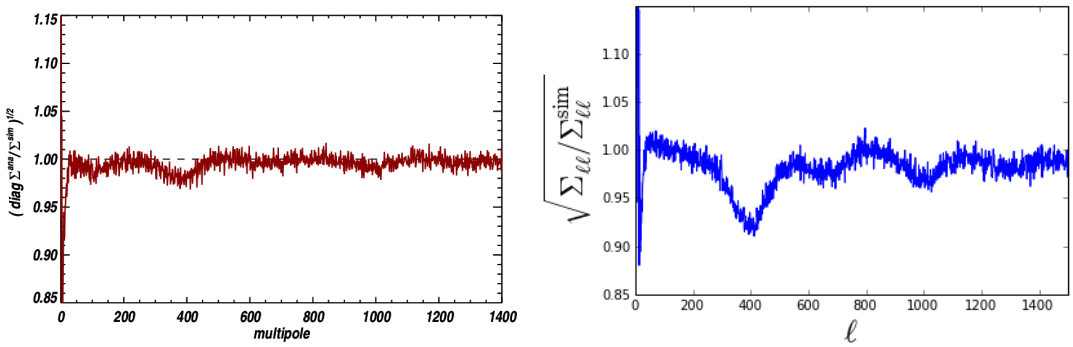

(a) (b)

Figure 5.12: Ratio between the estimation of the diagonal of the covariance matrix from simulations and the analytical calculation. In (a) is used the HiLLiPOP likelihood and the PSCG masks for the point sources. In (b) is shown the result using the Plik likelihood and the PCCS masks (Figure from M.Millea).

be significantly polarized but it scales with frequency following a power law with spectral index close to -3. It is then subdominant in *Planck* HFI channels and we can neglect its contribution (e.g. Tucci et al. (2005)). The contribution of polarized point sources is also expected to be negligible (Tucci & Toffolatti 2012).

Hence, the EE and TE power spectra models simply read:

$$C_\ell^{\rm model,E_iE_j} \propto C_\ell^{CMB,EE} + A_{dust}^{EE} C_\ell^{\rm dust,E_iE_j}, \tag{5.17}$$

$$C_\ell^{\rm model,T_iE_j} \propto C_\ell^{CMB,TE} + A_{dust}^{TE} C_\ell^{\rm dust,T_iE_j}. \tag{5.18}$$

In HiLLiPOP, we use physically motivated templates of foreground emission power spectra, based on *Planck* measurements. We assume a C_ℓ model for each foreground with a fixed spectral and ℓ dependency and rescale it with a free parameter A that should be equal to unity in the perfect case. Only the residual

point source are treated differently. An independent parameter fits their free amplitude at each cross-frequency.

The next sections are dedicated to a description of the various models and their physical basis.

5.6.1 Galactic dust

For the *Planck* HFI frequency used here, at low to intermediate multipoles, the dominant foreground is the residual Galactic emission both in temperature and in polarization. In Planck Collaboration XV (2014) and Planck Collaboration. Int XXII. (2014) residual Galactic dust emission is find to be compatible with a power law in multipoles, both in temperature and polarization. Our templates are built following the same methodology presented in Planck Collaboration Int. XXX (2014).

For the temperature, we first estimate the TT half-mission cross-power spectra at 353 GHz in different masks combinations (Fig. 5.13) and then subtract the best-fit CMB power spectrum from the Nominal mission data analysis of Planck Collaboration. XVI. (2014). The CIB power spectrum (see Planck Collaboration XXX 2014) is further subtracted. A good fit is obtained on the resulting power spectra using the power-law model $A\ell^{\alpha} + B$, where B describes the Poisson contribution from unresolved point sources. Both A and B depend on the mask used. It is worth stressing that compatibility of the shape of the Galactic dust component with a power law is restricted to a particular choice of point source mask. As described in sec. 5.5.3, the PCCS masks remove some Galactic structures and bright cirrus generating a knee in the residual dust power spectra around $\ell \sim 300$ (Fig. 5.14). The PSCG masks from the Consistency Group used in this analysis, treat more properly these cirrus and do not show this bias[1].

For EE and TE we again estimate half-mission cross-power spectra at 353 GHz in the different combinations of masks (Fig. 5.15 and Fig. 5.16) and then subtract the best-fit CMB power spectrum. We do not have contribution from CIB in polarization and polarized point sources are negligible[2]. Hence, a simple power-law model $A\ell^{\alpha}$ is considered. The values of α fitted are in agreement with the ones from Planck Collaboration Int. XXX (2014), although slightly flatter then the ones for temperature at high ℓ and at high frequency (Planck Collaboration. XVI. 2014).

Once A and α are obtained for each mask combination and for each mode, the templates for Eq. 5.16, Eq. 5.17 and Eq. 5.18 are constructed as follows:

$$C^{X_i X_j}_{\ell,\mathrm{dust}} = A \times c_{\nu_i} \times c_{\nu_j} \times \ell^{\alpha} \tag{5.19}$$

with $c_{\nu_i} = 353\ \mathrm{GHz} \rightarrow i$ the coefficients for rescaling from the 353 GHz to the frequency of interest. They are estimated using a map domain regression, at large angular scales, of the 353 GHz map after CMB removal. The extrapolated factors are given in Table 5.4 and are compatible with Planck Collaboration. Int XXII. (2014). When the template of Eq. 5.19 is used in the likelihood, it is multiplied by a single scaling parameter for each mode A^{TT}_{dust}, A^{EE}_{dust} and A^{TE}_{dust}. We expect these parameters to be compatible with one. For the estimation of cosmological parameters we use Gaussian priors on these amplitudes 1 ± 0.2, that reflect the uncertainty of the model (sec. 5.8.4).

[1] If we try to model dust using a simple power law in the case of the knee feature, there are consequences of this improper treatment on the estimation of cosmological parameters (e.g. shifts are up to 0.6σ for ω_b).

[2] In Planck Collaboration Int. XXX (2014) PCCS mask is used in order to prevent the brightest polarized sources from producing ringing in the power spectrum estimation, while avoiding the removal of dust emitting region and their statistical contribution to the angular power spectrum. We keep our PSCG masks for polarization

		$c_{100\ GHz}$	$c_{143\ GHz}$	$c_{217\ GHz}$
HiLLiPOP	I	0.01957	0.03982	0.13185
	Q/U	0.01703	0.03605	0.12498
Planck Collaboration. Int XXII. (2014)	I	0.0199	0.0387	0.1311
	Q/U	0.0179	0.0384	0.1263

Table 5.4: Values for the c_{ν_i} coefficients for rescaling the 353 GHz to the frequency of interest.

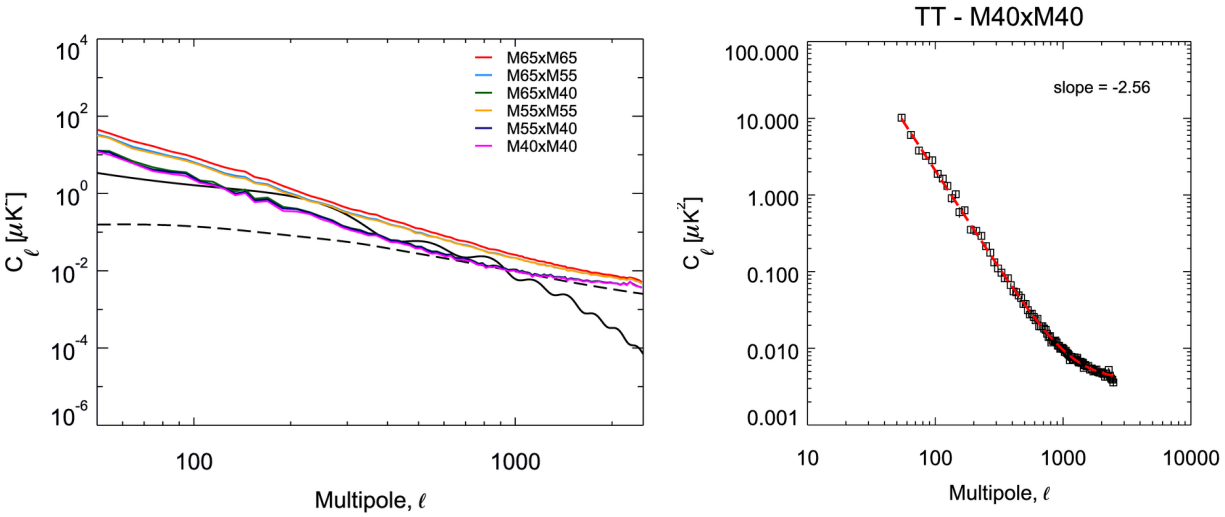

(a) (b)

Figure 5.13: (a) 353x353 TT power spectra. The dashed black line is the 353x353 CIB power spectrum and the black line is the CMB TT power spectrum. The color lines are the CMB and CIB subtracted 353x353 power spectra estimated for different set of masks as defined in sec. 5.3. (b) Fit of the CMB and CIB subtracted 353x353 TT power spectrum estimated for M40xM40. The black squares are the data and the red dashed line is the best fit to these data.

5.6.2 Unresolved point sources

Extragalactic radio sources contribute significantly to temperature fluctuations only at small angular scales. At frequencies higher than 100 GHz, the contribution of dusty galaxies should also be taken into account (Tucci et al. 2005). Due to its limited angular resolution, *Planck* cannot significantly constraint these foregrounds. To avoid modelling errors, dusty and radio sources are not considered separately but included in a scale independent term, $A_{\rm PS}^{T_iT_j}$, for each cross-frequency. In other words, we consider a Poisson-like flat power spectrum.

In sec.5.9, the agreement between the levels of unresolved PS expected from source counts and our Poisson terms amplitudes is discussed.

In polarization we can instead safely neglect point source contributions both from radio and dusty galaxies (Tucci et al. 2004).

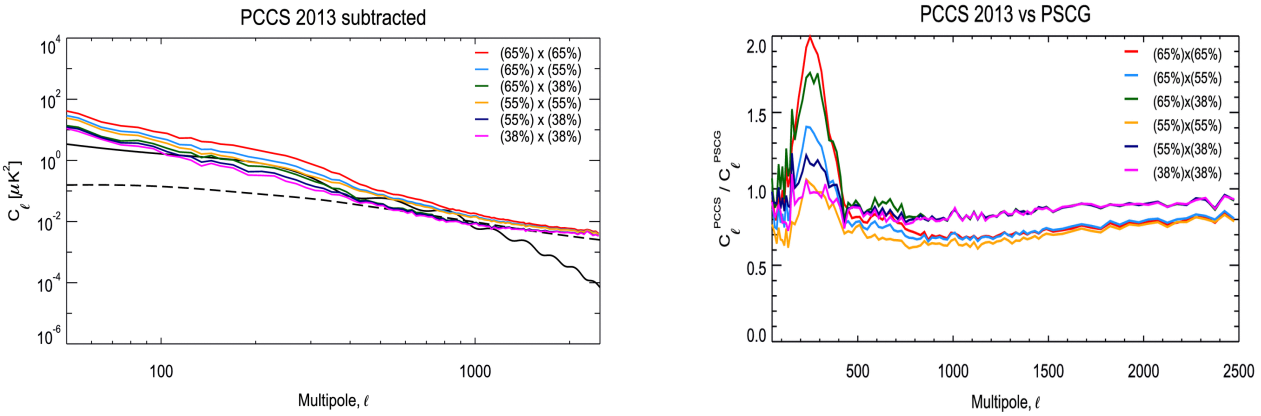

(a) (b)

Figure 5.14: (a) Effect of the PCCS 2013 mask on the shape of the power spectra of the dust. We see a knee in the in the power spectra around $\ell \sim 300$. (b) The $\ell \sim 300$ is clearly visible if we plot the ratio of the power spectra using the PCCS or the PSCG.

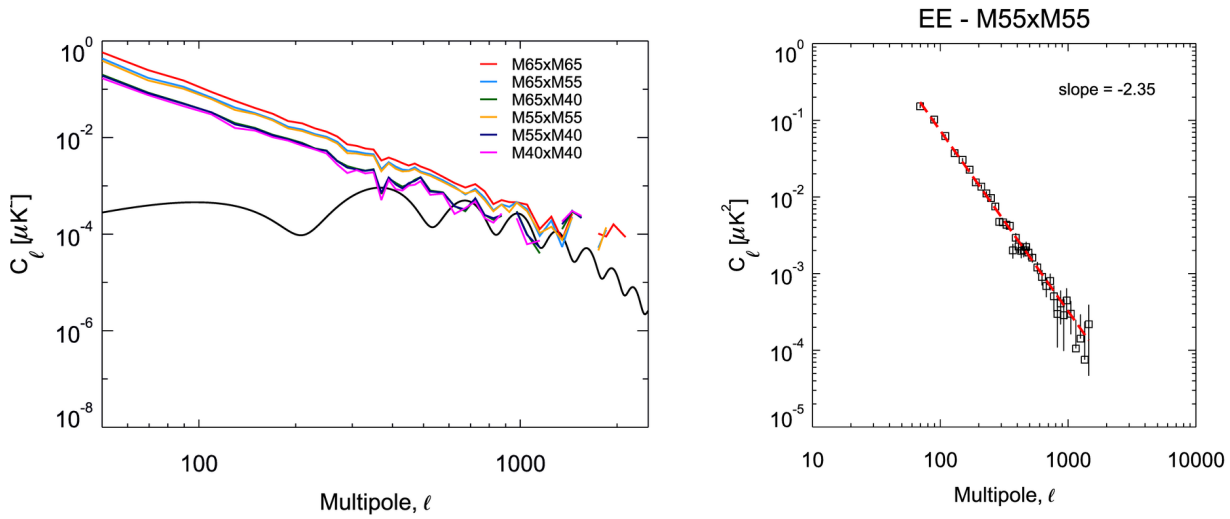

(a) (b)

Figure 5.15: (a) 353x353 EE power spectra. The black line is the CMB EE power spectrum. The color lines are the CMB subtracted 353x353 EE power spectra estimated for different set of masks as defined in sec. 5.3. (b) Fit of the CMB subtracted 353x353 EE power spectrum estimated for M55xM55. The black squares are the data and the red dashed line is the best fit to these data.

5.6.3 Cosmic Infrared Background

The frequencies above 353 GHz are dominated by Galactic and extragalactic infrared emission. The extragalactic component is the CIB produced by thermal radiation of dust heated by UV emission from young stars (sec.3.5). The CIB constitutes an important foreground, especially at 217 GHz, that needs to be treated properly at power spectrum level in our analysis. The CIB power spectrum templates that we

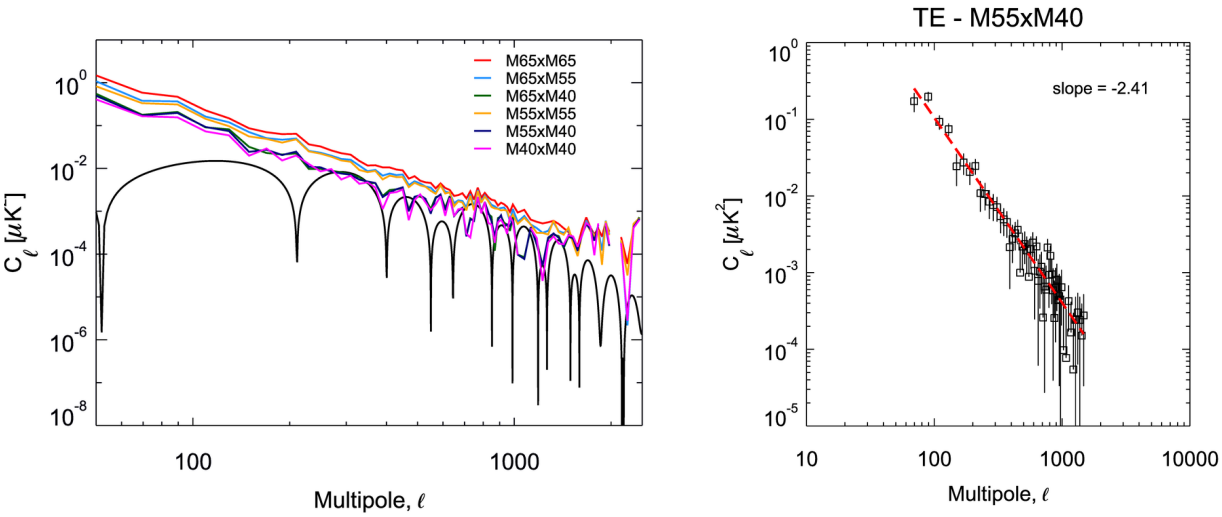

Figure 5.16: Left: 353x353 TE power spectra. The black line is the CMB TE power spectrum. The color lines are the CMB subtracted 353x353 TE power spectra estimated for different set of masks as defined in Table 5.2. Right: fit of the CMB subtracted 353x353 TE power spectrum estimated for M55xM40. The black squares are the data and the red dashed line is the best fit to these data.

use at each cross frequencies, are based on a halo model linking directly the galaxy luminosity to their host dark matter halo mass. They are presented in Planck Collaboration XXX (2014).

The halo model formalism, that is used also for the tSZ and the tSZ-CIB models described in sec.5.6.4 and 5.6.6 respectively, has the general expression (e.g. Planck Collaboration. XXIX. (2015))

$$C_\ell = C_\ell^{\mathrm{AB,1h}} + C_\ell^{\mathrm{AB,2h}}, \tag{5.20}$$

where A and B stand for tSZ effect or CIB emission, $C_\ell^{\mathrm{AB,1h}}$ is the 1-halo contribution, and $C_\ell^{\mathrm{AB,2h}}$ is the 2-halo term. The 1-halo term $C_\ell^{\mathrm{AB,1h}}$ is computed as

$$C_\ell^{\mathrm{AB,1h}} = 4\pi \int \mathrm{d}z \frac{\mathrm{d}V}{\mathrm{d}z\mathrm{d}\Omega} \int \mathrm{d}M \frac{\mathrm{d}^2\mathrm{N}}{\mathrm{d}M\mathrm{d}V} W_\mathrm{A}^{\mathrm{1h}} W_\mathrm{B}^{\mathrm{1h}}, \tag{5.21}$$

where $\frac{\mathrm{d}^2\mathrm{N}}{\mathrm{d}M\mathrm{d}V}$ is the dark-matter halo mass function from Tinker et al. (2008), $\frac{\mathrm{d}V}{\mathrm{d}z\mathrm{d}\Omega}$ the comoving volume element, and $W_{\mathrm{A,B}}^{\mathrm{1h}}$ is the window function that accounts for selection effects and total halo signal. The contribution of the 2-halo term, $C_\ell^{\mathrm{AB,2h}}$, accounts, instead, for correlation in the spatial distribution of halos over the sky.

For the CIB, the 2-halo term (i.e. the term that considers galaxies belonging to two different halos), is dominant at low and intermediate multipoles and is very well constrained by *Planck*. The 1-halo term, instead, is not well measured, and is degenerate with the shot noise. Hence, in Planck Collaboration XXX (2014) strong priors on the shot noises have been used to get the 1-halo term.
The power spectra template are available in Jy^{2}sr^{-1} units with the IRAS convention $\nu I(\nu)$ =cst. To convert them in $\mu\mathrm{K}^2_{\mathrm{CMB}}$ units we use the values in Table 5.5, taken from a slightly updated version of Table 6 in Planck Collaboration IX (2014). Then, our C_ℓ^{CIB} model is simply the C_ℓ CIB template, rescaled with a single parameter A_{CIB}, that is expected to be one (sec.5.8.4).

$$C_\ell^{X_iX_j,\ \mathrm{CIB}} = A_{\mathrm{CIB}} C_\ell^{X_iX_j,\ \mathrm{temp}} (c_i c_j)^{-1} \tag{5.22}$$

	$c_{100\ GHz}$	$c_{143\ GHz}$	$c_{217\ GHz}$
$U_{C\ IRAS}$ [MJy sr$^{-1}K^{-1}_{\rm CMB}$]	244.1	371.66	483.485

Table 5.5: Values for the c_{ν_i} coefficients for converting MJysr^{-1} units in $K_{\rm CMB}$ units for the frequency of interest (see Table 6 in Planck Collaboration IX (2014)).

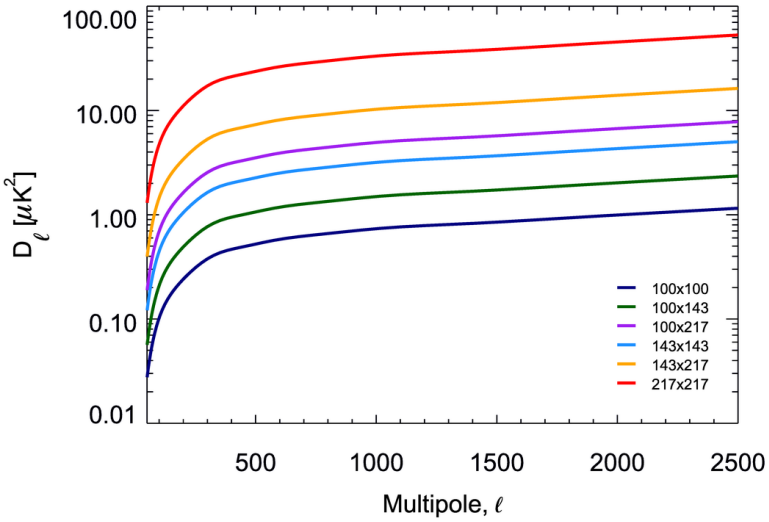

Figure 5.17: The CIB cross power spectra templates used in this analysis.

The cross power spectra templates are reported in Fig. 5.17. Note that at 100 GHz, the CIB is negligible, while $C_\ell^{217x217,\rm CIB}$ is 63.6 $\mu K^2_{\rm CMB}$ at $\ell = 3000$.

5.6.4 Unresolved thermal Sunyaev Zel'dovich (tSZ) component

At *Planck* intermediate frequencies, from 70 to 217 GHz, although the sky emission is dominated by the CMB, we are slightly sensitive to the distortion of the CMB black body caused by the tSZ effect (sec.1.3.6 and 3.5). To give an idea of the order of magnitude of the effect, the ground based CMB experiment SPT and ACT (sec. 6.3) find, in D_ℓ at ℓ=3000, a contribution of 9 μK$^2_{\rm CMB}$ at 100 GHz and 4 μK$^2_{\rm CMB}$ at 143 GHz. The effect is zero at 217 GHz. The template used is based on Tinker et al. (2008) for the mass function and Arnaud et al. (2010) for the universal pressure profile. It contains both the 1 and 2-halo terms defined in sec. 5.6.3 (Taburet et al. 2011). A full description can be found in Planck Collaboration. XXII. (2015). In Table 5.6 we report the conversion factors for the Compton parameter of Eq.1.101 to CMB temperature ($K_{\rm CMB}$), for each frequency channel of interested, after integrating over the instrumental bandpass. These numbers are taken from Table 1 of Planck Collaboration. XXII. (2015). The $C_\ell^{\rm tSZ}$ model used in the likelihood is normalised at 143 GHz and rescaled with a single parameter $A_{\rm tSZ}$, that is expected to be one.

$$C_\ell^{X_iX_j,\ \rm tSZ} = A_{\rm tSZ} C_\ell^{\rm tSZ,143} \frac{c_{\nu_i} c_{\nu_j}}{c^2_{143\ \rm GHz}}. \tag{5.23}$$

The templates are reported, for each cross frequency, in Fig. 5.18 (in D_ℓ). Note that, in the `Plik` likelihood is fitted instead the contribution of the tSZ to $D^{143x143}_{\ell=3000}$ at 143 GHz in μK$^2_{\rm CMB}$(Planck Collaboration

	$c_{100\ GHz}$	$c_{143\ GHz}$	$c_{217\ GHz}$
$T_{\rm CMB}\ g(\nu)\ K_{\rm CMB}$	-4.031	-2.785	0.187

Table 5.6: Values for the c_{ν_i} coefficients for converting MJysr^{-1} units in $K_{\rm CMB}$ units for the frequency of interest (see Table 6 in Planck Collaboration IX (2014)).

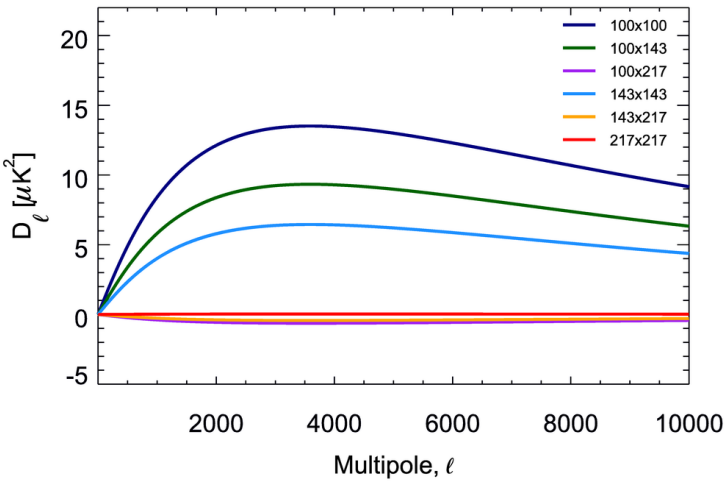

Figure 5.18: The tSZ power spectra templates. A global scaling, $A_{\rm tSZ}$, is let free in the analysis

A13 2015), and the template considered is different. As in the 2013 analysis, they use the Efstathiou & Migliaccio (2012) template with $\epsilon = 0.5$. However, cosmological parameter estimation is not very sensitive to the tSZ effect, and that templates are all very similar at $\ell < 2000$ and can not be distinguish by *Planck* alone data. In Planck Collaboration. XIII. (2015), a prior on the SZ effect coming from ACT and SPT data is used. This is described further in chapter 7.

5.6.5 Kinetic Sunyaev-Zeldovich (kSZ) component

As described in sec.1.3.6, the peculiar velocities of the clusters containing hot electron gas induce a frequency independent Kinetic Sunyaev-Zeldovich effect. The theory gives only upper bounds: the kSZ is believed to be $D_\ell < 7 K^2_{\rm CMB}$ at $\ell = 3000$. We use the template from M.Douspis and N.Aghanim (Fig. 5.19), and we rescale it with a parameter $A_{\rm kSZ}$

$$C_\ell^{\rm kSZ} = A_{\rm kSZ}\left(C_\ell^{\rm hKSZ} + C_\ell^{\rm pKSZ}\right), \tag{5.24}$$

where:

- $C_\ell^{\rm hKSZ}$ is the homogeneous kSZ, arising when the reionisation is complete. It is taken from Shaw et al. (2012);
- $C_\ell^{\rm pKSZ}$ is the contribution from the patchy (or inhomogeneous) reionisation that arises before the reionisation is complete from the proper motion of ionised bubbles around emitting sources (Aghanim et al. 1996). The power spectrum is taken from Battaglia et al. (2013).

The `Plik` likelihood considers only the homogeneous part. As for the tSZ, *Planck* alone can only put loose constraints on this effect so the difference does not impact parameter estimation.

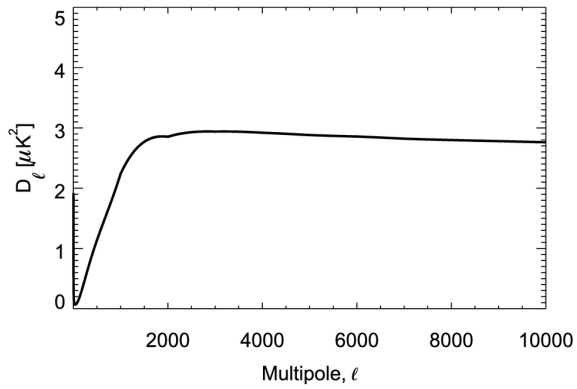

Figure 5.19: The frequency independent kSZ template from the *Planck* Consistency Working Group.

5.6.6 tSZ-CIB correlation

The halo model can naturally account for the correlation between two different source populations, each tracing the underlying dark matter but having different dependence on host halo properties (Addison et al. 2012). An angular power spectrum can thus be extracted for the correlation between unresolved clusters contributing to the tSZ effect, and the dusty sources that make up the CIB. While this latter has a peak in redshift distribution between $z \simeq 1$ and $z \simeq 2$, and is produced by galaxies in dark matter halos of 10^{11}-10^{13} $M_\odot$, the tSZ is mainly produced by local ($z < 1$) and massive dark matter halos (above 10^{14} $M_\odot$). This implies that the CIB and tSZ distributions present a very small overlap for the angular scales probed by *Planck*, and it is thus hard to detect (Planck Collaboration. XXIX. 2015). There are, however, constraints provided by the ground based CMB experiments ACT and SPT. The ACT collaboration set upper limits on the tSZ-CIB cross correlation $\rho < 0.2$ (at 95% C.L) (Dunkley et al. 2013) and the SPT collaboration reported $0.113^{+0.057}_{-0.051}$ (68% C.L) (George et al. 2014); a zero correlation is disfavoured at 99% confidence level.

We use the template from P.Serra (Fig. 5.20). The tSZ power spectrum template is based on Efstathiou & Migliaccio (2012), while for the CIB is used the template described in sec.5.6.3. The power spectra template are available in Jy^2sr^{-1} units with the convention $\nu I(\nu)$ =cst. To convert them in μK^2_{CMB} units we use again the values of Table 5.5.

We rescale with a single parameter $A_{\rm tSZxCIB}$

$$C_\ell^{X_iX_j,\ {\rm tSZxCIB}} = A_{\rm tSZxCIB} C_\ell^{X_iX_j,\ {\rm temp}} (c_i c_j)^{-1} \tag{5.25}$$

5.7 The likelihood function

Now that maps, ℓ-ranges, masks and residual foreground models have been described, we write down the likelihood function used in the analysis. First, we reduce the 15 cross-power spectra into 6 frequency cross-power spectra (100×100, 100×143, 100×217, 143×143, 143×217 and 217×217) in TT, EE,

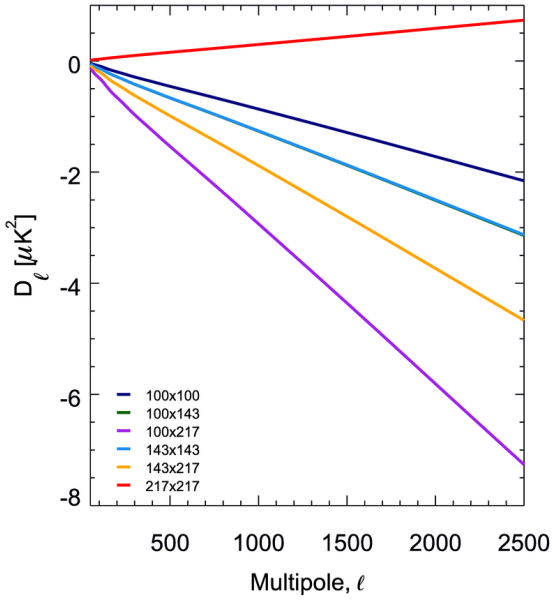

Figure 5.20: The tSZxCIB power spectra templates from the *Planck* Consistency Working Group.

and TE and compress the covariance matrix accordingly. The HiLLiPOP likelihood then reads

$$-2\ln\mathcal{L}(C_\ell^{\rm model}) = \sum_{\substack{X,Y\\X',Y'}}\sum_{\substack{i\leqslant j\\ i'\leqslant j'}}\sum_{\substack{\ell=\ell_{\rm min}^{X_iY_j}\\ \ell'=\ell_{\rm min}^{X'_{i'}Y'_{j'}}}}^{\substack{\ell_{\rm max}^{X_iY_j}\\ \ell_{\rm max}^{X'_{i'}Y'_{j'}}}} \mathcal{R}_\ell^{X_iY_j}\left[\Sigma_{\ell\ell'}^{X_iY_j,X'_{i'}Y'_{j'}}\right]^{-1}\mathcal{R}_{\ell'}^{X'_{i'}Y'_{j'}}. \tag{5.26}$$

$\mathcal{R}_\ell^{X_iX_j} = \hat{C}_\ell^{X_iX_j} - A_{\rm planck}c_ic_jC_\ell^{{\rm model},X_iX_j}$ denotes the residual of the estimated cross power spectra ($\hat{C}_\ell$) with respect to the model ($C_\ell^{\rm model}$) defined in Eq. 5.16, 5.17 and 5.18. These models come with a multiplication factor $A_{\rm planck}$ describing the error on the absolute calibration. It is allowed to vary around 1 with a Gaussian prior of 2.5‰ (Table 5.7). We use also 5 coefficients c_i for the relative calibration of each map with respect to the 143A map. More on calibration parameters can be found in sec. 5.8.5. The full covariance matrix Σ, is described in sec. 5.5. The frequency band (100, 143 and 217 GHz) is given by the i, j indices and the CMB modes (T, E) by X, Y. The multipole ranges $[\ell_{\rm min},\ell_{\rm max}]$ are chosen differently for each power spectrum to limit contaminations. Given the number of degree of freedom n_ℓ, we expect the χ^2 to be approximately Gaussian distributed with a mean of n_ℓ and a dispersion $\sqrt{2n_\ell}$, where $n_\ell = \ell_{\rm max} - \ell{\rm min} + 1$.

The model is a function of the 6 or more cosmological parameters (ΛCDM and possible extensions), and the nuisance parameters: $C_\ell^{\rm model}(\mathbf{\Omega}, \nu)$. As listed in Table 5.7, there are 6 instrumental parameters describing calibration, and a scaling parameters for each foreground modelling described in sec.5.6. Note that these latter includes different parameters for the different CMB modes considered. In polarisation there is only the corresponding $A_{\rm dust}$ to be considered, while in temperature there are the 6 free Poisson amplitudes (one for each of the 6 compressed cross-spectra) plus the 4 scaling parameters for the SZ and CIB sector, plus the dust parameter. At the end, we have a total of 19 free nuisance parameters in the full

name	definition	prior (if any)
	instrumental	
c_0	map calibration (100 GHz)	0.000 ± 0.002
c_1	map calibration (100 GHz)	0.000 ± 0.002
c_3	map calibration (143 GHz)	0.000 ± 0.002
c_4	map calibration (217 GHz)	0.002 ± 0.002
c_5	map calibration (217 GHz)	0.002 ± 0.002
$A_{\rm planck}$	absolute calibration	1 ± 0.0025
	foreground modelling	
$A_{\rm PS}^{100\times100}$	PS amplitude in TT (100x100 GHz)	
$A_{\rm PS}^{100\times143}$	PS amplitude in TT (100x143 GHz)	
$A_{\rm PS}^{100\times217}$	PS amplitude in TT (100x217 GHz)	
$A_{\rm PS}^{143\times143}$	PS amplitude in TT (143x143 GHz)	
$A_{\rm PS}^{143\times217}$	PS amplitude in TT (143x217 GHz)	
$A_{\rm PS}^{217\times217}$	PS amplitude in TT (217x217 GHz)	
$A_{\rm SZ}$	scaling parameter for the tSZ in TT	
$A_{\rm CIB}$	scaling parameter for the CIB in TT	
$A_{\rm dust}^{\rm TT}$	scaling parameter for the dust in TT	1.00 ± 0.20
$A_{\rm dust}^{\rm EE}$	scaling parameter for the dust in EE	1.00 ± 0.20
$A_{\rm dust}^{\rm TE}$	scaling parameter for the dust in TE	1.00 ± 0.20
$A_{\rm kSZ}$	scaling parameter for the kSZ effect	
$A_{\rm SZxCIB}$	scaling parameter for cross correlation SZ and CIB	

Table 5.7: Nuisance parameters for the `HiLLiPOP` likelihood

(TT, EE, TE) model. In Table 5.7, we also list the Gaussian prior, that are optionally used in the analysis, for the calibration and dust scaling factors. Other combinations have been tried during the development of the likelihood and the consequences of these different choices have been investigated (see sec. 5.8.4 and sec. 5.8.5). On all parameters, large flat prior to avoid non-physical values are always considered.

5.8 Robustness tests

In this section, we describe the tests we have performed in order to establish the robustness of the results with respect to some of the details of the foreground modelling, the data used, the masks, the multipole-range, and the implementation of the calibration coefficients.

5.8.1 Consistency between datasets

Although the results in chapter 7 have been obtained using HM data, along the process of validation of the likelihood, DS and Yr data have been extensively tested. Yr data do not differ substantially from HM data. The only difference is the inclusion or not of the 5th survey. HM data thus contains more statistics, but Yr data are more naturally related to the scanning strategy.

In Fig. 5.21 we show the parameters shifts for the temperature-only `HiLLiPOP` likelihood between the DS, Yr and HM data. The cosmological parameters do not show important variations with the exception of 0.6σ down shift for n_s in the DS configuration. HM and Yr data show a little discrepancy only on the estimate of θ.

Note that since calibration parameters are related to different maps, a dispersion is perfectly normal. The most visible shift are, however, in the values for the Poisson amplitude involving the 100 GHz channel, resulting in a lower value for the tSZ effect. Poisson amplitude are discussed further in sec.5.8.4.

The DS cross-spectra likelihood has higher signal to noise with respect to the HM likelihood, but low level uncorrected correlated noise and residual 4-k line systematics has driven the *Planck* collaboration to prefer the latter (Planck Collaboration. XIII. 2015). The cosmology is really little influenced by this choice but the final results presented in this thesis have been obtained using the HM likelihood.

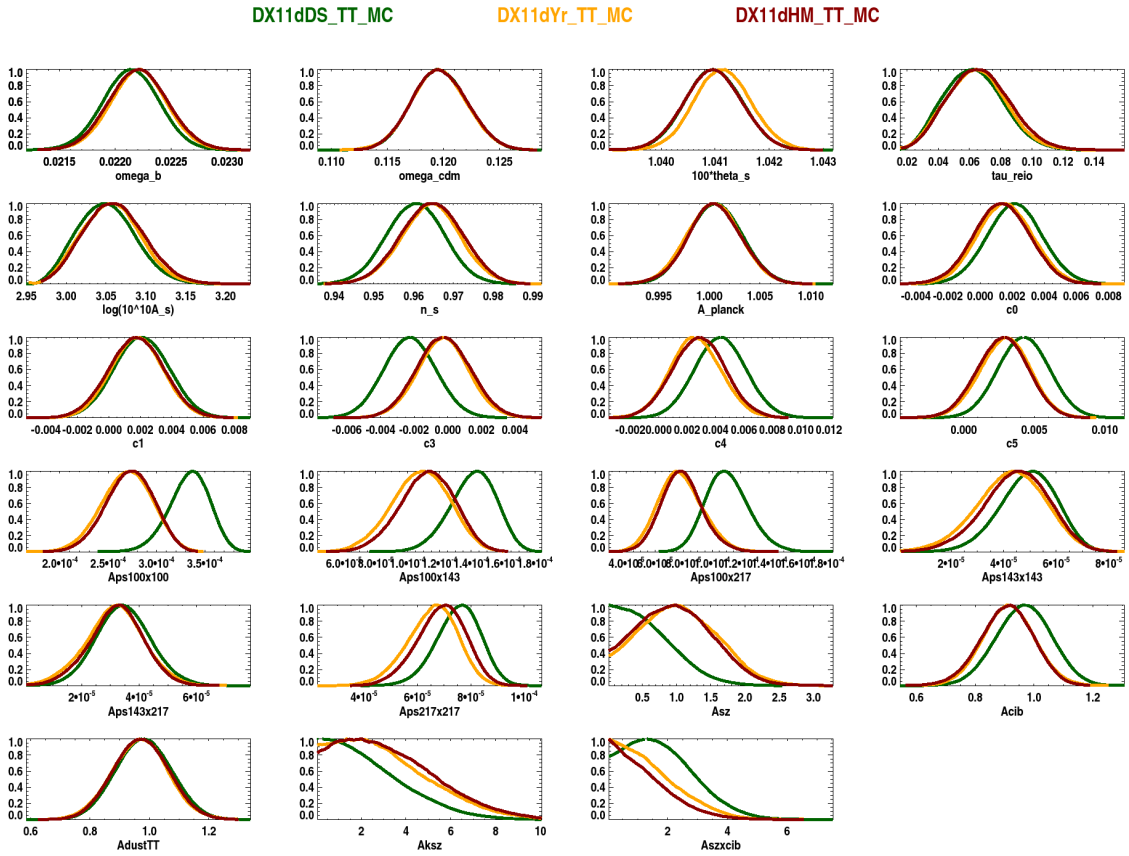

Figure 5.21: Posterior distribution for the temperature only HiLLiPOP likelihood (in combination with LowTEB) using DS data (green) or Yr data (yellow) or HM data (red).

5.8.2 Masks choice

In sec. 5.3 the masks used in the analysis have been presented. They are frequency dependent combination of Galactic, point source, CO and nearby galaxy masks. The M72, M62 and M48 masks associated to the 100 GHz, 143 GHz and 217 GHz channels, respectively, are described in Table 5.2. We refer to this set of masks as the *MaskSuperExt*.

Along the analysis we tried different masks. For the Galactic emission, for example, we have extensively used a more conservative set, M65, M55 and M40 that we will refer to as *MaskExt*. Also, the CO masks have been changed during the analysis, choosing, for the final analysis, a more conservative one. For HM data, the different value of $\chi^2_{\rm min}$ obtained with the different combination of mask are listed in Table 5.8.

The shift induced on the cosmological parameters are shown in Fig.5.22. Results are quite stable to the different masks. The SZ source masks, created using a Compton parameter Y map (Planck Collaboration XXI 2014), have not be retained in the final masks since the SZ emission is sub-dominant, and, as for the PCCS masks, the analytical approximations in the covariance matrix computation are less accurate.

mask name	$\chi^2_{\rm min}$	$\chi^2_{\rm min}/n_\ell$	$\Delta\chi^2/\sqrt{2n_\ell}$
MaskExt	9979.18	1.00	3.06
MaskExt (Conservative CO)	9990.67	1.05	3.14
MaskSuperExt (Conservative CO)	9949.69	1.04	2.85
MaskSuperExt (Conservative CO, SZ mask)	11622.6	1.22	14.95

Table 5.8: Values for the $\chi^2_{\rm min}$, $\chi^2_{\rm min}/n_\ell$ and $\Delta\chi^2/\sqrt{2n_\ell}$ (with $n_\ell = \ell_{\rm max} - \ell_{\rm min} + 1$=9556) using the HM TT `HiLLiPOP` likelihood (with `LowTEB` at low-ℓ) with different masks. If not specified the CO masks are the ones smoothed at 120 arcmin (sec.5.3). Conservative CO masks are instead smoothed at 30 arcmin, leaving more structures at high latitude. The impact of the SZ mask is important since the $\chi^2_{\rm min}$ values dramatically increases. Hence, this mask is not used in our analysis.

5.8.3 Extended ℓ-range

Dependence of the cosmological parameters on multipole-range is a complicate subject. In this section we extend the ℓ-range as detailed in Table 5.9 and check that there are no major changes. We do this for both DS and Yr, considering the case of temperature alone.

Cross-spectrum	baseline range	extended range
100 GHz × 100 GHz	[50,1200]	[50,1500]
100 GHz × 143 GHz	[50,1500]	[50,1700]
100 GHz × 217 GHz	[500,1500]	[50,1700]
143 GHz × 143 GHz	[50,2000]	[50,2000]
143 GHz × 217 GHz	[500,2500]	[50,2500]
217 GHz × 217 GHz	[500,2500]	[50,2500]

Table 5.9: Details of the extended ℓ-range. The $\ell_{\rm min}$ is lowered for the cross-spectra involving the 217 GHz. $\ell_{\rm max}$ is slightly shifted to higher values for the 100 GHz.

Lowering $\ell_{\rm min}$ the cross-spectra involving the 217 GHz, and rising $\ell_{\rm max}$ for the 100 GHz, we expect to have better constraints on the foregrounds. In Fig. 5.23 we see that this is indeed the case. The error bars for the dust and the CIB are tighter by more than a factor two. At 100 GHz, where the dust and the CIB have minor contributions, the extended ℓ-range allows a (weak) detection of the tSZ signal. This lowers the values of the Poisson amplitudes involving this frequency, now more in agreement with the external astrophysical results. The consistency of the Poisson amplitudes with their astrophysical determination is discussed further in sec.5.8.4. Also the up shift of CIB is compensated by a lower value for the Poisson amplitudes at 217 GHz. The cosmological parameters are not much sensitive to this extended ℓ-range. This is reassuring for the robustness of the foreground modelling. In any case, since especially lowering $\ell_{\rm min}$ we are extending the residual dust model to regions where its validity is not assured, we keep using the conservative ℓ-range of Table 5.3 for the results of chapter 7.

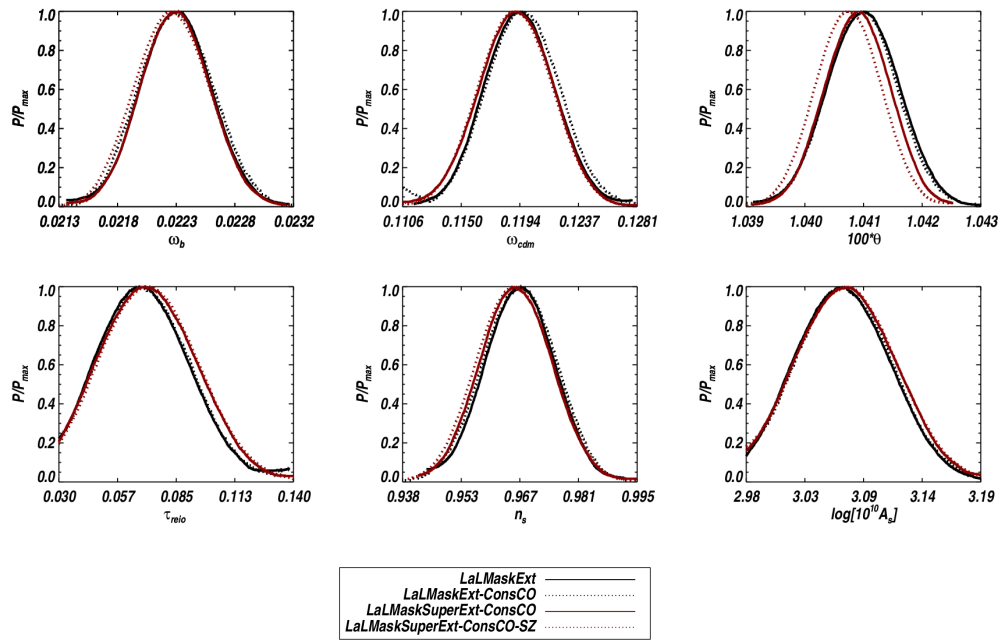

Figure 5.22: Posterior distributions for the six ΛCDM parameters obtained sampling the HM TT HiLLiPOP likelihood constructed using different masks. Note that changing the Galactic masks causes only little shifts in cosmological parameters and that the different CO masks have almost no impact. Adding the SZ mask has only a little impact on θ, but worsens considerably the $\chi^2_{\rm min}$ (Table 5.8). This mask is not used in our analysis.

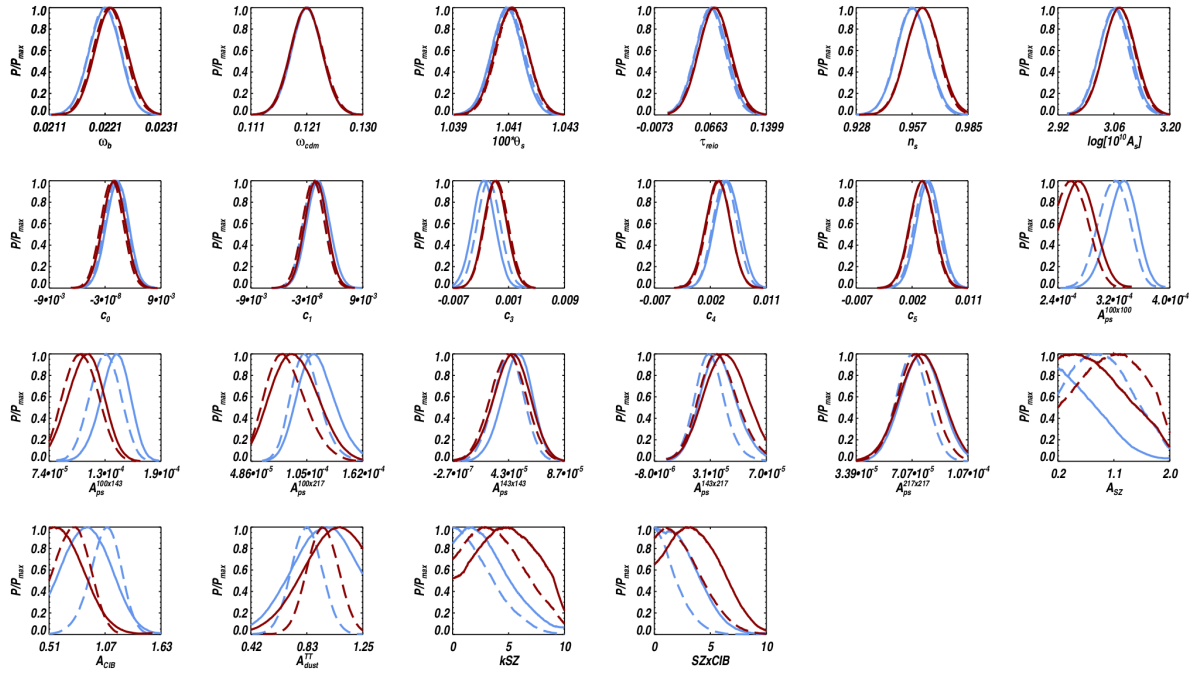

Figure 5.23: Posterior distributions from the TT `HiLLiPOP` likelihood (in combination with a τ prior 0.07 ± 0.02 to mimic the low-ℓ). In blue are shown DS and in red Yr data. Solid line correspond to normal ranges and dashed to the extended one described in Table 5.9.

5.8.4 Foreground modelling

We check here the consistency of the foreground models used in our analysis. We recall that we adjust each foreground component to the data using a single rescaling amplitude, that should be found compatible with one. The only exception are the residual point sources, for which an absolute amplitude is left free for each cross-spectra. These are discussed at the end of this section.

In temperature the dust amplitude is recovered almost perfectly ($A^{TT}_{\rm dust} = 0.99 \pm 0.11$) while the $A_{\rm CIB}$ estimation lies $1.7\,\sigma$ away (0.60 ± 0.24). Using the full (TT, EE, TE) likelihood, the dust TT remains perfectly compatible with one and the shift in the CIB amplitude is reduced to $0.5\,\sigma$ (0.89 ± 0.21). The polarized dust amplitudes ($A^{TE}_{\rm dust}$ and $A^{EE}_{\rm dust}$) are compatible within about $2\,\sigma$ with one: $A^{TE}_{\rm dust} = 0.69 \pm 0.14$ and $A^{EE}_{\rm dust} = 1.28 \pm 0.13$. Using *Planck* only data, we are not very sensitive to SZ components. In any case, the marginalized posteriors on $A_{\rm tSZ}$, $A_{\rm kSZ}$ and $A_{\rm tSZxCIB}$ are compatible with the expectations.

Compatibility with $A = 1$ for the foreground scaling parameters is a good test for the consistency of the internal *Planck* templates. We also test the stability of the cosmological results with respect to the use of priors on these scaling parameters, by considering a set of Gaussian priors, $A = 1 \pm 0.2$. The $\chi^2_{\rm min}$ values remain unchanged with almost no shift in cosmological parameters (Fig. 5.24). For the final results presented in this thesis, we have decided to use priors on the dust parameters as described in Table 5.7.

The expected amplitude of the Poisson amplitudes can be computed from any theoretical model that makes a prediction for the multi-frequency differential number counts dN/dS. In Planck Collaboration A13 (2015) is presented an accurate way for computing, for each cross-frequency, the expected amplitude, taking into account also the details of the construction for the point source masks, such as the fact that the flux cut varies across the sky or the "incompleteness" of the catalogue from which the mask are

built at each frequency. We show here only the comparison between the estimations obtained using the model of Tucci et al. (2011) for radio sources and our fitted values. In Table 5.10, results are reported in D_ℓ at $\ell = 3000$ in μK^2, while often presented as C_ℓ values in the posterior distribution plots. The estimates are presented only for the radio sources. Note that, while at 100 GHz the contribution from dusty galaxies is negligible, at 217 GHz it provides about five times more power than the radio sources. Hence, the disagreement at 217x217 is only apparent since the reported number takes into account only radio sources. For the other cross frequencies, we find good agreement between the priors from source counts and the posteriors from chains, with the exception of the 100 GHz where the prediction is lower than the measured value by around 6 σ. This could be a sign of foreground modelling error or residual systematic in the data and was not present in the 2013 analysis. We note again that increasing $\ell_{\rm max}$ at 100 GHz (sec.5.8.3) reduces the tension. In any case, we do not expect this discrepancy to affect parameters as very little cosmological information comes from the range in multipoles at 100 GHz which constrains the Poisson amplitude (Planck Collaboration A13 2015).

The preference for a higher value for the Poisson amplitude is clearly not only a chance adjustment in the foreground sectors. If we put a Gaussian prior compatible with the expected value for the $A_{\rm PS}^{100\times100}$, the rest of the nuisance parameters and the cosmology find solutions strongly incompatible with their expected values. Up to now, we have found no way to reconcile our $A_{\rm PS}^{100\times100}$ value with the predictions, and that also the Plik likelihood shows a similar tension.

As a further consistency test, we check the impact of cosmology on the foregrounds. In Fig. 5.25 we show the changes of the posterior distributions in the case of fixed cosmology. The nuisance and the cosmological parameters are not much correlated, the posteriors are almost identical but, as expected, slightly tighter. We postpone a more detailed discussion on the likelihood parameter correlation matrix to chapter 7.

	100 GHz × 100 GHz	143 GHz × 143 GHz	143 GHz × 217 GHz	217 GHz × 217 GHz
Radio	141	47	18	12
Dusty	∼0	-	-	∼Radio × 5
HiLLiPOP	372±38	58±21	53±24	105±18

Table 5.10: Estimation of the radio source Poisson amplitudes, given the Consistency point source masks (PSCG) used in this thesis and the model from Tucci et al. (2011). Entries are reported in D_ℓ at $\ell = 3000$ in μK^2. Rough estimations for dusty galaxies are also reported. The sum of the two is compared to the HiLLiPOP value obtained using TT only and a τ prior 0.07±0.02.

5.8.5 Effect of calibrations

In this section we discuss the impact of the calibration parameters on the results. We remind that we use 6 maps that we identify as 100A, 100B, 143A, 143B, 217A, 217B. Depending on which data we want to use, these maps can be obtained from HM, Yr or DS combinations.
In the likelihood function, a parameter c_i is associated to each of this map such as $c_0 = 100A, c_1 = 100B, c_2 = 143A, c_3 = 143B, c_4 = 217A, c_5 = 217B$. To break the degeneracy with the absolute amplitude we fix $c_2 = 143A = 1$, so we have 5 *relative* calibration parameters.
The way calibrations enter in the model is the following

$$\hat{C}_\ell^{model,X_iY_j} \propto A c^i c^j \left(C_\ell^{\rm CMB,XY} + \sum_{\rm fg} A_{\rm fg} C_\ell^{\rm fg} \right), \tag{5.27}$$

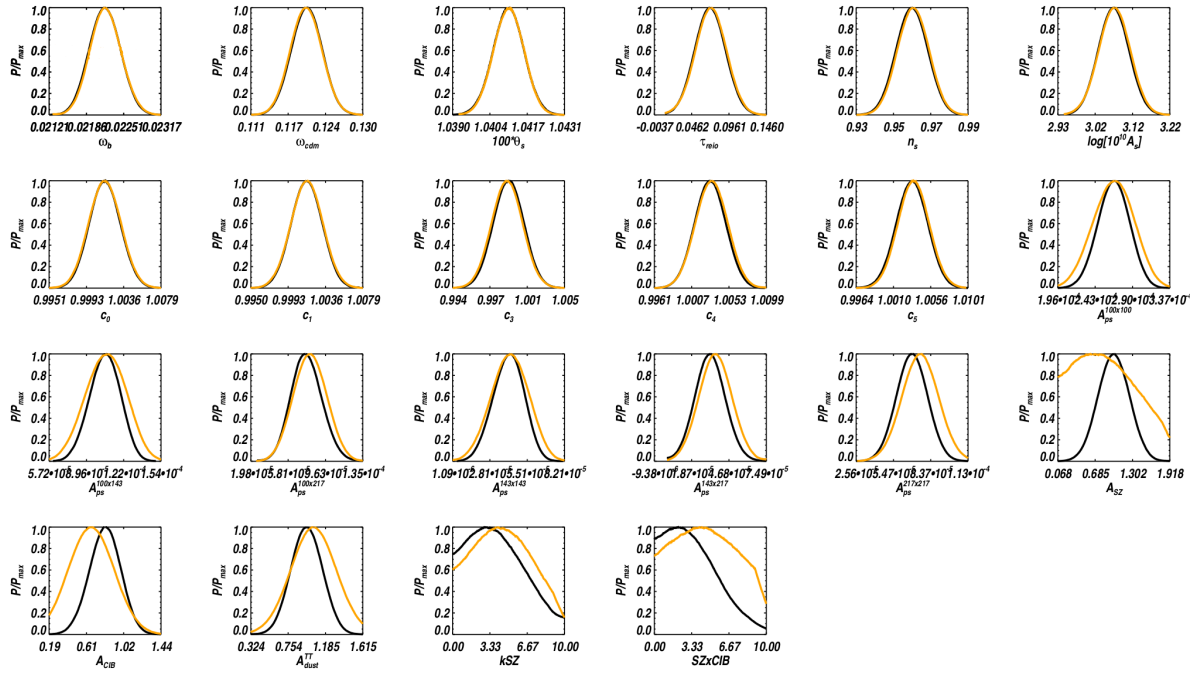

Figure 5.24: Posterior distribution for the TT `HiLLiPOP` likelihood considering Gaussian priors $A = 1 \pm 0.2$ on the foreground modelling parameters $A_{\rm SZ}$, $A_{\rm CIB}$, and $A_{\rm dust}$ (in black) or just flat large priors (in yellow). Results validate the foreground modelling with almost no shift on cosmological parameters.

with $X, Y \in \{T, E\}$. Strong priors, validated during the mapmaking process (Planck Collaboration. VIII 2015), are used on these parameters: a Gaussian prior $1 \pm 2 \times 10^{-3}$ for c_0, c_1 and c_3 and a Gaussian prior $1.002 \pm 2 \times 10^{-3}$ for c_4 and c_5. Note that the calibration priors on the 217 GHz maps is shifted up by 2‰. The parameter $A_{\rm planck}$ is the absolute calibration (sec. 5.7), and allows to propagate the calibration errors at the cross-spectra level and thus to the amplitude of the primordial power spectrum A_s. We use the same calibration factors for temperature and polarisation.

In Fig.5.26 the posterior distributions for the calibration parameters are shown. Even when strong Gaussian priors are used, there are $\sim \sigma$ level disagreements in the results. However, the estimation of cosmological parameters is not affected neither in the temperature alone case, nor for the full likelihood where the presence of polarisation could have had play a role (Fig.5.27). We have not found any instrumental reason for the calibration factor to vary between temperature and polarisation. We identify that the bad $\chi^2_{\rm min}$ value of the full likelihood configuration (9.7 σ) is probably due to this disagreement between calibrations. For the polarisation alone cases, the situation is more dramatic. The values of the cosmological parameter changes if the priors on calibrations are released as shown in Fig. 5.28.

As a possible solution we tried to take into account the difference between T and E calibration, adding, for the polarisation case, new parameters through the redefinition $c \to c(1+\epsilon)$. Clearly, the cases that are interesting to test are TE or the full likelihood. The calibrations in temperature are kept fixed and the ϵs are left free in the analysis. Unfortunately this does not cure the bad $\chi^2_{\rm min}$ for the full likelihood.

During these tests we noticed that the determination of the calibration coefficients through Eq. 5.27 suffers from highly non linear degeneracies and that a linearisation around 1 yields to more stable results. We thus redefine c_i as $1 + c_i$, where now the calibration parameters are centred on zero. The priors are

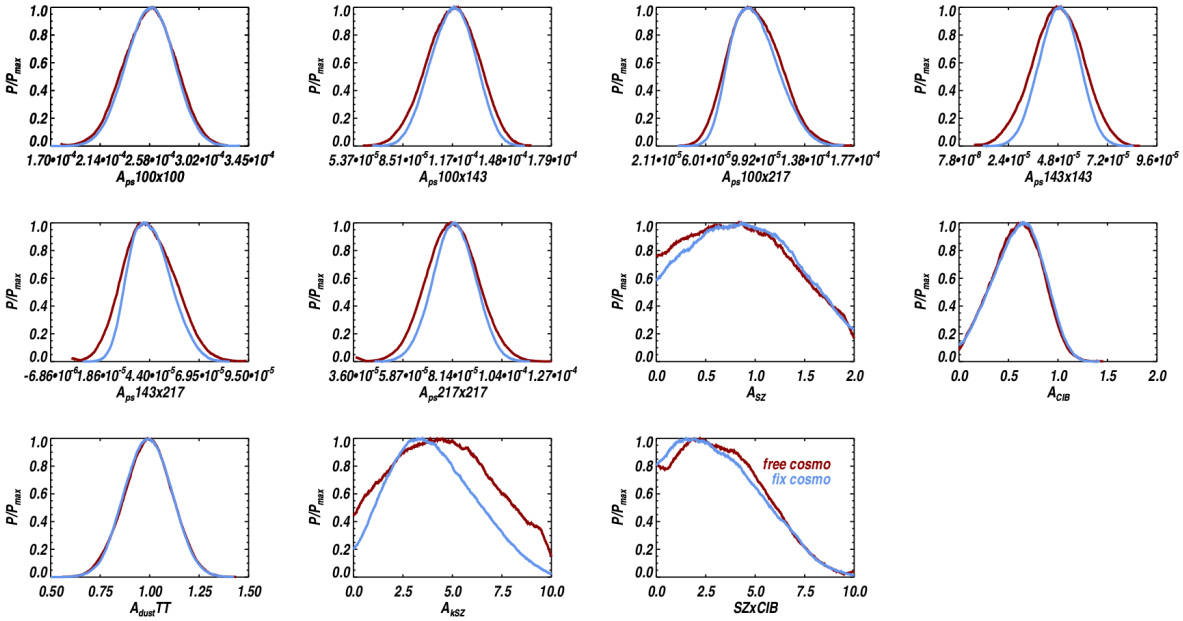

Figure 5.25: Posterior distribution for the foreground parameters of the TT HiLLiPOP likelihood (red) compared to the posteriors obtained fixing the cosmological parameters to their best fit (blue).

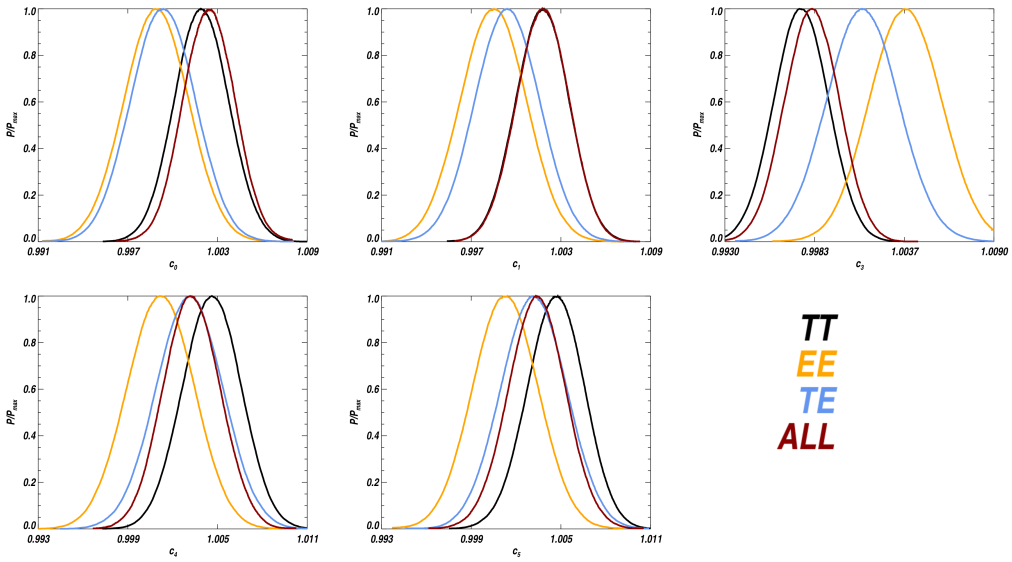

Figure 5.26: Posterior distribution for the 5 calibration parameters. Even in presence of strong priors there is a dispersion of values for the different modes.

shifted accordingly.

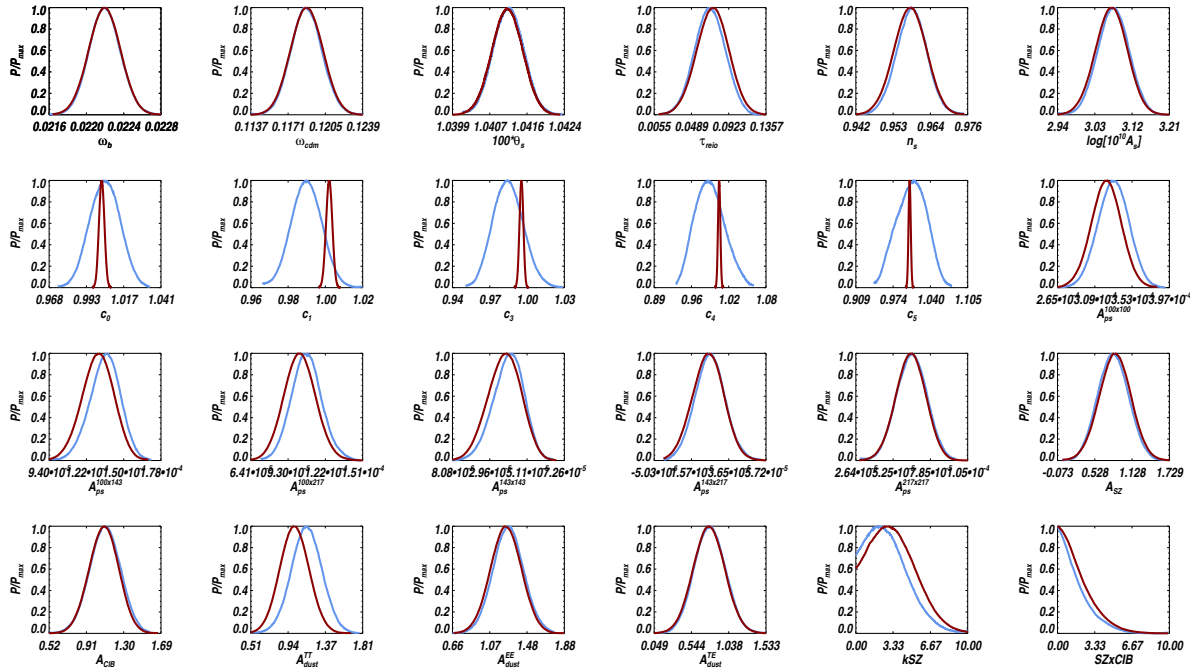

Figure 5.27: Posterior distributions for the full (TT+EE+TE) `HiLLiPOP` likelihood in case of strong Gaussian priors on calibration parameters (red) or letting the calibration free (blue).

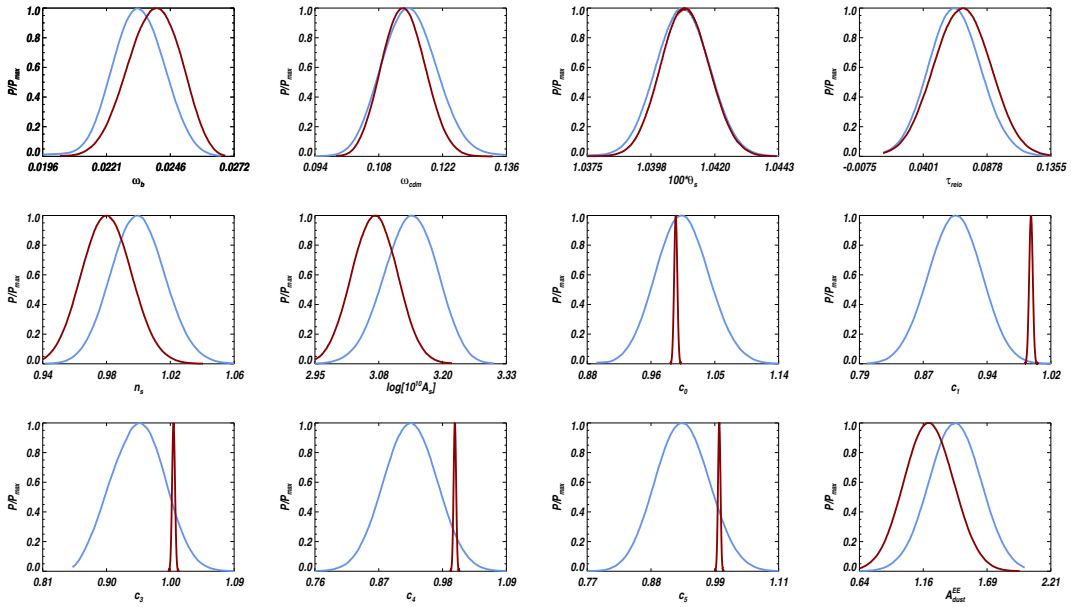

Figure 5.28: Posterior distributions for the EE `HiLLiPOP` likelihood in case of strong Gaussian priors on calibration parameters (red) or letting the calibration free (blue).

5.9 Comparison of likelihoods

The HiLLiPOP likelihood is one of the high-ℓ likelihood developed by the *Planck* Collaboration, along with Plik, CamSpec and Mspec. These codes have been used to perform data consistency checks, to test various analysis choices, and as a cross-check on the correctness of each code by comparing results among them. In this section we discuss their inter-comparison. In general, good agreement between the codes is found, with only minor differences in cosmological parameters. The Plik, CamSpec, and Mspec codes are, like HiLLiPOP, based on pseudo-C_ℓ estimators and an analytic computation of the covariance (Efstathiou 2004, 2006), with some differences in the approximations used. All of the codes use similar Galactic masks, but differ in point source masking as discussed in sec.5.5.3. The codes additionally differ in foreground modelling, data combinations used, and ℓ-ranges. The comparison shown here uses HM maps.

Figure 5.29 shows a comparison of the power spectra and error bars from each code. In temperature, we note that the HiLLiPOP spectra are globally lower than the other ones. This difference does not, however, lead to very large differences in cosmological parameters, but for a lower value for A_s. This is discussed further in chapter 7.
Note also an excess of power attributed to the CMB by Plik and CamSpec at high-ℓ at 100 GHz with respect to HiLLiPOP. Less power to the CMB means higher value for the foregrounds, hence higher Poisson power. This is consistent with the fact that the tension with astrophysical estimations of the Poisson amplitude (sec. 5.8.4), is slightly higher in HiLLiPOP with respect to the Plik likelihood (Planck Collaboration A13 2015). There is also a dip near $\ell = 1400$ at 217×217 in temperature. The dip is reduced by about $1\,\sigma$ for Mspec. Since this latter has a different dust cleaning procedure, the dip can be partially sourced by a chance CMB-galaxy correlation. However, this dip does not substantially affect the final results as it has been shown varying $\ell_{\rm max}$ in Planck Collaboration A13 (2015).

For TE and EE, the figure shows spectra which have been averaged across frequencies using minimum variance weights as calculated based on each codes' covariance matrix. Even with the present not complete level of understanding of systematics, the agreement between spectra is good.

In Fig. 5.30 is shown a ratio between the error bars from each code to the ones from the baseline Plik. The bins width is $\Delta\ell$=100, and thus, results are sensitive to the correlation structure of each code covariance matrix up to 100 multipoles into the off-diagonal. For all codes and for temperature and polarization, the correlation between multipoles separated by more than $\Delta\ell = 100$ is less than 3 %, thus Fig. 5.30 contains the majority of the relevant information about each code covariance.

The error bars for TT at 143×217 from our HiLLiPOP likelihood are tighter than the other codes. This is because we consider four 143×217 spectra, unlike the other likelihood that have only two spectra since they give zero weight to the cross where both the 143 and 217 GHz maps come from the same half-mission.

For TE and EE, after $\ell = 1000$ we see the HiLLiPOP estimation of error bars diverging slowly from the CamSpec value and a sudden jump after $\ell = 1750$. The reason for this discrepancy is in our ℓ-range (Table 5.3). Progressively less spectra are kept until, after $\ell = 1750$, there is only the 217×217 left. This is not the case for CamSpec which set the same $\ell_{\rm max}$ for all the cross-spectra.

The differences in ΛCDM parameters from TT are shown in Table. **??**. Generally, parameters agree to within a fraction of a σ. In particular, this shows the stability of the results with respect to Galactic cleaning procedure, since HiLLiPOP and Plik use different procedures with respect to Mspec. Additionally, point source masking, which is handled differently by HiLLiPOP and Plik (sec.5.8.4), does not lead to large shifts either.

The largest difference between HiLLiPOP and Plik is the lower value of $A_s e^{-2\tau}$, which is coherent with the global lower value of the spectra. Also note the bigger error bars in n_s that can be related to the

difference in foreground modelling, since n_s is the parameter more sensitive to the foregrounds.

These two parameter are also different between `Plik` and `CamSpec`. There is a difference in n_s, which is higher by about $0.45\,\sigma$ for `CamSpec`, with a related downward shift of $A_s e^{-2\tau}$. About half of this shift on n_s is likely due to the difference in the dust template used at relatively high-ℓ, *i.e.* in the regime where it is the hardest to determine the template accurately since the dust contribution is only a small fraction of the CIB + point source contributions . An additional $0.16\,\sigma$ difference can be attributed to the inclusion in `Plik` of the first 500 multipoles at 143×217 and 217×217, which are excised in `CamSpec`. This $0.3\,\sigma$ difference is believed to be illustrative of the *systematic* error on n_s associated with the uncertainties in the modelling of foregrounds, the largest systematic uncertainty in TT (Planck Collaboration A13 2015).

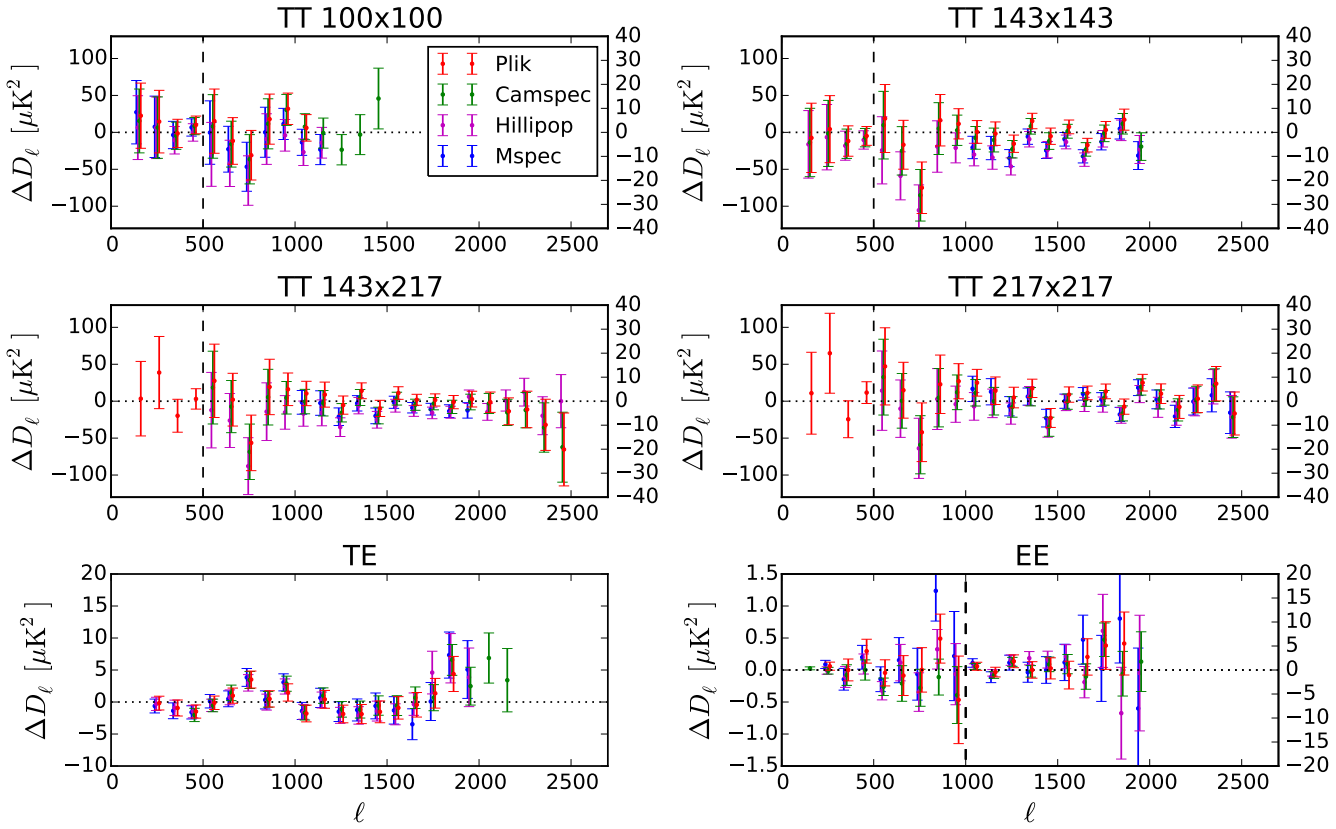

Figure 5.29: A comparison of power spectra residuals from different high-ℓ likelihood codes. A best-fit Galactic and extra-galactic foreground model, estimated *individually* by each code from a ΛCDM+τ-prior run, has been subtracted. A best-fit calibration factor has also been divided out of this best-fit model (as opposed to being multiplied into each spectrum). These plots thus show how much power (up to a calibration) each code attributes to the CMB, and power spectrum differences driving small cosmological parameter shifts between the codes are visible here. For easier visual comparison, a best-fit CMB model has been subtracted in each of the panels above, which here is the best-fit from `Plik`. The above power spectra are binned in bins of width $\Delta\ell = 100$, the y-scale changes at $\ell = 500$ for TT and $\ell = 1000$ for EE, as marked with vertical dashes (Planck Collaboration A13 2015).

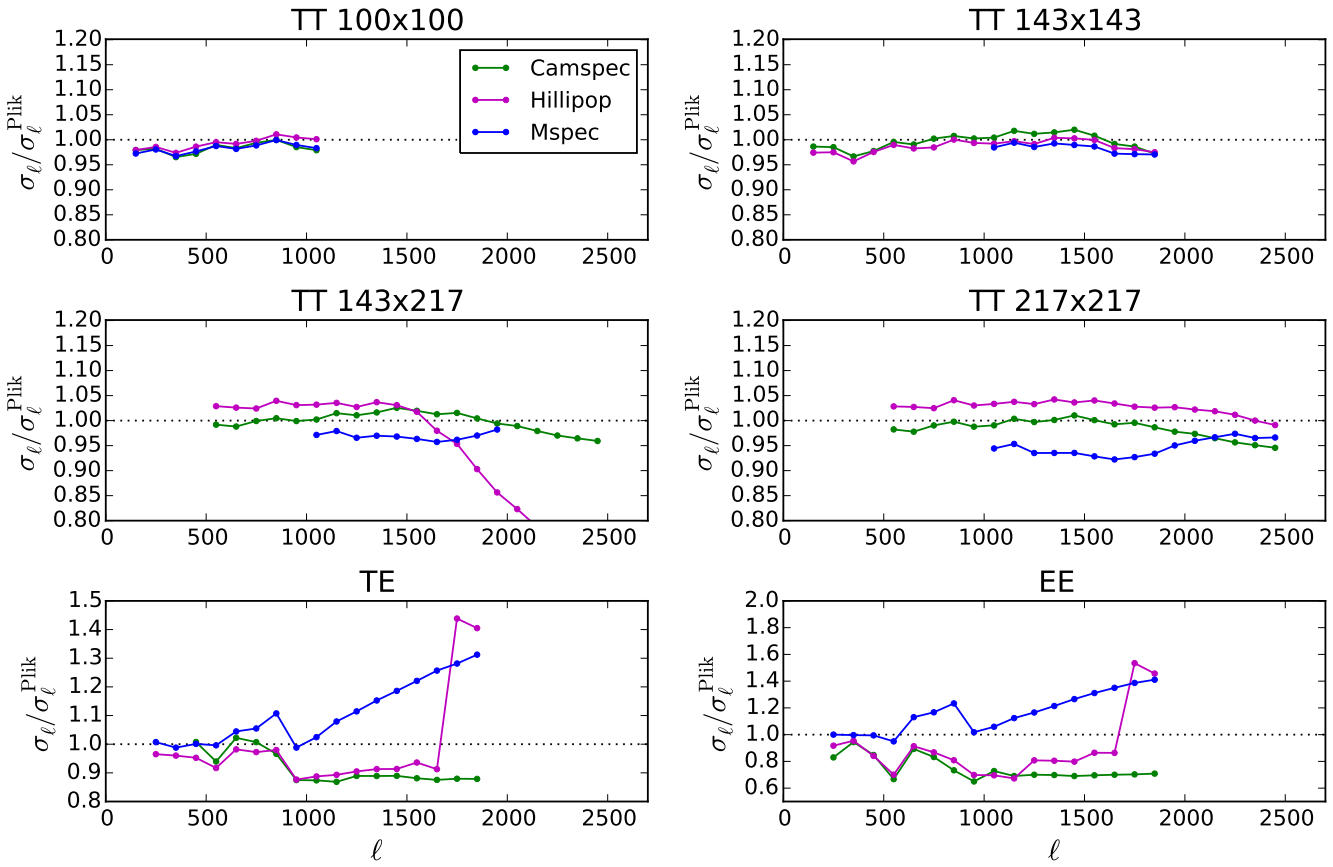

Figure 5.30: A comparison of error bars from the different high-ℓ likelihood codes. The error bars are given as a ratio to the `Plik` error bars and are for bins of width $\Delta\ell = 100$. Only regions which are within the ℓ range of both `Plik` and the code being compared are shown (Planck Collaboration A13 2015).

Parameter	Plik	CamSpec	HiLLiPOP	Mspec	XFaster (SMICA)
$\Omega_b h^2$	0.02219 ± 0.00023	0.02224 ± 0.00023	0.02218 ± 0.00023	0.02218 ± 0.00024	0.02184 ± 0.00024
$\Omega_c h^2$	0.1208 ± 0.0022	0.1201 ± 0.0023	0.1201 ± 0.0022	0.1204 ± 0.0024	0.1202 ± 0.0023
$100\theta_{\rm MC}$	1.0408 ± 0.00048	1.0407 ± 0.00048	1.0407 ± 0.00046	1.0409 ± 0.00050	1.041 ± 0.0005
τ	0.084 ± 0.018	0.087 ± 0.018	0.075 ± 0.019	0.075 ± 0.018	0.069 ± 0.019
$10^9 A_s e^{-2\tau}$	1.885 ± 0.014	1.877 ± 0.014	1.870 ± 0.011	1.878 ± 0.012	1.866 ± 0.015
n_s	0.962 ± 0.0063	0.965 ± 0.0066	0.961 ± 0.0072	0.959 ± 0.0072	0.960 ± 0.0071

Each column gives the results for various high-ℓ TT likelihoods at $\ell > 50$ when combined with a prior of $\tau = 0.07 \pm 0.02$. Note that the SMICA parameters were obtained for $\ell_{max} = 2000$.

Table 5.11: A comparison between the parameters of different high-ℓ codes (Planck Collaboration A13 2015).

5.10 Power spectra and residuals

In this section are presented the HM HiLLiPOP power spectra and residuals with respect to the ΛCDM best-fit model (chapter 7).

For each cross-spectrum, foreground and nuisance parameters can be fixed to their best-fit values and CMB only power spectra can be derived subtracting the foregrounds. Results are shown in Fig. 5.31 for TT together with the residuals with respect to the best fit values. The points are binned with $\Delta_\ell = 31$, and shown with their associated 1σ error bars. Note these errors are underestimated in the plots since we are neglecting ℓ-by-ℓ correlations.

For TT, as mentioned in (Planck Collaboration A13 2015), the 2013 deficit at $\ell \sim 1800$ due to imperfect removal of the 4K cooler line (chapter 3) is reduced as for the Plik likelihood. We also report a few $\sim \sigma$ deviation at ℓ=1450, and a deficit roughly in correspondence of the second and the third peak. Globally the temperature spectra are in very good agreement with the the ΛCDM best fit model.

Results for polarisation are shown in Fig. 5.32 for EE, and in Fig. 5.33 for TE. The inter frequency residuals with respect to the best fit model TT shows some deviation at a few μK^2 level (in ΔD_ℓ) that are averaged out in the co-added spectra of Fig. 5.2. These residual systematics can be due, for example, to temperature to polarisation leakage (Planck Collaboration A13 2015). However, in chapter 7 we will see that temperature and polarisation give compatible cosmology. Polarisation is thus used in this thesis.

In Table 5.12, the reduced χ^2 are calculated, for each cross-frequency residual plot, and for each mode, with respect to full the TT+EE+TE best fit model. In this case, the ℓ-by-ℓ correlations from the associated band covariance matrix are taken into account.

We show the level of foregrounds, after CMB subtraction, in Fig. 5.34 and Fig. 5.35. The level of each foreground contribution, fixed to the best fit value for the scaling parameter and the power spectrum shape described in sec. 5.6, are overplotted to the CMB-subtracted data. In polarisation, only the polarised dust emission is considered.

Conclusions

In this chapter we have presented the HiLLiPOP high-ℓ likelihood, a cross-spectra based Gaussian likelihood including both the *Planck* temperature and polarisation data. We have described the maps used and the frequency dependent masks for the Galactic, the CO-lines and the point source emissions. We have explained the computation of the covariance matrix, its validation at a few % precision through Monte Carlo simulations, and the role of the masks on its accuracy, leading to the conclusion that a proper cirrus

$\chi^2/N_{\rm dof}$	100x100	100x143	100x217	143x143	143x217	217x217
TT	0.98	0.92	0.87	1.16	1.04	1.15
EE	1.05	1.75	1.90	1.67	1.24	0.87
TE	1.10	1.24	1.26	0.84	1.02	1.51

Table 5.12: Reduced-χ^2 with respect to the TT+EE+TE best fit model for the cross-frequency spectra, calculated for the binned points ($\Delta = 31$) and their 1σ errors computed from the associated band covariance matrix, in the multipole range considered for the HiLLiPOP likelihood (Table 5.3).

treatment is needed. We have also described the foreground residuals template used in both temperature and polarisation.

Assuming the ΛCDM model, we have then presented the test performed to check the consistency between different datasets, the robustness to the mask choice and the ℓ-range, the validity of the residual foreground models or the impact of the calibration parameters. These latter reveal that there are still some untreated systematic effects in polarisation, but we will see that the impact for cosmological parameter estimation is negligible.

The HiLLiPOP results have then been compared to the other high-ℓ likelihood ones, showing good agreement for both spectra, error bars, and cosmological parameters. In the last section, the foreground subtracted cross power spectra and residuals are presented for TT, EE and TE, along with the reduced χ^2 with respect to the TT+EE+TE best fit, and the CMB subtracted foreground residuals. All show good agreement between the data and the model.

Before going to the results of chapters 7 and 8, we dedicate the next chapter to a brief description of the *Planck* low-ℓ likelihoods, the CMB lensing, the ACT and SPT small scales data, and the BAO and Supernovae distance measurements. These datasets will complement the HiLLiPOP likelihood and reduce the CMB intrinsic degeneracy, allowing to better constrain the cosmological parameters.

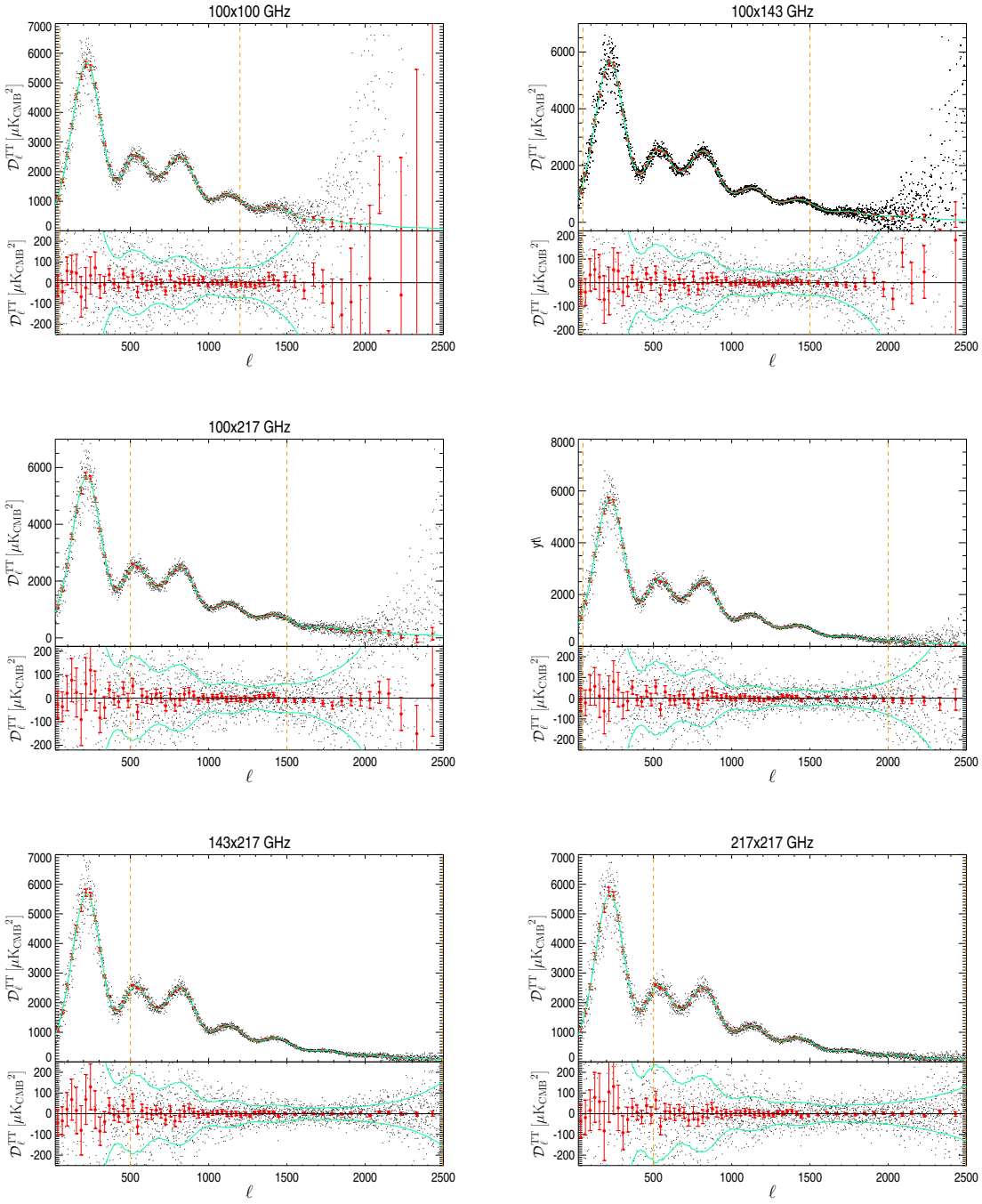

Figure 5.31: Foregrounds-subtracted TT cross-power spectra and residuals. For each cross-frequency, the top panel gives the best-fit CMB model (green curve) derived from a fit of the temperature data along with the estimated TT cross-power spectrum (gray points). The red points show averages in bands of width $\Delta = 31$ together with 1σ errors. The orange dotted vertical lines delimit the the considered multipole range (Table 5.3). The bottom panel shows the residuals with respect to the best fit model.

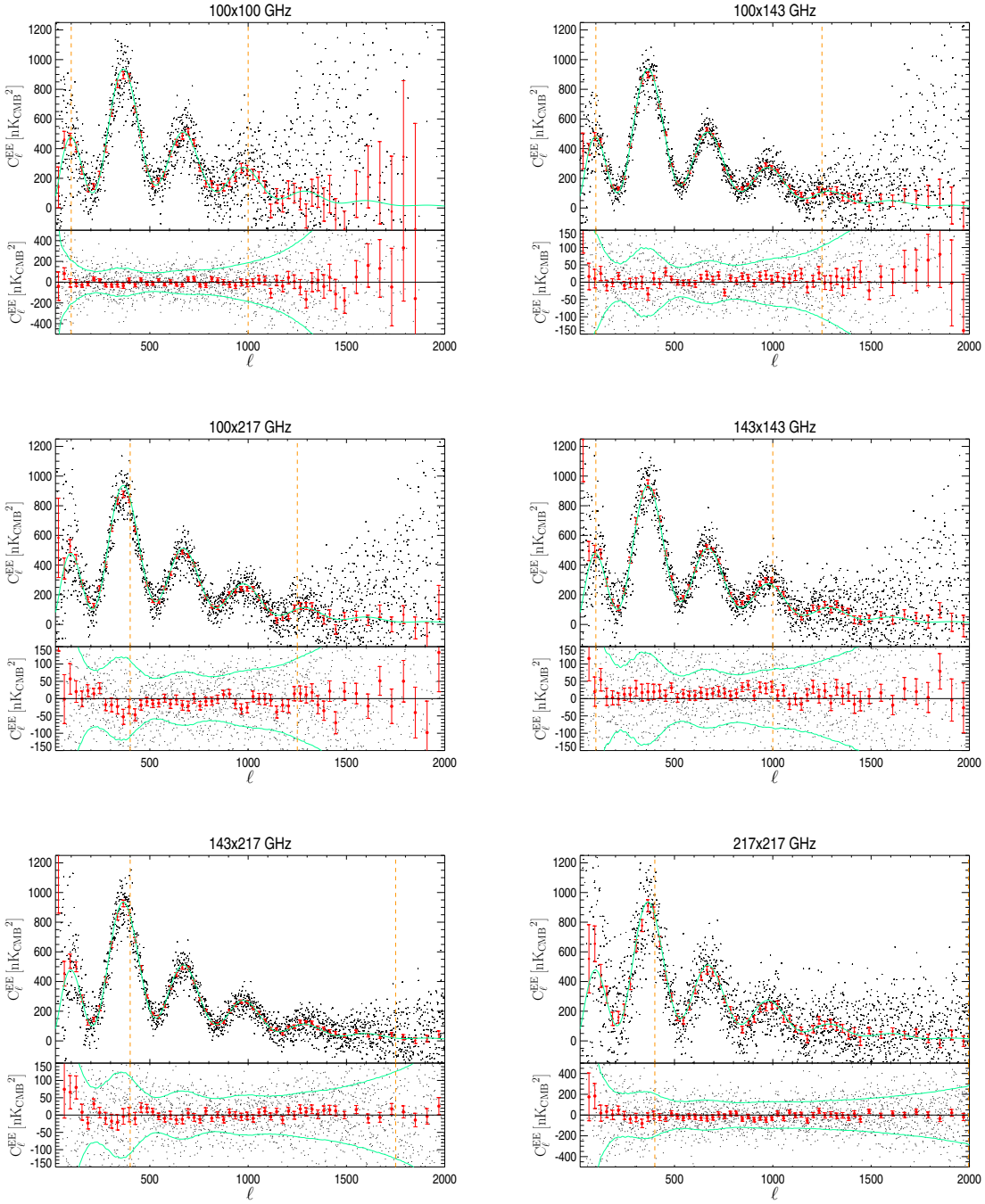

Figure 5.32: Same as Fig. 5.31, but for EE.

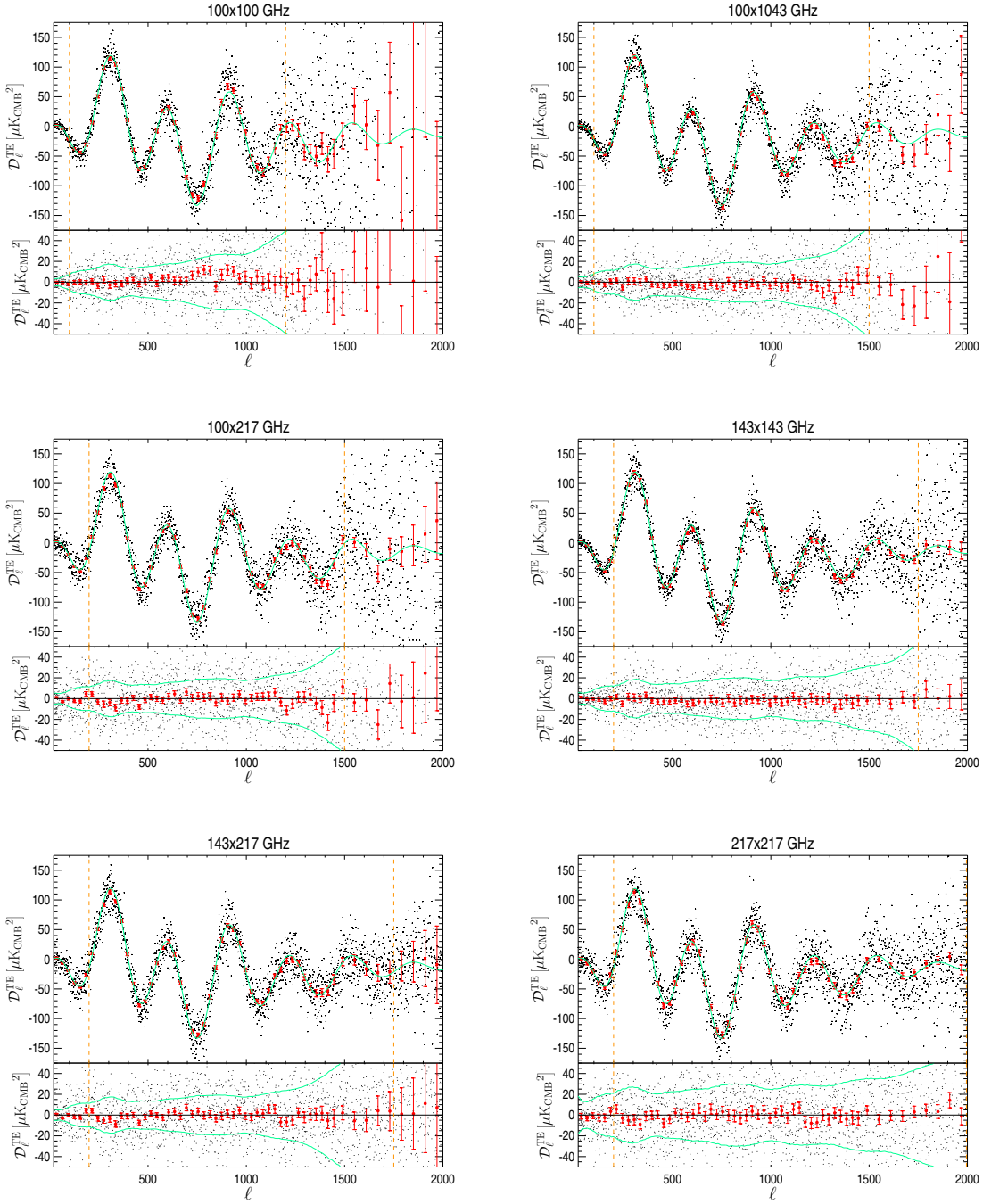

Figure 5.33: Same as Fig. 5.31, but for TE.

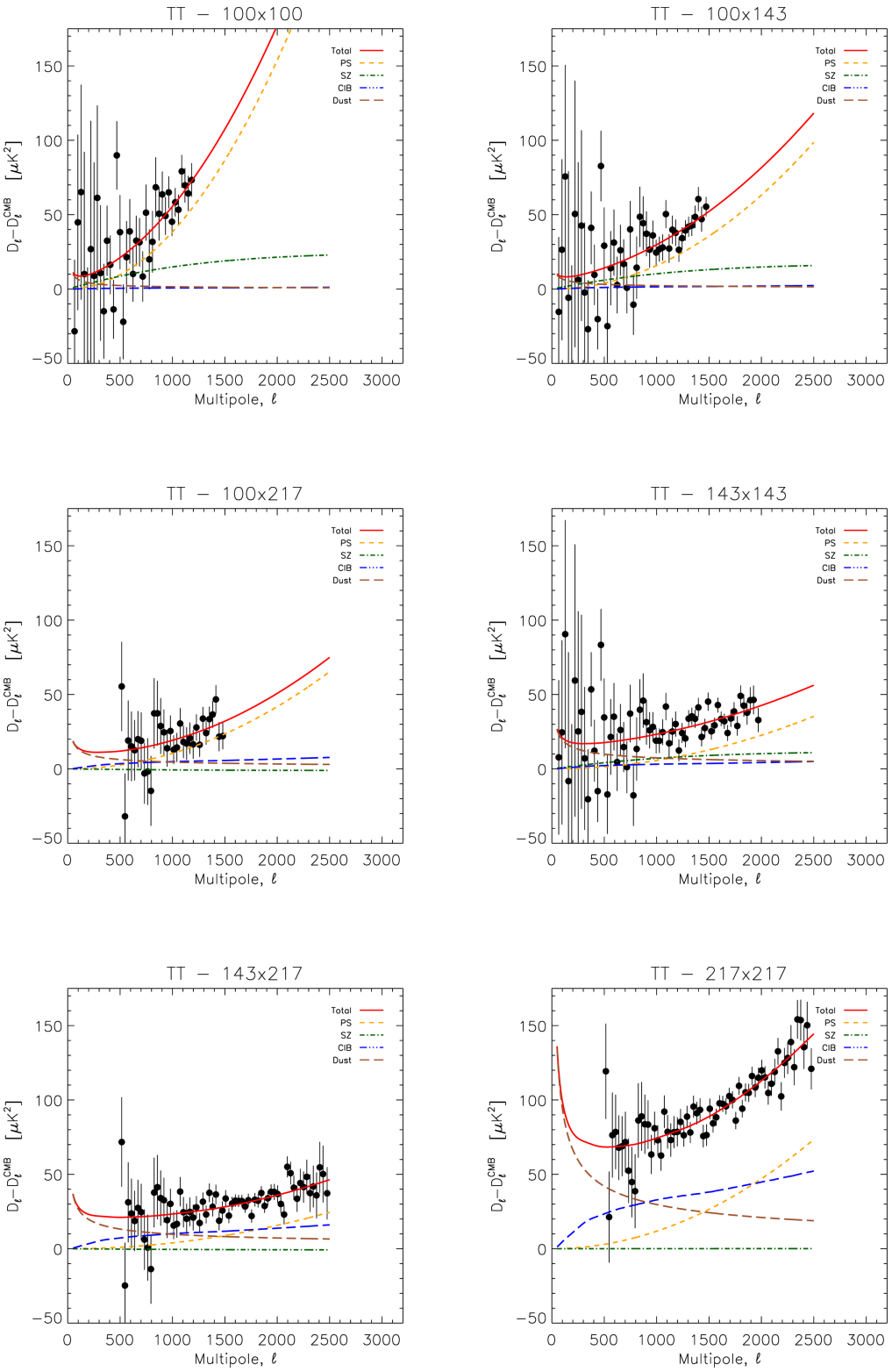

Figure 5.34: Temperature foreground residuals for all the cross-frequency spectra. The best fit level of each residual foreground contribution is also plotted.

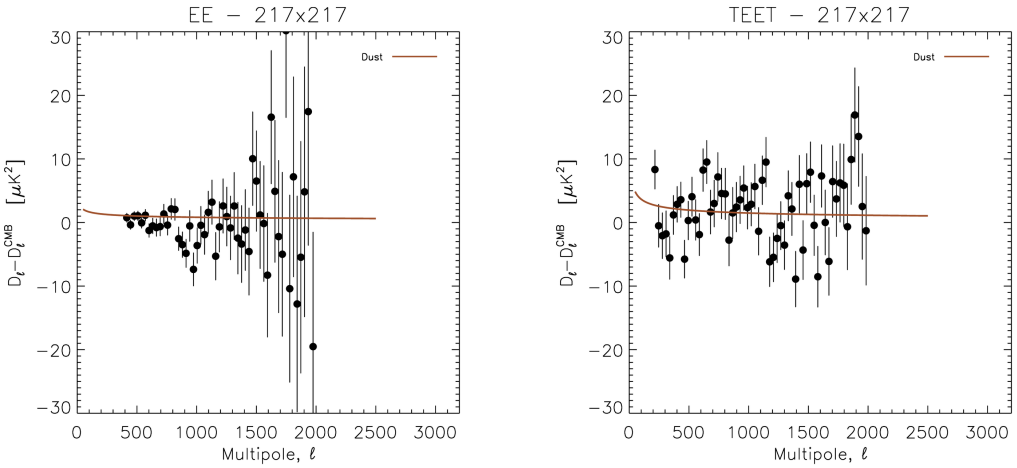

Figure 5.35: Polarization foreground residuals for the 217x217 cross-frequency. The best fit level of the polarised dust contribution is also plotted.

Chapter 6

Complementary datasets

In chapter 5 we have described in details the HiLLiPOP likelihood, a cross-spectra based approach at intermediate and high multipoles ($50 \leq \ell \leq 2500$), for both *Planck* temperature and polarisation data. With the aim of obtaining the best constraints on cosmological parameters, in chapter 7 and 8 we combine this likelihood with the complementary data presented here.

In sec. 6.1 we describe the *Planck* large scale information in temperature and polarisation that are fundamental to break the τ-A_s degeneracy. In sec. 6.2 we present the *Planck* lensing likelihood based on the power spectrum of the matter deflection field estimated from the 4-point correlation function. *Planck* data can also be combined with the small scale structure data from the CMB ground based experiment ACT and SPT. These are described in sec. 6.3. Although CMB alone has strong constraining power, the combination with late time distance measurements is a powerful lever arm to break the CMB degeneracies. In particular, we add Baryon Acoustic Oscillations (sec. 6.4) and Supernova Ia data (sec. 6.5). The combination with the complementary datasets described in this chapter improves cosmological constraints on the ΛCDM model, but are also fundamental to constrain neutrino extensions as is shown in chapter 8.

6.1 The Low-ℓ likelihood

The official *Planck* results are obtained combining the high-ℓ information with a joint pixel-based likelihood including both temperature and polarization for multipoles $\ell \leq 29$, dubbed `LowTEB` (sec. 6.1.1). For temperature, the formalism uses the cleaned `Commander` (Eriksen et al. 2004, 2008) maps, while for polarization the 70 GHz LFI maps are used, cleaned using the 30 GHz as a tracer for the synchrotron emission and the 353 GHz maps for dust emission. The pixel based approach computes an exact CMB likelihood function in pixel space, $\mathcal{L} = P(\mathbf{d}|C_\ell)$, with $\mathbf{d} \equiv M(\mathbf{p}) = \sum_{\ell m} a_{\ell m} Y_{\ell m}(\mathbf{p})$. Indeed, since the CMB anisotropies and noise are compatible with a Gaussian distribution with random phases (sec. 1.3.1), the $a_{\ell m}$ coefficient follow a multi-variate Gaussian distribution. The likelihood function, written in pixel space or, equivalently, in terms of the $a_{\ell m}$ coefficients, is Gaussian and therefore can be computed exactly (e.g. Gorski et al. (1994)). In chapter 7 and 8 the main results of the HiLLiPOP likelihood are obtained in combination with the `LowTEB` likelihood.

As a further test we also make use of the *lollipop* likelihood that extends the cross-spectra approach presented in chapter 5 to large angular scales (sec. 6.1.2). It is based on a modification of the Hamimeche-Lewis likelihood (Hamimeche & Lewis 2008) that has been proposed recently in Mangilli et al. (2015). Used on *Planck* HFI data, it allows a very precise constraint on τ that is interesting to combine with the high-ℓ HiLLiPOP likelihood, and we will use it to test the robustness of our results to the low-ℓ spectrum part.

6.1.1 Pixel based approach: LowTEB

The low-ℓ pixel based likelihood LowTEB contains both temperature and polarisation. The general formalism has been described for instance by Tegmark & de Oliveira-Costa (2001), Page et al. (2007), and in Planck Collaboration XV (2014).

In order to use low multipoles the likelihood adopts a HEALpix resolution of $N_{\rm side} = 16$ which has 3072 pixels per map; this accommodates multipoles up to $\ell_{\rm max} \simeq 3N_{\rm side} = 46$, and, considering separate maps of T, Q, and U, corresponds to a maximum of $N_{\rm pix} = 3 \times 3072 = 9216$ pixels. As described in Planck Collaboration A13 (2015), after component separation, the data are modelled as a sum of the cosmological CMB signal and instrumental noise, $\vec{m} = \vec{s} + \vec{n}$. The signal $\vec{s}$ is assumed to have auto- and cross-power spectra C_ℓ^{XY} (with $XY = \{TT, EE, BB, TE\}$) and, in analogy with Eq. 1.82, a pixel-space covariance matrix

$$S(C_\ell) = \sum_{\ell=2}^{\ell_{\rm max}} \sum_{XY} C_\ell^{XY} P_\ell^{XY}. \tag{6.1}$$

Here P_ℓ^{XY} is a beam-weighted sum over the corresponding Legendre polynomials. For temperature, the explicit expression is

$$(P_\ell^{TT})_{i,j} = \frac{2\ell+1}{4\pi} B_\ell^2 P_\ell(\hat{n}_i \cdot \hat{n}_j). \tag{6.2}$$

where $\hat{n}_i$ is a unit vector pointing towards pixel i, B_ℓ is the product of the Legendre transformed instrumental beam and the HEALpix pixel window, and P_ℓ is the Legendre polynomial of order ℓ[1].

The instrumental noise is also assumed to be Gaussian distributed. Its covariance matrix N depends on the *Planck* detector sensitivity and the scanning strategy (chapter 3). The full data covariance is $\mathrm{M} = S + \mathrm{N}$ and the likelihood reads

$$\mathcal{L}(C_\ell) = \frac{1}{|2\pi \mathrm{M}|^{1/2}} \exp\left(-\frac{1}{2}\vec{m}^{\mathrm{T}} \mathrm{M}^{-1} \vec{m}\right) \tag{6.3}$$

As mentioned in chapter 5, the inversion of the matrix and the computation of the determinant are computationally costly since they scales as $O(N_{\rm pix}^3)$. Hence, this direct approach can only be used at large angular scales, where the number of pixels is low.

Temperature

For temperature, as in 2013 (Planck Collaboration XV 2014), the Commander likelihood is used (Planck Collaboration. X. 2015). It is a component separation method that assumes an explicit parametrisation for the CMB and for the foreground models. These latter have been introduced in chapter 3.

A CMB map at an angular resolution of 1 ° FWHM (Fig 6.1(a)) is obtained combining, in the spherical harmonic domain, solutions from different combination of input channels at multiple resolutions. Commander employs detector and detector set maps rather then full frequency maps, excluding specific maps if there are significant systematic errors, but adding 9-year WMAP temperature sky maps (Bennett et al. 2013) and 408 MHz survey map (that carries information on synchrotron emission) (Haslam et al. 1981, 1982).

In Fig 6.1(b) are compared the 2013 and 2015 marginal posteriors low-ℓ power spectrum derived using a Blackwell-Rao estimator (Chu et al. 2005).

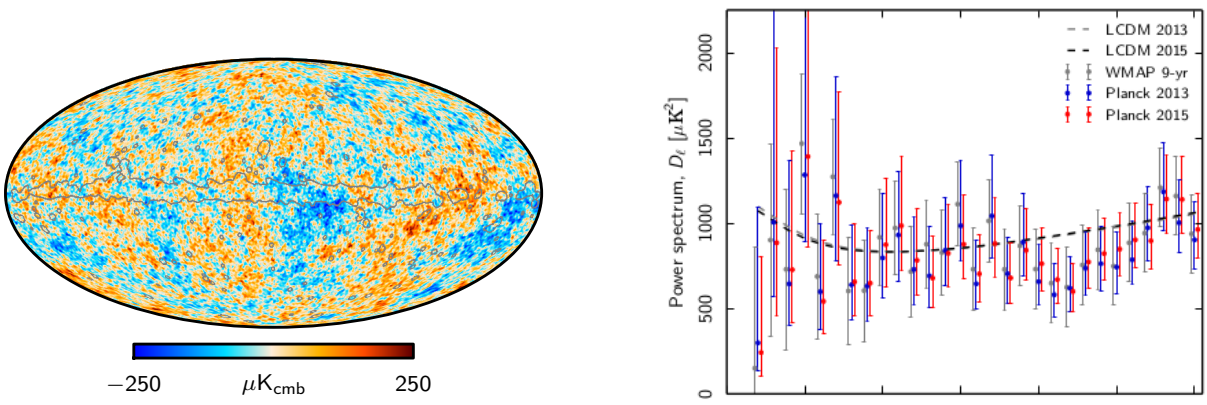

(a) (b)

Figure 6.1: (a) `Commander` CMB maps obtained combining *Planck* data with the 9-year WMAP and the 408 MHz Haslam et al. observations. The mask for temperature covers the 7% of the sky and its contours is showed in gray. The masked area has been filled with a constrained Gaussian realisation. (Planck Collaboration. X. 2015). (b) *Planck* 2013 (blue) and *Planck* 2015 (red) posteriors low-ℓ power spectrum derived using the `Commander` algorithm. The 9-year WMAP temperature spectrum is also shown for comparison in light gray points. The dashed lines show the best-fit ΛCDM obtained combining low- and high-ℓ data. Both figures are taken from Planck Collaboration A13 (2015).

Polarisation

In polarisation, the 70 GHz channel of the LFI instrument is used. The Surveys 2 and 4 have been conservatively removed since they did not pass some consistency tests (Planck Collaboration A13 2015).

The *Planck* Q and U 70 GHz maps are cleaned using 30 GHz maps to generate a template for low-frequency foreground contamination, and 353 GHz maps to generate a template for polarized dust emission. The final cleaned Q and U maps, shown in Fig. 6.2, retain a fraction $f_{\rm sky} = 0.46$ of the sky.

The template-fitting procedure starts defying $\vec{m} \equiv [Q, U]$ as

$$\vec{m} = \frac{1}{1-\alpha-\beta}\left(\vec{m}_{70} - \alpha\vec{m}_{30} - \beta\vec{m}_{353}\right), \tag{6.4}$$

where $\vec{m}_{70}$, $\vec{m}_{30}$, and $\vec{m}_{353}$ are band-pass-corrected versions of the 70, 30, and 353 GHz maps (Planck Collaboration III 2015; Planck Collaboration VII 2015), whereas α and β are the scaling coefficients for synchrotron and dust emission, respectively. The latter are estimated minimising the quantity

$$\chi^2 = (1-\alpha-\beta)^2 \vec{m}^{\rm T} {\rm C}_{S+{\rm N}}^{-1} \vec{m}\,, \tag{6.5}$$

where

$${\rm C}_{S+{\rm N}} \equiv (1-\alpha-\beta)^2 \langle \vec{m}\vec{m}^{\rm T}\rangle = (1-\alpha-\beta)^2 S(C_\ell) + {\rm N}_{70}\,. \tag{6.6}$$

Here ${\rm N}_{70}$ is the pure polarization part of the 70 GHz noise covariance. The C_ℓ power spectrum is taken form *Planck* 2015 best fit.

The best fit values obtained in the minimisation of Eq. 6.5 (using $f_{\rm sky}46\,\%$), correspond to spectral indices (with $2\,\sigma$ errors) $n_{\rm synch} = -3.39 \pm 0.40$ and $n_{\rm dust} = 1.50 \pm 0.16$, for synchrotron and dust emission respectively.

[1] For corresponding polarization components, see, *e.g.* Tegmark & de Oliveira-Costa (2001)

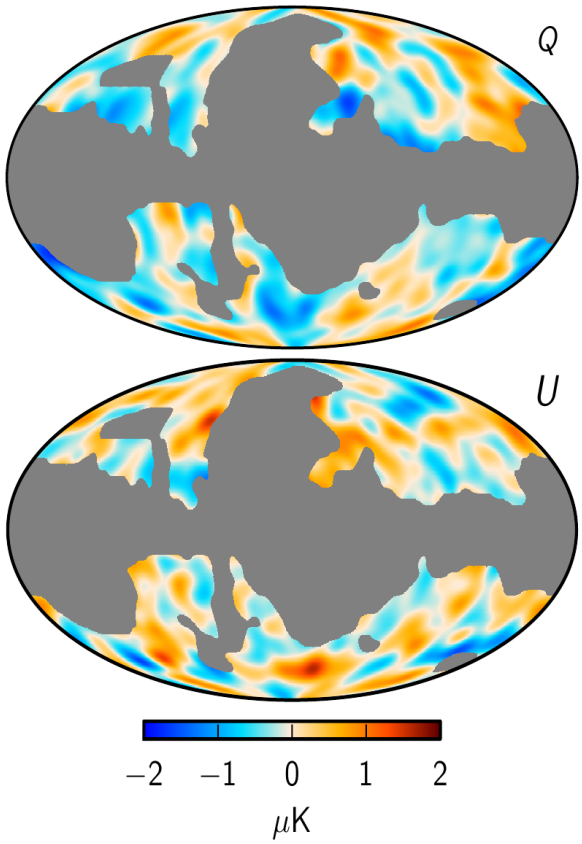

Figure 6.2: (a)Foreground cleaned, 70 GHz Q (top) and U (bottom) maps used for the low ℓ polarization part of the likelihood. Each of the maps covers 46 % of the sky (Planck Collaboration A13 2015).

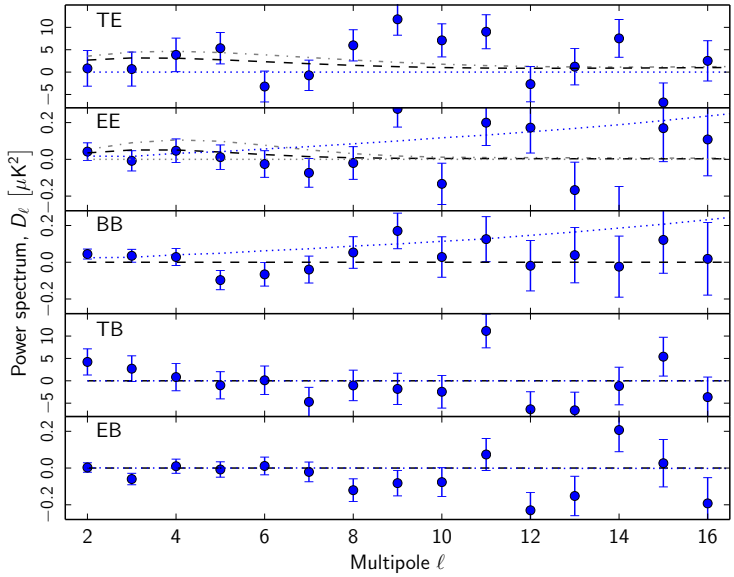

Figure 6.3: Polarised QML spectra from foreground cleaned maps. In the figure are also shown the 2013 best fit (dot-dashed), where $\tau = 0.089$ and the 2015 best fit (dashed), with a lower optical depth $\tau = 0.068$. In dotted blue is reported the the 70 GHz noise bias Planck Collaboration A13 (2015).

Low-ℓ spectra and parameters

From foreground-cleaned Q and U maps and `Commander` temperature map, the angular power spectra are derived using a quadratic maximum likelihood (QML) power spectrum estimator (Tegmark 1997; Tegmark & de Oliveira-Costa 2001). Figure 6.3 presents all five cross-polarisation power spectra (TE, EE, BB, TB, EB). In the case of EE and TE the *Planck* 2013 best fit power spectrum model are plotted. The *Planck* 2013 estimate for the optical depth $\tau = 0.089$, had been derived using the low-ℓ likelihood from *WMAP*-9 polarization maps (Bennett et al. 2013). This value is higher with respect to the one for the 2015 assumed model, which is $\tau = 0.068$. The optical depth τ, along with the scalar amplitude A_s, is the parameter that has the largest effect at low-ℓ. Indeed, temperature spectra are sensitive to the combination $A_s e^{-2\tau}$, while their lowest multipoles, that have not been reprocessed by reionisation, are only sensitive to A_s (sec. 1.3.6). Polarisation is instead sensitive to the combination $A_s\tau^2$ (sec. 1.4.5). To properly break the τ-A_s degeneracy, a combination of temperature and polarisation is needed. In Planck Collaboration. XIII. (2015), τ and A_s are left free in the analysis while the others parameters are fixed to their *Planck* 2015 ΛCDM best-fit value. The results are shown in Table 6.1. The low-ℓ only value of τ is lower than the previous WMAP estimation.

Parameter	ΛCDM
τ	0.067 ± 0.023
$\log[10^{10}A_s]$	2.952 ± 0.055
z_{re}	$8.9^{+2.5}_{-2.0}$
$10^9 A_s$	$1.92^{+0.10}_{-0.12}$
$A_s e^{-2\tau}$	$1.675^{+0.082}_{-0.093}$

Table 6.1: Results for the parameters (τ, A_s) that have been sampled in the `LowTEB` likelihood. Unsampled parameters are fixed to their ΛCDM 2015 best-fit fiducial values. All errors are 68 % c.l.(Planck Collaboration A13 2015).

6.1.2 A cross-spectra approach: *lollipop*

The pixel based approach requires the noise matrix to be reconstructed with extreme accuracy to avoid spurious bias on parameters reconstruction. This is indeed a difficult task due to the presence of residual systematics related to the instrument, the scanning strategy or the improper treatment of foregrounds. Previous studies, (Percival & Brown 2006; Hamimeche & Lewis 2008), developed a CMB analysis on large angular scales based on the likelihood definition in harmonic space in terms of *auto-spectra*, but these methods still need a perfect estimation of the noise and an accurate characterization of the systematics effects.

On the contrary, working in harmonic space using the *cross-spectra* method (as in chapter 5), allows to get rid of noise biases and to minimise the residual systematic effects by exploiting the cross-correlation between different CMB maps. In Mangilli et al. (2015) it is proposed to extend the cross spectra approach to large scales. The main difficulty with this low-ℓ extension is that the distribution of the $\hat{C}_\ell$ estimator is non Gaussian and the central limit theorem can not be invoked. The *lollipop* likelihood, for the estimation of spectra uses, as `HiLLiPOP`, the *Xpol* algorithm (sec. 5.4) based on pseudo-C_ℓ estimator. It is sub-optimal with respect to the QML mentioned in sec. 6.1.1, but ℓ-by-ℓ correlations are taken into account using Monte Carlo simulations. The level of correlation depends on the sky cut and the dataset considered. In Fig. 6.4(a) is shown the covariance matrix of the low-ℓ pseudo spectra directly

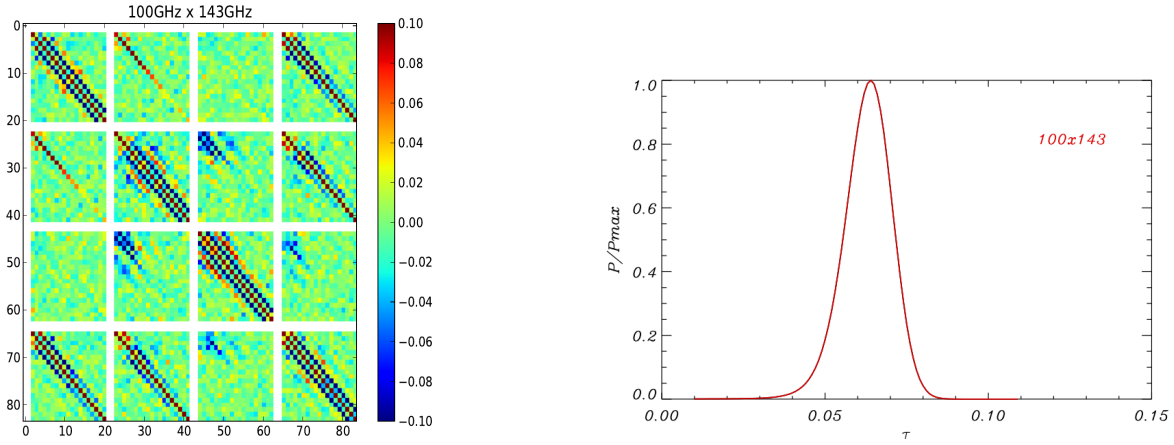

(a) (b)

Figure 6.4: (a) Correlation matrix for the 100 GHzx143GHz using 50% of the sky. Each block correspond to TT, EE, BB, TE Mangilli et al. (2015). (b) Posterior of the EE cross-spectrum obtained from the cross-correlation between HFI 100 and 143 GHz maps cleaned from dust and synchrotron by using the 353GHz and the 30GHz respectively.

derived in Mangilli et al. (2015) from MC simulations, for the *Planck* 100GHzx143GHz dataset using $f_{\rm sky}$=50%. The correlation are strong and can reach 50%.

In order to model the non-Gaussianity of the $\hat{C}_\ell$ estimators, the approximation that is proposed, is based on the modification of the Hamimeche&Lewis likelihood (H&L) (Hamimeche & Lewis 2008), adapted for the cross-spectra $C_\ell^{A\times B}$ and at low-ℓ. The general form of the H&L likelihood is defined for auto-spectra at intermediate and small scales ($\ell > 30$) as

$$-2ln\mathcal{L}(C_\ell^{th}|\hat{C}_\ell) = \sum_{\ell\ell'}[X_g]_\ell^T[M_f^{-1}]_{\ell\ell'}[X_g]_{\ell'}. \tag{6.7}$$

The $[M_f^{-1}]_{\ell\ell'}$ is the inverse of the C_ℓ-covariance matrix that allows to quantify the $\ell-\ell$ and the correlations of the T, E, B fields, while $[X_g]_\ell$ is the H&L transformed C_ℓ vector.

If the single EE field is considered the vector $[X_g]_\ell$ reads

$$[X_g]_\ell^{\rm EE} = \sqrt{C_\ell^{\rm EE,fid}}\mathbf{g}\left[\frac{\hat{C}_\ell^{\rm EE}}{C_\ell^{\rm EE,model}}\right]\sqrt{C_\ell^{\rm EE,fid}}, \tag{6.8}$$

where $g(x) = \sqrt{2(x - lnx - 1)}$.

For cross-spectra and at large angular scales, the $\hat{C}_\ell^{\rm EE}$ is not guaranteed to be positive. Mangilli et al. (2015) propose to add en effective offset o_ℓ^{EE} so that the function $g(x)$ is always well defined.

The offset can be derived form simulations, and depends on the shape of the C_ℓ at each ℓ but also on the noise level of the maps and on the masks used. There is, however, only a mild dependence on the fiducial model assumed.

The covariance matrix $[M_f]_{\ell\ell'}$ and the offset functions are computed from Monte Carlo simulations based on the correlated noise estimates derived from the jack-knives and for a given fiducial model.

$$[M_f]_{\ell\ell'} = \langle\left((C_\ell^{EE})_{\rm sim}^{AxB} - C_\ell^{\rm EE,fid}\right)\left((C_{\ell'}^{EE})_{\rm sim}^{AxB} - C_{\ell'}^{\rm EE,fid}\right)\rangle_{N_{\rm sim}}. \tag{6.9}$$

This ensures that the likelihood is unbiased and gives error bars that account for the systematic effects included in the simulations.

The *lollipop* likelihood version used in this thesis makes use of the EE cross-spectrum between HFI 100 and 143 GHz maps. These latter are cleaned using the 353 GHz as a template for the dust emission and the 30GHz for synchrotron emission. The *lollipop* likelihood considers a conservative skycut with $f_{\rm sky}$=0.5 and a multipole range $\ell = [4, 20]$.

The likelihood is sampled varying τ in the range $[0.01, 0.15]$ with a step $\Delta\tau = 0.001$ while all other parameters are fixed to the *Planck*-2015 best fit values. The degeneracy between A_s and τ is broken by fixing the amplitude of the first peak of the TT spectrum (directly related to $A_s e^{-2\tau}$) at $\ell = 200$. The results on the optical depth is showed in Fig. 6.4(b) and reads

$$\tau = 0.063 \pm 0.007 \quad (68\%, \textit{lollipop}). \tag{6.10}$$

There is a factor $\simeq 3$ improvement in the error-bars with respect to the `LowTEB` estimate presented in sec. 6.1.1. The result is promising but not definitive, since there can be residual systematics to be accounted for, that, properly treated, may reveal an even lower value for the optical depth. The *lollipop* likelihood will therefore used in this thesis as a benchmark to assess the dependency of the cosmological parameters in a limiting case (τ with a very small error).

6.2 The CMB lensing

The *Planck* collaboration achieved the most significant measurement of the CMB lensing potential at a level of 40σ (Planck Collaboration. XV. 2015). As mentioned in chapter 1, the CMB photons carrie informations about the late time universe through the gravitational deflection they experience in the path toward us. This effect is subtle but can be measured statistically with high angular resolution and low-noise data such as the one from *Planck*. CMB fluctuations are remapped from $\hat{\mathbf{n}}$ to $\hat{\mathbf{n}} + \nabla\phi(\hat{\mathbf{n}})$ where $\phi(\hat{\mathbf{n}})$ is the lensing potential, an integrated measurement of the mass distribution back to the last scattering surface (e.g. Lewis & Challinor (2006a)). It is sensitive to late time parameters that modify the growth of structures, as the neutrino mass (Smith et al. 2009).

The measurement of $C_\ell^{\phi\phi}$ is based on foreground cleaned SMICA (Appendix A.2) maps combining all the nine *Planck* frequencies band. Being mainly a small scale effect, most of the lensing information comes from the 143 and 217 GHz channels, which have small beams and low noise (see Table 3.1).

The lensing potential is reconstructed using a quadratic estimators that exploits the statistical anisotropy induced by lensing (Okamoto & Hu 2003). There are five possible estimators (the five combination of T, E and B neglecting BB) that are combined together to form a mininum-variance estimator $\hat{\phi}^{\rm MV}$ (Fig 6.5). The 4-point correlation function of the lensed CMB probes the power spectrum of the lensing potential since, at leading order, the connected part (trispectrum) is proportional to the latter (Hu 2001). There are also a disconnected part that, non zero even in absence of lensing, needs to be corrected for, relying partially on simulations (Planck Collaboration XVII 2014; Planck Collaboration. XV. 2015).

6.2.1 Lensing likelihood and parameter constraints

A likelihood can be constructed directly for the lensing power spectrum (Planck Collaboration. XV. 2015). This Gaussian log-likelihood in bandpowers of the estimate power spectrum is given by

$$-2\log\mathcal{L}_\phi = \mathcal{B}_i^\ell(\hat{C}_\ell^{\phi\phi} - C_\ell^{\phi\phi,\,\rm th})\left[\Sigma^{-1}\right]^{ij}\mathcal{B}_j^{\ell'}(\hat{C}_{\ell'}^{\phi\phi} - C_{\ell'}^{\phi\phi,\,\rm th}), \tag{6.11}$$

where i and j index the bins, $\mathcal{B}_i^\ell$ is the bandpower binning function for the i-th bin, and Σ the covariance matrix for the bin estimates.

As discussed in Planck Collaboration. XV. (2015) and Planck Collaboration. XIII. (2015), the primary parameter dependency of $C_\ell^{\phi\phi}$ is through A_s and $\ell_{\rm eq}$, where $\ell_{\rm eq} \propto 1/\theta_{\rm eq}$) is the angular multipole

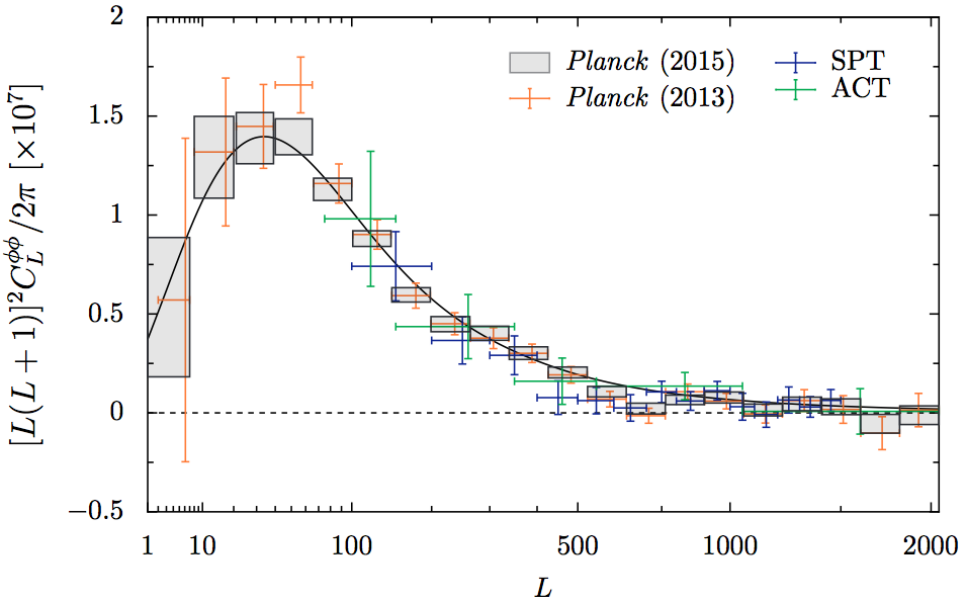

Figure 6.5: *Planck* 2015 full mission $C_\ell^{\phi\phi}$ measurement together with 2013 *Planck* measurement and SPT and ACT measurement. In black is shown the fiducial ΛCDM theory power spectrum. The figure is taken from (Planck Collaboration. XV. 2015).

corresponding to the horizon size at matter radiation equality. The lensing likelihood alone is able to constrain a combination of σ_8 and Ω_m with a few % precision

$$\sigma_8 \Omega_m^{0.25} = 0.591 \pm 0.021 \quad (68\%, \text{lensing}). \tag{6.12}$$

Combining lensing with high-ℓ temperature data, a constraint independent of the low-ℓ polarisation can be put on the optical depth since lensing partially breaks the A_s-τ degeneracy

$$\tau = 0.070 \pm 0.024 \quad (68\%, \texttt{Plik} + \texttt{Commander} + \text{lensing}). \tag{6.13}$$

This is true also for the lensing information encoded in the CMB temperature power spectrum, meaning that τ can be (weakly) constrained using high-ℓ data alone (chapter 7). When one tries to put constraints on non-flat models, the use of CMB temperature power spectrum alone suffers from the geometrical degeneracy (e.g. Stompor & Efstathiou (1999)), i.e. it provides multiple ways to combine late time parameters to give the same observed angular diameter distance. Therefore, one needs an information at another redshift and the addition of lensing allows a measurement of the curvature from CMB alone data

$$\Omega_k = -0.005^{+0.009}_{-0.007} \quad (68\%, \texttt{Plik} + \texttt{LowTEB} + \text{lensing}). \tag{6.14}$$

In principle, since the *Planck* power spectra are sensitive to the lensing smoothing of the acoustic peaks, the geometrical degeneracy is slightly broken also without using the lensing information from the trispectrum. There is however a subtle point: the temperature power spectrum prefers a larger lensing smoothing than expected from ΛCDM (around 2σ level) (Planck Collaboration. XVI. 2014; Planck Collaboration. XIII. 2015), pushing, for example, the curvature constraints to negative values, and, for what concern this thesis, neutrino masses to low values. This effect is partially regularised by the addition of the lensing likelihood. However, constraint on neutrino masses have been found to be sensitive to the lensing multipole range used. The more aggressive $8 \leqslant \ell \leqslant 2048$ range, with respect to the official conservative $40 \leqslant \ell \leqslant 400$ range, shows a mild preference for a non zero neutrino mass, but the multipole range $300 \leqslant \ell \leqslant 900$ fails some serious consistency tests Planck Collaboration. XV. (2015). The influence of lensing on the neutrino mass constraints of the `HiLLiPOP` likelihood is discussed in chapter 8.

6.3 The very high-ℓ data

Although *Planck* alone is able to put strong constraints on the cosmological parameters, its sensitivity on the foregrounds is limited. As discussed in chapter 5, for example, we have not much constraining power on the SZ effect. In order to tighten the constraints on foregrounds parameters, in chapter 7 and 8, we add the information from high resolution datasets from the Atacama Cosmology Telescope[2] (ACT) and the South Pole Telescope[3] (SPT) projects to the *Planck* CMB likelihood. Those additional data are called "very high-ℓ" (VHL) throughout this thesis.

Atacama Cosmology Telescope

We use the final ACT temperature power spectra presented in Das et al. (2014b). These are 148 GHz, 143x218 and 218 GHz power spectra built from observations on two different sky areas ("south" and "equatorial") and several seasons of observation, for multipoles between 1000 and 10000 (for 148 GHz) and 1500 to 10000 otherwise.

South Pole Telescope

Two distinct datasets from SPT are considered. The higher ℓ part, dubbed `SPT_high`, comes from the complete 24560 deg^2 SPT-Sz survey described in George et al. (2014). It results from observations at 95, 150 and 220 GHz. The cross-spectra cover the ℓ range between 2000 and 13000. We also include the Story et al. (2012) dataset, dubbed `SPT_low`, consisting of a 150 GHz power spectrum which ranges from $\ell = 650$ to 3000. All spectra are expressed in $K_{\rm CMB}$. In (Planck Collaboration. XVI. 2014), this latter dataset had been excluded, after a thorough evaluation of its compatibility with *Planck* data. Its combination with WMAP-7y data gave results in tension with *Planck* 2013 cosmology (Hou et al. 2014), pointing, for example, to a higher value of H_0. This was linked to a potential SPT/WMAP intercalibration systematic due to their limited multipole overlap and respective S/N ratios in that area. This systematic is much lower with the *Planck* data that extend to much higher ℓ than *WMAP*: at $\ell \geqslant 1800$ the agreement with *Planck* is good. Since the *Planck* calibration has changed since then, and we do not notice any incompatibility between *Planck* and ACT+SPT cosmology, we decided to use it in our analysis. In chapter 8, we give, however, results on neutrinos with and without `SPT_low` to test the robustness.

6.3.1 Foregrounds modelling

We chose to use as much as possible a model for astrophysical foregrounds coherent with what has been set-up for `HiLLiPOP`. For all datasets, we use the same template for tSZ, kSZ, CIB and tSZxCIB described in sec. 5.6. As these templates have been computed for the *Planck* frequencies, they need to be extrapolated to the ACT and SPT frequencies and bandpasses.

For tSZ we scale the template with the usual $f_\nu = x \coth x/2 - 4$ function where $x = h\nu/k_{\rm B}T_{\rm CMB}$ (sec. 5.6.4), using the effective frequencies given in Dunkley et al. (2013).

For CIB and tSZxCIB, we start from the templates in $Jy^2 sr^{-1}$ in the IRAS convention ($\nu I(\nu) = $ cste spectrum) for *Planck* frequencies and band-passes, already described in sec. 5.6.3 and sec. 5.6.6. Then, for CIB, we use the conversion factors from *Planck* to the ACT/SPT bandpasses, assuming, for the CIB, the Béthermin et al. (2012) spectral energy density (SED) combined with unit conversion factors to $K_{\rm CMB}$, for the ACT and SPT bandpasses (Lagache 2014). These factors are given in Table 6.2.

[2] http://www.princeton.edu/act/
[3] https://pole.uchicago.edu/

In the 2013 analysis (Planck Collaboration. XVI. 2014) the CIB has been modelled with a power law with spectral index $\gamma_{\rm CIB}$ not taking into account the transition from the 2-halo to the 1-halo clustering. This resulted in a tension between the *Planck* and *Planck* + VHL results (VHL preferred a stepper value for the spectral index $\gamma_{\rm CIB} = 0.4$ with respect to the value fitted with *Planck* alone $\gamma_{\rm CIB} = 0.8$).

Dataset	Frequency (GHz)	$MJy\ sr^{-1}/K_{CMB}$	HFI freq. (GHz)	conversion
ACT	148	401.936	143	0.85
	218	485.311	217	1.056
SPT	95	234.042	100	1.090
	150	413.540	143	0.7688
	220	477.017	217	1.061

Table 6.2: Conversion factors used for the foreground template extrapolation to ACT and SPT bandpasses (Lagache 2014).

For the tSZxCIB, for the $(\nu_1 \times \nu_2)$ cross-spectrum (from the ACT or SPT dataset), we scale the nearest HFI cross-spectrum $(\nu_1^P \times \nu_2^P)$ using the ratio :

$$S_{\nu_1,\nu_2} = \frac{f_{\nu_1} C_{\nu_2} + f_{\nu_2} C_{\nu_1}}{f_{\nu_1^P} C_{\nu_2^P} + f_{\nu_2^P} C_{\nu_1^P}} \tag{6.15}$$

prior to convert it to $K_{\rm CMB}$ using the above factors. As shown on Figure 6.6 this scaling applies within 10% for the HFI cross-spectra.

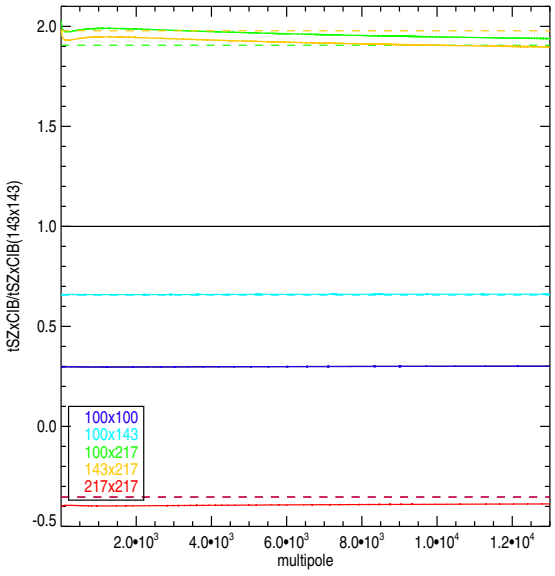

Figure 6.6: Ratios between the tSZxCIB cross spectra for HFI with the 143x143 GHz one (plain lines) compared with the ratios of the results of equation 6.15 for the same frequencies (dashed lines). The template follows the scaling from equation 6.15 to better than 10% on average.

We have to add to this common set of foreground templates a few more specific to each datasets:

- Point sources: We model the unresolved (and unmasked) point source components in the ACT and SPT spectra with one amplitude ($A_{\rm PS}$) parameter per cross-spectrum, in analogy with sec. 5.6.2. This thus introduces six additional nuisance parameters for the ACT, 6 for the `SPT_high` and one for the `SPT_low` datasets, respectively.

- Galactic dust: following Dunkley et al. (2013) and Das et al. (2014b), we model the dust contribution in the ACT power spectra as a power law :

$$\mathcal{B}_\ell^{dust}(i,j) \;=\; A_{dust}\left(\frac{\ell}{3000}\right)^{-0.7}\left(\frac{\nu_i\nu_j}{\nu_0^2}\right)^{3.8}\left[\frac{g(\nu_i)g(\nu_j)}{g(\nu_0)^2}\right] \tag{6.16}$$

  We therefore introduce two nuisance parameters A_{dust}, one for each part of the ACT dataset, and set the reference frequency ν_0 to 150 GHz.

  For the SPT datasets, following George et al. (2014), we use a fixed template, with amplitudes 0.16, 0.21 and 2.19 μK^2_{CMB} (at ℓ=3000) at 95, 150 and 218 GHz , respectively and an $\ell^{-1.2}$ spatial dependency.

6.3.2 Likelihoods

We compute one likelihood for each of the five *VHL* datasets following the method described in (Dunkley et al. 2013), the main difference being the use of the 2014 SPT spectra. We use the respective published window functions to bin the (CMB + foregrounds) model, and the released covariance matrices Σ to compute the likelihood[4]. In all cases, these include beam uncertainties. For the George et al. (2014) dataset, since we fit the relative calibration, we choose to use the covariance matrix which did not include calibration uncertainties.

We use a Gaussian approximation for the binned power spectra bandpowers C_b to write this likelihood

$$-2\mathcal{L} \;=\; \left(C_b - C_b^{th}\right)^T \Sigma^{-1}\left(C_b - C_b^{th}\right). \tag{6.17}$$

As we combine several datasets together, we introduced 9 additional nuisance parameters to account for their relative calibration uncertainties (at map level). As the different datasets have been calibrated in different ways we have to impose priors on some of them. The Das et al. (2014b) and Story et al. (2012) datasets have been calibrated on *WMAP* maps, while the more recent George et al. (2014) was calibrated on *Planck* 2013 maps. The *Planck* 2013 data presented a calibration offset with respect to *WMAP*. The 2015 release, on the contrary, due to an independent calibration, is now much closer to *WMAP*. Hence, we impose for the `SPT_high` dataset calibration parameters Gaussian priors centred on 1.01 with widths equal to 1,1 and 2% for each frequency, respectively.

Table 6.3 summarises the nuisance parameters associated to the VHL likelihoods.

We check in Fig. 6.7 that the new ACT+SPT data are consistent with the *Planck* ones. To this purpose we compare the *VHL* likelihood *alone* results to `HiLLiPOP`, determining independently the cosmology+nuisance parameters of each experiment. The ΛCDM cosmology is consistent between both experiments, and, as expected, the *VHL* data constraints on the (common) foreground parameters are tighter than in the `HiLLiPOP` case.

[4] http://lambda.gsfc.nasa.gov/product/

name	definition	prior (if any)
	SPT_high	
SPT_high_95_cal	map calibration (95 GHz)	1.01 ± 0.01
SPT_high_150_cal	map calibration (150 GHz)	1.01 ± 0.01
SPT_high_220_cal	map calibration (220 GHz)	1.01 ± 0.02
SPT_high_Aps_95x95	PS amplitude (95x95 GHz)	
SPT_high_Aps_95x150	PS amplitude (95x150 GHz)	
SPT_high_Aps_95x220	PS amplitude (95x220 GHz)	
SPT_high_Aps_150x150	PS amplitude (150x150 GHz)	
SPT_high_Aps_150x220	PS amplitude (150x220 GHz)	
SPT_high_Aps_220x220	PS amplitude (220x220 GHz)	
	SPT_low	
SPT_low_Aps	PS amplitude	
SPT_low_cal	map calibration	
	ACT_south/equat	
ACT_[field]_148_cal	map calibration (148 GHz)	
ACT_[field]_220_cal	map calibration (220 GHz)	
ACT_[field]_ADust	dust amplitude	
ACT_[field]_Aps_148x148	PS amplitude (148x148 GHz)	
ACT_[field]_Aps_148x220	PS amplitude (148x220 GHz)	
ACT_[field]_Aps_220x220	PS amplitude (220x220 GHz)	

Table 6.3: Nuisance parameters for the ACT and SPT likelihoods

6.4 The Baryon Acoustic Oscillations

Baryon Acoustic Oscillations (BAO) are the imprints left by acoustic waves in the primordial fluid on the structures we see today (e.g.Bassett & Hlozek (2010)). The measurements of the BAO feature in the correlation function of large-scale structure (LSS) have been obtained from different galaxy redshift surveys. They provide constraints on the distances at redshift $0.1 \leq z \leq 0.7$ (Anderson et al. 2014) and even up to $z \sim 2.3$ with Lyα forest (Delubac et al. 2015). The first convincing detection came in 2005 from the SDSS Data Release 3 (Eisenstein et al. 2005). BAO measurements are an extremely powerful complementary data set to *Planck* data since they are a precise and almost systematics-free geometrical measurement. This geometrical nature helps in breaking the degeneracies of CMB data and gives better constraints on ΛCDM and on extensions to models with curvature or with free parameters for dark energy. On the neutrinos side, the BAO allows to significantly lower the bound on the absolute mass scale and reduce also the error bars on $N_{\rm eff}$ (chapter 8). Interestingly, the addition of redshift space distortion (RSD) data from BOSS CMASS-DR11 to *Planck* data, shows a few sigma preference for a non-zero neutrino mass (Beutler et al. 2014). This is discussed further in sec. 8.1.7. We included in our analysis the latest BAO measurements, using only the low redshift datasets that are not in tension with *Planck* data[5].

[5]Lyman α BAO measurements, at higher redshift, have almost 3σ tension with *Planck* ΛCDM cosmology and bigger errors. In Planck Collaboration. XIII. (2015) and Aubourg et al. (2014) is argued that, this can be the sign of some still uncounted systematics in the more complex Lyα BAO reconstruction. We thus decided not to include this data in our final analysis.

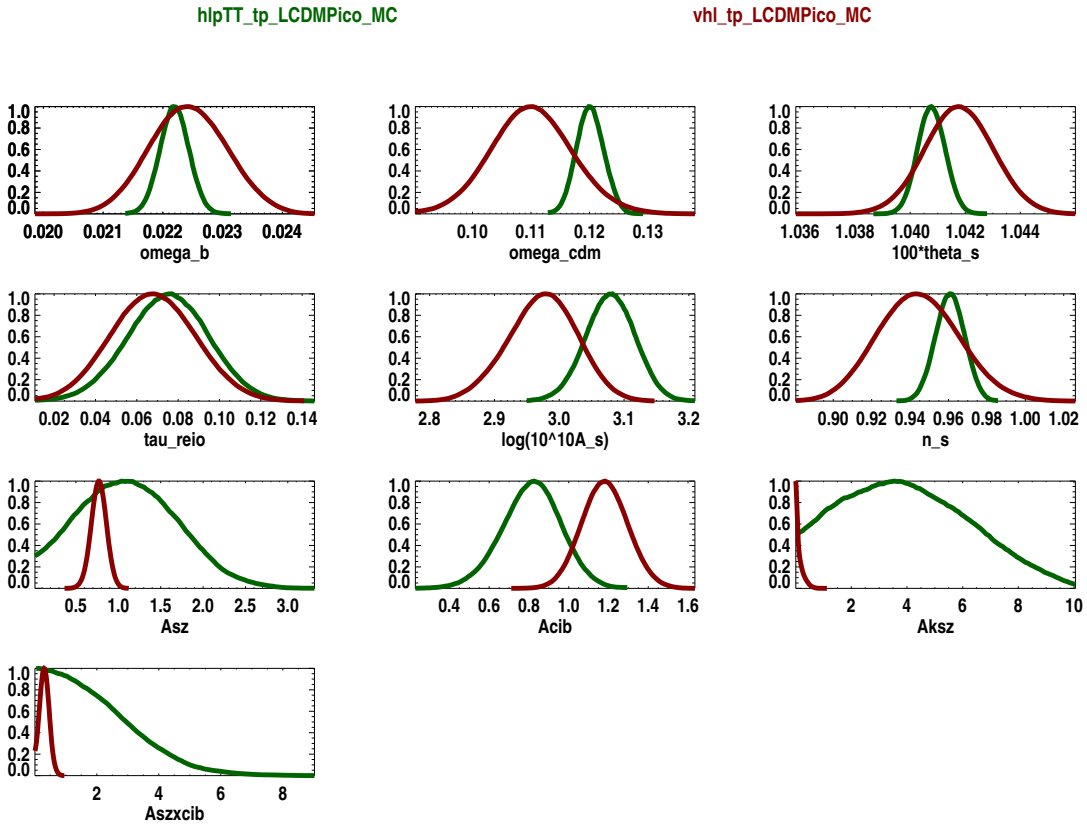

Figure 6.7: Posterior distributions of the cosmological and nuisance parameters obtained from the ACT SPT likelihood (in red) and from `HiLLiPOP` (in green). For the sake of simplicity we only display the parameters that are common to both likelihoods but all nuisance parameters are sampled in each case. A Gaussian prior $\tau = 0.07 \pm 0.02$ has been used in both cases.

6.4.1 A standard ruler

The measurements of the acoustic scale at various redshift, allow to infer the angular diameter distance D_A (Eq. 1.25) and $H(z)$ (Eq. 1.31). The acoustic length scale (Eq. 1.126) can be computed as the comoving distance that the sound waves could have travel from Big Bang to the baryon dragging epoch $z_{\rm drag}$, i.e the time at which the baryons are released from the Compton drag of the photons (Hu & Sugiyama 1996; Eisenstein & Hu 1998; Eisenstein et al. 1998). It depends on $\Omega_m h^2$ and $\Omega_b h^2$, that are well measured by the relative height of the CMB acoustic peaks. The scale is large, about 150 Mpc comoving, not much influenced by late-time non linear physics (Seo & Eisenstein 2005) and thus an excellent standard ruler.

The BAO measurements allow to access $H(z)r_s$ through separation along the line of sight and $D_A(z)r_s$ through separation transverse to the line of sight (Fig. 6.8). However, what is in generally inferred is the spherically averaged 2-point measurements, fixed by the projection of $r_s(z_{\rm drag})$

$$D_{\rm V}(z) = \left((1+z)^2 D_A^2 \frac{cz}{H(z)}\right)^{1/3}, \tag{6.18}$$

and only the latest DR11 release of SDSS data recommends to use the *anisotropic* measurement, i.e. $H(z)$ and D_A separately.

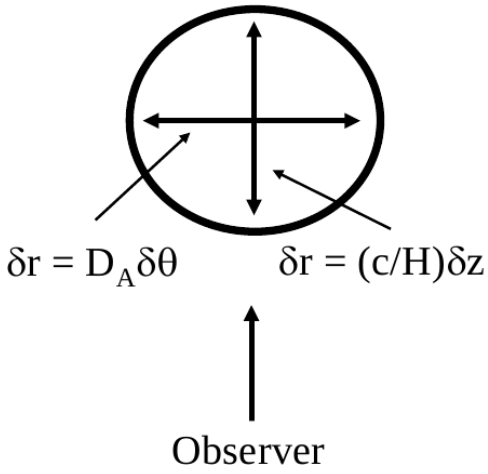

Figure 6.8: The BAO measurement allow to infer the angular diameter distance D_A and $H(z)$. The figure is taken from D. Einseinstein's talk at ESLAB

6.4.2 BAO measurements

Although we have tested various combination of the available BAO measurements, in our final configuration we use:

- low z ($z_{\rm eff} = 0.1$) measurement from 6dF (Beutler et al. 2011), giving

$$r_s(z_d)/D_V(z_{\rm eff}) = 0.336 \pm 0.015 \tag{6.19}$$

- the BOSS DR11 release (Anderson et al. 2014) including:
  - LOWZ measurement at $z_{\rm eff} = 0.32$

$$D_V(z_{\rm eff}) = (1264 \pm 25\ {\rm Mpc})\left(\frac{r_s}{r_s^{\rm fid}}\right) \tag{6.20}$$

  - CMASS anisotropic measurements at $z_{\rm eff} = 0.57$

$$D_A(z_{\rm eff}) = (1421 \pm 20\ {\rm Mpc})\left(\frac{r_s}{r_s^{\rm fid}}\right) \tag{6.21}$$

$$H(z_{\rm eff}) = \left(96.8 \pm 3.4\ {\rm Km\ s^{-1}Mpc^{-1}}\right)\left(\frac{r_s^{\rm fid}}{r_s}\right) \tag{6.22}$$

The $r_s/r_s^{\rm fid}$ term considers the difference in the calculation of the sound horizon between the Eisenstein et al. (1998) and the `CLASS` (or `CAMB`) definition[6].

To add the BAO information to our analysis, we minimise the following function

$$\chi^2_{\rm BAO} = (\mathbf{d}_z - \mathbf{d}_z^{\rm BAO})^\dagger C^{-1}_{\rm BAO}(\mathbf{d}_z - \mathbf{d}_z^{\rm BAO}) \tag{6.23}$$

[6]For example with Anderson et al. (2014) fiducial cosmology $r_s(z_{\rm drag})^{\rm fid} = 153.19$Mpc against the 149.28 Mpc from `CAMB`.

where $\mathbf{d}_z^{\rm BAO}$ is the vector including all the previous measurements and $C_{\rm BAO}$ is the covariance matrix. We use `CLASS` for the computation of geometrical observables. In Fig. 6.9 we report the comparison between the BAO results (assuming Gaussian measurement) obtained with 6dF and BOSS and the CMB estimation obtained with `HiLLiPOP` + `LowTEB` (with and without VHL data). The agreement is within 1σ.

In Aubourg et al. (2014) is reported the measurement

$$H_0 = 67.3 \pm 1.1 \text{ Km s}^{-1}\text{Mpc}^{-1} \quad (68\%, \text{BAO+SN (CMB-calibrated)}), \tag{6.24}$$

obtained from the combination of BAO and the Supernova Ia (SN) data (described in sec.6.5). This in agreement with our estimation from CMB TT alone

$$H_0 = 67.2 \pm 0.9 \text{ Km s}^{-1}\text{Mpc}^{-1} \quad (68\%, \text{CMB (TT)}). \tag{6.25}$$

The combined constraint yields a reduction in error bars

$$H_0 = 67.6 \pm 0.55 \text{ Km s}^{-1}\text{Mpc}^{-1} \quad (68\%, \text{CMB + BAO + SN}). \tag{6.26}$$

This is discussed further in chapter 7.

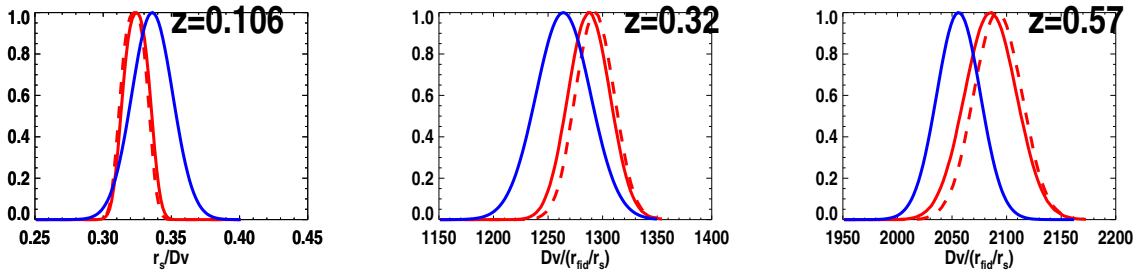

Figure 6.9: In blue are reported the measurements (assuming they are Gaussian) obtained by different galaxy redshift surveys: 6dF and BOSS (both for LOWZ and CMASS the isotropic measurement is considered). In red the posterior distributions of the same parameters obtained sampling the TT `HiLLiPOP` + `LowTEB` (solid red) or the `HiLLiPOP` +`LowTEB` with the addition of the VHL data (dashed red).

6.5 The Supernovae Ia

A Type Ia supernova (SN Ia) is the explosion of a white dwarf star with a carbon-oxygen nucleus in a binary star system (e.g. Ruiz-Lapuente (2007)). The white dwarf accretes matter from the nearby companion causing an elevation of the core temperature and density. Once the Chandrasekhar's limit (Chandrasekhar 1931) is attained, the electron degeneracy pressure is unable to prevent collapse, and, a substantial fraction of the matter in the white dwarf undergoes a runaway reaction, that is more important than the energy loss via neutrinos. The energy in enough to unbind the star in a supernova explosion. These explosions always release roughly the same amount of energy, and studies of relatively nearby type Ia supernovae have shown that they reach almost the same peak brightness in every case. Therefore they can be used as "standard candles" and their true distance can be determined. As discussed in chapter 1, SNe Ia have been fundamental in the discovery of the late time acceleration of the universe and constitutes a powerful complementary probe to CMB constraints. However, the standardization process

is complicated and one has to correct their absolute apparent magnitudes using light-curve shape, photometric color at maximum and host galaxy mass. In (Planck Collaboration. XVI. 2014) the discrepancy on the value of Ω_m between *Planck* and SNe Ia results, was interpreted as residual systematics errors in the SNe data not properly accounted for in the covariance matrix. Since then the SNe Ia data has been revised in depth and the Joint Light-curve Analysis (JLA) data (Betoule et al. 2014a) has been released.

6.5.1 The JLA compilation

The JLA compilation is the result of an extensive campaign to improve relative photometric calibration of SN Ia light curves and associated distances and contains 740 SNe. It contains a selection of 374 SNe Ia from SDSS-II (Sako et al. 2014) combined with the compilation of (Conley et al. 2011). This latter includes 242 spectroscopically confirmed SNe from (Guy et al. 2010) in the redshift range $0.2 < z < 1$, 14 very high redshift ($0.7 < z < 1.4$) SNe from the HST (Riess et al. 2007), and low-z ($z < 0.08$) data from various origins. The joint analysis of these data was indeed motivated by their complementarity in redshift, and the final sample covers the redshift range $0.01 < z < 1.2$, allowing stringent constraint on the expansion rate.

6.5.2 Supernovae model and distance estimates

The behaviour of SNe Ia is reasonably well captured by a parameter X_1 describing the time stretching of the light-curve, and another C describing the SN color at maximum brightness (e.g. Tripp (1998)). The distance estimator of Eq. 1.30, that is widely used in SN studies, is a linear model assuming that object with identical color shape and galactic environment have, on average, the same intrinsic luminosity for all redshift. In more details, Betoule et al. (2014a) use

$$\mu = m_{\rm B}^{\star} - (M_b - \alpha \times X_1 + \beta \times C) \tag{6.27}$$

where $\mu = 5log_{10}(D_L/10\text{pc})$ with D_L the luminosity distance defined in sec. 1.26. $m_{\rm B}^{\star}$ is the observed peak magnitude in the rest frame B-band and α, β and M_B are nuisance parameters. The absolute magnitude M_B, depends on the host galaxy properties but this dependency in not well understood. It is in general parametrised as a function of the host stellar mass $M_{\rm stellar}$ plus a bias Δ_M as follows

$$M_B = \begin{cases} M'_B & \text{if } M_{\rm stellar} < 10^{10} M_{\odot}, \\ M'_B + \Delta_M & \text{otherwise.} \end{cases} \tag{6.28}$$

The light-curve parameters ($m_{\rm B}^{\star}$, X_1, C) result from the fit of a model of the SN Ia spectral sequence to the photometric data. They use the SALT2 model (Guy et al. 2007), retrained on JLA data.

In a flat universe, SNe alone provide constraint on Ω_m but can not constrain H_0. Hence, to fit a ΛCDM cosmology to their data, Betoule et al. (2014a) have fixed $H_0 = 70\text{kms}^{-1}\text{Mpc}^{-1}$. Using the estimator of Eq. 6.27, they minimise the following χ^2

$$\chi^2_{\rm SN} = (\hat{\boldsymbol{\mu}} - \boldsymbol{\mu}_{\Lambda CDM}(z;\Omega_m))^{\dagger} C_{\rm SN}^{-1} (\hat{\boldsymbol{\mu}} - \boldsymbol{\mu}_{\Lambda CDM}(z;\Omega_m)) \tag{6.29}$$

where C the covariance matrix that includes both statistical end systematic uncertainties. The free parameters are thus Ω_m and the nuisances α, β, M'_B and Δ_m.

The result, using the JLA compilation alone for the dark matter density is

$$\Omega_m = 0.295 \pm 0.034 \quad (68\%, \text{JLA alone}), \tag{6.30}$$

and the fitted values for the nuisance parameters can be found in the first column of Table 6.4. In Fig. 6.10 is shown the Hubble diagram and their ΛCDM fit.

We included in our analysis the C++ code from Betoule et al. (2014a), providing the $\chi^2_{\rm SN}$ of Eq. 6.29 to be interfaced to `CLASS` computation of D_L, for a given set of cosmological (+ nuisances) parameters. Given the consistency between *Planck* and the JLA sample, the inclusion of such data in the analysis improves constraints on cosmological parameters as discussed in chapter 7 and 8. In Fig. 6.11 we show the posterior distribution of nuisance parameter of the JLA likelihood sampled together with the `HiLLiPOP` likelihood. The means and the 68% error bars are reported in the second column of Table 6.4 and are in excellent agreement with the JLA-alone analysis.

Parameter	JLA	`HiLLiPOP` TT + JLA
α	0.141 ± 0.006	0.140 ± 0.007
β	3.101 ± 0.075	3.101 ± 0.075
M'_B	-19.05 ± 0.02	-19.12 ± 0.02
Δ_M	-0.070 ± 0.023	-0.069 ± 0.021

Table 6.4: Fitted values for the nuisance parameters. The first column shows values from Betoule et al. (2014a), obtaining from JLA sample alone. In the second column are reported the values from the joint `HiLLiPOP` + `LowTEB` + JLA fit. The corresponding posterior distributions are shown in Fig. 6.11.

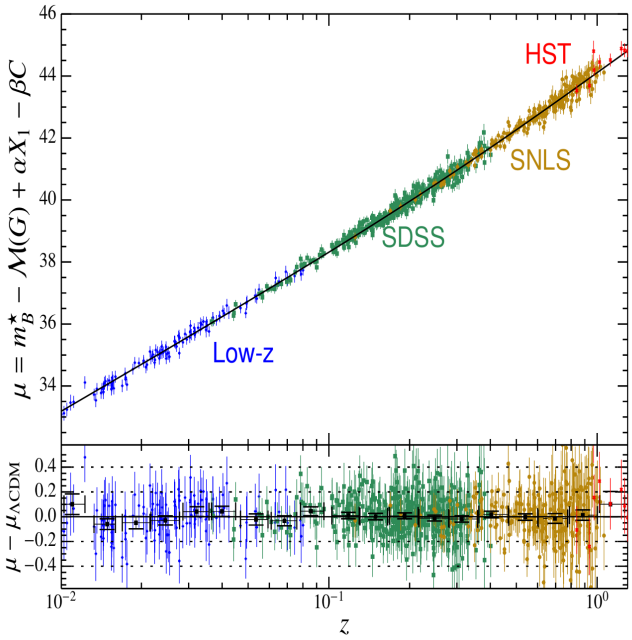

Figure 6.10: *Top*: the Hubble diagram for the JLA sample (described in the text). The black line is the best fit ΛCDM (with fixed $H_0 = 70 \mathrm{kms}^{-1}\mathrm{Mpc}^{-1}$). *Bottom*: Residuals as a function of redshift. (Betoule et al. 2014a)

Conclusions

In this chapter we have presented a panoramic view of the likelihoods used in this thesis to complement the high-ℓ `HiLLiPOP` likelihood (chapter 5). A fundamental piece are the low-ℓ data, especially the polarisation one, allowing to break the τ-A_s degeneracy. We have described the *Planck* pixel based likelihood

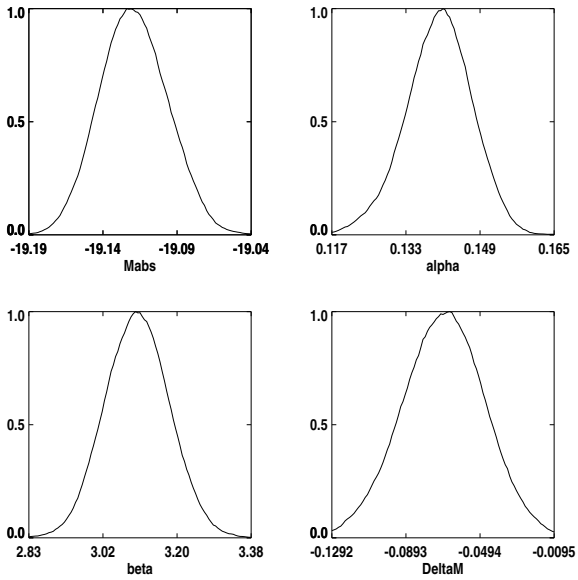

Figure 6.11: Posterior distribution for the nuisance paramaters of the JLA likelihood obtained sampling it in combination with `HiLLiPOP` and `LowTEB`.

and the innovative approach of a low-ℓ cross spectra likelihood, *lollipop*. We have also described the *Planck* lensing likelihood obtained from the CMB 4-point correlation function. Then, the small scale likelihood from the ground based CMB experiments ACT and SPT has been presented with particular attention to the residual foreground modelling and its consistence with the one used for the `HiLLiPOP` likelihood. In the last part of the chapter we have presented the low redshift BAO and the JLA Supernova compilation data used in this thesis, stressing on their compatibility with the *Planck* ΛCDM cosmology and their constraining power. The next chapters is dedicated to the discussion of the results: the precise constraints on the base ΛCDM model will be addressed in chapter 7, while its natural extensions into the neutrino sector will be discussed in chapter 8.

Chapter 7

ΛCDM cosmological parameters

This chapter presents the cosmological results based on the *Planck* full mission high-ℓ temperature and polarisation data. We use the `HiLLiPOP` likelihood described in chapter 5, optionally combined with the low-ℓ likelihood and the external datasets described in chapter 6. We test the "base" ΛCDM model, i.e. if *Planck* temperature and polarisation power spectra are consistent with the spatially-flat six-parameter cosmology described in chapter 1. We also consider the ΛCDM $+A_{\rm L}$ extension that allows to look for subtle effects from residual foregrounds and systematics in the data. As in Planck Collaboration. XVI. (2014); Planck Collaboration. XIII. (2015), we find a very good agreement between the data and the standard cosmological paradigm. The neutrino sector extension is postponed to chapter 8.

This chapter is organised as follows. In sec. 7.1 we specify the Boltzmann solver used for the computation of the theoretical spectra. We then present the results, using *Planck* high-ℓ temperature data alone in sec. 7.2.1, while the consistency with polarisation results is addressed in sec. 7.2.2. In sec. 7.2.3 we cross check the MCMC adaptive posteriors results with the ones obtained via the profile likelihood procedure. In sec. 7.2.4 the `HiLLiPOP` constraints are compared with the other results obtained in Planck Collaboration. XIII. (2015) using the baseline `Plik` likelihood, finding a very good agreement for both temperature and temperature plus polarisation results. In sec. 7.2.5 we discuss in more details the effects of the addition of the low multipoles data and, in sec. 7.2.6, we present the results on the $A_{\rm L}$ parameter and their implication on the constraints on the τ parameter (sec. 7.2.7). In sec. 7.3.1 we combine the *Planck* data with the ones from the CMB ground based experiments ACT and SPT, described in chapter 6. The addition of this very high-ℓ (VHL) data allows to put better constrains on the foregrounds. Moreover, the VHL seem to help treating the tension related to the $A_{\rm L}$ parameter. Finally, in sec. 7.4, we present the improved constraints when the powerful late time distance measurement data (BAO and Supernovae described in chapter 6) are added.

7.1 Boltzmann code(s)

The results of this thesis are obtained using the `CLASS` (Blas et al. 2011) Boltzmann equation solver which computes detailed spectra by evolving the cosmological background and perturbation equations. `CLASS`, written in C, is modular, thus flexible and well adapted to our analysis framework. It uses a commonly known notation, following the equations from Ma & Bertschinger (1995). Besides this, `CLASS` allows the definition of all the numerical precision parameters that enters the computations. We use two settings depending on the statistical methodology applied:

- For the Bayesian MCMC sampling of the posterior distribution (sec. 4.2) we use the default `CLASS` precision parameters since the nature of the algorithm itself smooths any discontinuity.

class parameter	value
tol_thermo_integration	10^{-3}
tol_perturb_integration	10^{-6}
reionization_optical_depth_tol	10^{-5}
l_logstep	1.08
l_linstep	25
perturb_sampling_stepsize	0.04
delta_l_max	1000
accurate_lensing	1

Table 7.1: High-precision settings of the CLASS non-default parameters used to reconstruct profile-likelihoods. The last parameter (accurate_lensing) is only usefull (and used) for *VHL* results (sec. 7.3.1).

- For the frequentist profile-likelihood method (sec. 4.3), we need to locate very precisely the multi-dimensional maximum (or $-2\ln\mathcal{L}$ minimum) and the algorithm requires $\frac{\partial C_\ell}{\partial \theta_i}$ to vary smoothly. Hence, we need more precision on CLASS computations, still keeping a not too demanding CPU time. We obtain satisfactory results with the non-default parameters described in Table 7.1, with a maximum of a factor two increase in computational time. We will refer to those settings as the *high-precision* ones.

Since in this chapter (and in the following) we compare our results to the *Planck* published ones, which use another Boltzman solver (CAMB), we need to ensure that both CLASS and CAMB give compatible results. We follow for this the prescription of Lesgourgues (2011), i.e. generate with CLASS a C_ℓ spectrum for a fixed cosmology with extremely high precision settings which we use as *reference*. The cosmology we use is the Plik +LowTEB best-fit (Planck Collaboration. XIII. 2015), for which we have at disposal also the best-fit spectrum obtained with CAMB, that we can compare to our reference. We also investigate how far the CLASS default and high-precision settings lie from the reference. Results are shown as an absolute and fractional difference in Fig. 7.1. The agreement between CLASS and CAMB (with the *Planck* settings) is at the μK^2 level. For high-ℓ, CAMB shows about $1\,\mu$K^2 more power which, in relative units, goes up to 1% difference at $\ell = 2500$. Such a level of disagreement does not impact significantly the determination of the standard ΛCDM parameters. This conclusion may not hold when testing subtle effects such as the one of the $A_{\rm L}$ parameter discussed in sec. 7.2.6.

We also note that the definition of θ_s is different. CAMB computes only an approximation of the sound horizon ($\theta_{\rm MC}$), while CLASS computes it exactly.

For some of the tests we made on the ΛCDM model, we have used the Pico software[1]. Pico is based on the interpolation between spectra trained on the CAMB Boltzmann solver. It is intended to accelerate the parameter estimation codes, with a good precision that can be improved by using a larger training set (Fendt & Wandelt 2007). As for CAMB, the only parameter that shows a discrepancy with class is θ_s, due to its different definition. In standard ΛCDM cases, and far from the boundary of the trained parameter space, Pico and CLASS give similar results. However, Pico is trained on an old CAMB version and so CLASS should be considered more precise. Similarly, the final results on $A_{\rm L}$ are obtained with CLASS since Pico only implements an approximation (sec. 7.2.6).

[1] https://sites.google.com/a/ucdavis.edu/pico/

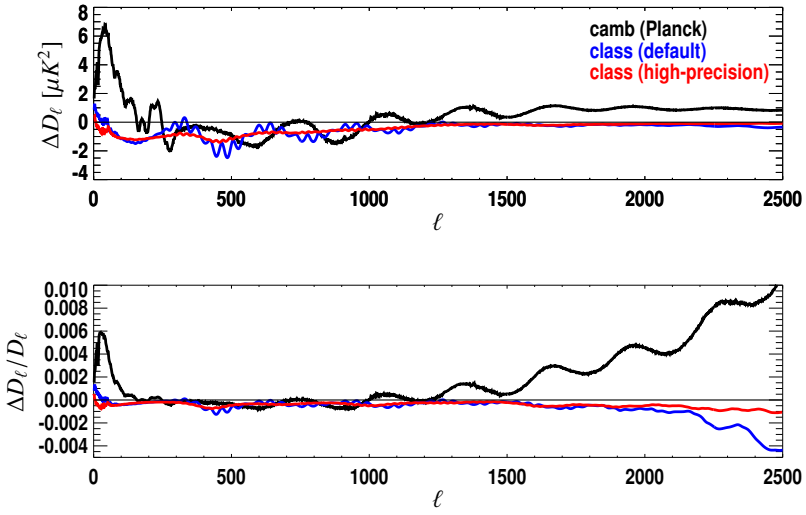

Figure 7.1: Absolute (upper panel) and relative (lower panel) difference of $D_\ell \equiv \ell(\ell+1)C_\ell/2\pi$ power spectra computed with different settings for CLASS and with CAMB. The reference is obtained from an extremely high precision run with CLASS. The red and blue spectra are obtained using the default and high-precison CLASS parameters as in Planck Collaboration A54 (2014). Since the cosmology is the fiducial *Planck* TT+LowTEB best-fit one (from Planck Collaboration. XIII. (2015)), the black curve shows the comparison to the released *Planck* spectrum which was obtained with CAMB.

7.2 *Planck* alone

In this section we discuss the constraints on the ΛCDM parameters obtained using the *Planck* data only. The HiLLiPOP likelihood is able to put strong limits on the parameters since the range of probed scales is sufficiently large (sec.7.2.5). However, we also make use of the information for the low-ℓ part via the LowTEB likelihood (chapter 6).

7.2.1 Temperature results

The results from our high-ℓ likelihood, using temperature alone, are presented in combination with LowTEB. The values for the parameters can be found in Table 7.2, while the posterior distributions are shown in Fig. 7.2. In the following, we comment on some of them.

The precise measurements provided by *Planck* of the position of the acoustic peaks in the CMB temperature power spectrum allow to put robust constraint on the acoustic scale. At 1σ the precision is at the 0.05%.

$$100\theta_s = 1.04175 \pm 0.00044 \quad (68\%, \texttt{HiLLiPOP} + \texttt{LowTEB}). \tag{7.1}$$

The value of the Hubble constant H_0 is more model dependent, and its value depend on the assumption on the primordial power spectrum or even on the fixed mass for the neutrinos (Ichikawa 2008; Planck Collaboration. XVI. 2014). We find a 1.5% constraint on H_0

$$H_0 = (67.5 \pm 1.0)\ \mathrm{Kms}^{-1}\mathrm{Mpc}^{-1} \quad (68\%, \texttt{HiLLiPOP} + \texttt{LowTEB}). \tag{7.2}$$

As shown in Fig. 7.3, this measurement of H_0 suffers from a degeneracy with the matter density Ω_m ,

	TT	
par	best fit	68% limits
$\Omega_b h^2$	0.0222	0.02221 ± 0.00023
$\Omega_{\rm cdm} h^2$	0.119	0.1192 ± 0.0022
$100\theta_s$	1.042	1.04175 ± 0.00044
τ	0.072	0.072 ± 0.020
$log(10^{10} A_s)$	3.070	3.068 ± 0.038
n_s	0.966	0.9645 ± 0.0071
Ω_m		0.311 ± 0.013
H_0		67.5 ± 1.0
σ_8		0.816 ± 0.015
$A_{\rm planck}$	1.001	1.0007± 0.0025
c_0	0.00164	0.0016 ± 0.0016
c_1	0.00159	0.0016 ± 0.0016
c_3	-0.000247	-0.0004 ± 0.0015
c_4	0.00258	0.0026 ± 0.0017
c_5	0.00272	0.0027 ± 0.0017
$A_{ps}^{100x100}$	0.000250	0.000258 ± 2.4e-05
$A_{ps}^{100x143}$	0.000107	0.000114 ± 1.7e-05
$A_{ps}^{100x217}$	7.710e-5	9.0e-05 ± 1.6e-05
$A_{ps}^{143x143}$	4.250e-5	4.7e-05 ± 1.2e-05
$A_{ps}^{143x217}$	3.260e-5	3.8e-05 ± 1.0e-05
$A_{ps}^{217x217}$	7.810e-5	7.6e-05 ± 9e-06
$A_{\rm sz}$	1.500	1.09 ±0.56
$A_{\rm cib}$	0.920	0.81 ±0.14
$A_{\rm dust}^{\rm TT}$	0.955	0.93 ± 0.09
A_{ksz}	1.680	3.58 ± 2.22
A_{szxcib}	0.000151	1.93 ± 1.38

Table 7.2: Best fit and MCMC results for the parameters of the base ΛCDM cosmology computed using the `HiLLiPOP` likelihood on *Planck* TT spectra at high-ℓ and using the `LowTEB` likelihood at low-ℓ. We also show derived parameters and the nuisance parameters for `HiLLiPOP` likelihood. Corresponding posteriors distribution can be found in Fig. 7.2. These results have been obtained using `CLASS`.

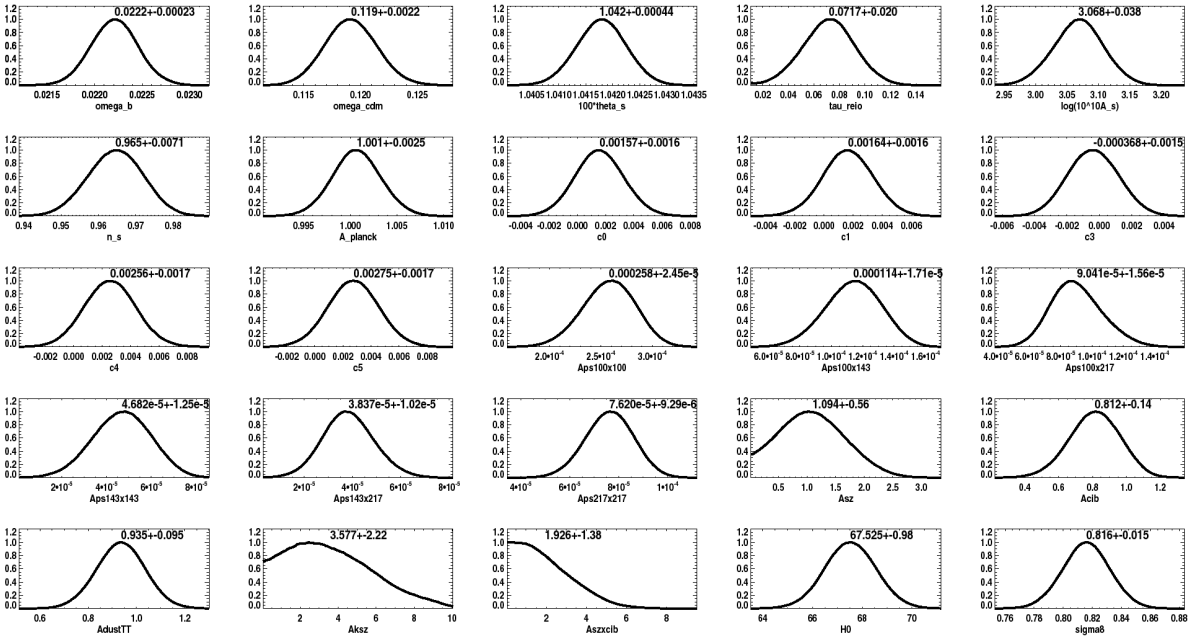

Figure 7.2: Posterior distributions for the temperature only `HiLLiPOP` likelihood in combination with the `LowTEB` likelihood. We show the six ΛCDM parameters and the nuisances (described in Table 5.7) plus two interesting derived parameters: H_0 and σ_8. The means and the 68% errors can be found in Table 7.2. These results have been obtained using `CLASS`.

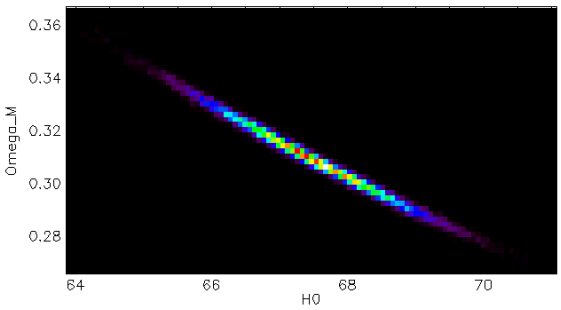

Figure 7.3: The degeneracy between H_0 and Ω_m. The figure is the 2D posterior distribution obtained from the MCMC sampling of the TT `HiLLiPOP` + `LowTEB` likelihood. The Boltzmann code `CLASS` has been used.

since the two are only constrained in the combination $\Omega_m h^3$. We find

$$\Omega_m = 0.311 \pm 0.013 \quad (68\%, \texttt{HiLLiPOP} + \texttt{LowTEB}). \tag{7.3}$$

The relative heights of the acoustic peaks allow to constrain the density parameters $\Omega_b h^2$ and $\Omega_{\rm cdm} h^2$ with a precision of 1% and 2%, respectively. Changes in these density parameters, however, can be compensated by changes in n_s and there is thus a partial degeneracy (Planck Collaboration. XVI. 2014).

A smaller scalar spectral index n_s, means that the density perturbations with longer wavelengths are stronger, and with shorter wavelengths weaker. This has the effect of raising the CMB power spectrum on one side and lowering it on the other. Hence, it is also partially degenerate with τ. This is because

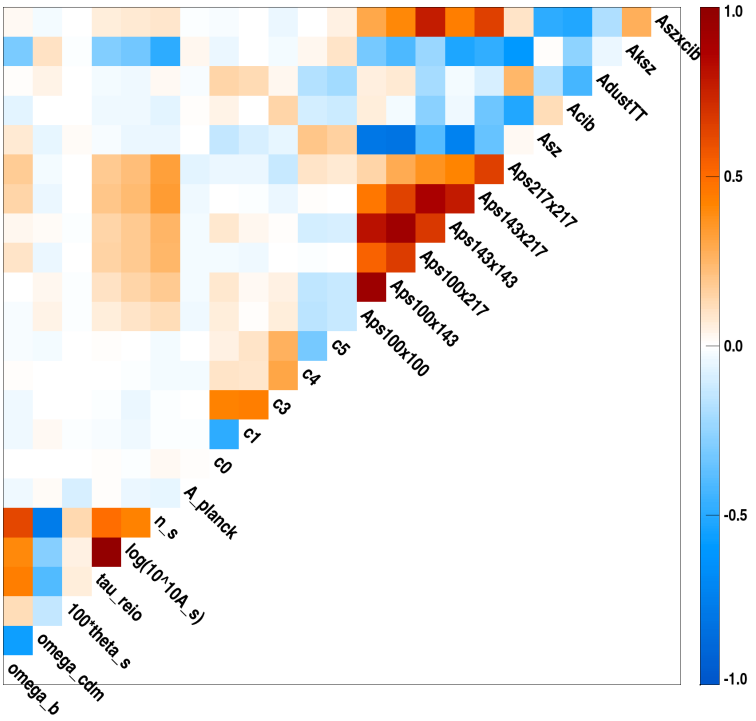

Figure 7.4: Covariance matrix of the posterior distribution obtained sampling the `HiLLiPOP` temperature alone likelihood in combination with `LowTEB`. The Boltzmann code `CLASS` has been used.

the temperature low-ℓ part does not depend on τ while intermediate and small scales are suppressed as $e^{-2\tau}$. This degeneracy can be broken using low-ℓ polarisation data. In this case, the constraint on n_s, at the ∼1% precision using the `HiLLiPOP` likelihood alone, shrink to 0.7%

$$n_s = 0.9645 \pm 0.0071 \quad (68\%, \texttt{HiLLiPOP} + \texttt{LowTEB}). \tag{7.4}$$

This is a 5σ detection of a deviation of the scalar spectral index from exact scale invariance. Even the high-ℓ part of the spectra, i.e. `HiLLiPOP` alone, is sufficient to reach this conclusion. However, the value of n_s is the most sensitive to systematic errors coming from an improper modelling of the foregrounds (chapter 5).

Via the amplitude of the lensing smoothing effect, it is possible to put a constraint on the amplitude of the matter (linear) power spectrum on the scale of $8h^{-1}$Mpc

$$\sigma_8 = 0.816 \pm 0.015 \quad (68\%, \texttt{HiLLiPOP} + \texttt{LowTEB}), \tag{7.5}$$

that lies almost 1σ lower than the corresponding `Plik` value.

The high-ℓ likelihood alone, thanks to the effect of lensing, can also put a (weak) constraint on the optical depth to reionisation with mean value $\tau_{\rm reio} \sim 0.1$. This estimation is higher than the one obtained using the low-ℓ only likelihood (sec. 6.1). The constraint also comes from the relative power between small and large scales and thus depends on the choice for the low-ℓ likelihood. With our configuration

par (Pico)	TT	EE	TE	full
$\Omega_b h^2$	0.02227 ± 0.00024	0.02416 ± 0.00091	0.02222 ± 0.00024	0.02231 ± 0.00015
$\Omega_{\rm cdm} h^2$	0.1190 ± 0.0022	0.1119 ± 0.0037	0.1194 ± 0.0020	0.1182 ± 0.0013
$100\theta_{\rm MC}$	1.0409 ± 0.0005	1.0407 ± 0.0008	1.0409 ± 0.0005	1.0410 ± 0.0003
τ_{reio}	0.072 ± 0.020	0.077 ± 0.020	0.067 ± 0.020	0.077 ± 0.020
n_s	0.966 ± 0.007	1.003 ± 0.013	0.972 ± 0.010	0.966 ± 0.005
$log[10^{10} A_s]$	3.070 ± 0.038	3.086 ± 0.041	3.060 ± 0.041	3.078 ± 0.034

Table 7.3: Pico mean and error bars for the six ΛCDM parameters obtained sampling the HiLLiPOP likelihood using respectively TT only, EE only and TE only data, and the combination of the three. For the low-ℓ data we use the LowTEB likelihood. The posterior distributions, in the different cases, are shown in Fig. 7.5.

we have

$$\tau_{\rm reio} = 0.072 \pm 0.020 \quad (68\%, \texttt{HiLLiPOP} + \texttt{LowTEB}), \tag{7.6}$$

0.5σ lower than the Plik value. We postpone the discussion on the reasons for these differences to sec. 7.2.4.

In Table 7.2 and in Fig. 7.2 we also show the results on the foreground parameters. These has been already discussed in chapter 5. We will address the constraints on foregrounds when adding the ground based CMB data at very high multipoles (sec.7.3.1).

The correlation matrix for all the parameters is reported in Fig. 7.4. It is almost a block matrix. The lower corner describes the correlation between the cosmological parameters. We recognise the strong τ-A_s degeneracy, and the correlation between n_s, the density parameters, and again τ, as described before. Cosmology is decoupled from the calibration coefficients but shows some correlation with the kSZ and the PS amplitudes. The latter are strongly correlated among them. The upper corner shows the astrophysical nuisances correlations and has a complex structure.

7.2.2 Consistency between temperature and polarisation

As discussed in chapter 1, the CMB polarisation is a unique source of information about inflation and the reionisation epoch. For the aim of this thesis, what is more relevant is that the addition of polarisation can break some degeneracies among the parameters that cannot be accurately resolved with the temperature data alone.

Furthermore, as described in sec. 3.5 and 5.6, the thermal dust is the only relevant foreground contamination in polarisation. A more detailed discussion on the effect of polarisation on cosmological parameters can be found in Zaldarriaga et al. (1997) or Galli et al. (2014). Interestingly, if we could have used the $C_\ell^{\rm EE}$ spectra in the whole range $\ell_{\rm min} = 30$, $\ell_{\rm max} = 2500$ of *Planck*, we would have had the best constraints on the parameters. This is particularly true for the angular size of the sound horizon θ_s, whose effect is to shift the position of the peaks, better determined by polarisation since their dependence on the gradient of velocity makes them sharper (sec.1.4).

$C_\ell^{\rm EE}$ are, in theory, also better than temperature in constraining the reionisation optical depth τ_{reio} and the amplitude of the primordial power spectrum $log[10^{10} A_s]$. However, there is a strong worsening of the constraining power of EE spectra, due to an increasing degeneracy between n_s and other parameters, if $\ell_{\rm min} < 130$ are excluded from the analysis (Galli et al. 2014). This is indeed our case (Table 5.3) since we are contaminated by Galactic dust emission at low multipole. This loss of information when cutting

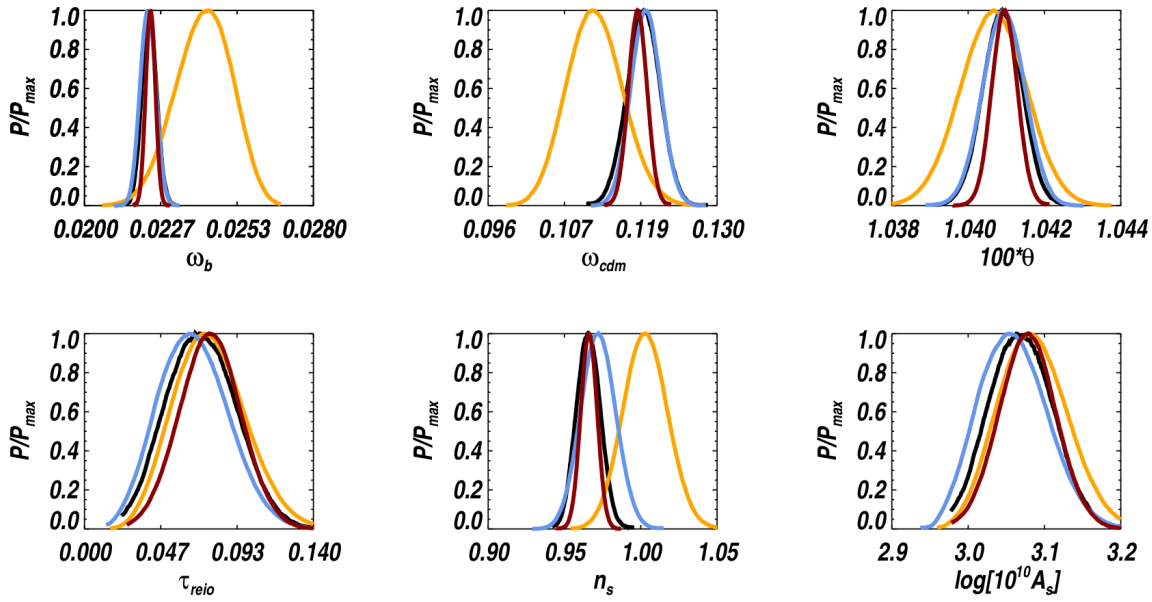

Figure 7.5: Marginalised constraints on base ΛCDM parameters, for the different CMB modes. TT is in black, while the full likelihood result is in red. They are compatible within less than 0.4σ. We also show the TE posteriors in blue. The constraining power of this latter is quite similar to TT only. Finally, in yellow, there are the looser constraints from the noisier EE only spectra. The mean values and error bars can be found in Table 7.3. In all cases, the `HiLLiPOP` likelihood is combined with the `LowTEB` likelihood for the low-ℓ. These results are obtained with `Pico`.

the low-ℓ part of the spectra is specific of the polarisation; in temperature there are only marginal effects since the low-ℓ part is noisier.

Using $C_\ell^{\rm TE}$, one can put constraints comparable to $C_\ell^{\rm TT}$ on most of the cosmological parameters and even stronger for $\Omega_{\rm cdm}h^2$, allowing to test the robustness of the results.

The `HiLLiPOP` results on the base ΛCDM model are summarised in Table 7.3 and Fig. 7.5. The results are consistent between TT and TE spectra within $\sim 0.3\sigma$, with the exception of n_s where the discrepancy is higher but still within less than 1σ. The error bars of TT and TE are almost the same, with $\Omega_{\rm cdm}h^2$ slightly better constrained in TE as expected.

The EE parameters are less in agreement with up to 3σ discrepancies. Since the EE spectra are noisier than the TT one, their constraining power is significantly smaller than those of TT. The value of the spectral index in EE is 2.8σ higher than the TT one[2].

The full (TT, TE, EE) likelihood parameters are more compatible with TT results, showing deviations of less than 0.2σ, with only $\Omega_{\rm cdm}h^2$ at 0.4σ. This confirms that the small level of systematics still present in polarisation do not affect much the final results. On the contrary, adding polarisation improves the error bars up to $\sim 40\%$.

We report in Table 7.4 the best fit χ^2 values when considering TT, EE, TE, or the full data. The number of degrees of freedom (n_ℓ) is simply the total number of multipoles considered, as described in

[2]This is a peculiarity of our HM results, DS and Yr results still pointing to a (even if not very significant) deviation from scale invariance.

CMB mode	χ^2	n_ℓ	χ^2/n_ℓ	$\Delta\chi^2/\sqrt{(2n_\ell)}$
TT	9949.7	9556	1.04	2.85
EE	7309.5	7256	1.01	0.44
TE	9322.5	8806	1.06	3.89
TTTEEE	27824.2	25618	1.09	9.8

Table 7.4: `HiLLiPOP` goodness of fit. The $\Delta\chi^2 = \chi^2 - n_\ell$ is the difference from the mean (n_ℓ) assuming the model follows a χ^2 distribution. $\Delta\chi^2/\sqrt{(2n_\ell)}$ expresses $\Delta\chi^2$ in units of standard deviation.

Table 5.3.

7.2.3 Profile likelihood results

In chapter 4 we have discussed the importance of a verification of MCMC results using the profile likelihood analysis. This has also been done in Planck Collaboration A54 (2014) for the 2013 release. Here we study the parameters of the ΛCDM model to check that the results of the profile likelihood analysis are still in agreement with the MCMC ones. We use the `HiLLiPOP` temperature alone likelihood in combination with the `LowTEB` one. Note that the results have been obtained using `Pico`. The first column of Table 7.3 has to be compared with the first column in Table 7.5. The agreement is almost perfect for the means and the error bars, which is expected given the Gaussian shape of the cosmological parameter posteriors.

We also compute the contribution of the fit of the nuisance parameters to the full error budget. In Table 7.5 the error bars given for the full, "statistical" and "nuisance", errors at 68%CL.
The "nuisance errors" are estimated as follows:

- we first obtain the profile likelihood for each cosmological parameter, from these profiles we extract both the global error on each parameter (see black curve of Fig. 7.6), and the best fit with a corresponding set of nuisance parameters values
- we then recompute the likelihood profiles for each cosmological parameter, fixing the nuisance to the ones obtained for the best fit (red curve of figure 7.6). From these profiles we extract the "statistical only" error contribution to the global error.
- the "nuisance error" is obtained by quadratically subtracting the statistical uncertainty from the total uncertainty.

This procedure has been used for instance in Aad et al. (2014) or Lorenzo Martinez (2013).

The $\Omega_b h^2$ and n_s parameters are the most impacted by the nuisance. The parameter which is less sensitive to the nuisances is θ_{MC}. These are consistent with the MCMC correlation matrix of Fig. 7.4. The same analysis also has been performed for the `Plik` and `CamSpec` likelihood in Planck Collaboration A13 (2015). The "statistical" error for all the parameters are the same for all likelihoods, pointing out that the differences on the full error do depend on the nuisance modelling that are used to build the likelihood functions.

7.2.4 Comparison with the `Plik` likelihood

In chapter 5 we have presented a comparison between the different high-ℓ likelihoods. Here we investigate in more details the differences between the posterior distributions of the six base ΛCDM parameters, obtained with MCMC sampling of the `HiLLiPOP` or the baseline `Plik` likelihoods (Fig. 7.7).

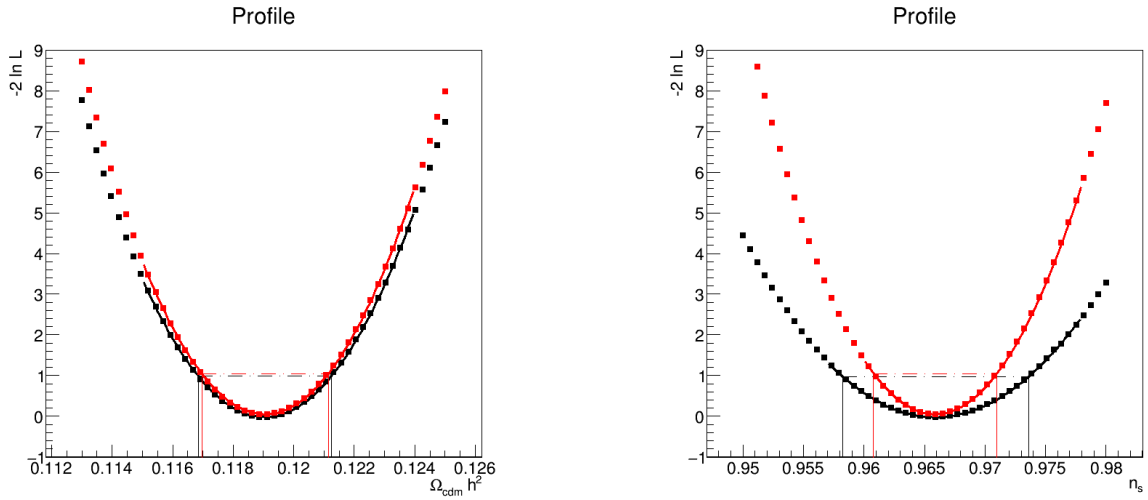

(a) (b)

Figure 7.6: The profiles likelihood for two representative parameters: $\Omega_{\rm cdm}h^2$ (a) and n_s (b). The full profile is in black while the profile in red is obtained fixing the nuisance to their best fit values. The impact of the fit of the nuisance parameters is strong for n_s and smaller for $\Omega_{\rm cdm}h^2$.

Parameter (`Pico`)	profiles	stat and "nuisance" errors	nuis/tot(%)
$\Omega_b h^2$	0.02228 ± 0.00025	0.02228 ± 0.00018 (stat data) ±0.00017 (nuis)	67
$\Omega_{cdm}h^2$	0.1190 ± 0.0022	0.1190 ± 0.0021 (stat data) ±0.0007 (nuis)	30
$100\theta_{MC}$	1.04088 ± 0.00047	1.04088 ± 0.00046 (stat data) ±0.00009 (nuis)	20
τ_{reio}	0.072 ± 0.021	0.072 ± 0.017 (stat data) ±0.012 (nuis)	56
$ln[10^{10}A_s]$	3.070 ± 0.039	3.070 ± 0.033 (stat data) ±0.022 (nuis)	55
n_s	0.9659 ± 0.0077	0.9659 ± 0.0051 (stat data) ±0.0058 (nuis)	75

Table 7.5: The profiles errors are given for the full profile fit and then split between the "nuisance error" (coming from the nuisance parameter determination) and the "statistical" error coming from the dataset. We also give the "nuisance/total" ratio to better size the impact of the nuisance.

Parameter (`CAMB`)	`Plik` (TT)	`Plik` (full)
$\Omega_b h^2$	0.02222 ± 0.00023	0.02225 ± 0.00016
$\Omega_{\rm cdm}h^2$	0.1197 ± 0.0022	0.1198 ± 0.0015
$100\theta_{\rm MC}$	1.04085 ± 0.00047	1.04077 ± 0.00032
τ_{reio}	0.078 ± 0.019	0.079 ± 0.017
n_s	0.9655 ± 0.0062	0.9645 ± 0.0049
$log[10^{10}A_s]$	3.089 ± 0.036	3.094 ± 0.034

Table 7.6: Means and 68% error bars for the six ΛCDM parameters obtained sampling the `Plik` likelihood. These results are taken from Table 3 in Planck Collaboration. XIII. (2015), they have to be compared to the values in the first and last column of Table 7.3, respectively. Note that `Plik` results are obtained with `CAMB`.

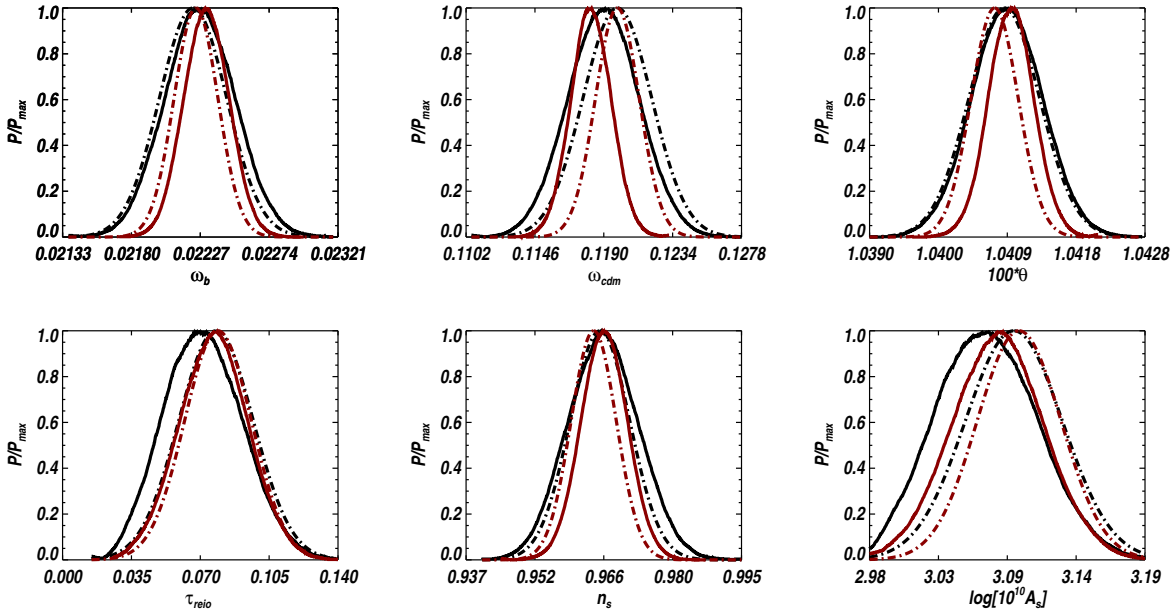

Figure 7.7: Marginalized constraints for the base ΛCDM model obtained with the `HilliPOP` likelihood using TT only (black solid line) and the full temperature and polarization data (red solid line). For comparison `Plik` TT (dashed black) and `Plik` full data (dashed red) results are also shown. The high$-\ell$ information is always complemented with `LowTEB`.

The high$-\ell$ information is always completed with the `LowTEB` likelihood for the low-ℓ. The results from `Plik` are reported in Table 7.6, to be compared with Table 7.3. When considering the TT data only, almost all parameters are compatible with the baseline within approximately $0.1\,\sigma$ with the exception of $\Omega_{\rm cdm}h^2$ where the shift is slightly higher (about $0.4\,\sigma$). The approximately $0.5\,\sigma$ difference in τ and $A_{\rm s}$ is related to a mild preference of the `HiLLiPOP` likelihood for a lower $A_{\rm L}$ (sec. 7.2.6). Error bars from the baseline `Plik` and `HiLLiPOP` are nearly identical with only a slightly bigger error bar on n_s for our likelihood.

When considering the full data set, the shifts with respect to the baseline `Plik` still remain within about $0.5\,\sigma$. We observe also the same trend for a lower $\Omega_{\rm cdm}h^2$. The difference in τ and $A_{\rm s}$ is instead alleviated by the compatibility of $A_{\rm L}$ for the full likelihoods. Again error bars are nearly identical between the two likelihoods.

7.2.5 Low-ℓ data

We have presented results using the `HiLLiPOP` likelihood (that has $\ell_{\rm min}$=50) in combination with the `LowTEB` likelihood. In this section we focus on the results from different choices for the low-ℓ information and discuss the implication on the cosmological parameters.

Along this thesis, we sometimes mimic the low-ℓ information with a Gaussian prior on the optical depth $\tau = 0.07 \pm 0.02$. An essential remark is that using a prior on it should be considered as a mere instrument of comparison and diagnostic. Even if it is useful to break the τ-A_s degeneracy, a Gaussian prior is not a clean solution. On the other hand, the inclusion of the low-ℓ likelihood in temperature and polarisation has a complicated influence on the parameters due to the way the solution adjust the tension between temperature low-ℓ and high-ℓ data.

In Fig.7.8 are compared the posterior distributions obtained using the LowTEB likelihood or only a τ prior, with the optional addition of the Commander likelihood that carries the temperature only information within $\ell_{\rm min}$ =2 and $\ell_{\rm max}$ =29.

The main shift between the τ prior and the LowTEB case is 0.5σ on n_s. As discussed earlier, there is a correlation between τ and the scalar spectral index coming from the comparison between the low-ℓ and high-ℓ part. Hence, a prior on τ, with respect to the more complex information coming from temperature and polarisation, is expected to have a different influence on n_s. The other parameters shift by no more than 0.2σ. Interestingly the shift on τ for Plik between the two low-ℓ configurations (τ prior or LowTEB), is a factor two bigger than for HiLLiPOP. As mentioned before, this is linked to $A_{\rm L}$ (sec. 7.2.6) and symptomatic of a tension between temperature low-ℓ and high-ℓ data that is worsened when the full low-ℓ (polarization and temperature) information is added. However, the resulting shift in n_s is similar for the two high-ℓ likelihoods.

The addition of the Commander likelihood drives the cosmological parameters, obtained from the high-ℓ + prior, to values closer to the HiLLiPOP + LowTEB case. This effect is clear again on n_s and stable with respect to the considered Commander ℓ-range[3]. On the contrary, there is almost no shift on τ. This is just because the temperature only Commander likelihood does not contain much information on τ and the prior drives this parameter.

From Fig. 7.9, we can see that the high-ℓ likelihoods alone can put a constrain on τ, even if weak, as mentioned in sec. 7.2.1. However, due to the τ-A_s degeneracy, the profile likelihood technique is more suited to this problem, so we refer to sec. 7.2.7 for a more precise result. It is also interesting to have a look on what is the information added if we use a different likelihood for the low-ℓ as a preliminary version of the *lollipop* likelihood built on the EE 100 GHz×143 GHz (sec. 6.1). The validation of this likelihood is still on-going but it provides a strong constraint on the τ parameter, pointing to a low value. This drives also the constrain on A_s. Due to the degeneracy n_s-τ, n_s is pushed to lower values and this is compensated by shifts in the density parameters.

7.2.6 The $A_{\rm L}$ parameter

In sec. 6.2 we briefly described the *Planck* lensing likelihood built on the lensing information encoded in the non-Gaussian trispectrum of the CMB. From the measured trispectrum it is possible to measure the power spectrum $C_\ell^{\phi\phi}$ of the lensing potential. This is consistent with the prediction from the best-fit ΛCDM model and can be tested by the introduction of the parameter $A_{\rm L}^{\phi\phi}$ that scales the theoretical lensing trispectrum (Planck Collaboration. XVI. 2014; Planck Collaboration. XIII. 2015). The joint analysis with the *Planck* likelihood gives

$$A_{\rm L}^{\phi\phi} = 0.95 \pm 0.04 \quad (68\%, \texttt{Plik +LowTEB}), \tag{7.7}$$

in agreement with the expected value of unity.

Lensing also affects the CMB temperature power spectrum smoothing the acoustic peaks and troughs (e.g. Seljak (1996)). As can be seen in Fig. 7.10, it becomes an order unity effect at $\ell \gtrsim 3000$ (in the absence of any other secondary effects) since the unlensed CMB power spectrum has very little power on these scales due to the Silk damping.

With a Boltzman solver (sec.7.1) one can compute the angular power spectra of both the temperature/polarization anisotropies C_ℓ and of the lensing potential $C_\ell^{\phi\phi}$. The latter is then used to "lens" the

[3]The Commander likelihood is available for different value of $\ell_{\rm max}$

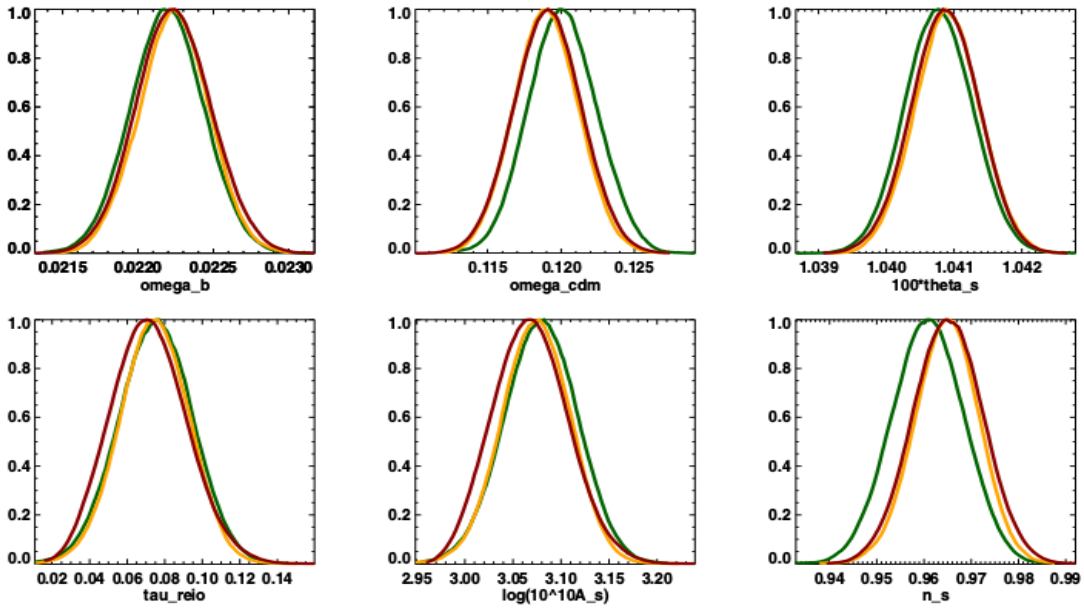

Figure 7.8: Posterior distributions for HiLLiPOP likelihood for the high-ℓ part ($\ell_{\rm min}$=50) adding for the low-ℓ part the standard τ Gaussian prior $0.007 \pm 0,02$ (green), τ prior + Commander between $\ell_{\rm min}$=2 and $\ell_{\rm max}$=29 (yellow), and the LowTEB likelihood (red).

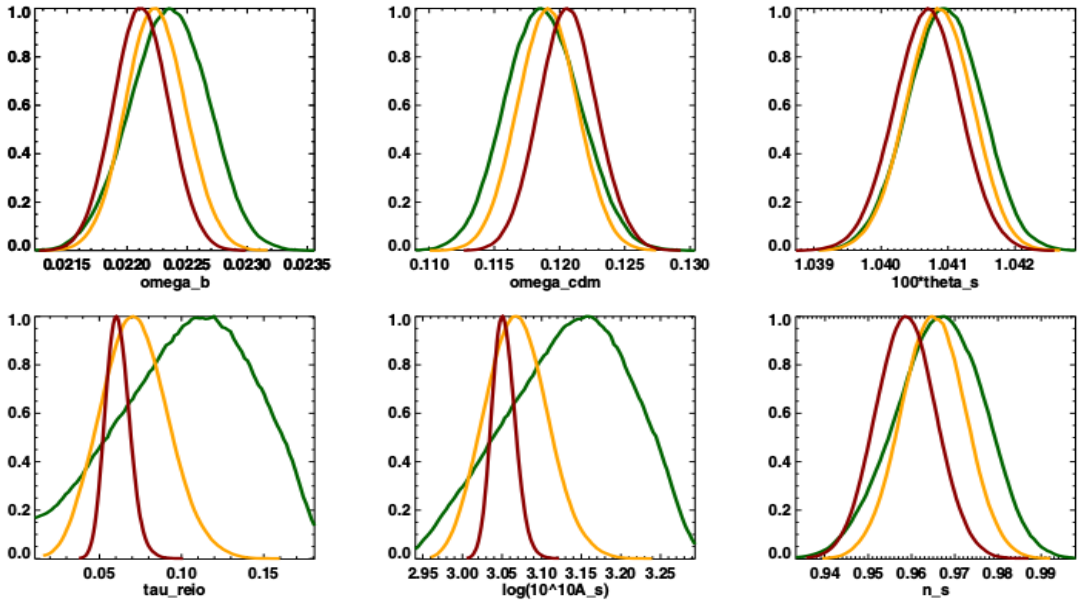

Figure 7.9: Posterior distribution for the base ΛCDM parameters obtained from the TT HiLLiPOP likelihood alone (green), HiLLiPOP +*lollipop* EE 100x143 (red), and HiLLiPOP +LowTEB (bflike) (yellow).

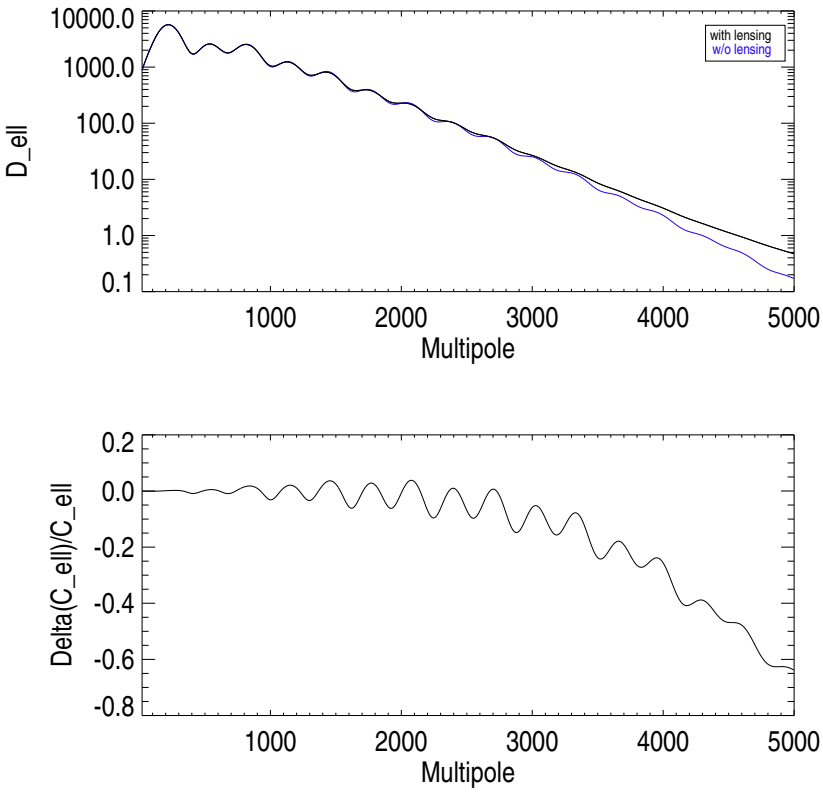

Figure 7.10: In the upper panel we show a comparison between the lensed (black) and the unlensed (blue) temperature spectrum obtained with `CLASS`. The lower panel show the difference between the two. In absence of foregrounds, the effect becomes dominant at $\ell \gtrsim 3000$.

CMB spectra i.e. redistribute the power while preserving the brightness in a rather complicated way (e.g Lewis & Challinor 2006b): $(C_\ell, C_\ell^{\phi\phi}) \to \tilde{C}_\ell$.

The parameter $A_{\rm L}$, in analogy with $A_{\rm L}^{\phi\phi}$, can be introduced with the aim of measuring the degree of lensing of the CMB power spectra. The idea, originally introduced in Calabrese et al. (2008), is to rescale the lensing potential and modify the standard scheme into: $(C_\ell, A_{\rm L} C_\ell^{\phi\phi}) \to \tilde{C}_\ell$. Sampling the likelihood, with this parameter free, gives two interesting pieces of informations:

1. from the $A_{\rm L}$ posterior one can check the consistency of the data with the model, which should be compatible with one for standard cosmology.

2. by marginalising over $A_{\rm L}$ one can, to first order, remove the information due to the lensing from the CMB power-spectra.

As it was the case for the first release (Planck Collaboration. XVI. 2014), *Planck* determines a value of the $A_{\rm L}$ parameters discrepant at more than 2σ with one. The full-mission measurement, based on the `Plik +LowTEB` likelihood is (Planck Collaboration. XIII. 2015)

$$A_{\rm L} = 1.22 \pm 0.10 \quad (68\%, \texttt{Plik +LowTEB (CAMB/MCMC)}). \tag{7.8}$$

Note, however, that there is a significant deviation from zero, meaning that there is a clear detection of lensing at the power spectra level.

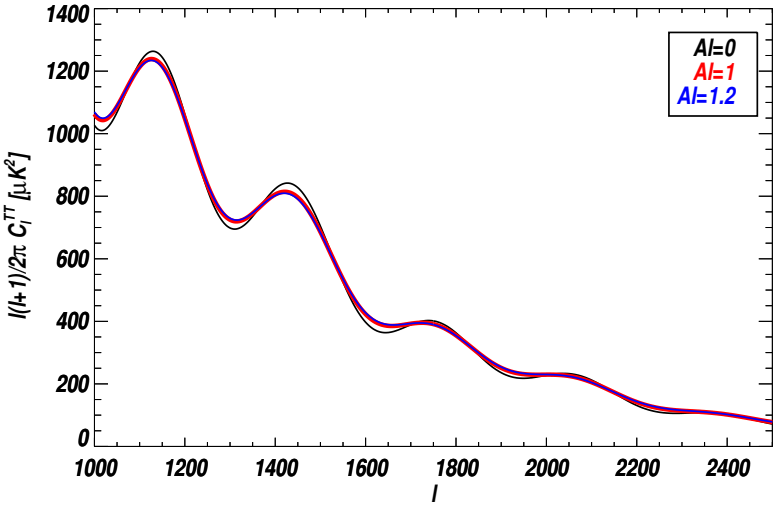

Figure 7.11: The fine impact of different $A_{\rm L}$ on the CMB temperature spectrum (obtained with CLASS): the case $A_{\rm L}$=0 (in black) corresponds to the unlensed $C_\ell^{\rm TT}$, $A_{\rm L}$=1 (in red) is the standard case considered when testing the ΛCDM model, and $A_{\rm L}$=1.2 (in blue) corresponds to the value fitted by the *Planck* high-ℓ likelihood.

The $A_{\rm L}$ discrepancy from unity acts, in *Planck* temperature spectra, as if there were more lensing than expected. As can be seen in Fig. 7.11, the effect is not strong but it is sufficient to affect extensions beyond the standard ΛCDM theory as the ones on curvature or neutrinos (Planck Collaboration. XIII. 2015). This latter is discussed further in chapter 8.

The tension affects also the measurement of two ΛCDM fundamental quantities, the reionization optical depth τ and the primordial scalar perturbations amplitude A_s. As discussed in sec. 7.2.1, the high-ℓ A_s-τ degeneracy, can be broken by any low-ℓ polarisation measurement (as the LowTEB likelihood that carries essentially the EE information), but can be also relieved by the smoothing effect of lensing. This means that a deviation from unity of $A_{\rm L}$ impacts also our ΛCDM estimation of A_s and τ. An overestimation of the lensing effect drives a large A_s value which in turn drives a large value of τ, according to the $A_s e^{-2\tau}$ degeneracy.

The origin of the 2σ discrepancy was attributed, since the 2013 release of data, to the difficulties that ΛCDM model has in fitting the low-ℓ part of the spectrum from the high-ℓ data and, possibly, to μK^2 level foreground residuals (Planck Collaboration. XVI. 2014). In this section we discuss to which extent the HiLLiPOP likelihood shows the same preference for a higher $A_{\rm L}$.

First we revise the $A_{\rm L}$ estimation of Plik performing the measurements using CLASS and the profile likelihood technique. This allows a direct comparison between the Plik and HiLLiPOP estimation of $A_{\rm L}$ that is shown in Fig. 7.12.

We obtain a result that is larger than the one reported in Eq. 7.8

$$A_{\rm L} = 1.26^{+0.11}_{-0.10} \quad (68\%, \texttt{Plik} + \texttt{LowTEB}\ (\texttt{CLASS/profile})). \tag{7.9}$$

As discussed in sec. 7.1, this higher value is due to the use of CLASS instead of CAMB. Since it is obtained with high precision settings we think it is more precise. With the same settings, the HiLLiPOP results reads

$$A_{\rm L} = 1.22^{+0.11}_{-0.10} \quad (68\%, \texttt{HiLLiPOP} + \texttt{LowTEB}). \tag{7.10}$$

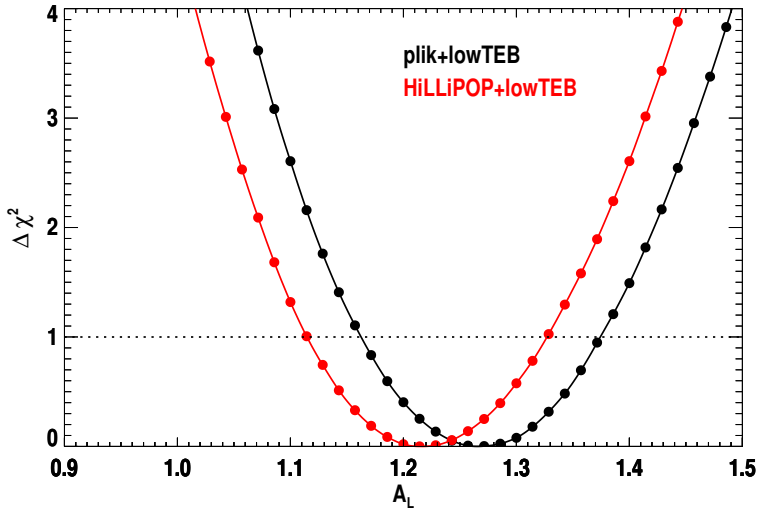

Figure 7.12: Profile-likelihoods of the $A_{\rm L}$ parameter using two different *Planck* high-ℓ likelihoods (black for `Plik`, red for `HiLLiPOP`) and adding the low-ℓpart (`LowTEB`).The results are obtained using `CLASS` with the high-precision settings described in sec. 7.1.

This estimate of $A_{\rm L}$, despite being lower than the `Plik` one, still shows a 2σ discrepancy with one. This tendency is slightly reduced if we use the polarisation. In Table 7.7 and in Fig. 7.13 can be found the profile likelihood results for all the modes. Note that the values of $A_{\rm L}$ in TE and EE allow to confirm a detection of lensing in the polarised spectra, even if less significant than in TT[4]. The full likelihood result is

$$A_{\rm L} = 1.13^{+0.08}_{-0.08} \quad (68\%, \texttt{HiLLiPOP (TT,EE,TE)+LowTEB}). \tag{7.11}$$

The estimate of $A_{\rm L}$, as stated previously, is sensitive to the low-ℓ information. For illustration purpose, we report in Table 7.8 the means and 68% errors on the $A_{\rm L}$ parameter obtained with different low-ℓ choices. Indeed, for these results, we used the faster but less precise `Pico` which has also a slightly different definition of $A_{\rm L}$

$$C_\ell = A_{\rm L} \times C_\ell^{\rm lensed} + (1 - A_{\rm L}) \times C_\ell^{\rm scalar}, \tag{7.12}$$

so they have to be read as a test on the stability of the parameter. The addition of the `LowTEB` is the worst case possible, whereas the `HiLLiPOP` likelihood alone value is compatible with one.

Moreover, we find that the value is sensitive (at the σ-fraction level) to the different datasets described in sec. 5.2, hence if we use DS or Yr instead of HM. This has also been found for the `Plik` likelihood, where a lower value of $A_{\rm L}$ using DS has been attributed to the presence of correlated noise (sec. 3.4). Finally, we have also observed shifts with respect to the sky coverage or the beams used, even if minor.

The deviations in $A_{\rm L}$ between `Plik` and `HiLLiPOP` are difficult to interpret, but the different parametrisation of the foregrounds, resulting in different correlation between parameters plays a non negligible role. In Fig. 7.14 we compare the correlation matrices of the posterior distributions for the `HiLLiPOP` and `Plik` likelihoods when sampling $A_{\rm L}$. The correlation between cosmological parameters present significant divergences in the $A_{\rm L}$-n_s-A_s block. However, the ΛCDM + $A_{\rm L}$ posteriors are very similar between `HiLLiPOP`, `Plik` and `CamSpec`, since the marginalisation over $A_{\rm L}$ alleviates the tensions.

[4]It is worth mentioning that central values for $A_{\rm L}$ in TE and EE shows few σ shifts between the various high-ℓ likelihoods. This is true even between `Plik` and `CamSpec` that agree on their TT value.

data	$A_{\rm L}$
TT	$1.22^{+0.11}_{-0.10}$
EE	$1.22^{+0.24}_{-0.22}$
TE	$1.11^{+0.21}_{-0.20}$
TTEETE	$1.13^{+0.08}_{-0.08}$

Table 7.7: `HiLLiPOP` profile-likelihood results (obtained using `CLASS` high-precision settings of sec. 7.1) for the $A_{\rm L}$ parameter for TT, EE, TE and the full combination. The `LowTEB` likelihood is always used for the low-ℓ part.

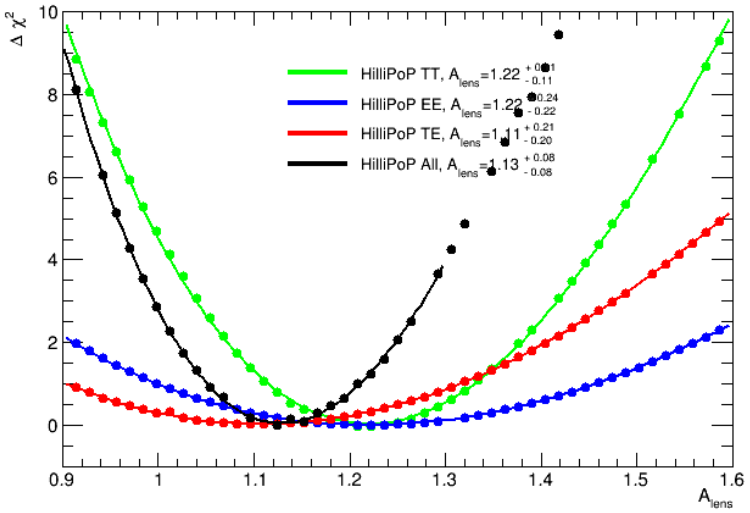

Figure 7.13: Profile-likelihoods of the $A_{\rm L}$ parameter using the `HiLLiPOP` likelihood in combination with the low-ℓpart (`LowTEB`) for TT (green), EE (blue), TE (red) and full (black) likelihood. The results are obtained using `CLASS` with the high-precision settings described in sec. 7.1. The results are also reported in Table 7.7.

	$A_{\rm L}$ (`Pico`)
no low-ℓ	1.06 ± 0.13
τ prior	1.05 ± 0.10
τ prior + `Commander`	1.11 ± 0.09
`Commander`	1.12 ± 0.11
lollipop	1.08 ± 0.10
lollipop + `Commander`	1.11 ± 0.09

Table 7.8: Means and 68% error for the posterior distribution of the $A_{\rm L}$ parameter obtained with the `HiLLiPOP` (Yr) TT only likelihood in combination with different informations for the low-ℓ. Results have been obtained with `Pico`, where $A_{\rm L}$ has a slightly different definition. It is, however, interesting to see the shifts.

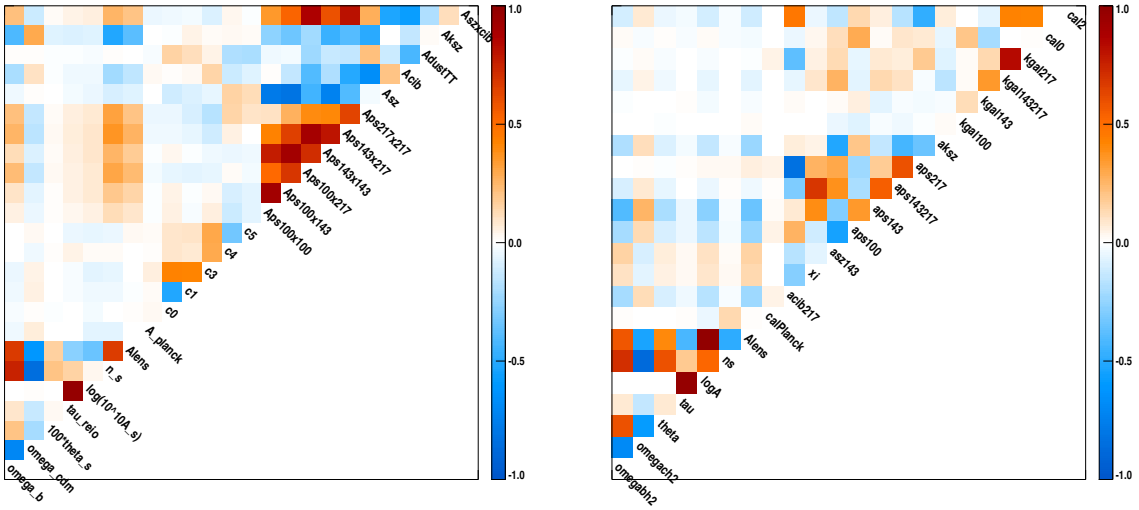

(a) (b)

Figure 7.14: Correlation matrix extracted from MCMC chains obtained when sampling the ΛCDM + $A_{\rm L}$ model with the `HiLLiPOP` likelihood (a) and the `Plik` likelihood (b). The high-ℓ part is always combined with `LowTEB`. The definition of `Plik` nuisances can be found in (Planck Collaboration A13 2015)

In both likelihoods, however, there are complex correlations with foreground parameters. Adding information to better constrain the foregrounds is then useful and can be achieved using the VHL data. This is done is sec. 7.3.1. Its influence on $A_{\rm L}$ is discussed in sec. 7.3.2.

Regularising the $A_{\rm L}$ problem is important since its deviation from unity is accompanied by changes in all the other parameters with a complex chain of degeneracies. As already anticipated, this is true for ΛCDM extensions as non-flat models where $A_{\rm L} > 1$ drives $\Omega_k < 0$ (Planck Collaboration. XIII. 2015). Also, massive neutrinos have the same effect of an $A_{\rm L} < 1$, so the limit is pushed to lower value. This is discussed in more details in chapter 8. How $A_{\rm L}$ and the mismatch between low and high multipoles influence also our estimate of the optical depth is discussed in sec.7.2.7.

7.2.7 Constraints on τ

The optical depth τ can be measured via the effect of reionisation on the low multipoles of the EE spectra (sec. 1.4.5). This is a challenging issue since the signal is small and very good knowledges of instrumental systematics and polarised foreground emissions are required. Before the *Planck* low-ℓ result, the *WMAP* estimate was

$$\tau = 0.089 \pm 0.014 \quad (68\%, \textit{WMAP}\ \text{(Bennett et al. 2013)}), \tag{7.13}$$

where the error does not include a significant uncertainty due to foreground modelling (Komatsu et al. 2009). As briefly described in sec. 6.1, τ can be constrained using the latest *Planck* low-ℓ polarisation data alone (Table 6.1). This estimate is lower than the one of Eq. 7.13 but consistent with the revised measurement from *WMAP* data cleaned with the *Planck* 353 GHz polarised map (Planck Collaboration A13 2015). Interestingly, these values are in tension with the high value of τ coming from the high-ℓ part

alone. Making use of the profile-likelihood method, which, as emphasized in chapter 4, is particularly well suited to study strongly correlated variables as τ and A_s[5], we find for `Plik`

$$\tau = 0.175^{+0.035}_{-0.045} \quad (68\%, \texttt{Plik}), \tag{7.14}$$

that is almost 3σ higher than the low-ℓ estimation. With the `HiLLiPOP` likelihood instead we have

$$\tau = 0.13^{+0.049}_{-0.038} \quad (68\%, \texttt{HiLLiPOP}). \tag{7.15}$$

which is a less than 2σ deviation.

When combining the high-ℓ likelihoods with the `LowTEB` information we get

$$\tau = 0.078 \pm 0.018 \ (68\%, \texttt{Plik} + \texttt{LowTEB}), \tag{7.16}$$

for the `Plik` likelihood, and for the `HiLLiPOP` likelihood

$$\tau = 0.071 \pm 0.020 \ (68\%, \texttt{HiLLiPOP} + \texttt{LowTEB}). \tag{7.17}$$

In Fig. 7.15 we show these results for the two likelihoods. We note that most of the constraint in this regime indeed comes from the CMB lensing, since marginalisation over $A_{\rm L}$ almost destroys the constraint.

The discrepancies on τ in the base ΛCDM cosmology, that are present also on the A_s estimates, are a reflect of the $A_{\rm L}$ differences. Because the `Plik` value for $A_{\rm L}$ is higher than the `HiLLiPOP` one, it shifts τ towards a higher value. When adding the lensing measurement (sec. 6.2), which somehow brings $A_{\rm L}$ back close to unity, the shift is cancelled and one recovers a value more compatible with the low-ℓ alone estimate.

The $A_{\rm L}$ parameter tension (sec. 7.2.6) is not yet completely understood. There are indications however, that differences with the `Plik` value could come from the different parametrisation of the foregrounds and from the complex structure of the correlations between the corresponding astrophysical nuisance parameters (Fig. 7.14). Having $A_{\rm L}$ as much as possible compatible with its expected unitary value allows a more reliable estimation of τ even if using the power spectrum information alone, i.e not regularising the problem adding the lensing likelihood (sec. 6.2). To better constrain the foreground parameters, in sec. 7.3, we use the VHL CMB results of the SPT and ACT experiments.

7.3 Adding the very high-ℓ data

In sec. 6.3 we described the available data from the ground based, high-resolution Atacama Cosmology Telescope (ACT) and South Pole Telescope (SPT). In sec. 7.3.1 we discuss their impact on the parameter estimations, both for cosmology and for the foregrounds. They help regularising the $A_{\rm L}$ tension discussed in sec.7.2.6 allowing to revise our limits on the optical depth (sec. 7.3.2).

7.3.1 Impact on foregrounds

Since the signal to noise ratio is already high for the *Planck* full mission data, the results presented in Planck Collaboration. XIII. (2015) do not use the ACT and SPT small-scale measurements directly. However, the thermal and kinetic SZ effects are almost unconstrained by the *Planck* data alone. The VHL data are much more sensitive to these effects, and a combined prior for the tSZ and the kSZ has

[5] At each step, the variable studied (here τ) is *fixed* and the minimization is performed with respect to all other parameters. There is no more any (τ, A_s) degeneracy.

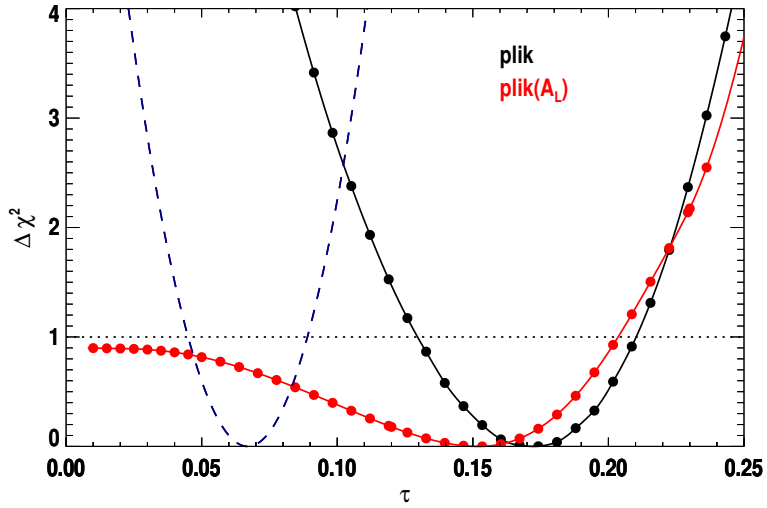

(a)

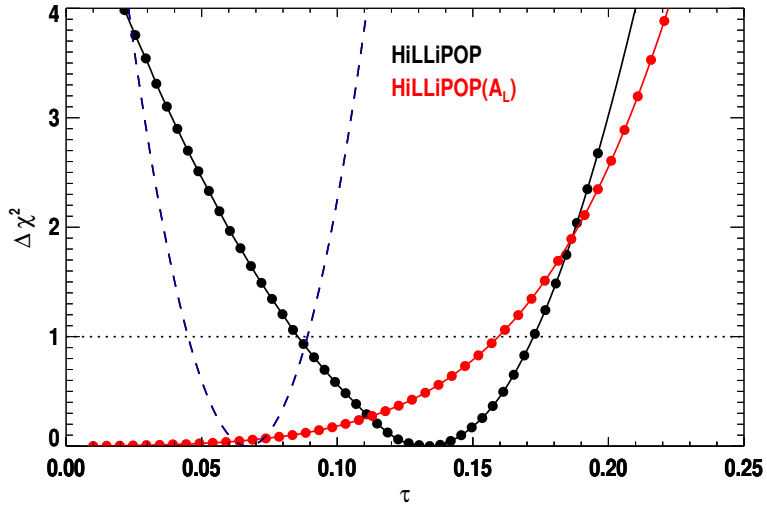

(b)

Figure 7.15: (a) Profile-likelihoods of the τ parameter using only the `Plik` likelihood, in the ΛCDM case i.e $A_{\rm L} = 1$ (in black) and marginalising over $A_{\rm L}$ (in red). Also shown in dashed, is the result of the *Planck* low-ℓ analysis. (b) Same thing for the `HiLLiPOP` likelihood.

been extrapolated and added in the `Plik` likelihood, that follows the degeneracy first found in Reichardt et al. (2013)

$$A_{\rm kSZ}^{\rm plik} + 1.6A_{\rm tSZ}^{\rm plik} = (9.5 \pm 3)\mu K^2, \tag{7.18}$$

where $A_{\rm kSZ}^{\rm plik}$ is the contribution of the kSZ at $D_{\ell=3000}$ and $A_{\rm tSZ}^{\rm plik}$ the one of tSZ at $D_{\ell=3000}^{143x143}$ at 143 GHz, both in μK^2 (sec. 5.6.4).

In this section, we present the `HiLLiPOP` temperature results in combination with the VHL data, arguing that a better constraining power for the foregrounds is useful for our likelihood and that they

help to regularise the $A_{\rm L}$ deviation from unity (sec. 7.2.6) and consequently the τ-A_s values.

The posterior distributions for the cosmological and the nuisance parameters in common with the HiLLiPOP likelihood are reported in Fig. 7.16. The means and errors are presented in Table 7.9.

Unlike the combination of Plik + VHL reported in Planck Collaboration. XIII. (2015), we find a 15% gain in error bars for the cosmological parameters that reaches 24% for n_s, the most sensitive one to foregrounds. The difference with Plik probably comes from the different parametrisation of the foregrounds that induces different correlations between parameters. For HiLLiPOP, the correlation matrix is shown in Fig. 7.17. It has a complex structure. The strong anti-correlation between the $A_{\rm cib}$ parameter and the point source amplitudes of ACT and SPT is a consequence of the way the CIB is extrapolated at high-ℓ (sec. 5.6.3).

As anticipated, we have now lower values for τ and A_s (Table 7.9). Note also a $\sim 1\sigma$ shift in $\Omega_b h^2$.

The VHL data have a stronger constraining power on the SZ parameters than *Planck* alone (sec. 6.3). As in Planck Collaboration. XIII. (2015), looking at the posterior distribution in the $A_{\rm tSZ}$-$A_{\rm kSZ}$ subspace (Fig. 7.18), we can infer the correlation

$$A_{\rm kSZ} + 3.5A_{\rm tSZ} = 3.15 \pm 0.25. \tag{7.19}$$

In Eq. 7.19 we recognise a linear combination as in Eq. 7.18, but with different coefficients because of our different definitions of $A_{\rm tSZ}$ and $A_{\rm kSZ}$ (sec. 5.6). Our result is consistent with the Plik one[6]. In yellow in Fig. 7.16 we also report the posterior distributions obtained when sampling the HiLLiPOP + LowTEB likelihood imposing the prior from Eq. 7.19 on the $A_{\rm tSZ}$ and $A_{\rm kSZ}$ parameters. The resulting foreground parameters are adjusted on the prior but the cosmological parameters remain consistent with our standard TT case.

7.3.2 Revised constraints on $A_{\rm L}$ and τ

In the 2013 release, the $A_{\rm L}$ divergence from unity was stronger when the *Planck* spectra were combined with the VHL data. From 2013 to this release, several aspects of data processing have been revised (for example calibration, see chapter 3), hence, we do not expect the VHL to have the same impact on the parameters. Interestingly we find that small scale information alleviates the tension of $A_{\rm L}$ with unity as can be seen in Table 7.10. Note that excluding the SPT_low data, the value of $A_{\rm L}$ is slightly higher, meaning that the intermediate multipoles[7] are important for the regularisation of $A_{\rm L}$.

In the light of the fact that the HiLLiPOP + VHL combination provides, for the ΛCDM + $A_{\rm L}$ cosmology, a value of $A_{\rm L}$ compatible with unity, we can revise the ΛCDM constraint on τ (hence with fixed $A_{\rm L} = 1$). We have

$$\tau = 0.060 \pm 0.017 \ (68\%, \texttt{HiLLiPOP} + \text{VHL} + \texttt{LowTEB}), \tag{7.20}$$

0.6σ lower than the HiLLiPOP result in Eq. 7.6.

The HiLLiPOP +VHL combination provides also a lower value for σ_8

$$\sigma_8 = 0.811 \pm 0.013 \ (68\%, \texttt{HiLLiPOP} + \text{VHL} + \texttt{LowTEB}), \tag{7.21}$$

that shifts in the right direction for alleviating the tension between CMB and clusters estimations. Indeed, in Planck Collaboration. XX. (2014), allowing the $\sum m_\nu$ parameter to vary, helps in reducing this tension since a lower $A_{\rm L}$ acts similarly to a massive neutrino. Working in a configuration with a regularised $A_{\rm L}$ offers the possibility of putting a more reliable limit on the sum of neutrino masses, as described in chapter 8.

[6]Note that since the tSZ and kSZ template are not exactly the same, even though very similar, this is true only approximatively.

[7]The SPT_low data covers the multipole range [650, 3000] (sec. 6.3).

	TT+VHL	
par	best fit	68% limits
$\Omega_b h^2$	0.0220	0.0220 ± 0.00019
$\Omega_{\rm cdm} h^2$	0.120	0.120 ± 0.0020
$100\theta_s$	1.042	1.042 ± 0.00040
τ	0.0594	0.0586 ± 0.017
$log(10^{10} A_s)$	3.046	3.045 ± 0.032
n_s	0.963	0.963 ± 0.0054
Ω_m		0.315 ± 0.012
H_0		67.193 ± 0.88
σ_8		0.811 ± 0.013
$A_{\rm planck}$	1.002	1.002 ± 0.0025
c_0	0.00215	0.00208 ± 0.0015
c_1	0.00209	0.00216 ± 0.0015
c_3	0.000605	0.000547 ± 0.0015
c_4	0.00192	0.00189 ± 0.0016
c_5	0.00208	0.00213 ± 0.0016
$A_{ps}^{100x100}$	0.000284	0.000285 ± 1.25e-5
$A_{ps}^{100x143}$	0.000132	0.000133 ± 6.26e-6
$A_{ps}^{100x217}$	9.000e-5	8.998e-5 ± 6.16e-6
$A_{ps}^{143x143}$	6.090e-5	6.114e-5 ± 3.94e-6
$A_{ps}^{143x217}$	4.010e-5	3.986e-5 ± 2.75e-6
$A_{ps}^{217x217}$	7.460e-5	7.475e-5 ± 4.56e-6
$A_{\rm sz}$	0.894	0.816 ± 0.092
$A_{\rm cib}$	1.110	1.085 ± 0.064
$A_{\rm dust}^{\rm TT}$	0.916	0.927 ± 0.060
A_{ksz}	4.400e-6	0.287 ± 0.23
A_{szxcib}	0.221	0.329 ± 0.16

Table 7.9: Best fit and 68% limits for the parameters of the base ΛCDM cosmology computed using MCMC for sampling the `HiLLiPOP` likelihood on *Planck* TT spectra at high-ℓ in combination with the VHL likelihood, and using the `LowTEB` likelihood at low-ℓ. We also show derived cosmological parameters and the nuisance parameters for `HiLLiPOP` likelihood, omitting, for simplicity, the VHL nuisances. The corresponding posteriors distribution can be found in Fig. 7.16. Results are obtained using `CLASS`.

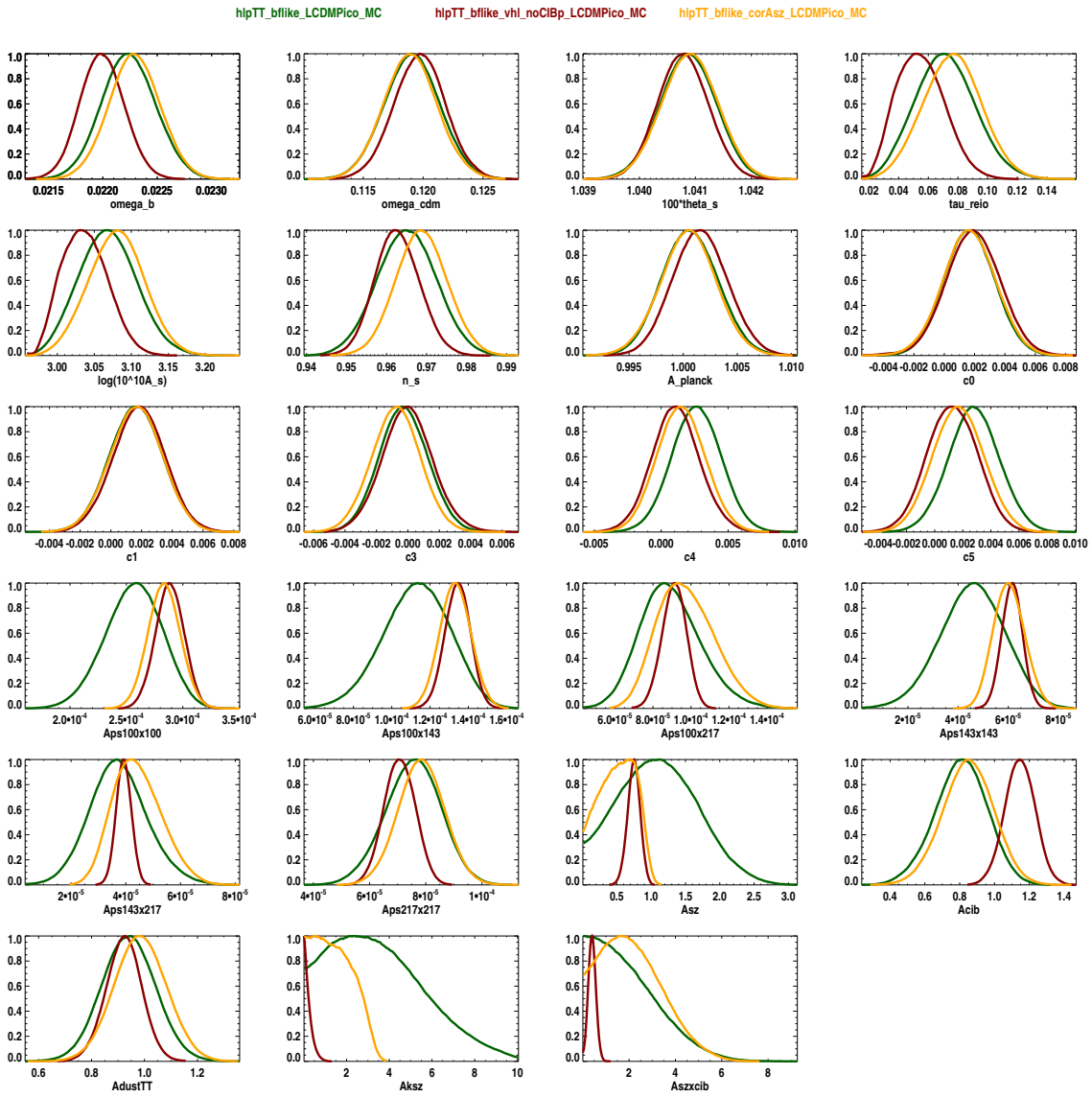

Figure 7.16: Posterior distributions for the common parameters for the `HiLLiPOP` TT likelihood (in green) and the `HiLLiPOP` TT + VHL likelihood (in red). For comparison, is also shown the `HiLLiPOP` TT results when the prior of Eq. 7.19 is imposed on the SZ foregrounds (in yellow). All results are in combination with the `LowTEB` likelihood. Means and 68% error bars for can be found in Table 7.9.

7.4 Adding BAO and Supernovae

The BAO data are an extremely valuable complementary dataset to *Planck*, that allows to break degeneracies from CMB only measurements. They provide a reliable geometrical measurements since they are largely unaffected by the uncertainties in the non linear evolution of the matter density field (Planck Collaboration. XIII. 2015). In sec. 6.4 we report in details the datasets included in this analysis, in good agreement with *Planck* ΛCDM cosmology.

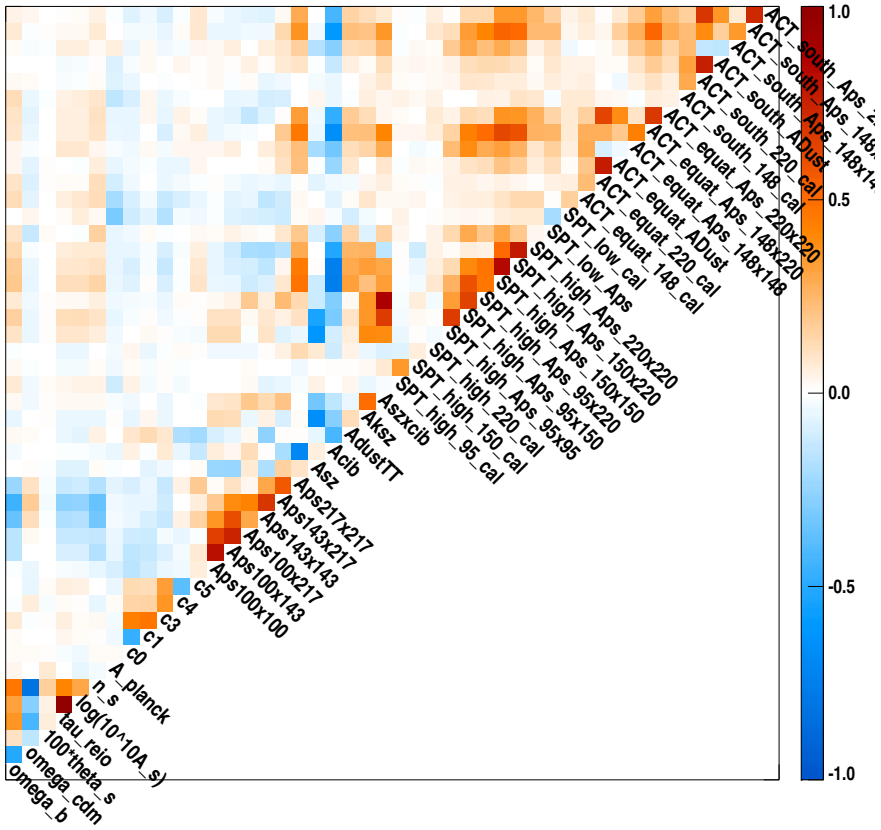

Figure 7.17: Covariance matrix obtained when sampling the `HiLLiPOP` + VHL likelihood in combination with the `LowTEB` likelihood for the low-ℓ part.

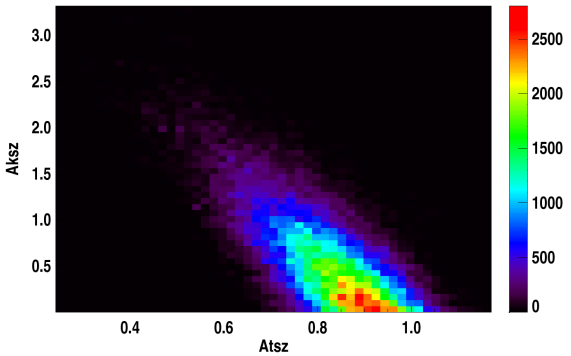

Figure 7.18: 2D posterior distribution for the tSZ and kSZ scaling parameters. The degeneracy direction is in agreement with the one found in SPT data (Reichardt et al. 2013).

	$A_{\rm L}$
HiLLiPOP (TT) + VHL + LowTEB	$1.04^{+0.08}_{-0.07}$
HiLLiPOP (TT) + VHL - SPT_low + LowTEB	$1.09^{+0.07}_{-0.07}$
HiLLiPOP (All) + VHL + LowTEB	$1.05^{+0.05}_{-0.05}$

Table 7.10: HiLLiPOP +VHL profile-likelihood results (obtained using CLASS high-precision settings of sec. 7.1) for the $A_{\rm L}$ parameter for TT or the full combination (TT+EE+TE, named "all") and using the LowTEB likelihood for the low-ℓ part. For TT is also reported the value of $A_{\rm L}$ when SPT_low is not considered in the VHL data.

par	HiLLiPOP (TT) + BAO + JLA	HiLLiPOP (TT,EE,TE) + BAO + JLA
$\Omega_b h^2$	0.0221 ± 0.00018	0.0222 ± 0.00011
$\Omega_{\rm cdm} h^2$	0.119 ± 0.0012	0.119 ± 0.00094
$100\theta_s$	1.042 ± 0.00037	1.042 ± 0.00026
τ	0.0641 ± 0.016	0.0708 ± 0.013
$log[10^{10}A_s]$	3.052 ± 0.031	3.060 ± 0.029
n_s	0.966 ± 0.0039	0.965 ± 0.0030
H_0	67.72 ± 0.52	67.80 ± 0.43
Ω_m	0.307 ± 0.0070	0.307 ± 0.0057

Table 7.11: Means and 68% errors for the cosmological parameters (plus the derived H_0 and Ω_m) when adding late time measurement data to the HiLLiPOP + LowTEB + VHL combination. Results are obtained using CLASS.

Beside BAO, another interesting complementary probe are type Ia supernovae. The JLA sample (Betoule et al. 2014b), is also in good agreement with *Planck* data (sec. 6.5).

Although mostly useful when trying to constrain extensions to the ΛCDM cosmology, as non flat models or theories with a non standard dark energy sector, these late time distance measurements have a strong impact on the error bars even in ΛCDM. In Fig. 7.19 we report the posterior distributions for the temperature HiLLiPOP likelihood in combination with the BAO+JLA information. The same is done in Fig. 7.20 for the full HiLLiPOP likelihood. The values of the cosmological parameters can be found in Table 7.11.

BAO and supernovae prefer a slightly higher value for H_0 and a lower value for Ω_m with respect to the HiLLiPOP temperature only solution. These causes little adjustments of the other parameters as a lower value for $\Omega_{\rm cdm} h^2$, in turn pushing for a lower n_s, following the degeneracies described in the previous sections. The reduction on the error bars are important, There is a 40% gain in the error bars of Ω_m and H_0 (and thus in $\Omega_{\rm cdm} h^2$). There is also a 30% gain in the error for n_s. Full likelihood results are more compatible with late time distance measurements and the posteriors for the parameters are stable. The gain in error bars is less strong since the presence of polarisation already tighten the constraints.

Conclusions

In this chapter we have used the HiLLiPOP likelihood in combination with other datasets to test the ΛCDM model and found good agreement between the two. We started describing the constraints on

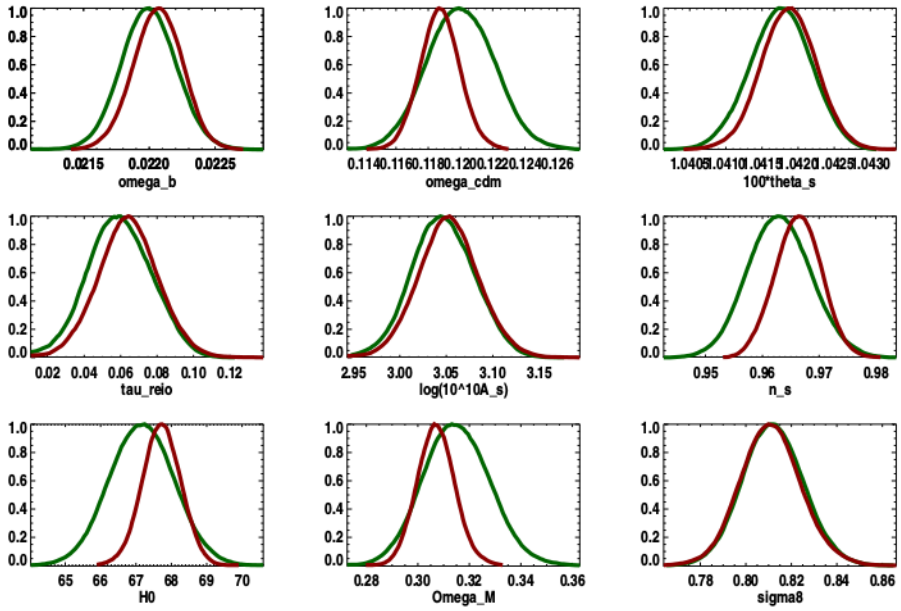

Figure 7.19: The posterior distributions for the `HiLLiPOP` likelihood in temperature only, in combination with the VHL and the `LowTEB` likelihoods for the low-ℓ and very high-ℓ respectively (green) are compared with the addition of the BAO and SN data (red).

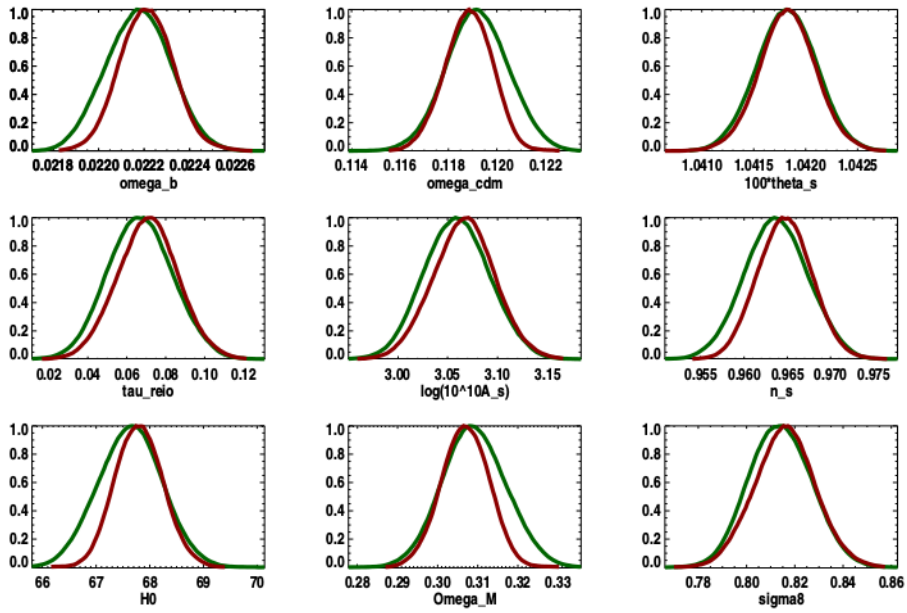

Figure 7.20: The posterior distributions for the `HiLLiPOP` likelihood using TT,EE and TE, in combination with the VHL and the `LowTEB` likelihoods for the low-ℓ and very high-ℓ respectively (green) are compared with the addition of the BAO and SN data (red).

cosmological parameters obtained using the *Planck* CMB data only. The full-sky maps and the good control on the foregrounds given by the wide frequency coverage, allow to constraint the positions of the CMB power spectrum peaks with sub-% precision, and the density parameters with a few % precision. We have obtained a 5σ detection of a deviation from scale invariance for the scalar spectral index n_s. Also, we have shown the consistency between temperature and polarisation results and some interesting check as the robustness of the results to the two different statistical methods presented in chapter 4, and the agreement with the `Plik` likelihood.

Given the level of sensitivity of the *Planck* data we can look for subtle systematic effects in the temperature data. We have thus discussed the $A_{\rm L}$ deviation from unity and shown that the addition of the VHL data regularise the problem allowing a more proper estimation of the τ parameter. Also, the addition of the BAO and Supernova data shrink the error bars up to a 40% gain and results stayed consistent with the ΛCDM model. In the next chapter we will consider the straightforward extensions of the standard model in the neutrino sector.

Chapter 8

Neutrino results

In chapter 7 we have shown that *Planck* data are consistent with the standard ΛCDM paradigm. We have also tested the effect of the inclusion of the complementary datasets described in chapter 6. The base ΛCDM model considered, as detailed in sec. 1.5, includes a fixed value for the absolute scale of neutrino masses $\Sigma m_\nu = 0.06$ eV, which is expected in the normal hierarchy scenario when the lightest neutrino is assumed massless, and a neutrino energy density resulting from the presence of only three active families, $N_{\rm eff} = 3.046$ (chapter 2). In this chapter we investigate the simplest extensions to this baseline model:

- In sec. 8.1, fixing $N_{\rm eff} = 3.046$ to its standard value, the Σm_ν parameter is left free in the analysis. The TT only constraint and the implications of the $A_{\rm L}$ tension, pointed out in the previous chapter, are discussed. The robustness with respect to different dataset choices is tested and a final constraint is obtained when combining late time distance measurements with the CMB.

- In sec. 8.2, the sum of neutrino masses is again fixed to the standard $\Sigma m_\nu = 0.06$ eV value and $N_{\rm eff}$ is left free, allowing the presence of ("neutrino-like") degrees of freedom, that were relativistic during radiation domination (chapter 2). We discuss the results obtained either in temperature or polarisation.

The two parameters Σm_ν and $N_{\rm eff}$, describe effects that took place, respectively, at late and early epochs in the evolution of the universe. Their signatures on the CMB spectra are sufficiently uncorrelated so that, in scenarios with both parameters left free, the results do not vary substantially from the two separate cases described above (Planck Collaboration. XVI. 2014; Planck Collaboration. XIII. 2015).

8.1 Constraints on the absolute scale of neutrino masses

As discussed in chapter 2, the CMB anisotropies are weakly sensitive to neutrino masses. In practice, when fitting Σm_ν we consider a simplified degenerate scenario in which the mass differences between the three neutrinos are not taken into account[1]. The effects of massive neutrino in temperature and polarisation power spectra are similar (e.g.Lesgourgues et al. (2013)). However, the *Planck* polarisation spectra do not have enough signal to noise ratio to improve much over constraints extracted from TT only data. Nevertheless, polarisation is useful in breaking other parameter degeneracies, resulting in tighter constraints for the parameters in the combination TT, EE and TE with respect to TT (chapter 7).

[1]To speed up computational time in `CLASS` we consider only one massive neutrino with mass Σm_ν and two massless ones. Our results are insensitive to this kind of implementation details.

As discussed in chapter 4, the presence of the physical boundary $\Sigma m_\nu > 0$ is a case for which the profile likelihood analysis technique is very adequate. Hence, in this section, we make regular use of this technique. Moreover, the shape of the profile near the minimum is an indicator of the goodness of fit and thus of possible residual systematics effects.

8.1.1 High-ℓ temperature alone and the $A_{\rm L}$ issue

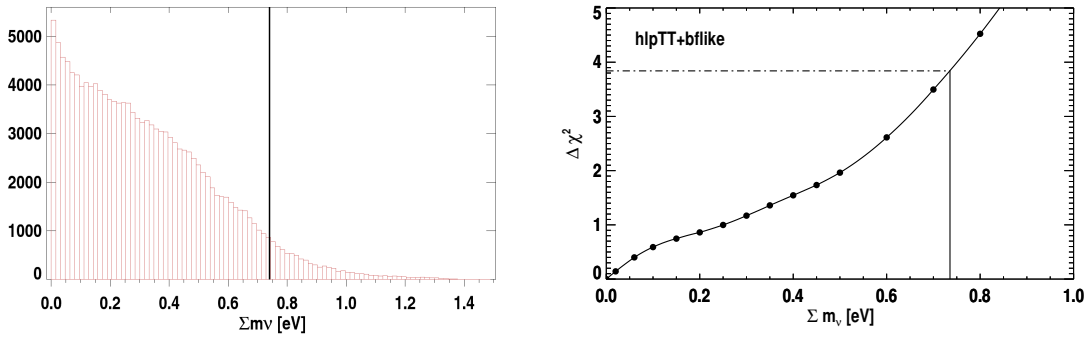

(a) (b)

Figure 8.1: (a) Posterior distribution of the sum of neutrino masses obtained when sampling the TT `HiLLiPOP` likelihood in combination with the `LowTEB` likelihood. The black line indicates the 95% upper limit (Eq. 8.1), obtained by cutting the area of the histogram. (b) Profile likelihood of Σm_ν in the same case. From the cut at 3.84, one can extract the approximate limit $\Sigma m_\nu < 0.74$ eV at 95% CL.

We start by analysing the constraint using only temperature data at high-ℓ. In Fig. 8.1(a) we report the MCMC posterior obtained when sampling the `HiLLiPOP` TT likelihood (chapter 5) in combination with the `LowTEB` likelihood (sec. 6.1.1) at low-ℓ. We obtain

$$\Sigma m_\nu < 0.74 \text{ eV} \quad (95\%, \texttt{HiLLiPOP} + \texttt{LowTEB}). \tag{8.1}$$

Fig. 8.1(b) displays the corresponding likelihood profile of Σm_ν. It shows a strange flex near the minimum. As discussed in chapter 4, in the presence of a boundary, the Feldman-Cousin (FC) prescription allows a proper analytical estimation of an upper limit in the case of a parabolic profile. If the shape is not parabolic one can only set approximative limits, unless relying on simulations[2]. Also, non trivial features near the minimum can be interpreted as hints of possible residual systematic effects. Hence, the Gaussian (i.e. analytic) FC procedure can not be safely applied in this case and we are not able to set a proper constraints. In the case of a parabolic profile with a minimum at zero the 95% upper limit is obtained cutting the $\Delta\chi^2$ at 3.84. One can still use this recipe to obtain an approximated constraint neglecting what happens near $\Sigma m_\nu \sim 0$. Doing this, we find the exactly the same result as the MCMC one of Eq. 8.1.

The non trivial shape of the profile likelihood requires further studies. In chapter 7 we have pointed out that the *Planck* TT likelihoods have a preference for a high value of $A_{\rm L}$. Since neutrinos free-streaming prevents clustering on small scales (chapter 2), massive neutrinos suppress the lensing power. This suppression has the same effect as a low $A_{\rm L}$ value. Thus, the tension that drives $A_{\rm L}$ can induce

[2]This has not been done in this thesis due to the complexity of foreground simulations.

an artificially tight constraint, i.e. the *Planck* TT only minimum of the profile is pulled down to non-physical (negative) Σm_ν values resulting in a too "optimistic" limit (Planck Collaboration. XVI. 2014; Planck Collaboration A54 2014).

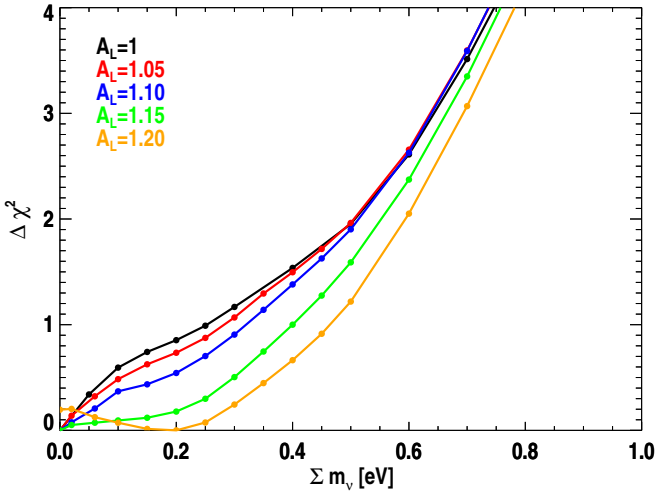

Figure 8.2: The impact of different $A_{\rm L}$ on the Σm_ν profile. For each profile the $A_{\rm L}$ parameter is fixed to the indicated value. The standard case when $A_{\rm L} = 1$ is shown in black.

In Fig. 8.2 we "profile" the Σm_ν parameter for different fixed value of $A_{\rm L}$ using as before TT only (in combination with the `lowTEB` likelihood). The previously discussed standard case with $A_{\rm L} = 1$ is in black. Considering larger fixed values for $A_{\rm L}$, the flex is smoothed out. For $A_{\rm L} = 1.2$ there is non-significant preference for a neutrino mass. Indeed, when we are proposing a model with over-amplified lensing effect ($A_{\rm L} \gtrsim 1.2$), leaving Σm_ν free, the ΛCDM + Σm_ν cosmology adjusts itself to the less lensed data increasing the best fit value for Σm_ν. Indeed, the data are better fitted by a model where massive neutrinos, through free-streaming, have erased more structures, resulting in a lower lensing effect on the spectra. This emphasises the need to regularise the $A_{\rm L}$ problem to obtain a robust upper limit for Σm_ν. As discussed in sec. 7.3, the addition of the VHL data (chapter 6) results in a $A_{\rm L}$ value in agreement with unity. In sec. 8.1.2 we thus also consider the ACT and SPT spectra.

8.1.2 The addition of VHL data

When we add VHL data, the shape of the profile changes. As is shown in Fig. 8.3, the flex, present in the *Planck* TT only case, is not there any more. We remind that for the two profiles $A_{\rm L}$ is kept fixed at one. However, in chapter 7 we have shown that the addition of VHL data shifts the fitted $A_{\rm L}$ parameter from $1.22^{+0.11}_{-0.10}$ to $1.04^{+0.08}_{-0.07}$. The resulting effect on Σm_ν is similar to the one described in Fig. 8.2, justifying the statement that whatever pushes $A_{\rm L}$ to higher values, pushes also the neutrino mass constraint to lower values and with an unphysical "flex shape".

Adding VHL data, we find a minimum χ^2 around ~0.3 eV. However, this is not significant: recalling that the 68% CL is obtained by cutting the profile at 1, we can infer from Fig. 8.3 that it has barely a 1σ significance. An approximated 95% limit gives $\Sigma m_\nu \lesssim 0.86$ eV.

In Fig. 8.3, we also show (in red) the result obtained excluding the `SPT_low` dataset (sec. 6.3) from the VHL combination. This latter dataset has a more important multipole overlap with *Planck* data than the other high-ℓ datasets and removing it, the $A_{\rm L}$ parameter is slightly higher ($A_{\rm L} = 1.09 \pm 0.07$, see

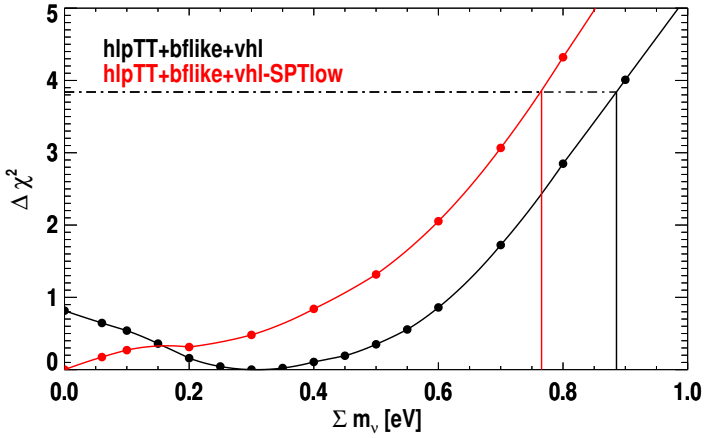

Figure 8.3: Profile likelihood result obtained scanning the `HiLLiPOP` TT likelihood in combination with the `LowTEB` and the VHL data (in black), compared to the case where we exclude `SPT_low` data (in red).

Table 7.10). As a result, we have a tighter constraint on Σm_ν but we recover a flex. This is a very subtle effect and since we cannot definitively conclude which combination is better, we will adopt in the following the most conservative VHL result, i.e. including the `SPT_low` data.

8.1.3 BAO and Supernova data

In sec. 2.5.2 we have seen that, beside their impact on lensing and on the early ISW effect, neutrinos affect the angular diameter distance to last scattering D_A (Eq. 1.25), constrained with *Planck* data via the position of the first acoustic peak. In flat models, as the one we consider, this is degenerate with H_0. At fixed θ_* (Eq. 1.125), the higher the neutrino mass, the larger D_A and the smaller expansion rate at low redshift. The addition of the latest BAO measurements (sec. 6.4), strongly improves the constraint on Σm_ν, and gives to the profile a nice parabolic shape (red in Fig. 8.4). The same effect is observed with JLA data since an independent measurement of Ω_m helps in breaking the degeneracies (black in Fig. 8.4). In Table 8.1 we report the FC limits in these cases. Note that there is no preference for massive neutrinos any more.

Data	$\sum m_\nu$ (95% CL)
`HiLLiPOP` (TT) + `LowTEB` +VHL+JLA	< 0.52 eV
`HiLLiPOP` (TT) + `LowTEB` +VHL+BAO	< 0.23 eV

Table 8.1: 95% constraints obtained via the FC prescription on Σm_ν. Relative profiles can be found in Fig. 8.4.

8.1.4 Robustness with respect to the low-ℓ data

In sec. 7.3.2 we have discussed the interplay between $A_{\rm L}$ and the reionisation optical depth τ. The addition of VHL data, regularising the $A_{\rm L}$ tension, gives an estimate of the value of τ that is consistent with the one obtained from HFI low-ℓ polarisation spectra using the *lollipop* likelihood (sec. 6.1.2). Since the Σm_ν constraint depends on lensing, and thus on the value of τ, we do not expect to see much variation

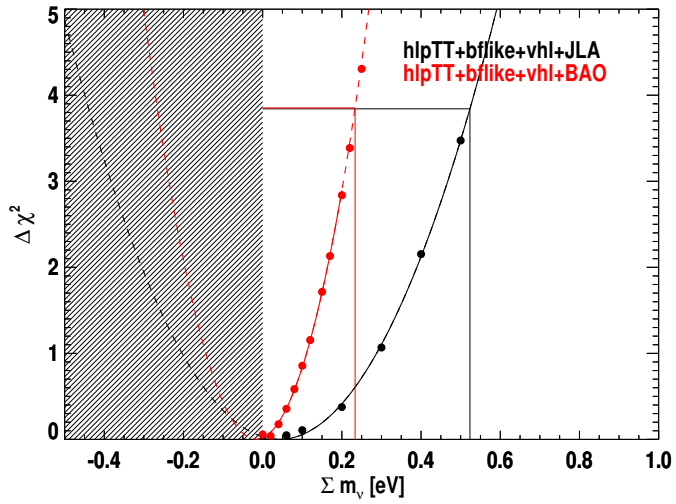

Figure 8.4: Profile likelihood for HiLLiPOP TT + LowTEB in combination with VHL + JLA (black), and VHL + BAO (red). Since the shapes of the profiles are parabolic, in Table 8.1 we report the 95% constraints obtained via the FC prescription.

of this constraint if we switch to *lollipop* instead of LowTEB for the large scale information. In Fig. 8.5, we show that this is indeed the case.

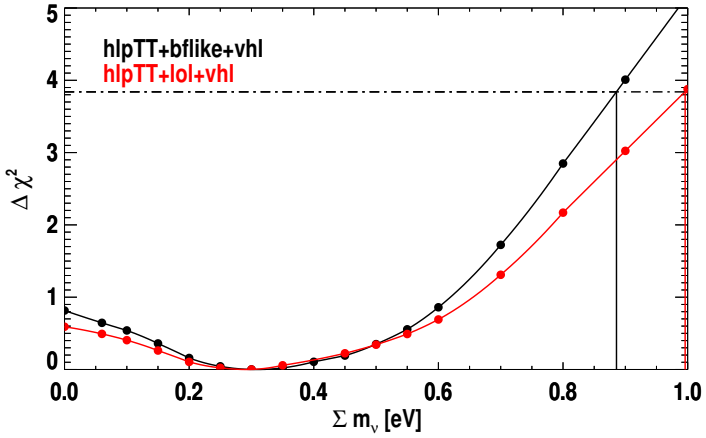

Figure 8.5: The baseline HiLLiPOP (TT) + LowTEB + VHL (in black) is compared to the combination HiLLiPOP (TT) +*lollipop* + VHL (in red).

8.1.5 High-ℓ polarisation

We now consider the full (TT, EE, TE) HiLLiPOP likelihood. We expect polarisation to help in breaking some of the degeneracies in CMB temperature data, allowing for a better constraint. In chapter 7 we have discussed the consistency between temperature and polarisation. From Table 7.4 we see that EE and TE spectra have separately good χ^2. However, their combination with temperature is more problematic. In chapter 5, for example, we have pointed out a calibration-like issue between temperature and polarisation that can be responsible for the bad value for the global χ^2. Nevertheless, the ΛCDM results from the

full HiLLiPOP likelihood are in good agreement with temperature alone. In Fig. 8.6, we show the Σm_ν profile for the full likelihood compared to the temperature result. The upper limit is reduced but the profile near the minimum has a strange behaviour, showing again a flex. However, we have argued that the temperature result is somewhat over-corrected which may lead to such an effect. Anyway, the addition of BAO data completely drives the constraints and we will see in sec. 8.1.6 that the limits in the two cases are not much different.

The essential role of BAO is also clear if we try to obtain a limit for the Σm_ν using the polarisation spectra only. In Fig. 8.7 is shown the profile for TE alone[3] (black curve). In this case the low signal to noise ratio does not allow to gain over the constraint coming from the non-relativistic transition at decoupling (sec. 2.5.2), and we recover $\Sigma m_\nu < 1.2$ eV (95%)[4]. Adding BAO and JLA, we find $\Sigma m_\nu < 0.24$ eV, which is very competitive with the TT limit discussed just below.

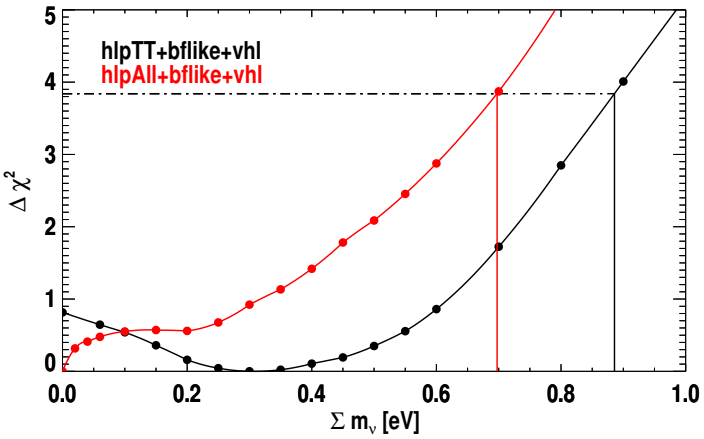

Figure 8.6: The baseline HiLLiPOP (TT) + LowTEB + VHL (in black) is compared to the full HiLLiPOP likelihood +LowTEB + VHL (in red).

8.1.6 Our best upper limit

For our final upper limit for Σm_ν, we combine *Planck* CMB measurements with both BAO and SN measurements. The value obtained from HiLLiPOP TT (+LowTEB + VHL) (Fig. 8.8), reads

$$\Sigma m_\nu < 0.22 \text{ eV} \quad (95\%, \texttt{HiLLiPOP (TT)} + \texttt{LowTEB} + \text{VHL} + \text{BAO} + \text{JLA}). \tag{8.2}$$

When the full HiLLiPOP likelihood is used, we obtain

$$\Sigma m_\nu < 0.20 \text{ eV} \quad (95\%, \texttt{HiLLiPOP (TT,EE,TE)} + \texttt{LowTEB} + \text{VHL} + \text{BAO} + \text{JLA}). \tag{8.3}$$

These two values are consistent with the official *Planck* result. Moreover, the parabolic shape of the profile and the position of the minimum, give us confidence that no obvious unaccounted systematic effects are driving the constraint. In addition, this solution is fully compatible with $A_L = 1$.

[3] Note EE do not contain enough information to constrain Σm_ν.

[4] This limit is similar to the WMAP TT alone result (Hinshaw et al. 2013) which did not have enough sensitivity to see the lensing effect.

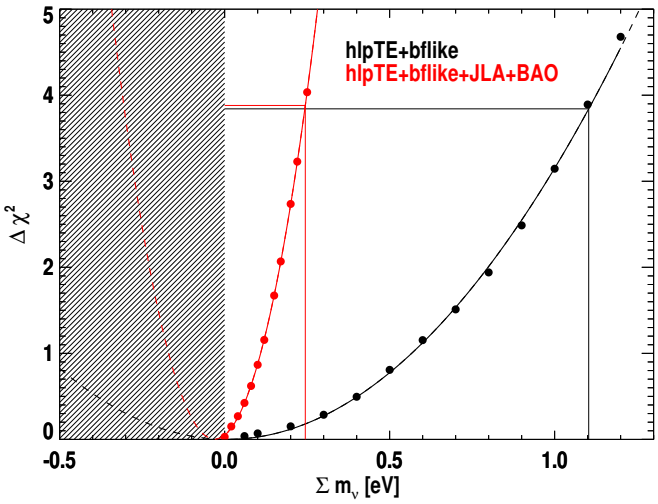

Figure 8.7: Profile likelihood for the Σm_ν parameter using the TE `HiLLiPOP` likelihood (in black), and in combination with BAO and JLA data (in red). Note the `LowTEB` likelihood is always used at low-ℓ. Since the profiles are parabolic we apply the FC procedure described in chapter 4.

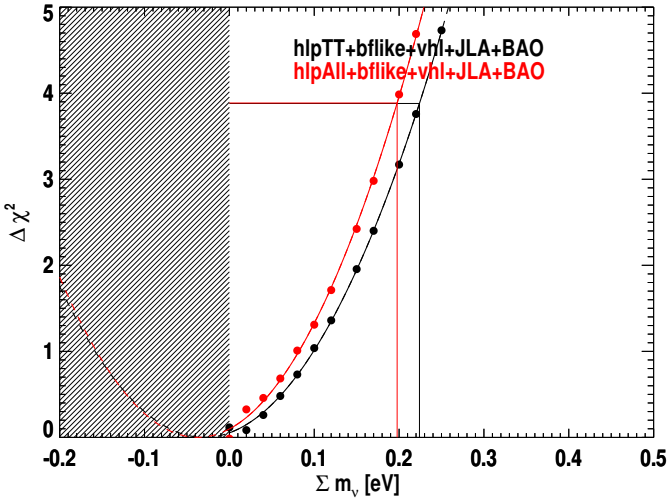

Figure 8.8: Profile likelihood for the combination `HiLLiPOP` (TT) + `LowTEB` + VHL + BAO + JLA (black) and the one with the addition `HiLLiPOP` TE and EE spectra (red). Since the profiles are parabolic we apply the FC procedure described in chapter 4. The resulting upper limits can be found in Eq. 8.2 and 8.3, respectively.

8.1.7 Is there a hint for a neutrino mass?

Several results in the literature show a preference for a non zero neutrino mass of the order of 0.3 or 0.4 eV. Beutler et al. (2014) reported a measurement of a neutrino mass 0.34 ± 0.14 eV, using Redshift-space distortion (RSD) measurements from BOSS, in combination with *Planck* 2013 chains marginalised over $A_{\rm L}$. A neutrino mass was also proposed to help reducing the tension on the σ_8 parameter between the CMB cosmology, and its estimate from cluster counts or weak-lensing data (Planck Collaboration. XX.

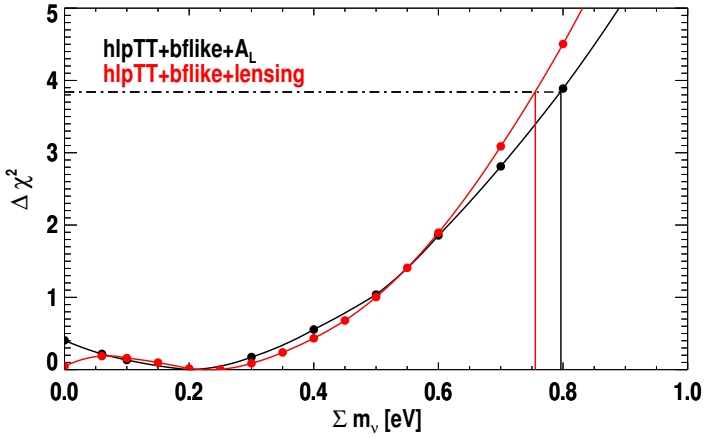

Figure 8.9: Profile likelihood obtained using the `HiLLiPOP` TT + `LowTEB` likelihood: in black when marginalising over $A_{\rm L}$, while in red adding the *Planck* lensing likelihood.

2014; Planck Collaboration. XIII. 2015).

A similar preference (~ 0.2 eV) is obtained if $A_{\rm L}$ is left free together with Σm_ν (black in Fig. 8.9). This latter case is similar to what we obtain with the addition of the lensing likelihood, built from the 4-point CMB correlation function (red line). Indeed, the addition of the lensing likelihood, mitigates the preference for a high $A_{\rm L}$ value. As noted in Planck Collaboration. XIII. (2015), this cures also the cosmological parameter values in the dark energy sector and for the models with curvature: *Planck* TT + lensing has no more preference for a negative Ω_k or for an equation of state for the dark energy in the phantom domain. For neutrino masses, it gives a best fit value for Σm_ν of about 0.2 eV (note that the `Plik` likelihood shows a similar preference when combined with `Commander` and lensing, with $\Sigma m_\nu = 0.41^{+0.18}_{-0.35}$). However, lensing has not a strong preference for this solution and there is only a $\Delta\chi^2_{\rm lens} \simeq 1$ between the TT+ lensing and the TT alone cosmology. Moreover, the preference for massive neutrinos comes at the price of a low value for H_0 (the anticorrelation between the two has been already pointed out in sec. 7.2.1). The addition of the Efstathiou (2014) H_0 prior ((70.6 ± 3.3) Kms^{-1}Mpc^{-1}), removes the preference for a non zero mass. We do not include lensing in our baseline, since with VHL data it is statistically irrelevant and may even introduce some systematic errors (sec. 6.2).

In sec. 8.1.2 we also noted that, with the addition of VHL data, there is a tiny hint for a neutrino mass. Some characteristic of this best fit solution are given in Table 8.2. Although the value of σ_8 has decreased a lot and it is in better agreement with the cluster counts measurements, the values of H_0 is low and Ω_m high, in disagreement with direct H_0 measurements, Supernova and BAO data.

As we have also seen in sec. 8.1.3, the preference for a best fit at 0.3 eV for Σm_ν disappears when adding BAO and SN, pointing rather toward a systematic effect still to be understood.

8.2 Constraints on the effective number of neutrino species

In the previous section we have investigated the well motivated extension of the ΛCDM model where the sum of the masses of the three standard active neutrinos is left free to vary. Here we fix Σm_ν to its standard minimal value (0.06 eV), and we consider a ΛCDM + $N_{\rm eff}$ cosmology. The number of effective neutrinos $N_{\rm eff}$ (defined in Eq. 2.25), accounts for all degrees of freedom, other than photons, produced well before recombination and still relativistic at decoupling. As discussed in sec. 2.5, an excess in $N_{\rm eff}$ with respect to the expected 3.046 value, could point to the presence of light relics in the Universe,

Par	best fit (CLASS)
H_0	64.7
Ω_m	0.348
σ_8	0.764
$f\sigma_8(0.57)$	0.453

Table 8.2: Best fit values of some of parameter of the ΛCDM + Σm_ν cosmology obtained with HiLLiPOP (TT) + VHL +bflike.

like axions or massless sterile neutrinos[5]. The measurement of $N_{\rm eff}$ is also important since its precise estimation allows to exclude $N_{\rm eff} = 0$ at high confidence, establishing an (indirect) evidence of the cosmic neutrino background.

The effect of $N_{\rm eff}$ on the CMB temperature spectra appears mainly on the damping tail. It is proportional to the ratio between the angular scale of photon diffusion and the sound horizon, in turn proportional to the square root of the Hubble parameter (sec. 2.5.3). There is thus a positive $N_{\rm eff}$-H correlation, i.e. increasing the number of extra degree of freedom also increases the expansion rate and the recombination takes place earlier in cosmic history.

The posterior distribution for the $N_{\rm eff}$ parameter is almost Gaussian. In this case, the profile likelihood technique is not mandatory and one finds results equivalent to the MCMC analysis. They are thus presented here using both techniques.

8.2.1 Temperature constraints

We start by analysing the constraint from the temperature HiLLiPOP likelihood in combination with LowTEB at large scales. We measure (black profile in Fig. 8.11)

$$N_{\rm eff} = 3.77 \pm 0.55 \quad (68\%, \texttt{HiLLiPOP TT +LowTEB}), \tag{8.4}$$

which is 1.4σ higher than the standard 3.046. This result is slightly different from the official *Planck* result that is 3.13 ± 0.32. Because of the $N_{\rm eff}$-H_0 correlation, our ΛCDM + $N_{\rm eff}$ cosmology prefers a high H_0 value (the best fit is at 73.7 $\rm kms^{-1}Mpc^{-1}$), a low Ω_m (0.278) and a high σ_8 (0.842). This results thus alleviates the tensions with direct H_0 measurements but increase the one, mentioned in sec. 8.1.7, with weak lensing and cluster counts on σ_8. Moreover, there is a positive correlation between $N_{\rm eff}$ and the spectral index n_s. Increasing the number of neutrino species induces more damping at small scales in the CMB TT power spectrum, which can be compensated by an increase of n_s. Our best fit value for n_s, in this ΛCDM + $N_{\rm eff}$ cosmology, is indeed 0.992, 4σ higher than the TT ΛCDM value of Table 7.2, which could be a sign of residual foreground contamination. The high value of $N_{\rm eff}$, also tends to delay the matter-radiation equality, enhancing the TT CMB power spectrum peaks and is thus positively correlated to $\Omega_c h^2$. All these correlations can be observed in the correlation matrix displayed in Fig. 8.10, obtained using our MCMC.

Note that the χ^2 improvement in this extended cosmology with respect to the standard ΛCDM is better by only 2 units for an absolute value of 9949.7. The preference for the high value of Eq. 8.4 are discarded changing the low-ℓ information or adjusting the foregrounds. These solutions are investigated below.

[5]Note that in this configuration, we can not search for massive sterile neutrinos since we are considering massless extra degree of freedom.

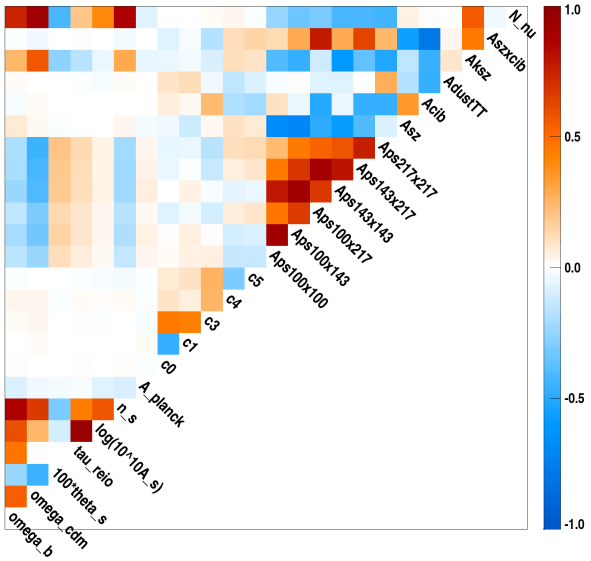

Figure 8.10: Correlation matrix obtained from the ΛCDM + $N_{\rm eff}$ chains sampled using the `HiLLiPOP` TT likelihood in combination with `LowTEB`. Note that $N_{\rm eff}$ is strongly correlated with n_s and $\Omega_c h^2$.

Different low-ℓ choices

We test the dependency of the estimate of $N_{\rm eff}$ with respect to the low-ℓ information. Either using a τ prior or the *lollipop* likelihood (sec. 6.1.2), we now find values compatible with the standard 3.046 one (Table 8.4 and Fig. 8.11). The two profiles are very similar. This is not surprising since the *lollipop* likelihood is similar to a pure τ prior (sec 6.1.2). Moreover, $N_{\rm eff}$ influences the early universe and is thus uncorrelated with a late time parameter like the reionisation optical depth. When the `LowTEB` likelihood is used for the low-ℓ, however, the estimate of $N_{\rm eff}$ increases, although most of the $N_{\rm eff}$ constraint comes from the high-ℓ tail of the temperature spectra[6]. This can be interpreted as a consequence of the low/high-ℓ tension in the TT power spectrum, discussed in chapter 7. Indeed, this is confirmed by the high value of $N_{\rm eff}$ found when the low-ℓ temperature `Commander` likelihood is added to the τ prior case (green profile in Fig. 8.11).

Overall these results show that the $N_{\rm eff}$ estimate is not very robust to the low-ℓ data choice.

The impact of foregrounds

In Fig. 8.12 we show the profile likelihoods for $N_{\rm eff}$ obtained using our temperature likelihood, in combination with the `LowTEB` likelihood at low-ℓ, and adding different constraints on the foregrounds. First we note that with the addition of the VHL data, both with (in red) or without `SPT_low` (in blue), the results show a $\sim 1.5\sigma$ discrepancy with the standard value of 3.046. Indeed, if the profile minimum positions

[6] A similar effect is present for the `Plik` likelihood where there is a $\sim \sigma$ increase in $N_{\rm eff}$ with respect to the case with a τ prior.

Data	$N_{\rm eff}$ (68% CL)
HiLLiPOP (TT) + LowTEB	$3.77^{+0.55}_{-0.55}$
HiLLiPOP (TT) + tau prior + Commander	$3.70^{+0.55}_{-0.52}$
HiLLiPOP (TT) + tau prior	$3.05^{+0.67}_{-0.52}$
HiLLiPOP (TT) + *lollipop*	$3.03^{+0.67}_{-0.52}$

Table 8.3: The values of the $N_{\rm eff}$ parameter for different choices of the low-ℓ information. The τ prior is the standard Gaussian prior 0.07 ± 0.02. The corresponding profiles can be found in Fig. 8.11.

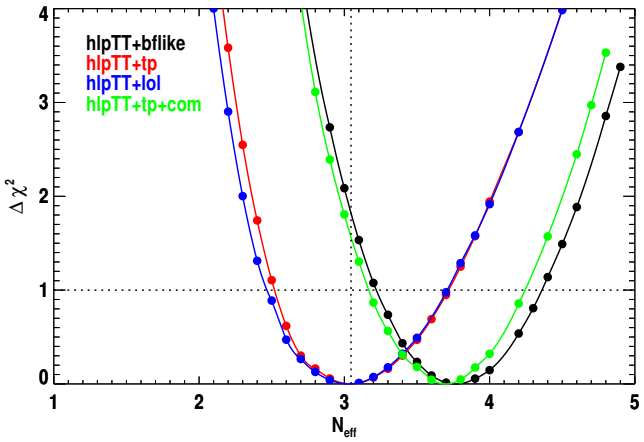

Figure 8.11: Profiles for the $N_{\rm eff}$ parameter for the HiLLiPOP (TT) likelihood in combination with different choices of the low-ℓ information. The black curve is obtained with the LowTEB likelihood. The τ prior case (standard Gaussian prior 0.07 ± 0.02) is in red. The τ prior + Commander case is in green. The *lollipop* likelihood is also considered (in blue). The corresponding mean and errors can be found in Table. 8.3. The vertical dotted line indicates the standard 3.046 value.

are slightly lower than in the TT alone case, the error bars are also tighter (Table 8.4). In Fig. 8.13 we report the posterior distributions for the cosmological parameters in the ΛCDM + $N_{\rm eff}$ case. As already discussed, both TT alone (in red) and TT+VHL case (in green), have high values for the spectral index n_s and $\Omega_c h^2$, with respect to the ΛCDM cosmology[7]. Looking again at the correlation matrix of Fig. 8.10, we remark a correlation between $N_{\rm eff}$, n_s and $\Omega_c h^2$ with the kSZ component. Hence, we sample the TT HiLLiPOP likelihood, in the ΛCDM + $N_{\rm eff}$ case, adding the prior on the SZ foregrounds of Eq. 7.19. As discussed in sec. 7.3.1, this prior is extracted from the VHL data and constrains the degeneracy between the kSZ and the tSZ components. The resulting posterior distributions for the cosmological parameters are shown in yellow in Fig. 8.13. The prior drives the cosmology closer to the ΛCDM case (lower values of n_s and $\Omega_c h^2$, and a higher value for θ_s), pushing $N_{\rm eff}$ toward its standard value. This shows that, when we open up the parameter space, the poor control on even small residual foreground contaminations can play a role on our estimates. Mostly constrained by the temperature damping tail, $N_{\rm eff}$ is especially sensitive to temperature foregrounds. Hence, we do not consider this results as being robust enough and, in the

[7]Note also that even with $N_{\rm eff}$ free, there is a discrepancy on the estimate of $\Omega_b h^2$ between TT and TT+VHL, as mentioned in sec. 7.3.1

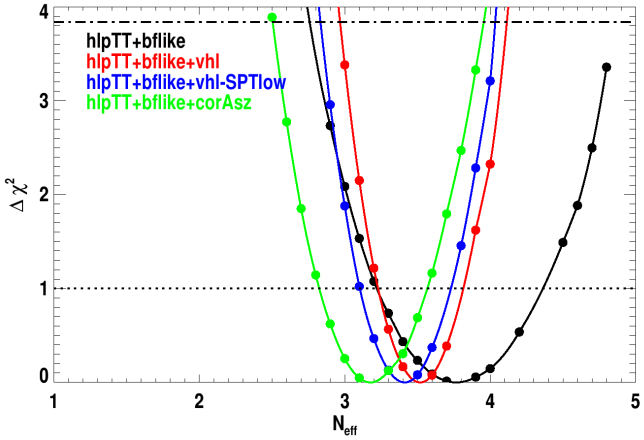

Figure 8.12: Profile likelihoods of the $N_{\rm eff}$ parameter obtained using the HiLLiPOP TT likelihood in combination with the LowTEB for the low-ℓ, and with different choices for the high-ℓ: addition of the VHL (in red), addition of VHL but excluding SPT_low (in blue), using the prior on the SZ foreground of Eq. 7.19 (in green). The TT+LowTEB case of Eq. 8.4 is shown in black for comparison. Means and error bars can be found in Table 8.4.

following section, we report the constraint from polarisation, where the contamination from foreground is much smaller.

Data	$N_{\rm eff}$ (68% CL)
HiLLiPOP (TT) + LowTEB	3.77±0.55
HiLLiPOP (TT) + LowTEB +VHL	3.52±0.30
HiLLiPOP (TT) + LowTEB +VHL -SPT_low	3.41±0.31
HiLLiPOP (TT) + LowTEB + prior SZ	$3.18^{+0.39}_{-0.35}$

Table 8.4: Means and errors on $N_{\rm eff}$ obtained with the profile likelihood technique using the TT HiLLiPOP likelihood in combination with other datasets. These numbers correspond to Fig. 8.12.

8.2.2 Polarisation results

We analyse the constraints coming from polarisation. In Fig. 8.14, we report the results for the TE and EE. Due to the low signal to noise ratio, the EE result is only a weak constraint compatible with 3.046 at $\sim 1\sigma$ level.

The TE based constraint is, on the contrary, even statistically better than the TT one thanks to the lower impact of foregrounds, and it will be considered as our baseline

$$N_{\rm eff} = 2.89^{+0.46}_{-0.42} \quad (68\%, \texttt{HiLLiPOP (TE) + LowTEB}). \tag{8.5}$$

8.2.3 Robustness of the TE result

We would like to assess how robust the constraint coming from the TE spectra is. We first test the impact of the low-ℓ information used. The HiLLiPOP TE likelihood in combination with a τ prior or with the

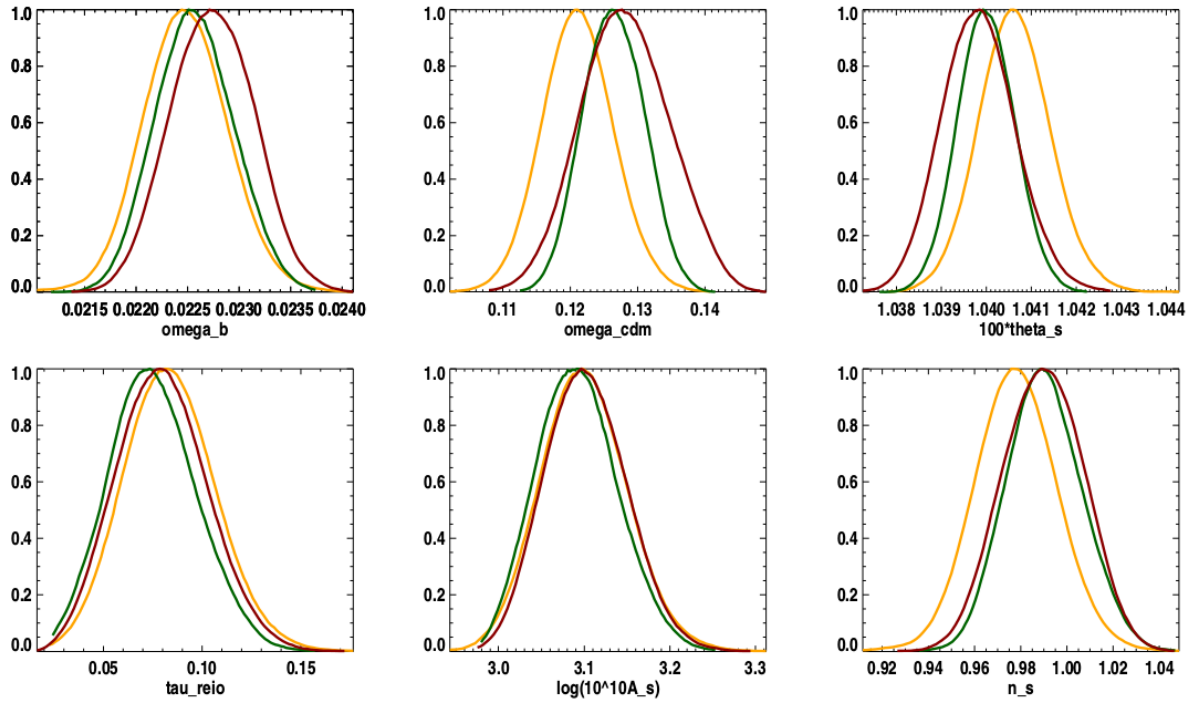

Figure 8.13: Posterior distributions for the cosmological parameters in the ΛCDM + $N_{\rm eff}$ case. The combination `HiLLiPOP` TT + `LowTEB` is in red. The case where the VHL likelihood has been added is shown in green. The case where the "very high-ℓ" constraining power on foregrounds is mimicked by a prior on the SZ residuals (Eq. 7.19) is in yellow.

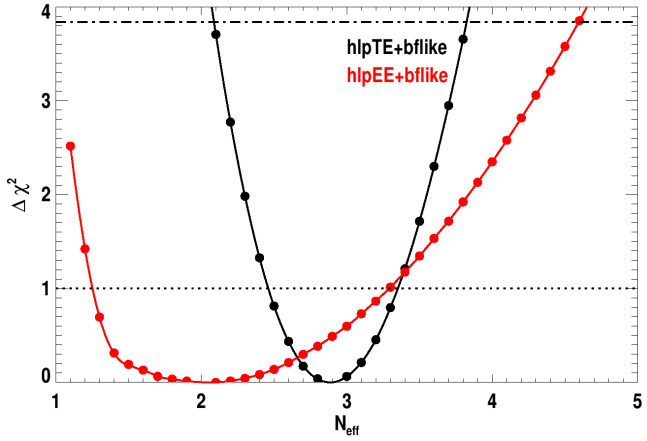

Figure 8.14: Profile likelihood for `HiLLiPOP` likelihood in combination with the `LowTEB` at low-ℓ. The results are are shown in black for TE and in red for EE. The asymmetry of the EE limit comes from the underline neutrino model assumed. We are, indeed, considering two massless and one massive (0.06 eV) active neutrino, so $N_{\rm eff}$, in `CLASS`, is greater than one by definition.

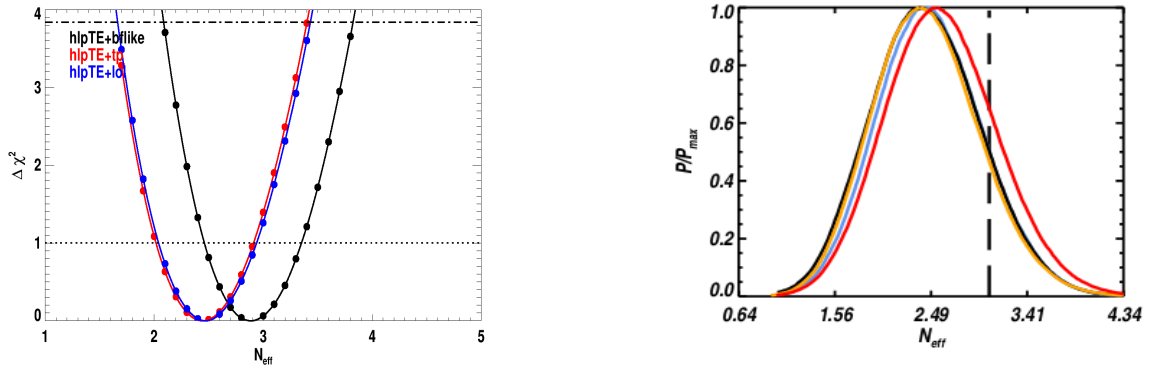

(a) (b)

Figure 8.15: (a) Profiles for the $N_{\rm eff}$ parameter for the `HiLLiPOP` TE likelihood in combination with different choices of the low-ℓ information. The black curve is obtained with the `LowTEB` likelihood. The τ prior case (standard Gaussian prior 0.07 ± 0.02) is in red. The *lollipop* likelihood is also considered (in blue). The corresponding mean and errors can be found in Table. 8.5. (b) Posterior distribution of the $N_{\rm eff}$ parameter obtained with different prior for the polarised dust parameter $A^{\rm TE}_{\rm dust}$: standard prior (black), no prior (blue), $A^{\rm TE}_{\rm dust}$ fix at one (yellow) or at zero (red).

lollipop likelihood gives the results of Table 8.5 and Fig. 8.15(a). As for temperature, the estimates are lower than the `LowTEB` case but still compatible at $\sim 1\sigma$ level with the standard 3.046 value.

We have used the polarisation results to get rid of the residual foregrounds present in temperature. Indeed, in TE, the only expected contamination comes from polarised dust emission, which is low (chapter 5). In Fig. 8.15(b), we show that the $N_{\rm eff}$ estimate is indeed very stable to various choices for the prior used for the dust. Even in the case where the dust is completely neglected (in red).

Data	$N_{\rm eff}$ (68% CL)
`HiLLiPOP` (TE) + `LowTEB`	$2.89^{+0.46}_{-0.42}$
`HiLLiPOP` (TE) + tau prior	2.49 ± 0.46
`HiLLiPOP` (TE) + *lollipop*	2.50 ± 0.46

Table 8.5: The values of the $N_{\rm eff}$ parameter for different choices of the low-ℓ information. The τ prior is the standard Gaussian prior 0.07 ± 0.02. The corresponding profiles can be found in Fig. 8.15(a).

8.2.4 Our best constraint

To further improve the $N_{\rm eff}$ constraint, we add the distance measurements of chapter 6. Indeed, an increase in $N_{\rm eff}$, not only increases the expansion rate so that the universe is younger at recombination, but also increases H(z) at lower redshift. Therefore adding BAO and Supernovae data, we obtain a 20% error bars reduction in $N_{\rm eff}$. The profile likelihood results can be found in Fig. 8.16 and related numbers in Table 8.6. The addition of late time distance measurements also allows to get rid of the low-ℓ dependency: the results using a τ prior or *lollipop* are now compatible, and consistent with the standard

scenario. The HiLLiPOP TE result in combination with LowTEB likelihood reads

$$N_{\rm eff} = 3.03^{+0.34}_{-0.31} \quad (68\%, \texttt{HiLLiPOP TE} + \texttt{LowTEB} + \text{BAO} + \text{JLA}). \tag{8.6}$$

This result excludes $N_{\rm eff} = 4$ at more than 99% CL.

Data	$N_{\rm eff}$ (68% CL)
HiLLiPOP (TE) + LowTEB + BAO+JLA	$3.03^{+0.34}_{-0.31}$
HiLLiPOP (TE) + *lollipop* + BAO+JLA	$2.95^{+0.33}_{-0.32}$

Table 8.6: Results from the profile likelihood analysis of the $N_{\rm eff}$ parameter using the TE HiLLiPOP likelihood in combination with others. Relative profile can be found in Fig. 8.16.

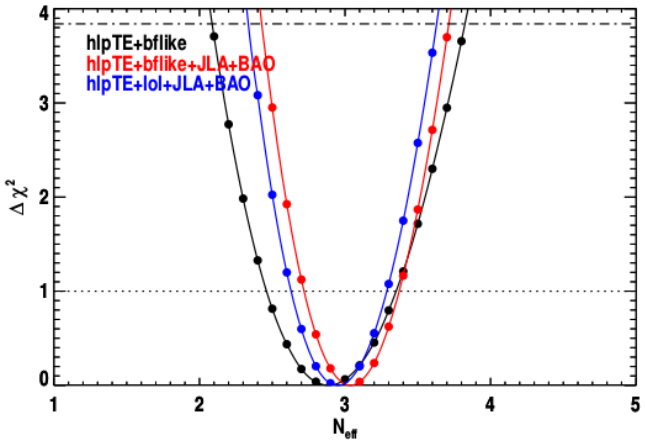

Figure 8.16: Profile likelihoods of the $N_{\rm eff}$ parameter using the TE HiLLiPOP likelihood. In black is shown the *Planck* alone value obtained when adding the LowTEB likelihood at low-ℓ. In red the final result with the addition of BAO and Supernovae. In blue, the combination with the *lollipop* likelihood is also shown for comparison. Means and errors can be found in Table 8.6.

Conclusions

In this chapter we have presented the separate constraints on the two parameters Σm_ν and $N_{\rm eff}$. For the former we have highlighted, with the help of the profile likelihood technique, a dependence on the $A_{\rm L}$ parameter that need to be properly treated since it causes either a overoptimistic limit for Σm_ν or a weak preference for a non zero neutrino mass. It is however the addition of BAO and Supernova data that drives the constraint to a rather stable upper-limit. For $N_{\rm eff}$, the temperature only constraint is sensitive to small foreground residuals in the data and we have thus decided to use the competitive and less foreground dependent TE constraint. The results are compatible with the standard ΛCDM scenario.

Conclusions

The *Planck* satellite, in service from 2009 to 2013, has produced a high-quality measurement of the anisotropies of the Cosmic Microwave Background that will continue to be scientifically explored in the years to come. The work described in this thesis, has been done simultaneously to the treatment and release of the 2015 full mission temperature and polarisation data, and is focused on the estimation of the energy content and the evolutionary properties of our universe, encoded in a set of cosmological parameters $\mathbf{\Omega}$ of the big bang model. The CMB is, indeed, a unique probe from which all these parameters can be estimated consistently.

In this thesis, the *Planck* data are used to construct the `HiLLiPOP` likelihood function from CMB power spectra, $\mathcal{L}(C_\ell(\mathbf{\Omega}), \boldsymbol{\psi})$, where $\boldsymbol{\psi}$ accounts for all the astrophysical and instrumental effects. The design of this high-ℓ likelihood is described in details. The likelihood compares data and models on the basis of the cross-power spectra that are estimated from the high resolution HFI 100, 143 and 217 GHz maps. Although the lower HFI frequencies are dominated by the CMB signal, an unbiased estimation of the underlining properties of the universe needs a careful treatment of the foreground emissions, both in temperature and polarization. Hence, frequency dependent masks are applied to the maps to limit these contaminations. The correlations between modes and multipoles that appear due to the complex masking, are encoded into the covariance matrix, that is estimated semi-analytically and is tested with Monte Carlo simulations. Even after this careful masking strategy, the likelihood has to account for astrophysical foreground residuals. These include mainly thermal radiation from diffuse Galactic dust both in temperature and polarization. In temperature, point sources, CIB and SZ effect are also considered. Physically motivated templates are used. Different choices for these templates have been tested as well as their effect on cosmological and instrumental parameters.

Once the likelihood is designed, the conventional approach for parameter estimation is based on Bayesian inference. In this methodology the likelihood is multiplied by some priors (encoding the a-priori knowledge on the parameter of interest) leading to a posterior distribution. A sampling of this posterior distribution is done using Markov Chains Monte Carlo (MCMC). The standard Metropolis-Hasting algorithm converges slowly and needs long and computationally costly pre-tuning of the proposal distribution. In this thesis is described the implementation of an Adaptive MCMC code where an on-the-fly adaptation of the proposal matrix is performed, allowing to bypass the pre-tuning phase and to squeeze the computational time needed for proper convergence of the algorithm. This method is extensively used in the analysis to obtain cosmological parameters posterior distributions.

Although widespread in cosmology, Bayesian methods have some limitations: it is difficult to find a consistent choice for priors and some volume effects may arise from the projection of a multidimensional space onto only one direction when estimating the error on individual parameters. Unlike the Bayesian ones, Frequentist methods have some interesting properties such as the invariance of the maximum likelihood estimate with respect to the choice of the set of cosmological parameters. For most parameters with near Gaussian distributions, the two methods give comparable results. We show that this is true also

for the sum of the neutrino masses, where the presence of the physical boundary requires some dedicated techniques.

The combination of the *Planck* experimental measurements, of the accurate theoretical predictions resulting from the CLASS Boltzmann Code, and of the aforementioned statistical tools, allows to set tight constraints on the cosmological parameters, revealing good consistency between the data and the standard ΛCDM cosmological model. Several results are given, using both methodologies and combining our likelihood to other cosmological datasets. An example is reported in Table **??**. The level of precision

par	value
$\Omega_b h^2$	0.0221 ± 0.00018
$\Omega_{\rm cdm} h^2$	0.119 ± 0.0012
$100\theta_s$	1.042 ± 0.00037
τ	0.0641 ± 0.016
$log[10^{10} A_s]$	3.052 ± 0.031
n_s	0.966 ± 0.0039
H_0	67.72 ± 0.52
Ω_m	0.307 ± 0.0070

Table 8.7: ΛCDM cosmological parameters obtained using the temperature HiLLiPOP likelihood in combination with LowTEB, VHL and BAO and JLA data.

of the likelihood enables us to identify subtle residual systematic effects in the data. The temperature spectra, for example, contain more lensing than expected within a ΛCDM model, resulting in a 2σ deviation from unity for the $A_{\rm L}$ parameter. We show that this preference for a high $A_{\rm L}$, translates, in a high value of the optical depth τ (and A_s as a consequence of the τ-A_s degeneracy), in tension with the low-ℓ estimate coming from polarisation alone measurements.

The addition of small scale data from the ground based experiments ACT and SPT, regularises the $A_{\rm L}$ issue

$$A_{\rm L} = 1.04^{+0.08}_{-0.07} \quad (68\%, \texttt{HiLLiPOP (TT) +LowTEB +ACT/SPT}),$$

and, consequently the tension between the low- and high-ℓ estimate of τ, driving it back to a lower value

$$\tau = 0.060 \pm 0.017 \ (68\%, \texttt{HiLLiPOP (TT) +LowTEB + ACT/SPT}).$$

Letting the sum of neutrino mass Σm_ν free, the overestimation of lensing drives the constraint on the absolute scale of neutrino masses to artificially low value. On the other hand, the $A_{\rm L}$ regularisation points toward a weak preference for a neutrino mass with a minimum of the χ^2 around 0.3 eV. This non-significant preference is erased if the BAO and the Supernova data are added. Our robust constraint, reads

$$\Sigma m_\nu < 0.20 \text{ eV} \quad (95\%, \texttt{HiLLiPOP (TT,EE,TE) + LowTEB + ACT/SPT + BAO/JLA}).$$

We also investigate the constraint on the number of effective neutrinos, i.e. the energy density of any relic particle, other than photons, still relativistic at decoupling. We show how the temperature results, although consistent with the standard 3.046 values, have a dependency on the residual foreground

modelling. Since it is almost independent of the foregrounds, the competitive constraint coming from the TE spectra, is then considered more robust.

Our best constraint, again with the addition of BAO and Supernovae data is

$$N_{\rm eff} = 3.03^{+0.34}_{-0.31} \quad (68\%, \texttt{HiLLiPOP}\ (\rm TE) + \texttt{LowTEB} + \rm BAO + JLA).$$

This result excludes $N_{\rm eff} = 4$ at more than 99% CL.

Appendix A

Planck products

Here we briefly revise some of the *Planck* products, namely the catalogue of compact sources, the clusters catalogue (sec.A.1) and the component separation maps (sec.A.2).

A.1 Catalogues

From the *Planck* data is possible to produce catalogues of compact sources or clusters. For our analysis is important to treat these emissions in order not to bias the estimation of cosmological parameter as discussed in chapter 5.

A.1.1 Catalogue of Compact Sources

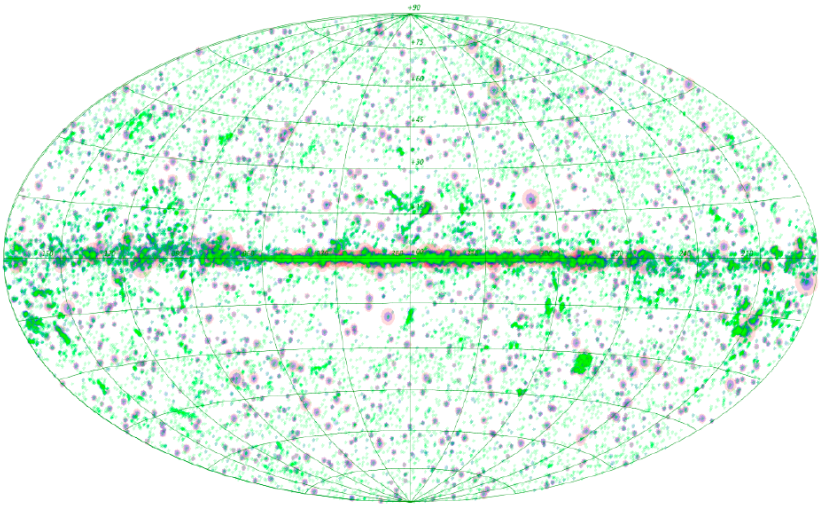

Figure A.1: Sky distribution (in Aitoff projection) of the PCCS sources at three different channels: 30 GHz (pink circles); 143 GHz (magenta circles); and 857 GHz (green circles). (Planck Collaboration. XXVIII. 2014).

The Planck Catalogue of Compact Sources (PCCS) (Planck Collaboration. XXVIII. 2014) is a sample of reliable Galactic and extragalactic sources (non thermal radio sources and thermal sources), ex-

Table A.1: Planck Catalogue of Compact Sources (PCCS) characteristics. Adapted from Planck Collaboration. XXVIII. (2014).

Freq. (GHz)	30	44	70	100	143	217	353	545	857
S/N threshold:									
Full sky	4.0	4.0	4.0	4.6	4.7	4.8	...	...	...
Extragalactic zone	...	...	...	...	...	...	4.9	4.7	4.9
Galactic zone	...	...	...	...	...	...	6.0	7.0	7.0
Number of sources	1256	731	939	3850	5675	16070	13613	16933	24381

tracted directly from the nominal mission maps[1]. The total number of sources in the catalogue ranges from 1256 at 30 GHz to 24381 source at 857 GHz (TableA.1). Compact sources are detected in each frequency maps by looking for peaks after convolving with a linear filter that preserve the amplitude of the source while reducing large scale structure and small scale fluctuation in the vicinity of the sources. In particular for the HFI high frequency channels, ad-hoc techniques (e.g. combinations of S/N and χ^2 between observed and predicted behaviour of the source, studies of nearby pixels for rejecting artefact not removed by the filter) have been implemented to reduce the number of spurious detections with minimal impact on the number of real sources found (Planck Collaboration. XXVIII. 2014).

The source selection for the PCCS is made on the basis of S/N. Since background properties vary substantially with the frequency and the sky direction, the S/N has been adapted to each case. At 100, 143, and 217 GHz, the S/N needed to achieve the reliability goal of 80% is determined defining an extragalactic zone (48% of the sky) but then applied all-sky. This is not the case for the higher frequencies where there is the need to control confusion from Galactic cirrus emission (Planck Collaboration. XXVIII. 2014). The filamentary structure of Galactic cirrus at small angular scales is often visible as knots in Planck maps. To control their spurious detection, different S/N cuts have been chosen for the Galactic and extragalactic zone. S/N cuts are summarised in TableA.1.

Cirrus emission at 353 GHz is relevant for the construction of an adapted mask for cosmological parameter estimation and has an impact on our dust model as discussed in sec.5.6.1.

A.1.2 Catalogue of clusters

The 2015 release includes also a catalogue of SZ sources (PSZ2; (Planck Collaboration. XXVII. 2015)), based on the full mission data and, at present, the largest SZ-selected sample of galaxy clusters. It contains 1653 detection, of which 1203 are confirmed with external datasets.

The galaxy clusters are the most massive formed structures and their evolution with mass and redshift is a sensitive cosmological probe of the late-time universe. They are composed of dark matter but also stars, cold gas and dust in galaxies, and a hot ionised intra-cluster medium (ICM). The ICM, which is the majority of the baryonic material by mass, emits in the X-rays via thermal bremsstrahlung and line emission, and boosts in energy the cosmic microwave background photons via inverse Compton, causing a redshift-independent spectral distortion of photons reaching us along the line of sight to the cluster (the thermal SZ, see sec.1.3.6). X-ray surveys (like ROSAT) are unique in their purity but they suffer from selection biases that favour low-redshift systems, due, for example, to flux limitations. On the contrary SZ surveys provide a nearly mass-limited census of the cluster population at high redshift, where abundance is strongly sensitive to cosmological parameters. The SZ survey observable is the spherically integrated Comptonisation parameter (Y_{SZ}) which is related to the integrated electron pressure and hence

[1]It will also be extended and upgraded for the latest release.

the total thermal energy of the cluster gas, that correlates to the mass (Planck Collaboration. XXVII. 2015).

Galaxy clusters provide unique constraints on the normalisation of the matter density fluctuations (σ_8), the mean matter density (Ω_m), and on extensions of the minimal model including the dark energy sector and neutrinos (Planck Collaboration. XXIV 2015).

A.2 Component separation maps

Component separation deals with the extraction of actual CMB signal from the measured maps. Although not used for cosmological parameter estimation, these maps are useful for the reconstruction of the gravitational lensing (chapter 6), of the Integrated Sachs–Wolfe effect (ISW), or for the constraints on non-Gaussianity and isotropy and statistic. In Planck, four component separation algorithms are used and good consistency between them is found in both temperature and polarization (Planck Collaboration. IX. 2015). In Fig.A.2 results in temperature from the four different algorithm are shown, clearly visually consistent outside the mask. In polarization, on angular scales grater then 10° ($\ell \lesssim 20$), systematics are non negligible compared to the expected cosmological signal. Polarization maps for the 2015 release has then been high-pass filtered to remove large angular scales. Residual systematics have been dramatically reduced from 2013 and the 2016 planned release will include all angular scales.

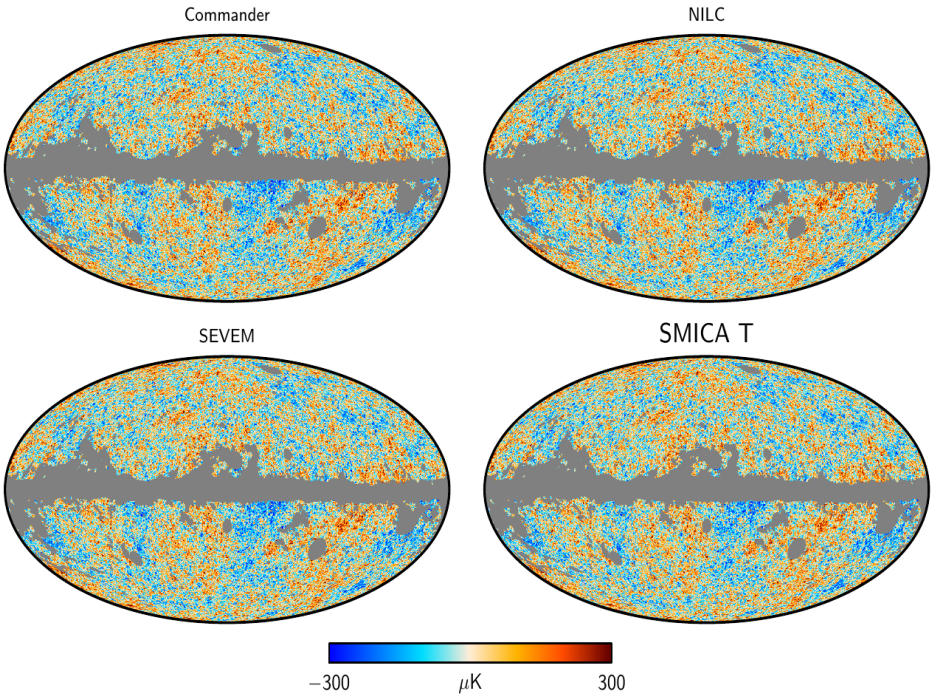

Figure A.2: Component-separated CMB temperature maps at full resolution, FWHM 5′ , $N_{\rm side}$ = 2048. (Planck Collaboration. IX. 2015).

The four methods for component separation are described in Planck Collaboration. XII. (2014) and Planck Collaboration. IX. (2015). Here we just briefly summarise their main characteristics.

There are two types of methods: methods assuming only knowledge of the blackbody spectrum, with few hypothesis on the shape of foreground emissions, and minimising the variance of the CMB compo-

nent (NILC and SEVEM); and methods with explicit parametrisations of the CMB and the foreground models (SMICA and `Commander`).

NILC It is an implementation of the Internal Linear Combination (ILC) method in the *needlet* domain. The ILC methods, first proposed for foreground cleaning in the analysis of COBE data, combine multi-frequency observations to extract the CMB, in general in the spherical wavelet domain. The methods assume that the amplitude of CMB emission is frequency independent in thermodynamic units and that CMB fluctuations are not correlated to foreground signals. The CMB is then estimated as a linear combination of sky maps such that the variance of the estimate is minimum. NILC uses needlets, a special type of spherical wavelets with good localisation in both pixel space and harmonic space. Needlets have compact support in the harmonic domain, while still being very well localised in the pixel domain (Delabrouille et al. 2009). The extension to polarization is achieved performing separation also on E and B modes.

SEVEM The Spectral Estimation Via Expectation Maximisation produces CMB maps cleaning foreground emissions with template subtraction directly in map domain. The coefficients in front of each template are obtained such that the the final CMB maps have minimum variance. In practice, foreground templates are constructed by differentiating pairs of maps at different frequencies to subtract the CMB contribution. Operating in the map domain, the extension to polarization of this algorithm is more natural with the direct inclusion of Q and U maps.

SMICA This method reconstructs a CMB map as a linear combination in the harmonic domain of n input frequency maps with weights that depend on multipole ℓ. In SMICA (Spectral Matching Independent Component Analysis) the model for the data is a superposition of CMB, noise and foregrounds. The latter are not parametrically modelled; instead, the total foreground emission is represented by d templates with arbitrary frequency spectra, angular spectra and correlations. Using a maximum likelihood approach, the best fit values for the arbitrary parameters (the emission law can be supposed known only for one or more components, fixing a model for all the others) that are used to construct the model are found (semi-blind analysis). These are then used to calculate the different weights to combine the frequency maps in the spherical harmonics domain to produce the final CMB map. Maps of the total foreground emission in each frequency channel can also be produced. As for NILC the extension to polarization is done performing separation directly on E and B modes.

`Commander` This is a Bayesian parametric method that works in the map domain. The algorithm is described in some more details in sec. 6.1.1. Physical parametrisation in terms of amplitude and frequency spectra are chosen and then a joint solution for all components is obtained by sampling from the posterior distribution with a Gibbs algorithm. Bayesian sampling methods are described in chapter 4.

This richness in frequencies allows to separate the various foregrounds. Hence, adopting specific models for the different components, a set of maximum-posterior astrophysical parameter maps is obtained (Fig.3.14) for the various foreground emissions (Planck Collaboration. X. 2015). Fig.3.15(a) and 3.15(b) provide an overview of the main components in temperature and polarisation in terms of the brightness temperature rms.

Component separation methods has limitations in the cosmological parameter estimation with respect to the likelihood approach used in this thesis. For example, they do not take into account calibration and beam uncertainties. `Commander` and `SMICA` fit only for relative calibration between frequency channels, but uncertainties from this process are not propagated into the maps. NILC and SEVEM assume perfect

calibration for the frequency channels (Planck Collaboration. IX. 2015). The likelihood approach described in chapter 5 is more suited for precision cosmology and does take into account also these kind of uncertainties.

Component separation maps obtained via the `Commander` algorithm are discussed in sec.3.5.

Remerciements

Vola il tempo lo sai che vola e va,
forse non ce ne accorgiamo
ma più ancora del tempo che non ha età,
siamo noi che ce ne andiamo.

F. De André

Merci à tous ceux qui ont passé du temps à lire ce manuscrit. Donc merci aux membres du jury et surtout merci à mes rapporteurs qui ont du faire ça en août. Désolée pour ma vision un peu personnelle de la syntaxe et la grammaire. Un merci en plus au directeur du LAL Achille Stocchi, sans lui je n'aurais pas pu l'écrire.

Merci à mon directeur de thèse pour avoir répondu *rtfm* juste pour rigoler, pour son regard aigu sur les choses et la patience dont il a fait preuve quand je faisais ma tête de mule. Merci surtout de m'avoir plus d'une fois sauvée de moi même. Merci à mon grognon préféré Mat pour tout le temps qu'il a passé à m'expliquer les mêmes choses. Je suis assez convaincue qu'il faut juste dire que t'as toujours raison. Tu sais combien ça me coûte. Désolée pour la connerie dans le couloir, reste! Merci à Benji pour des scripts dignes de ce nom, pour un peu d'ordre dans mon entropie invasive et pour tout le temps passé à décider quelles chaînes il faillait faire en priorité. Merci à Sophie, il faut un peu de douceur dans ce groupe Planck. Merci à Olivier pour savoir toujours trouver les trucs importants dans le papiers. Merci à François pour avoir toujours de la nouvelle physique à chercher, c'était ça mon idée de la science. Je vous dois mon futur, n'importe où il m'amène.

Merci Gemma pour les MCMC et toutes nos petits dîners avec Giulia et la Pimpa. Merci à Marco pour son style Tucci et à Rosaria pour tous les dimanches à courir derrière Gabi. Merci pour l'encouragement constant, je ne me suis jamais sentie seule. Merci clairement à ma Mangilli, pour pas devenir trop mielleuse je ne nommerai ici que les compositions de fruits pourri du CESFO et le CMB1. Merci à Jonà et au sky patrol quand même. Merci à Erminia, je suis encore inscrite au fan club! Et à Silvia pour le temps que elle m'a dédiée pour le travail et les autres conneries.

Merci à tous les gens des bureaux qui m'ont accueilli à l'APC, avec toujours un carte pour le ministère et une petite demi heure pour quelque match à QPUC. Merci d'avoir fait semblant que je ne savais pas les réponses juste parce que les questions étaient en français. Merci en particulier à Loic qui a tout compris de moi, à Alex pour son style avec moustache, à mes merveilleux Ben Ben et Mamatino. Merci pour les soirées aux diamants, notre heureux petit coin série télé (même si la pizza avec viande c'est pas de la pizza). Donc merci aussi à Pierrrrre et Pauline, à Romain, à Flavian. À Agnès pour son enthousiasme contagieux. Merci à Xou, qui a une grande place dans mon coeur. Merci pour les chansons Disney et les mardi séries ou fils, grande giove! Merci à Sofia et Giulio pour un liste super longue des choses dont le fait d'avoir un toit à Paris.

Merci à Paris pour être si belle et avec des vélib. Même si ça caille et le tomates sont mieux en Italie. Merci aux ritals super cool que j'y ai trouve. Merci à rue d'Alesia 84. Merci à Simone pour les fêtes qui se terminent toujours avec *o' sarracin*. À Francesco pour sa cuisine expérimentale *pappa del cane* et *cenci*. Avec toi on ne peut pas s'ennuyer, *non ti allontanare dal telefono! (e congratulazioni!)*. C'est ton français niveau trois qui nous a fait rencontré les architectes. Merci à Stefano pour sa sagesse sur n'importe quel sujet. Merci à Maria sa douceur sévère et son courage. *Tu puoi!*. Avec vous je me sens à la maison. Merci à la Tonga, sans toi je serai perdue. Merci à Ju&Ri, pour les bulles de savon et toute la compréhension qu'il y a derrière. On a dit tous à Rome, non? Même Barcellona ça me va. Le futur fait moins peur si je nous imagine tous dans la même ville.

Merci aussi aux ritals d'Orsay et famille. À Dario qui a appris à dire *potetre* à tous les russes et aux habitants du 18eme. À Isa qui lui laisse manger la croûte de la pizza et à Matilde qui dit *birra*! Je veux rester avec vous! Venez avec moi! Merci à Sanfo qui nous a quitté pour l'est de la tonne de jambon avec Marta et Anna (et Caterina !) mais qui est capable de tout ajuster quand il revient. À Carmela la gnocca et ses blagues à l'anglaise et pour quand elle se marre pour les blagues folles de Lapo. À Michele qui est le seul qui organise, le seul qui nous gère. À Bracco avec son approche artistique à la vie (et ses colloque Filippo l'enthousisate et Riccardo le beau). Merci au mardi (et mercredi, jeudi, vendredi, lundi) ritals. A Cri, Cate, Silvia, Giorgio et les autres.

Merci aussi aux mercredi (et lundi, si affinités) piscine. A Bongrand et mon chouchou Garrido (Luz tranquille, il est tout pour toi). Pour le soutien du premier et l'absence totale d'empathie de l'autre. Je n'aurais pas survécu sans vous. Désolée de ne pas être au niveau de Sophie pour les blagues crades. Merci à Sophie, pour les blagues crades et pour les muffins. Et pour m'avoir appris le français (je sais tu peux pas tout corriger). Tu me manques! Merci à Olga qui était avec moi déjà à Seillac. Merci aussi pour les chaussettes aux JRJC. Le 21 j'espère être la! Merci à Yasmine qui m'a supportée en pleine crise fin thèse et qui même si elle peut se cacher derriere son violoncelle est une personne très grande. Bien sûre merci à Sandra aussi. Je suis en train de chercher un façon pour couper *holà espinelli* de mon tableau et l'amener avec moi. J'aurais moins de nostalgie. Ça passe tout le tableau en RER?

Un petit merci aux RER, qui marche nickel pour le standard italien Ahh, nickel! Ça me rappelle Tic tac! Donc merci à Rémi et Vlad pour toutes les fois qui ils ont cherché de me tuer. Je vous adore! Avec vous on peut jamais faire un voyage tranquille comme avec le RER qui me ramène toutes les soirs à Paris, loin de la nature d'Orsay dit avec l'accent espagnol d'Hector. Tout le plaisir est pour moi. Tu nous as abandonne pour l'APC, t'as bien fait.

Je profite qu'on (re)parle de l'APC pour remercier Luca et Salvo, et Chiara, avec lesquels j'aurais voulu passer plus de temps. Et mon adoré Poletz qui est toujours la quand je me rends ridicule pour n'importe quelle raison. Merci aussi à le David sans e, Petroni virgola. Bon courage pour ta vie française.

Merci au LAL. À la patience du service mission et personnel pour toutes mes questionnes débiles de bureaucratie variées (ou non). À tous les gens qui sont passés dans mon bureau pour savoir si je tennais le coup. Aux *stagists* et thésards de première et deuxième année. Je suis un peu jalouse que vous restiez.

Mais surtout merci à mes troisième année. Aux groupe *the ultimate redactor*. A Choppy, qui n'à rien à voir avec nous en fait, mais qui avait un compte à régler avec le tracking. Merci pour avoir toujours attendu le noctilien avec moi. Faut juste changer d'avis sur les intellectuels. Et mettre des subjectifs. Ça va de pair. Merci à Marjia pour les spéculos, son humour noir sur la vie et pour nous rappeler que des fois on était trop dépressifs. Merci à Cirillo, Philippeeee viens ici que je te bute!!! Pour son soutien aux dauphins mais surtout à moi! On t'aime tous Cyril, c'est vrai Ouaoua? On aime Ouaoua aussi. Même si tu bouffes trop de burgers. Faut pas écouter Calvin&Hobbes à propos de Pittsburgh. Et t'es un super

cosmologist! Merci à Alexis même si des fois il a des chaussettes blanches, il reste le plus beau d'entre nous. Merci à Pauline pour l'avoir laissé passer de super w-e rédaction avec nous! Il était le seul à savoir jouer au volley. Même Roman était nul comme nous tous. Merci à Roman pour les commands Latex et aussi pour t'être souvent sacrifié pour aller chercher les sushi. J'ai peur que si il y a des ours qui crèvent la dalle c'est parce qu'on a bouffé tous les saumons. Merci à Moretto pour la clef et la place pour la brosse à dent. Pour les fleurs et les cadeaux aussi. J'ai compris que c'était un bon mariage quand on a était d accord sur le choix de Miss Camembert. Coupe pas tes cheveux! Et merci à Laura qui est un conteneur très très grand. C'était un honneur de partager le fond avec toi. Mais viens, c'est temps qu'on finisse.

Un dernier merci à ma famille et mes amis de la vie précédente. *Ailleurs n'est jamais loin quand on aime.*

Bibliography

2012, Fundamental Physics at the Intensity Frontier

Aad, G., Abbott, B., Abdallah, J., et al., Measurement of the Higgs boson mass from the $H \rightarrow \gamma\gamma$ and $H \rightarrow ZZ^* \rightarrow 4\ell$ channels in pp collisions at center-of-mass energies of 7 and 8 TeV with the ATLAS detector. 2014, Phys. Rev. D, 90, 052004

Abazajian, K. N., Arnold, K., Austermann, J., et al., Neutrino Physics from the Cosmic Microwave Background and Large Scale Structure. 2013, ArXiv e-prints, arXiv:1309.5383

Abe, K., Adam, J., Aihara, H., et al., Precise Measurement of the Neutrino Mixing Parameter θ_{23} from Muon Neutrino Disappearance in an Off-Axis Beam. 2014, Phys. Rev. Lett., 112, 181801

Addison, G. E., Dunkley, J., & Spergel, D. N., Modelling the correlation between the thermal Sunyaev Zel'dovich effect and the cosmic infrared background. 2012, MNRAS, 427, 1741, arXiv:1204.5927

Ade, P. A. R., Aikin, R. W., Barkats, D., et al., Detection of B-Mode Polarization at Degree Angular Scales by BICEP2. 2014, Physical Review Letters, 112, 241101, arXiv:1403.3985

Aghanim, N., Desert, F. X., Puget, J. L., & Gispert, R., Ionization by early quasars and cosmic microwave background anisotropies. 1996, A&A, 311, 1, arXiv:astro-ph/9604083

Akeret, J., Seehars, S., Amara, A., Refregier, A., & Csillaghy, A., CosmoHammer: Cosmological parameter estimation with the MCMC Hammer. 2012, ArXiv e-prints, arXiv:1212.1721

Allison, R. & Dunkley, J., Comparison of sampling techniques for Bayesian parameter estimation. 2014, MNRAS, 437, 3918, arXiv:1308.2675

Anderson, L. et al., The clustering of galaxies in the SDSS-III Baryon Oscillation Spectroscopic Survey: Baryon Acoustic Oscillations in the Data Release 10 and 11 galaxy samples. 2014, Mon.Not.Roy.Astron.Soc., 441, 24, arXiv:1312.4877

Andrieu, C. & Moulines, E., On the ergodicity properties of some adaptive MCMC algorithms. 2006, Ann. Appl. Probab., 16, 1462

Arnaud, M., Pratt, G. W., Piffaretti, R., et al., The universal galaxy cluster pressure profile from a representative sample of nearby systems (REXCESS) and the Y_{SZ} - M_{500} relation. 2010, A&A, 517, A92, arXiv:0910.1234

Aseev, V. N., Belesev, A. I., Berlev, A. I., et al., Upper limit on the electron antineutrino mass from the Troitsk experiment. 2011, Phys. Rev. D, 84, 112003, arXiv:1108.5034

ATLAS Collaboration. 2013, Combined measurements of the mass and signal strength of the Higgs-like boson with the ATLAS detector using up to 25 fb^{-1} of proton-proton collision data, Tech. Rep. ATLAS-CONF-2013-014, CERN, Geneva

Aubourg, É., Bailey, S., Bautista, J. E., et al., Cosmological implications of baryon acoustic oscillation (BAO) measurements. 2014, ArXiv e-prints, arXiv:1411.1074

Aver, E., Olive, K. A., Porter, R. L., & Skillman, E. D., The primordial helium abundance from updated emissivities. 2013, J. Cosmology Astropart. Phys., 11, 17, arXiv:1309.0047

Bardenet, R. 2013, Chapter "Monte Carlo methods" in Proceedings of the 2012 IN2P3 School of Statistics (EDP Sciences)

Bashinsky, S. & Seljak, U., Signatures of relativistic neutrinos in CMB anisotropy and matter clustering. 2004, Phys. Rev. D, 69, 083002, arXiv:astro-ph/0310198

Bassett, B. & Hlozek, R. 2010, Baryon acoustic oscillations, ed. P. Ruiz-Lapuente, 246

Bassett, B. A. & Kunz, M., Cosmic distance-duality as a probe of exotic physics and acceleration. 2004, Phys. Rev. D, 69, 101305, arXiv:astro-ph/0312443

Bassett, B. A., Tsujikawa, S., & Wands, D., Inflation dynamics and reheating. 2006, Reviews of Modern Physics, 78, 537, arXiv:astro-ph/0507632

Battaglia, N., Natarajan, A., Trac, H., Cen, R., & Loeb, A., Reionization on Large Scales. III. Predictions for Low-l Cosmic Microwave Background Polarization and High-l Kinetic Sunyaev-Zel'dovich Observables. 2013, ApJ, 776, 83, arXiv:1211.2832

Baumann, D., TASI Lectures on Inflation. 2009, ArXiv e-prints, arXiv:0907.5424

Baumann, D., Jackson, M. G., Adshead, P., et al., Probing Inflation with CMB Polarization. 2009, 1141, 10, arXiv:0811.3919

Bennett, C. L., Halpern, M., Hinshaw, G., et al., First-Year Wilkinson Microwave Anisotropy Probe (WMAP) Observations: Preliminary Maps and Basic Results. 2003, ApJS, 148, 1, arXiv:astro-ph/0302207

Bennett, C. L., Larson, D., Weiland, J. L., et al., Nine-year Wilkinson Microwave Anisotropy Probe (WMAP) Observations: Final Maps and Results. 2013, ApJS, 208, 20, arXiv:1212.5225

Benoit, A., Sirbi, A., & Bradshaw, T. 1997, in Sixth European Symposium on Space Environmental Control Systems, ed. T. D. Guyenne, 400–497

Berg, B. A. 2004, Markov Chian Monte Carlo simulations and their statistical analysis (World Scientific)

Bersanelli, M., Mandolesi, N., Butler, R. C., et al., Planck pre-launch status: Design and description of the Low Frequency Instrument. 2010, A&A, 520, A4, arXiv:1001.3321

Béthermin, M., Daddi, E., Magdis, G., et al., A Unified Empirical Model for Infrared Galaxy Counts Based on the Observed Physical Evolution of Distant Galaxies. 2012, ApJ, 757, L23, arXiv:1208.6512

Betoule, M., Kessler, R., Guy, J., et al., Improved cosmological constraints from a joint analysis of the SDSS-II and SNLS supernova samples. 2014a, arXiv, 4064, arXiv:1401.4064

Betoule, M. et al., Improved cosmological constraints from a joint analysis of the SDSS-II and SNLS supernova samples. 2014b, Astron.Astrophys., 568, A22, arXiv:1401.4064

Betts, S., Blanchard, W. R., Carnevale, R. H., et al., Development of a Relic Neutrino Detection Experiment at PTOLEMY: Princeton Tritium Observatory for Light, Early-Universe, Massive-Neutrino Yield. 2013, ArXiv e-prints, arXiv:1307.4738

Beutler, F., Blake, C., Colless, M., et al., The 6dF Galaxy Survey: baryon acoustic oscillations and the local Hubble constant. 2011, MNRAS, 416, 3017

Beutler, F. et al., The clustering of galaxies in the SDSS-III Baryon Oscillation Spectroscopic Survey: Signs of neutrino mass in current cosmological datasets. 2014, Mon.Not.Roy.Astron.Soc., 444, 3501, arXiv:1403.4599

BICEP2/Keck and Planck Collaborations, Joint Analysis of BICEP2/Keck Array and Planck Data. 2015, Physical Review Letters, 114, 101301, arXiv:1502.00612

Bischoff, C., Hyatt, L., McMahon, J. J., et al., New Measurements of Fine-Scale CMB Polarization Power Spectra from CAPMAP at Both 40 and 90 GHz. 2008, ApJ, 684, 771, arXiv:0802.0888

Blas, D., Lesgourgues, J., & Tram, T., The Cosmic Linear Anisotropy Solving System (CLASS). Part II: Approximation schemes. 2011, JCAP, 07, 034

Blondel, S. 2013, Theses, Université Paris Sud - Paris XI

Bock, J., Chen, D., Mauskopf, P., & Lange, A., A novel bolometer for infrared and millimeter-wave astrophysics. 1995, Space Science Reviews, 74, 229

Box, G. E. P. & Muller, M. E., A Note on the Generation of Random Normal Deviates. 1958, Ann. Math. Statist., 29, 610

Brown, M. L., Ade, P., Bock, J., et al., Improved Measurements of the Temperature and Polarization of the Cosmic Microwave Background from QUaD. 2009, ApJ, 705, 978, arXiv:0906.1003

Calabrese, E., Slosar, A., Melchiorri, A., Smoot, G. F., & Zahn, O., Cosmic microwave weak lensing data as a test for the dark universe. 2008, Phys. Rev. D, 77, 123531, arXiv:0803.2309

Carlstrom, J. E., Holder, G. P., & Reese, E. D., Cosmology with the Sunyaev-Zel'dovich Effect. 2002, ARA&A, 40, 643, arXiv:astro-ph/0208192

Casadei, D. & Kröninger, K., Objective Bayesian analysis of counting experiments with correlated sources of background. 2015, ArXiv e-prints, arXiv:1504.02566

Challinor, A. & Peiris, H. 2009, in American Institute of Physics Conference Series, Vol. 1132, American Institute of Physics Conference Series, ed. M. Novello & S. Perez, 86–140

Chandrasekhar, S., The Maximum Mass of Ideal White Dwarfs. 1931, A&A, 74, 81

Chiang, H. C., Ade, P. A. R., Barkats, D., et al., Measurement of Cosmic Microwave Background Polarization Power Spectra from Two Years of BICEP Data. 2010, ApJ, 711, 1123, arXiv:0906.1181

Christensen, N., Meyer, R., Knox, L., & Luey, B., Bayesian methods for cosmological parameter estimation from cosmic microwave background measurements. 2001, Classical and Quantum Gravity, 18, 2677

Chu, M., Eriksen, H. K., Knox, L., et al., Cosmological parameter constraints as derived from the Wilkinson Microwave Anisotropy Probe data via Gibbs sampling and the Blackwell-Rao estimator. 2005, Phys. Rev. D, 71, 103002

Coles, P. & Lucchin, F., The origin and evolution of cosmic structure. 2002, Wiley Edition

Conley, A., Guy, J., Sullivan, M., et al., Supernova Constraints and Systematic Uncertainties from the First Three Years of the Supernova Legacy Survey. 2011, ApJS, 192, 1, arXiv:1104.1443

Cooke, R. J., Pettini, M., Jorgenson, R. A., Murphy, M. T., & Steidel, C. C., Precision Measures of the Primordial Abundance of Deuterium. 2014, ApJ, 781, 31, arXiv:1308.3240

Couchot, F., Delabrouille, J., Kaplan, J., & Revenu, B., Optimised polarimeter configurations for measuring the Stokes parameters of the cosmic microwave background radiation. 1999, A&AS, 135, 579, arXiv:astro-ph/9807080

Croft, R. A. C., Weinberg, D. H., Bolte, M., et al., Toward a Precise Measurement of Matter Clustering: Lyalpha Forest Data at Redshifts 2-4. 2002, The Astrophysical Journal, 581, 20

Das, S., Louis, T., Nolta, M. R., et al., The Atacama Cosmology Telescope: temperature and gravitational lensing power spectrum measurements from three seasons of data. 2014a, J. Cosmology Astropart. Phys., 4, 14, arXiv:1301.1037

Das, S., Louis, T., Nolta, M. R., et al., The Atacama Cosmology Telescope: temperature and gravitational lensing power spectrum measurements from three seasons of data. 2014b, J. Cosmology Astropart. Phys., 4, 14, arXiv:1301.1037

Das, S. & Souradeep, T., SCoPE: an efficient method of Cosmological Parameter Estimation. 2014, J. Cosmology Astropart. Phys., 7, 18, arXiv:1403.1271

Davidon, W. & Laboratory, A. N. 1959, Variable metric method for minimization, AEC research and development report (Argonne National Laboratory)

Delabrouille, J., Cardoso, J.-F., Le Jeune, M., et al., A full sky, low foreground, high resolution CMB map from WMAP. 2009, A&A, 493, 835, arXiv:0807.0773

Delabrouille, J., Puget, J. ., Gispert, R., & Lamarre, J. ., Scanning strategies for the Planck mission. 1998, ArXiv Astrophysics e-prints, arXiv:astro-ph/9810478

Delubac, T. et al., Baryon Acoustic Oscillations in the Lyalpha forest of BOSS DR11 quasars. 2015, Astron.Astrophys., 574, A59, arXiv:1404.1801

Dodelson, S. 2003, Modern Cosmology, Academic Press (Academic Press), iSBN: 9780122191411

Dodelson, S. & Widrow, L. M., Sterile neutrinos as dark matter. 1994, Phys. Rev. Lett., 72, 17

Dulk, G. A., Radio Emission from the Sun and Stars. 1985, Annual Review of Astronomy and Astrophysics, 23, 169

Dunkley, J., Bucher, M., Ferreira, P. G., Moodley, K., & Skordis, C., Fast and reliable Markov chain Monte Carlo technique for cosmological parameter estimation. 2005, Monthly Notices of the Royal Astronomical Society, 356, 925

Dunkley, J., Calabrese, E., Sievers, J., et al., The Atacama Cosmology Telescope: likelihood for small-scale CMB data. 2013, J. Cosmology Astropart. Phys., 7, 25, arXiv:1301.0776

Dupac, X. & Tauber, J., Scanning strategy for mapping the Cosmic Microwave Background anisotropies with Planck. 2005, A&A, 430, 363, arXiv:astro-ph/0409405

Durrer, R. 2008, The Cosmic Microwave Background (Cambridge University Press)

Efstathiou, G., Myths and truths concerning estimation of power spectra: the case for a hybrid estimator. 2004, Monthly Notices of the Royal Astronomical Society, 349, 603, arXiv:http://mnras.oxfordjournals.org/content/349/2/603.full.pdf+html

Efstathiou, G., Hybrid estimation of cmb polarization power spectra. 2006, Mon.Not.Roy.Astron.Soc., 370, 343, arXiv:astro-ph/0601107

Efstathiou, G., H_0 revisited. 2014, MNRAS, 440, 1138, arXiv:1311.3461

Efstathiou, G. & Migliaccio, M., A simple empirically motivated template for the thermal Sunyaev-Zel'dovich effect. 2012, MNRAS, 423, 2492, arXiv:1106.3208

Eisenstein, D. J. & Hu, W., Baryonic Features in the Matter Transfer Function. 1998, ApJ, 496, 605, arXiv:astro-ph/9709112

Eisenstein, D. J., Hu, W., & Tegmark, M., Cosmic Complementarity: H0 and Omegam from Combining Cosmic Microwave Background Experiments and Redshift Surveys. 1998, The Astrophysical Journal Letters, 504, L57

Eisenstein, D. J., Zehavi, I., Hogg, D. W., et al., Detection of the Baryon Acoustic Peak in the Large-Scale Correlation Function of SDSS Luminous Red Galaxies. 2005, ApJ, 633, 560, arXiv:astro-ph/0501171

Eriksen, H. K., Jewell, J. B., Dickinson, C., et al., Joint Bayesian Component Separation and CMB Power Spectrum Estimation. 2008, ApJ, 676, 10, arXiv:0709.1058

Eriksen, H. K., O'Dwyer, I. J., Jewell, J. B., et al., Power Spectrum Estimation from High-Resolution Maps by Gibbs Sampling. 2004, ApJS, 155, 227, arXiv:astro-ph/0407028

Feldman, G. J. & Cousins, R. D., Unified approach to the classical statistical analysis of small signals. 1998, Phys. Rev. D, 57, 3873, arXiv:physics/9711021

Fendt, W. A. & Wandelt, B. D., Pico: Parameters for the Impatient Cosmologist. 2007, ApJ, 654, 2, arXiv:astro-ph/0606709

Fermi, E., Tentativo di una Teoria Dei Raggi Beta. 1934, Il Nuovo Cimento (1924-1942), 11, 1

Ferrara, A. & Pandolfi, S., Reionization of the Intergalactic Medium. 2014, ArXiv e-prints, arXiv:1409.4946

Filliard, C. 2012, PhD thesis, thèse de doctorat dirigée par Perdereau, O. Champs, particules, matières Paris 11 2012

Fixsen, D. J., Cheng, E. S., Gales, J. M., et al., The Cosmic Microwave Background Spectrum from the Full COBE FIRAS Data Set. 1996, ApJ, 473, 576, arXiv:astro-ph/9605054

Fletcher, R. 1970, Comput. J., 317

Foreman-Mackey, D., Hogg, D. W., Lang, D., & Goodman, J., emcee: The MCMC Hammer. 2013, PASP, 125, 306, arXiv:1202.3665

Franco, D., Jollet, C., Kouchner, A., et al., Mass hierarchy discrimination with atmospheric neutrinos in large volume ice/water Cherenkov detectors. 2013, Journal of High Energy Physics, 2013

Friedman, A., Über die Krümmung des Raumes. 1922, Zeitschrift für Physik, 10, 377

Galli, S., Benabed, K., Bouchet, F. m. c., et al., CMB polarization can constrain cosmology better than CMB temperature. 2014, Phys. Rev. D, 90, 063504

Gelman, A., Roberts, G. O., & Gilks, W. R., Efficient Metropolis Jumping Rules. 1996, In J. M. Bernado et al., Oxford University Press, 599

Gelman, A. & Rubin, D. B., Inference from Iterative Simulation Using Multiple Sequences. 1992, Statistical Science, 7, 457–472

Geman, S. & Geman, D., Stochastic Relaxation, Gibbs Distributions, and the Bayesian Restoration of Images. 1984, Pattern Analysis and Machine Intelligence, IEEE Transactions on, PAMI-6, 721

George, E. M., Reichardt, C. L., Aird, K. A., et al., A measurement of secondary cosmic microwave background anisotropies from the 2500-square-degree SPT-SZ survey. 2014, ArXiv e-prints, arXiv:1408.3161

Geyer, C. J. 1991, Markov Chain Monte Carlo Maximum Likelihood (School of Statistics)

Giachero, A., Artusa, D. R., Avignone, F. T., et al. 2015, in European Physical Journal Web of Conferences, Vol. 95, European Physical Journal Web of Conferences, 4024

Gilks, W. R., Richardson, S., & Spiegelhalter, D. J. 1996, Markov Chian Monte Carlo in practice (Chapmanand Hall/CRC)

Giunti, C. & Kim, C. W. 2007, Fundamentals of Neutrino Physics and Astrophysics (Oxford, UK: Oxford University Press), 1–728

Gonzalez-Morales, A. X., Poltis, R., Sherwin, B. D., & Verde, L., Are priors responsible for cosmology favoring additional neutrino species? 2011, ArXiv e-prints, arXiv:1106.5052

Goodman, J. & Weare, J., Ensemble samplers with affine invariance. 2010, Comm. App. Math. and Comp. Sci, 5

Gorski, K. M., Hinshaw, G., Banday, A. J., et al., On determining the spectrum of primordial inhomogeneity from the COBE DMR sky maps: Results of two-year data analysis. 1994, ApJ, 430, L89, arXiv:astro-ph/9403067

Górski, K. M., Hivon, E., Banday, A. J., et al., HEALPix: A Framework for High-Resolution Discretization and Fast Analysis of Data Distributed on the Sphere. 2005, ApJ, 622, 759, arXiv:astro-ph/0409513

Groom, D. E. et al., Review of particle physics. Particle Data Group. 2000, Eur. Phys. J., C15, 1

Gunn, J. E. & Peterson, B. A., On the Density of Neutral Hydrogen in Intergalactic Space. 1965, ApJ, 142, 1633

Guth, A. H., Inflationary universe: A possible solution to the horizon and flatness problems. 1981, Phys. Rev. D, 23, 347

Guy, J., Astier, P., Baumont, S., et al., SALT2: using distant supernovae to improve the use of type Ia supernovae as distance indicators. 2007, A&A, 466, 11, arXiv:astro-ph/0701828

Guy, J., Sullivan, M., Conley, A., et al., The Supernova Legacy Survey 3-year sample: Type Ia supernovae photometric distances and cosmological constraints. 2010, A&A, 523, A7, arXiv:1010.4743

Haario, H., Saksman, E., & Tamminen, J., An adaptive Metropolis algorithm. 2001, Bernoulli, 7, 223

Hamann, J., Evidence for extra radiation? Profile likelihood versus Bayesian posterior. 2012, J. Cosmology Astropart. Phys., 3, 21, arXiv:1110.4271

Hamann, J., Hannestad, S., Raffelt, G. G., & Wong, Y. Y. Y., Observational bounds on the cosmic radiation density. 2007, J. Cosmology Astropart. Phys., 8, 21, arXiv:0705.0440

Hamimeche, S. & Lewis, A., Likelihood analysis of CMB temperature and polarization power spectra. 2008, Phys. Rev. D, 77, 103013, arXiv:0801.0554

Hanson, D., Hoover, S., Crites, A., et al., Detection of B-Mode Polarization in the Cosmic Microwave Background with Data from the South Pole Telescope. 2013, Physical Review Letters, 111, 141301, arXiv:1307.5830

Haslam, C. G. T., Klein, U., Salter, C. J., et al., A 408 MHz all-sky continuum survey. I - Observations at southern declinations and for the North Polar region. 1981, A&A, 100, 209

Haslam, C. G. T., Salter, C. J., Stoffel, H., & Wilson, W. E., A 408 MHz all-sky continuum survey. II - The atlas of contour maps. 1982, A&AS, 47, 1

Hastings, W. K., Monte Carlo sampling methods using Markov chains and their applications. 1970, Biometrika, 57, 97, arXiv:http://biomet.oxfordjournals.org/content/57/1/97.full.pdf+html

Henrot-Versillé, S., Robinet, F., Leroy, N., et al., Improved constraint on the primordial gravitational-wave density using recent cosmological data and its impact on cosmic string models. 2015, Classical and Quantum Gravity, 32, 045003

Heymans, C., Van Waerbeke, L., Miller, L., et al., CFHTLenS: the Canada-France-Hawaii Telescope Lensing Survey. 2012, MNRAS, 427, 146, arXiv:1210.0032

Hinshaw, G., Larson, D., Komatsu, E., et al., Nine-year Wilkinson Microwave Anisotropy Probe (WMAP) Observations: Cosmological Parameter Results. 2013, ApJS, 208, 19, arXiv:1212.5226

Hivon, E., Górski, K. M., Netterfield, C. B., et al., MASTER of the Cosmic Microwave Background Anisotropy Power Spectrum: A Fast Method for Statistical Analysis of Large and Complex Cosmic Microwave Background Data Sets. 2002, The Astrophysical Journal, 567, 2

Hobson, M. P., Efstathiou, G., & Lasenby, A. N. 2006, General Relativity (Cambridge University Press)

Hobson, M. P., Jaffe, A. H., Liddle, A. R., Mukherjee, P., & Parkinson, D. 2010, Bayesian methods in cosmology (Cambridge University press)

Hou, Z., Keisler, R., Knox, L., Millea, M., & Reichardt, C., How massless neutrinos affect the cosmic microwave background damping tail. 2013, Phys. Rev. D, 87, 083008, arXiv:1104.2333

Hou, Z., Reichardt, C. L., Story, K. T., et al., Constraints on Cosmology from the Cosmic Microwave Background Power Spectrum of the 2500 deg^2 SPT-SZ Survey. 2014, ApJ, 782, 74, arXiv:1212.6267

Hu, W., Structure Formation with Generalized Dark Matter. 1998, ApJ, 506, 485, arXiv:astro-ph/9801234

Hu, W., Angular trispectrum of the cosmic microwave background. 2001, Phys. Rev. D, 64, 083005, arXiv:astro-ph/0105117

Hu, W., Lecture Notes on CMB Theory: From Nucleosynthesis to Recombination. 2008, ArXiv e-prints, arXiv:0802.3688

Hu, W. & Dodelson, S., Cosmic Microwave Background Anisotropies. 2002, ARA&A, 40, 171, arXiv:astro-ph/0110414

Hu, W. & Sugiyama, N., Anisotropies in the cosmic microwave background: an analytic approach. 1995, ApJ, 444, 489, arXiv:astro-ph/9407093

Hu, W. & Sugiyama, N., Small-Scale Cosmological Perturbations: An Analytic Approach. 1996, The Astrophysical Journal, 471, 542

Hu, W. & White, M., A CMB polarization primer. 1997, New A, 2, 323, arXiv:astro-ph/9706147

Hubble, E., A Relation between Distance and Radial Velocity among Extra-Galactic Nebulae. 1929, Proceedings of the National Academy of Science, 15, 168

Ichikawa, K., Neutrino mass constraint from CMB and its degeneracy with other cosmological parameters. 2008, Journal of Physics Conference Series, 120, 022004, arXiv:0711.2622

Ichiki, K., CMB foreground: A concise review. 2014, Progress of Theoretical and Experimental Physics, 2014, arXiv:http://ptep.oxfordjournals.org/content/2014/6/06B109.full.pdf+html

James, F. 2007, Statistical Methods in Experimental Physics (World Scientific)

James, F. & Roos, M., Minuit - a system for function minimization and analysis of the parameter errors and correlations. 1975, Computer Physics Communications, 10, 343

Jefferys, H. 1983, Theory of probability (3d ed.) (Clarendon, Oxford)

Jimenez, R., Kitching, T., Peña-Garay, C., & Verde, L., Can we measure the neutrino mass hierarchy in the sky? 2010, J. Cosmology Astropart. Phys., 5, 35, arXiv:1003.5918

Jones, W. C., Bhatia, R., Bock, J. J., & Lange, A. E., A Polarization Sensitive Bolometric Receiver for Observations of the Cosmic Microwave Background. 2003, Proc. SPIE, 4855, 227

Jones, W. C., Montroy, T. E., Crill, B. P., et al., Instrumental and analytic methods for bolometric polarimetry. 2007, A&A, 470, 771, arXiv:astro-ph/0606606

Kamionkowski, M., Kosowsky, A., & Stebbins, A., Statistics of cosmic microwave background polarization. 1997, Phys. Rev. D, 55, 7368, arXiv:astro-ph/9611125

KATRIN collaboration, KATRIN: A next generation tritium beta decay experiment with sub-eV sensitivity for the electron neutrino mass. 2001, ArXiv High Energy Physics - Experiment e-prints, arXiv:hep-ex/0109033

Kobayashi, M. & Maskawa, T., CP-Violation in the Renormalizable Theory of Weak Interaction. 1973, Progress of Theoretical Physics, 49, 652, arXiv:http://ptp.oxfordjournals.org/content/49/2/652.full.pdf+html

Kofman, L., Linde, A., & Starobinsky, A. A., Reheating after Inflation. 1994, Phys. Rev. Lett., 73, 3195

Kogut, A., Spergel, D. N., Barnes, C., et al., First-Year Wilkinson Microwave Anisotropy Probe (WMAP) Observations: Temperature-Polarization Correlation. 2003, The Astrophysical Journal Supplement Series, 148, 161

Komatsu, E., Dunkley, J., Nolta, M. R., et al., Five-Year Wilkinson Microwave Anisotropy Probe Observations: Cosmological Interpretation. 2009, The Astrophysical Journal Supplement Series, 180, 330

Komatsu, E., Smith, K. M., Dunkley, J., et al., Seven-year Wilkinson Microwave Anisotropy Probe (WMAP) Observations: Cosmological Interpretation. 2011, ApJS, 192, 18, arXiv:1001.4538

Kopp, J., Machado, P. A. N., Maltoni, M., & Schwetz, T., Sterile neutrino oscillations: the global picture. 2013, Journal of High Energy Physics, 5, 50, arXiv:1303.3011

Kosowsky, A., Cosmic microwave background polarization. 1996, Annals of Physics, 246, 49, arXiv:astro-ph/9501045

Kovac, J. M., Leitch, E. M., Pryke, C., et al., Detection of polarization in the cosmic microwave background using DASI. 2002, Nature, 420, 772, arXiv:astro-ph/0209478

Kowalski, M., Rubin, D., Aldering, G., et al., Improved Cosmological Constraints from New, Old, and Combined Supernova Data Sets. 2008, ApJ, 686, 749, arXiv:0804.4142

Lagache, G., Color corrections and unit conversions for HFI, ACT, SPT and Hershel/SPIRE. 2014, Planck internal note

Lagache, G., Puget, J.-L., & Dole, H., Dusty Infrared Galaxies : Sources of the Cosmic Infrared Background. 2005, Annual Review of Astronomy and Astrophysics, 43, 727–768

Lamarre, J.-M., Puget, J.-L., Ade, P. A. R., et al., Planck pre-launch status: The HFI instrument, from specification to actual performance. 2010, A&A, 520, A9

Larson, D., Dunkley, J., Hinshaw, G., et al., Seven-year Wilkinson Microwave Anisotropy Probe (WMAP) Observations: Power Spectra and WMAP-derived Parameters. 2011, The Astrophysical Journal Supplement Series, 192, 16

Lasserre, T., Light sterile neutrinos in particle physics: Experimental status. 2014, Physics of the Dark Universe, 4, 81, arXiv:1404.7352

Lazarian, A. & Finkbeiner, D., Microwave emission from aligned dust. 2003, New Astronomy Reviews, 47, 1107 , proceedings of the Workshop on The Cosmic Microwave Background Radiation and its Polarization

LBNE Collaboration, Adams, C., Adams, D., et al., The Long-Baseline Neutrino Experiment: Exploring Fundamental Symmetries of the Universe. 2013, ArXiv e-prints, arXiv:1307.7335

Leitch, E. M., Kovac, J. M., Halverson, N. W., et al., Degree Angular Scale Interferometer 3 Year Cosmic Microwave Background Polarization Results. 2005, ApJ, 624, 10, arXiv:astro-ph/0409357

Lemaitre, G., Expansion of the universe, A homogeneous universe of constant mass and increasing radius accounting for the radial velocity of extra-galactic nebulae. 1931, MNRAS, 91, 483

Lesgourgues, J., The Cosmic Linear Anisotropy Solving System (CLASS) III: Comparision with CAMB for LambdaCDM. 2011, ArXiv e-prints, arXiv:1104.2934

Lesgourgues, J., Mangano, G., Miele, G., & Pastor, S. 2013, Neutrino Cosmology (Cambridge University Press)

Lesgourgues, J. & Tram, T., The Cosmic Linear Anisotropy Solving System (CLASS) IV: efficient implementation of non-cold relics. 2011, JCAP, 09, 032

Lewis, A., Efficient sampling of fast and slow cosmological parameters. 2013, Phys. Rev. D, 87, 103529, arXiv:1304.4473

Lewis, A. & Bridle, S., Cosmological parameters from CMB and other data: A Monte Carlo approach. 2002, Phys. Rev. D, 66, 103511, arXiv:astro-ph/0205436

Lewis, A. & Challinor, A., Weak gravitational lensing of the CMB. 2006a, Phys. Rep., 429, 1, arXiv:astro-ph/0601594

Lewis, A. & Challinor, A., Weak gravitational lensing of the CMB. 2006b, Phys. Rep., 429, 1, arXiv:astro-ph/0601594

Lorenzo Martinez, N. 2013, Theses, Université Paris Sud - Paris XI

Luzzi, G., Génova-Santos, R. T., Martins, C. J. A. P., De Petris, M., & Lamagna, L., Constraining the evolution of the CMB temperature with SZ measurements from Planck data. 2015, ArXiv e-prints, arXiv:1502.07858

Lyth, D. H. & Liddle, A. R., The Primordial Density Perturbation. 2000, Cambridge University Press

Ma, C.-P. & Bertschinger, E., Cosmological Perturbation Theory in the Synchronous and Conformal Newtonian Gauges. 1995, ApJ, 455, 7, arXiv:astro-ph/9506072

Maggiore, M. 2004, A Modern Introduction to Quantum Field Theory, Oxford Master Series in Physics (Oxford University Press)

Majorana, E., Theory of the Symmetry of Electrons and Positrons. 1937, Nuovo Cim., 14, 171

Maki, Z., Nakagawa, M., & Sakata, S., Remarks on the Unified Model of Elementary Particles. 1962, Progress of Theoretical Physics, 28, 870, arXiv:http://ptp.oxfordjournals.org/content/28/5/870.full.pdf+html

Mangilli, A., Plaszczynski, S., & Tristram, M., Large-scale CMB temperature and polarization cross-spectra likelihoods. 2015, ArXiv e-prints, arXiv:1503.01347

Marsaglia, G., Xorshift RNGs. 2003, Journal of Statistical Software, 8, 1

Mather, J. C., Fixsen, D. J., Shafer, R. A., Mosier, C., & Wilkinson, D. T., Calibrator Design for the COBE Far Infrared Absolute Spectrophotometer (FIRAS). 1999, The Astrophysical Journal, 512, 511

Maurin, L. 2013, PhD thesis, thèse de doctorat dirigée par Rosset, Cyrille [Champs, particules, matières] Paris 7 2013

McMaster, W. H., Polarization and the Stokes Parameters. 1954, Am. J. Phys., 22, 351

Mena, O. & Parke, S., Unified graphical summary of neutrino mixing parameters. 2004, Phys. Rev. D, 69, 117301, arXiv:hep-ph/0312131

Metropolis, N., Rosenbluth, A. W., Rosenbluth, M. N., Teller, A. H., & Teller, E., Equation of State Calculations by Fast Computing Machines. 1953, The Journal of Chemical Physics, 21, 1087

Metropolis, N. & Ulam, S., The Monte Carlo Method. 1949, Journal of the American Statistical Association, 44, 335

Mohapatra, R. N. & Senjanović, G., Neutrino Mass and Spontaneous Parity Nonconservation. 1980, Phys. Rev. Lett., 44, 912

Montroy, T. E., Ade, P. A. R., Bock, J. J., et al., A Measurement of the CMB EE Spectrum from the 2003 Flight of BOOMERANG. 2006, ApJ, 647, 813, arXiv:astro-ph/0507514

Nash, J. C. 1990, Compact Numerical Methods for Computers: Linear Algebra and Function Minimisation (ed. Bristol, England: Adam Hilger)

Okamoto, T. & Hu, W., Cosmic microwave background lensing reconstruction on the full sky. 2003, Phys. Rev. D, 67, 083002, arXiv:astro-ph/0301031

Olive, K. et al., Review of Particle Physics. 2014, Chin.Phys., C38, 090001

Page, L., Hinshaw, G., Komatsu, E., et al., Three-Year Wilkinson Microwave Anisotropy Probe (WMAP) Observations: Polarization Analysis. 2007, ApJS, 170, 335, arXiv:astro-ph/0603450

Palanque-Delabrouille, N., Yèche, C., Borde, A., et al., The one-dimensional Ly-alpha forest power spectrum from BOSS. 2013, A&A, 559, A85, arXiv:1306.5896

Peiris, H. V., Komatsu, E., Verde, L., et al., First-Year Wilkinson Microwave Anisotropy Probe (WMAP) Observations: Implications For Inflation. 2003, ApJS, 148, 213, arXiv:astro-ph/0302225

Penzias, A. A. & Wilson, R. W., A Measurement of Excess Antenna Temperature at 4080 Mc/s. 1965, ApJ, 142, 419

Percival, W. J. & Brown, M. L., Likelihood methods for the combined analysis of CMB temperature and polarisation power spectra. 2006, Mon.Not.Roy.Astron.Soc., 372, 1104, arXiv:astro-ph/0604547

Perlmutter, S., Aldering, G., Goldhaber, G., et al., Measurements of Ω and Λ from 42 High-Redshift Supernovae. 1999, ApJ, 517, 565, arXiv:astro-ph/9812133

Peskin, M. E. & Schroeder, D. V. 1995, An introduction to quantum field theory, Advanced book program (Boulder (Colo.): Westview Press Reading (Mass.)), autre tirage : 1997

Piacentini, F., Ade, P. A. R., Bock, J. J., et al., A Measurement of the Polarization-Temperature Angular Cross-Power Spectrum of the Cosmic Microwave Background from the 2003 Flight of BOOMERANG. 2006, ApJ, 647, 833, arXiv:astro-ph/0507507

Pisanti, O., Cirillo, A., Esposito, S., et al., PArthENoPE: Public algorithm evaluating the nucleosynthesis of primordial elements. 2008, Computer Physics Communications, 178, 956, arXiv:0705.0290

Planck Collaboration, Planck early results. XIX. All-sky temperature and dust optical depth from Planck and IRAS. Constraints on the "dark gas" in our Galaxy. 2011, A&A, 536, A19, arXiv:1101.2029

Planck Collaboration A54, Planck intermediate results. XVI. Profile likelihoods for cosmological parameters. 2014, A&A, 566, A54

Planck Collaboration. I. , Planck 2013 results. I. Overview of products and scientific results. 2014, A&A, 571, A1, arXiv:1303.5062

Planck Collaboration. I., Planck 2015 results. I. Overview of products and scientific results. 2015, ArXiv e-prints, arXiv:1502.01582

Planck Collaboration. Int XXII., Planck intermediate results. XXII. Frequency dependence of thermal emission from Galactic dust in intensity and polarization. 2014, ArXiv e-prints, arXiv:1405.0874

Planck Collaboration. IX., Planck 2015 results. IX. Diffuse component separation: CMB maps. 2015, ArXiv e-prints, arXiv:1502.05956

Planck Collaboration. VI, Planck 2013 results. VI. High Frequency Instrument data processing. 2014, A&A, 571, A6, arXiv:1303.5067

Planck Collaboration. VII, Planck 2015 results. VII. HFI TOI and beam processing. 2015, ArXiv e-prints, arXiv:1502.01586

Planck Collaboration. VIII, Planck 2015 results. VIII. High Frequency Instrument data processing: Calibration and maps. 2015, ArXiv e-prints, arXiv:1502.01587

Planck Collaboration. X., Planck 2015 results. X. Diffuse component separation: Foreground maps. 2015, ArXiv e-prints, arXiv:1502.01588

Planck Collaboration. XI., Planck 2015 results. XI. CMB power spectra, likelihoods, and robustness of parameters. 2015, ArXiv e-prints, arXiv:1507.02704

Planck Collaboration. XII., Planck 2013 results: Component separation. 2014, A&A, 571, A12

Planck Collaboration. XIII., Planck 2015 results. XIII. Cosmological parameters. 2015, ArXiv e-prints, arXiv:1502.01589

Planck Collaboration. XV., Planck 2015 results. XV. Gravitational lensing. 2015, ArXiv e-prints, arXiv:1502.01591

Planck Collaboration. XVI., Planck 2013 results: Cosmological parameters. 2014, A&A, 571, A16

Planck Collaboration XVII, *Planck* 2013 results: Gravitational lensing by large-scale structure. 2014, A&A, 571, A17

Planck Collaboration. XX. , Planck 2013 results. XX. Cosmology from Sunyaev-Zeldovich cluster counts. 2014, A&A, 571, A20, arXiv:1303.5080

Planck Collaboration. XXI., Planck 2013 results. XXI. Power spectrum and high-order statistics of the Planck all-sky Compton parameter map. 2014, A&A, 571, A21, arXiv:1303.5081

Planck Collaboration. XXII., Planck 2015 results. XXII. A map of the thermal Sunyaev-Zeldovich effect. 2015, ArXiv e-prints, arXiv:1502.01596

Planck Collaboration. XXIV, Planck 2015 results. XXIV. Cosmology from Sunyaev-Zeldovich cluster counts. 2015, ArXiv e-prints, arXiv:1502.01597

Planck Collaboration. XXIX. , A29 The thermal Sunyaev-Zeldovic effect-cosmic infrared background correlation. 2015, In preparation

Planck Collaboration. XXVII., Planck 2015 results. XXVII. The Second Planck Catalogue of Sunyaev-Zeldovich Sources. 2015, ArXiv e-prints, arXiv:1502.01598

Planck Collaboration. XXVIII., Planck 2013 results: The Planck Catalogue of Compact Sources. 2014, A&A, 571, A28

Planck Collaboration. XXX., Planck 2013 results. XXX. Cosmic infrared background measurements and implications for star formation. 2013, arXiv, arXiv:1309.0382v1

Planck early results. II., Planck early results. II. The thermal performance of Planck. 2011, A&A, 536, A2, arXiv:1101.2023

Planck Collaboration VI, *Planck* 2013 results: High Frequency Instrument Data Processing. 2014, A&A, 571, A6

Planck Collaboration IX, *Planck* 2013 results: HFI spectral response. 2014, A&A, 571, A9

Planck Collaboration XV, *Planck* 2013 results: CMB power spectra and likelihood. 2014, A&A, 571, A15

Planck Collaboration XXI, *Planck* 2013 results: All-sky Compton parameter map and characterization. 2014, A&A, 571, A21

Planck Collaboration XXX, *Planck* 2013 results: Cosmic infrared background measurements and implications for star formation. 2014, A&A, 571, A30

Planck Collaboration III, *Planck* 2015 results. III. LFI systematic uncertainties. 2015, in preparation

Planck Collaboration VII, *Planck* 2015 results. VII. High Frequency Instrument data processing: Time-ordered information and beam processing. 2015, A&A, submitted, arXiv:1502.01586

Planck Collaboration Int. XXX, Planck intermediate results. XXX. The angular power spectrum of polarized dust emission at intermediate and high Galactic latitudes. 2014, A&A, submitted, arXiv:1409.5738

Plaszczynki, S., Generating long streams of 1/f alpha noise. 2007, Fluctuation and Noise Letters, 07, R1, arXiv:http://www.worldscientific.com/doi/pdf/10.1142/S0219477507003635

Puget, J.-L., Abergel, A., Bernard, J.-P., et al., Tentative detection of a cosmic far-infrared background with COBE. 1996, A&A, 308, L5

QUIET Collaboration: D. Araujo, Bischoff, C., Brizius, A., et al., Second Season QUIET Observations: Measurements of the Cosmic Microwave Background Polarization Power Spectrum at 95 GHz. 2012, The Astrophysical Journal, 760, 145

Racine, B. 2014, PhD thesis, thèse de doctorat dirigée par Patanchon, Guillaume Champs, particules, matières Paris 7 2014

Reichardt, C. L., Stalder, B., Bleem, L. E., et al., Galaxy Clusters Discovered via the Sunyaev-Zel'dovich Effect in the First 720 Square Degrees of the South Pole Telescope Survey. 2013, ApJ, 763, 127, arXiv:1203.5775

Riess, A. G., Filippenko, A. V., Challis, P., et al., Observational Evidence from Supernovae for an Accelerating Universe and a Cosmological Constant. 1998, The Astronomical Journal, 116, 1009

Riess, A. G., Strolger, L.-G., Casertano, S., et al., New Hubble Space Telescope Discoveries of Type Ia Supernovae at z gt 1: Narrowing Constraints on the Early Behavior of Dark Energy. 2007, ApJ, 659, 98, arXiv:astro-ph/0611572

Robertson, H. P., Kinematics and World-Structure III. 1936, ApJ, 83, 257

Rosset, C., Tristram, M., Ponthieu, N., et al., Planck pre-launch status: High Frequency Instrument polarization calibration. 2010, A&A, 520, A13, arXiv:1004.2595

Ruiz-Lapuente, P., Dark energy, gravitation and supernovae. 2007, Classical and Quantum Gravity, 24, 91, arXiv:0704.1058

Sako, M., Bassett, B., Becker, A. C., et al., The Data Release of the Sloan Digital Sky Survey-II Supernova Survey. 2014, ArXiv e-prints, arXiv:1401.3317

Seljak, U., Gravitational Lensing Effect on Cosmic Microwave Background Anisotropies: A Power Spectrum Approach. 1996, ApJ, 463, 1, arXiv:astro-ph/9505109

Seo, H.-J. & Eisenstein, D. J., Baryonic Acoustic Oscillations in Simulated Galaxy Redshift Surveys. 2005, The Astrophysical Journal, 633, 575, n/a

Shaw, L. D., Rudd, D. H., & Nagai, D., Deconstructing the Kinetic SZ Power Spectrum. 2012, ApJ, 756, 15, arXiv:1109.0553

Sievers, J. L., Achermann, C., Bond, J. R., et al., Implications of the Cosmic Background Imager Polarization Data. 2007, ApJ, 660, 976, arXiv:astro-ph/0509203

Skilling, J., Nested Sampling. 2004, AIP Conference Proceedings, 735, 395

Skilling, J., Nested sampling for general Bayesian computation. 2006, Bayesian Anal., 1, 833

Smith, K. M., Cooray, A., Das, S., et al. 2009, in American Institute of Physics Conference Series, Vol. 1141, American Institute of Physics Conference Series, ed. S. Dodelson, D. Baumann, A. Cooray, J. Dunkley, A. Fraisse, M. G. Jackson, A. Kogut, L. Krauss, M. Zaldarriaga, & K. Smith, 121–178

Smith, T. L., Das, S., & Zahn, O., Constraints on neutrino and dark radiation interactions using cosmological observations. 2012, Phys. Rev. D, 85, 023001, arXiv:1105.3246

Smoot, G. F., Bennett, C., Kogut, A., et al., Structure in the COBE differential microwave radiometer first year maps. 1992, Astrophys.J., 396, L1

Steinhardt, P. J. & Turner, M. S., Prescription for successful new inflation. 1984, Phys. Rev. D, 29, 2162

Stompor, R. & Efstathiou, G., Gravitational lensing of cosmic microwave background anisotropies and cosmological parameter estimation. 1999, MNRAS, 302, 735, arXiv:astro-ph/9805294

Story, K. T., Reichardt, C. L., Hou, Z., et al., A Measurement of the Cosmic Microwave Background Damping Tail from the 2500-square-degree SPT-SZ survey. 2012, ArXiv e-prints, arXiv:1210.7231

Story, K. T., Reichardt, C. L., Hou, Z., et al., A Measurement of the Cosmic Microwave Background Damping Tail from the 2500-Square-Degree SPT-SZ Survey. 2013, ApJ, 779, 86, arXiv:1210.7231

Strumia, A. & Vissani, F., Neutrino masses and mixings and... 2006, ArXiv High Energy Physics - Phenomenology e-prints, arXiv:hep-ph/0606054

Sunyaev, R. A. & Zeldovich, I. B., Microwave background radiation as a probe of the contemporary structure and history of the universe. 1980, ARA&A, 18, 537

Sunyaev, R. A. & Zeldovich, Y. B., Small-Scale Fluctuations of Relic Radiation. 1970, Ap&SS, 7, 3

Taburet, N., Hernández-Monteagudo, C., Aghanim, N., Douspis, M., & Sunyaev, R. A., The ISW-tSZ cross-correlation: integrated Sachs-Wolfe extraction out of pure cosmic microwave background data. 2011, MNRAS, 418, 2207, arXiv:1012.5036

Tauber, J. A., Norgaard-Nielsen, H. U., Ade, P. A. R., et al., Planck pre-launch status: The optical system. 2010, A&A, 520, A2

Tegmark, M., How to measure CMB power spectra without losing information. 1997, Phys. Rev. D, 55, 5895, arXiv:astro-ph/9611174

Tegmark, M. & de Oliveira-Costa, A., How to measure CMB polarization power spectra without losing information. 2001, Phys. Rev. D, 64, 063001

The Polarbear Collaboration: P. A. R. Ade, Akiba, Y., Anthony, A. E., et al., A Measurement of the Cosmic Microwave Background B-mode Polarization Power Spectrum at Sub-degree Scales with POLARBEAR. 2014, ApJ, 794, 171, arXiv:1403.2369

Tinker, J., Kravtsov, A. V., Klypin, A., et al., Toward a Halo Mass Function for Precision Cosmology: The Limits of Universality. 2008, ApJ, 688, 709, arXiv:0803.2706

Traschen, J. H. & Brandenberger, R. H., Particle production during out-of-equilibrium phase transitions. 1990, Phys. Rev. D, 42, 2491

Tripp, R., A two-parameter luminosity correction for Type IA supernovae. 1998, A&A, 331, 815

Tristram, M., Filliard, C., Perdereau, O., et al., Iterative destriping and photometric calibration for Planck-HFI, polarized, multi-detector map-making. 2011, A&A, 534, A88, arXiv:1103.2281

Tristram, M. & Ganga, K., Data analysis methods for the cosmic microwave background. 2007, Reports on Progress in Physics, 70, 899, arXiv:0708.1429

Tristram, M., Macías-Pérez, J. F., Renault, C., & Santos, D., XSPECT, estimation of the angular power spectrum by computing cross-power spectra with analytical error bars. 2005, MNRAS, 358, 833, arXiv:astro-ph/0405575

Tucci, M., Martínez-González, E., Toffolatti, L., González-Nuevo, J., & De Zotti, G., Predictions on the high-frequency polarization properties of extragalactic radio sources and implications for polarization measurements of the cosmic microwave background. 2004, MNRAS, 349, 1267, arXiv:astro-ph/0307073

Tucci, M., Martinez-Gonzalez, E., Vielva, P., & Delabrouille, J., Limits on the detectability of the CMB B-mode polarization imposed by foregrounds. 2005, Mon.Not.Roy.Astron.Soc., 360, 935, arXiv:astro-ph/0411567

Tucci, M. & Toffolatti, L., The Impact of Polarized Extragalactic Radio Sources on the Detection of CMB Anisotropies in Polarization. 2012, Advances in Astronomy, 2012, 52, arXiv:1204.0427

Tucci, M., Toffolatti, L., de Zotti, G., & Martínez-González, E., High-frequency predictions for number counts and spectral properties of extragalactic radio sources. New evidence of a break at mm wavelengths in spectra of bright blazar sources. 2011, A&A, 533, 57

Ulam, S., Richtmyer, R. D., & von Neumann, J., STatistical methods in neutron diffusion. 1947, Los Alamos Scientific Laboratory report, LAMS-551

Verde, L., A practical guide to Basic Statistical Techniques for Data Analysis in Cosmology. 2007, arXiv:0712.3028

Viel, M., Haehnelt, M. G., & Springel, V., The effect of neutrinos on the matter distribution as probed by the intergalactic medium. 2010, J. Cosmology Astropart. Phys., 6, 15, arXiv:1003.2422

Walker, A. G., On Milne's theory of world-structure. 1937, Proceedings of the London Mathematical Society, 2-42, 90

Walsh, B., Markov Chain Monte Carlo and Gibbs Sampling. 2004

Weinberg, S., Baryon- and Lepton-Nonconserving Processes. 1979, Phys. Rev. Lett., 43, 1566

Wilks, S. S., The Large-Sample Distribution of the Likelihood Ratio for Testing Composite Hypotheses. 1938, Ann. Math. Statist., 9, 60

Wolfenstein, L., Neutrino oscillations in matter. 1978, Phys. Rev. D, 17, 2369

Yoshimura, M., Catastrophic Particle Production under Periodic Perturbation. 1995, Progress of Theoretical Physics, 94, 873, arXiv:hep-th/9506176

Zaldarriaga, M. & Harari, D. D., Analytic approach to the polarization of the cosmic microwave background in flat and open universes. 1995, Phys. Rev. D, 52, 3276, arXiv:astro-ph/9504085

Zaldarriaga, M. & Seljak, U., All-sky analysis of polarization in the microwave background. 1997, Phys. Rev. D, 55, 1830, arXiv:astro-ph/9609170

Zaldarriaga, M. & Seljak, U. c. v., Gravitational lensing effect on cosmic microwave background polarization. 1998, Phys. Rev. D, 58, 023003

Zaldarriaga, M., Spergel, D. N., & Seljak, U., Microwave Background Constraints on Cosmological Parameters. 1997, ApJ, 488, 1, arXiv:astro-ph/9702157